

**PROCESS-BASED CROSS-SHORE MODELLING
OF BARRED BEACHES**

(met een samenvatting in het Nederlands)

PROEFSCHRIFT

**Ter verkrijging van de graad van doctor aan de Universiteit Utrecht
op gezag van de rector magnificus, Prof. dr. W.H. Gispen,
ingevolge het besluit van het college voor Promoties in het
openbaar te verdedigen op vrijdag 22 november 2002
des middags te 12:45 uur**

door

Berend Tamme Grasmeijer

geboren op 20 augustus 1969 te Delfzijl

Promotores:
Prof.dr.ir. L.C. van Rijn
Prof.dr. J.H.J. Terwindt
Prof.dr. P. Hoekstra

Faculteit Ruimtelijke Wetenschappen
Universiteit Utrecht

Process-based cross-shore modelling of barred beaches

Netherlands Geographical Studies 302

Process-based cross-shore modelling of barred beaches

Bart Grasmeijer

Utrecht 2002

The Royal Dutch Geographical Society/
Faculty of Geographical Sciences, Utrecht University

This publication is identical to a thesis submitted in partial fulfilment of the requirements for the degree of Doctor (Ph.D.) at Utrecht University, The Netherlands, 22 November 2002.

Promotores Prof.Dr.Ir. L.C. van Rijn
Faculteit Ruimtelijke Wetenschappen, Universiteit Utrecht
Prof.Dr. J.H.J. Terwindt
Faculteit Ruimtelijke Wetenschappen, Universiteit Utrecht
Prof.Dr. P.Hoekstra
Faculteit Ruimtelijke Wetenschappen, Universiteit Utrecht

Examination committee:

Prof.Dr.Ir. M.J.F. Stive	Delft University of Technology
Prof.Dr.Ir. J.A. Battjes	Delft University of Technology
Prof.Dr. B. O' Connor	University of Liverpool
Dr.Ir. J. van de Graaff	Delft University of Technology
Dr.Ir. J.S. Ribberink	University of Twente

Acknowledgements

The present work was performed as part of the Coast3D project funded by the European Commission's research program MAST under Contract Number MAS3-CT97-0086. I would like to thank Steve Elgar, Robert Guza and Falk Feddersen for providing the Duck94 data. Background data for Egmond aan Zee was provided by Rijkswaterstaat in the framework of the Kust*2000 program.

ISBN 90-6809-338-X

Copyright © Bart T. Grasmeyer, p/a Faculty of Geographical Sciences, Utrecht University, 2002.

Niets uit deze uitgave mag worden vermenigvuldigd en/of openbaar gemaakt door middel van druk, fotokopie of op welke andere wijze dan ook zonder voorafgaande schriftelijke toestemming van de uitgevers.

All rights reserved. No part of this publication may be reproduced in any form, by print or photo print, microfilm or any other means, without written permission by the publishers.

Printed in the Netherlands by Labor Grafimedia b.v. – Utrecht.

Aan mijn ouders

"No science can be true, unless human reasoning is valid."
C.S. Lewis

Process-based cross-shore modelling of barred beaches

Netherlands Geographical Studies 302

Process-based cross-shore modelling of barred beaches

Bart Grasmeijer

Utrecht 2002

The Royal Dutch Geographical Society/
Faculty of Geographical Sciences, Utrecht University

This publication is identical to a thesis submitted in partial fulfilment of the requirements for the degree of Doctor (Ph.D.) at Utrecht University, The Netherlands, 22 November 2002.

Promotores Prof.Dr.Ir. L.C. van Rijn
Faculteit Ruimtelijke Wetenschappen, Universiteit Utrecht
Prof.Dr. J.H.J. Terwindt
Faculteit Ruimtelijke Wetenschappen, Universiteit Utrecht
Prof.Dr. P.Hoekstra
Faculteit Ruimtelijke Wetenschappen, Universiteit Utrecht

Examination committee:

Prof.Dr.Ir. M.J.F. Stive	Delft University of Technology
Prof.Dr.Ir. J.A. Battjes	Delft University of Technology
Prof.Dr. B. O' Connor	University of Liverpool
Dr.Ir. J. van de Graaff	Delft University of Technology
Dr.Ir. J.S. Ribberink	University of Twente

Acknowledgements

The present work was performed as part of the Coast3D project funded by the European Commission's research program MAST under Contract Number MAS3-CT97-0086. I would like to thank Steve Elgar, Robert Guza and Falk Feddersen for providing the Duck94 data. Background data for Egmond aan Zee was provided by Rijkswaterstaat in the framework of the Kust*2000 program.

ISBN 90-6809-338-X

Copyright © Bart T. Grasmeyer, p/a Faculty of Geographical Sciences, Utrecht University, 2002.

Niets uit deze uitgave mag worden vermenigvuldigd en/of openbaar gemaakt door middel van druk, fotokopie of op welke andere wijze dan ook zonder voorafgaande schriftelijke toestemming van de uitgevers.

All rights reserved. No part of this publication may be reproduced in any form, by print or photo print, microfilm or any other means, without written permission by the publishers.

Printed in the Netherlands by Labor Grafimedia b.v. – Utrecht.

Aan mijn ouders

"No science can be true, unless human reasoning is valid."
C.S. Lewis

Figures	10
Tables.....	15
Voorwoord.....	17
1. Introduction	19
1.1. Central problem definition and objective	19
1.2. Nearshore processes	20
1.2.1. Waves	20
1.2.2. Mean currents	23
1.2.3. Oscillatory flows	27
1.2.4. Sediment transport.....	29
1.3. Nearshore bar formation and migration mechanisms.....	32
1.3.1. Harmonic wave overtake concept.....	32
1.3.2. Breakpoint concept.....	32
1.3.3. Infragravite wave concept	33
1.3.4. Conclusions	35
1.4. Nearshore bar migration mechanisms in a small-scale wave flume.....	35
1.4.1. Introduction	35
1.4.2. Hydrodynamics across a nearshore bar	37
1.4.3. Transport processes over a nearshore bar.....	39
1.4.4. Comparison of small-scale wave flume data and field data	42
1.4.5. Conclusions	45
1.5. Modelling nearshore bar behavior	45
1.5.1. Modelling of hydrodynamics	46
1.5.2. Modelling of sand transport.....	48
1.5.3. Modelling of morphodynamics	49
1.6. Research objectives and outline	51
2. Experimental data	53
2.1. Introduction	53
2.2. Instruments and measurement errors.....	54
2.3. Small-scale laboratory experiments	55
2.4. Large-scale laboratory experiments: Delta Flume.....	59
2.5. Large-scale laboratory experiments: Grosser Wellenkanal.....	60
2.6. Large-scale field experiments: Egmond aan Zee	63
2.6.1. Field site	63
2.6.2. Experimental setting.....	65
2.6.3. Process measurements	69
2.6.4. Basic experimental data.....	72
2.7. Data from earlier experiments	80
3. Modelling of waves and currents in the nearshore.....	81
3.1. Introduction	81
3.2. Model description.....	83

3.2.1.	Wave transformation	83
3.2.2.	Cross-shore flow	85
3.2.3.	Longshore flow	85
3.2.4.	Orbital velocities	86
3.2.5.	Input parameters; fixed and free parameters	89
3.3.	Parametric versus probabilistic approach	90
3.3.1.	Introduction	90
3.3.2.	Comparison with small-scale laboratory data	91
3.3.3.	Comparison with large-scale laboratory data	94
3.3.4.	Comparison with field data, Duck, NC, USA	95
3.3.5.	Comparison with field data, Egmond aan Zee, the Netherlands	101
3.3.6.	Discussion	106
3.3.7.	Conclusions	109
3.4.	Effect of changing free model parameters on model results	109
3.4.1.	Introduction	109
3.4.2.	Effect on model results: qualitatively	111
3.4.3.	Effect on model results: quantitatively (model performance)	119
3.4.4.	Conclusions	126
3.5.	Importance of low-frequency waves	127
3.5.1.	Introduction	127
3.5.2.	Magnitude and origin of low-frequency waves	127
3.5.3.	Conclusions	131
3.6.	Discussion and conclusions	131
4.	Modelling of sediment transport in the nearshore	137
4.1.	Introduction	137
4.2.	Description of transport model	137
4.2.1.	Introduction	137
4.2.2.	Suspended load transport	138
4.2.3.	Bed-load transport	141
4.2.4.	Bed shear stress formulations	141
4.3.	Modelling the bed roughness	144
4.3.1.	Introduction	144
4.3.2.	Principles of bed roughness	145
4.3.3.	Measured bed roughness	145
4.3.4.	Predicting bed roughness	149
4.3.5.	Discussion and conclusions	159
4.4.	Modelling the current-related suspended transport rate	160
4.4.1.	Introduction	160
4.4.2.	Large-scale laboratory experiments	160
4.4.3.	Large-scale field experiments	165
4.4.4.	Discussion and conclusions	170
4.5.	Modelling the wave-related suspended transport rate	171
4.5.1.	Introduction	171
4.5.2.	Wave-related suspended transport formula	173
4.5.3.	Large-scale laboratory experiments	175

4.5.4.	Large-scale field experiments.....	177
4.5.5.	Discussion and conclusions.....	178
4.6.	Modelling the bed-load transport rate.....	179
4.6.1.	Introduction.....	179
4.6.2.	Comparison of bed-load transport formulae.....	180
4.6.3.	Comparison of bed-load formulae using large-scale flume data.....	182
4.6.4.	Comparison of bed-load formulae using field data.....	184
4.6.5.	Discussion and conclusions.....	186
4.7.	Relative contribution of transport components.....	187
4.7.1.	Introduction.....	187
4.7.2.	Measured transport rates.....	188
4.7.3.	Predicted transport rates.....	191
4.8.	Discussion and conclusions.....	194
5.	Modelling of nearshore profile development.....	197
5.1.	Introduction.....	197
5.2.	Model description.....	198
5.3.	Model performance.....	200
5.4.	Sensitivity for free model parameters.....	201
5.4.1.	Introduction.....	201
5.4.2.	Bed roughness.....	202
5.4.3.	Wave front slope.....	203
5.4.4.	Wave-related transport factor.....	204
5.4.5.	Conclusions.....	205
5.5.	Model-data comparison.....	205
5.5.1.	Introduction.....	205
5.5.2.	Storm scale: Laboratory experiments.....	205
5.5.3.	Storm scale (days-weeks): Egmond aan Zee.....	208
5.5.4.	Storm scale (months): Duck, NC, USA.....	214
5.5.5.	Seasonal scale (months): Egmond aan Zee.....	218
5.5.6.	Seasonal scale: a shoreface nourishment.....	222
5.6.	Effect of wave chronology.....	227
5.7.	Discussion and conclusions.....	229
6.	Synthesis.....	233
6.1.	Hydrodynamics.....	233
6.2.	Sediment transport.....	235
6.3.	Morphodynamics.....	237
	Samenvatting.....	240
	Summary.....	241
	Curriculum vitae.....	242
	References.....	243

FIGURES

1.1. Terminology used to describe waves and currents in the nearshore (after Komar, 1998).	20
1.2. Shoaling and breaking of waves across a nearshore profile.	20
1.3. Schematic diagram of a sinusoidal (deep water) wave, a skewed (shoaling) wave, and a skewed and asymmetric (nearly breaking) wave.	21
1.4. Wave groups and bound long waves.	22
1.5. Schematic diagram of the vertical profile of the mean cross-shore and longshore current in the nearshore (after Svendsen and Lorenz, 1989).	23
1.8. Schematic diagram of longshore momentum balance.	26
1.9. Orbital motion under waves approaching the shore.	28
1.10. Ripple height versus peak orbital velocity for a sand bed with a grain diameter D_{50} of 0.24 mm and waves with a period T of 4 s; after the bed form model of Van Rijn (1993).	30
1.11. Transport processes in asymmetric wave motion over a plane bed (left) and a rippled bed (right).	31
1.12. Hydraulic parameters across a barred profile in a small-scale wave flume. A) significant wave height and set-down, B) fraction of breaking waves, C) depth-averaged mean current, measured and computed based on Equation (1.2), D) onshore and offshore high-frequency peak near bed orbital velocities, E) onshore and offshore low-frequency peak near bed orbital velocities, F) bar profile.	37
1.13. Transport rates in a small-scale wave flume based on velocity and concentration measurements across a barred profile. A) net and current-related transport rates, B) high- and low-frequency wave-related transport rates, C) bar profile.	40
1.14. Transport rates and bed level changes across barred profile in small-scale wave flume. A) bed level changes, B) transport rates.	41
1.15. Schematic diagram of vertical distribution of oscillatory transport in field (after Vinent and Green, 1990).	42
1.16. Schematic diagram of oscillatory and mean fluxes (at 0.04 m and 0.1 m above the bed) across a bar profile in the field (after Osborne and Greenwood, 1992).	43
1.17. Roller effect on vertical structure of undertow velocities.	47
2.1. A conceptual view of the small-scale wave flume of Delft University of Technology	56
2.2. Photo showing instruments used in the small-scale wave flume of Delft University of Technology. The instruments are: acoustic sediment transport meter (left), electro magnetic current meter (middle), and pump sampler (right). The profile follower and wave gauge are not shown.	57
2.3. Photo of the Delta Flume of Delft Hydraulics.	59
2.4. A conceptual view of the Delta Flume of Delft Hydraulics.	60
2.5. A conceptual view of the Grosser Wellenkanal of the University of Hannover and the Technical University of Braunschweig.	61
2.6. Photo's of: 1) carriage with which the bed profile was measured during experiments in the Grosser Wellenkanal (top left), 2) 5F-ASTM (three sensors shown) and OBS (top right) mounted at the same elevation as the lowest 5F-ASTM sensor, and 3) Instrumented tripod in which the instruments were mounted (lower left).	62
2.7. Map of the Holland coast showing the Egmond field site. Note that the beach-pole numbering corresponds to the distance in km from Den Helder.	63
2.8. Average wave directions of offshore wave fields based on data from wave buoy YM6 at about 21 m water depth, 30 km from the shore, between 1 January 1990 and 1 January 2000.	64
2.9. Monthly-averaged significant wave height and period based on data from wave buoy YM6 at about 21 m water depth, 30 km from the shore, between 1 January 1990 and 1 January 2000.	64
2.10. The Water and Beach Profiler (Water and Strand Profiler (WESP) in Dutch).	66
2.11. Nearshore bathymetry of the field site near Egmond aan Zee measured on 18 October 1998. The box marks the field site.	67
2.12. Longshore-averaged (over 500 m) cross-shore profile based on 11 profiles measured near the coast of Egmond aan Zee on 18 October 1998. The nearshore bathymetry of the entire field site is shown in Figure 2.11.	67
2.13. Offshore wave conditions during EU-COAST3D pilot campaign; 16 March – 9 May 1998.	68

2.14. Offshore wave conditions during EU-COAST3D main campaign; 12 October – 20 November 1998.	69
2.15. Instruments attached to vertically movable arm on the CRIS. The instruments shown are: three OBS sensors at 0.02, 0.04 and 0.10 m above the bed and an EMF at 0.10 m (lower foreground), 5F-ASTM sensors between 0.10 and 1.0 m above the bed (background) and bed sensor (middle). The pressure sensor mounted at $z = 0.60$ m, two other EMF sensors mounted at $z = 2.0$ and 3.0 m, and the sand ripple profiler are not shown.	70
2.16. CRIS being towed by WESP.	70
2.17. Range of positions at which sand transport measurements were done with the CRIS during the EU-COAST3D pilot and main campaigns.	71
2.18. WESP deploying instrumented tripod.	71
2.19. Depth relative to mean sea level versus cross-shore distance on 18 October 1998 at Egmond, and locations of instruments.	72
2.20. Correlation between H^2 and u_{low} as a function of the relative wave height $H_{1/3}/h$. Each data point is the average of 10 or more tests and the error bars denote the standard error.	73
2.21. Fraction of breaking waves Q_b as a function of the relative wave height $H_{1/3}/h$. Each data point is the average of 10 or more tests and the error bars denote the standard error between the tests.	74
2.22. Sediment grain sizes of bed material versus cross-shore distance on 7 April and 10 November 1998 at Egmond aan Zee.	76
2.23. Depth relative to mean sea level and sediment grain sizes of suspended material versus cross-shore distance during the EU-COAST3D pilot measurement campaign at Egmond aan Zee. The bed profile measured on 7 April 1998 is shown as a reference.	77
2.24. Grain size of suspended sediment versus mobility number during the EU-COAST3D pilot campaign at Egmond aan Zee.	77
3.1. Breaking criterion probabilistic mode (A) and parametric mode (B), where $\tan \alpha =$ bed slope.	83
3.2. Orbital velocity skewness u_{on}/\hat{u} as a function of h/L , based on small-scale wave flume data (TUDB2), large-scale wave flume data (LIPIID) and field data (Egmond aan Zee).	88
3.3. Measured and computed wave heights, TUD B2.	91
3.4. Wave height distributions at all measurement locations for small-scale laboratory TUDB2 tests. For locations see Figure 3.3.	92
3.5. Measured and predicted undertow velocities; TUD B2.	93
3.6. Measured and predicted onshore and offshore near bed peak orbital velocities; TUD B2.	93
3.7. Measured (symbols) and predicted (lines) wave heights using model in parametric and probabilistic mode; Delta Flume LIPII, test 1B.	94
3.8. Measured and predicted undertow velocities using the model in parametric mode and probabilistic mode; Delta Flume LIPII, Test 1B.	95
3.9. Measured and predicted near bed peak orbital velocities using the model in parametric mode and probabilistic mode; Delta Flume LIPII, Test 1B.	95
3.10. Locations of co-located current meters and pressure sensors during the measurement campaign in 1994 near Duck, NC, USA. The bed profile measured on September 21, 1994 is shown as a reference.	96
3.11. Measured and predicted H_{rms} from offshore (top panel) to onshore (bottom panel) versus time; 21-23 September 1994, Duck, NC, USA; for measurement locations see Figure 3.10.	98
3.12. Measured and predicted cross-shore mean current \bar{u} from offshore (D1, top panel) to onshore (D6, bottom panel) versus time; 21-23 September 1994, Duck, NC, USA; for measurement locations see Figure 3.10.	99
3.13. Measured and predicted longshore mean current \bar{v} from offshore (D1, top panel) to onshore (D6, bottom panel) versus time; 21-23 September 1994, Duck, NC, USA; for measurement locations see Figure 3.10.	100
3.14. Model error statistics for waves (A), cross-shore currents (B) and longshore currents (C); 21-23 September 1994, Duck, NC, USA.	101
3.15. Locations of instruments during the measurement campaign in 1998 near Egmond aan Zee, the Netherlands. The bed profile measured on October 26, 1998 is shown as a reference.	101

3.16. Measured (symbols) and modelled (curves) wave height H_{rms} from offshore (E2, top panel) to onshore (E6, bottom panel) versus time; 26-28 October 1998, Egmond aan Zee, the Netherlands.	102
3.17. Measured (symbols) and modelled (curves) cross-shore current \bar{u} from offshore (E1, top panel) to onshore (E7, bottom panel) versus time; 26-28 October 1998, Egmond aan Zee, the Netherlands.	103
3.18. Measured (symbols) and modelled (curves) longshore current \bar{v} from offshore (E1, top panel) to onshore (E7, bottom panel) versus time; 26-28 October 1998, Egmond aan Zee, the Netherlands.	105
3.19. Model error statistics for waves (A), cross-shore currents (B), longshore currents (C), onshore orbital velocity (D) and offshore orbital velocity (C); 26-28 October 1998, Egmond aan Zee, the Netherlands.	106
3.20. Measured, computed and Rayleigh wave height distributions at four locations near the coast of Egmond aan Zee. For locations see Figure 3.15.	107
3.21. Effect of wave-related bed roughness on the predicted wave height variation across a nearshore profile near the coast of Egmond aan Zee, the Netherlands.	111
3.22. Effect of wave-related bed roughness on the predicted longshore current variation across a nearshore profile near the coast of Egmond aan Zee, the Netherlands.	112
3.23. Effect of wave-related bed roughness on predicted cross-shore current variation across a nearshore profile near the coast of Egmond aan Zee, the Netherlands.	112
3.24. Effect of wave-related bed roughness on predicted peak near-bed orbital velocities across a nearshore profile near the coast of Egmond aan Zee, the Netherlands.	113
3.25. Effect of varying the current-related bed roughness on predicted longshore current variation across a nearshore profile near the coast of Egmond aan Zee, the Netherlands.	114
3.26. Effect of varying the breaker criterion on predicted wave height variation across a nearshore profile near the coast of Egmond aan Zee, the Netherlands.	115
3.27. Effect of varying the breaker criterion on predicted longshore current variation across a nearshore profile near the coast of Egmond aan Zee, the Netherlands.	116
3.28. Effect of varying the breaker criterion on predicted cross-shore current variation across a nearshore profile near the coast of Egmond aan Zee, the Netherlands.	116
3.29. Effect of varying the horizontal mixing coefficient on predicted longshore current variation across a nearshore profile near the coast of Egmond aan Zee, the Netherlands.	117
3.30. Effect of varying the wave front slope on predicted cross-shore current variation across a nearshore profile near the coast of Egmond aan Zee, the Netherlands.	118
3.31. Effect of varying the wave front slope on predicted longshore current variation across a nearshore profile near the coast of Egmond aan Zee, the Netherlands.	118
3.32. Cross-shore distribution of the breaker dissipation D_{br} and roller dissipation D_r with $\beta = 0.03$ and $\beta = 0.1$.	119
3.33. Locations of instruments during the measurement campaign in 1998 near Egmond aan Zee, the Netherlands. The bed profile measured on September 26, 1998 is shown as a reference.	120
3.34. Wave model error statistics at Egmond showing the effect of changing the breaker criterion γ . For measurement locations see Figure 3.33.	120
3.35. Wave model error statistics at Egmond showing the effect of changing the wave-related roughness height $k_{s,w}$. For measurement locations see Figure 3.33.	121
3.36. Cross-shore current model error statistics at Egmond showing the effect of changing the breaker criterion γ . For measurement locations see Figure 3.33.	121
3.37. Cross-shore current model error statistics at Egmond showing the effect of the wave-related roughness height $k_{s,w}$. For measurement locations see Figure 3.33.	122
3.38. Cross-shore current model error statistics at Egmond showing the effect of changing the wave front slope β . For measurement locations see Figure 3.33.	122
3.39. Longshore current model error statistics at Egmond showing the effect of changing the breaker criterion γ . For measurement locations see Figure 3.33.	123
3.40. Longshore current model error statistics at Egmond showing the effect of changing the wave-related roughness height $k_{s,w}$. For measurement locations see Figure 3.33.	124

3.41. Longshore current model error statistics at Egmond showing the effect of changing the current-related roughness height $k_{s,c}$. For measurement locations see Figure 3.33.....	124
3.42. Longshore current model error statistics at Egmond showing the effect of changing the horizontal mixing coefficient ε . For measurement locations see Figure 3.33.....	125
3.43. Longshore current model error statistics at Egmond showing the effect of changing the wave front slope β . For measurement locations see Figure 3.33.....	126
3.44. Measured onshore and offshore low-frequency near-bed peak orbital velocities. Flume test TUD B2.....	127
3.45. Correlation function between short wave energy H^2 and co-located long-wave surface elevation η_{low} at $x = 10$ m (for location see Figure 3.44).....	128
3.46. Minimum cross-correlation values across the bar profile.....	129
3.47. Cross-correlation between H^2 and onshore, respectively offshore propagating long wave at $x = 10$ m. For location see Figure 3.44.....	130
3.48. Principle sketch of measured and computed undertow velocities. The measurements generally reveal a shoreward shift of the body of the current profile that is not modelled.....	134
3.49. Roller effect on vertical structure of undertow velocities.....	135
4.1. Ripple length versus significant near bed orbital diameter $d_{0,1/3}$ (A) and ripple height versus significant orbital diameter $d_{0,1/3}$ (B).....	146
4.2. Examples of bed forms measured in the nearshore of Egmond aan Zee, the Netherlands.....	148
4.3. Measured bed forms and near bed concentrations as a function of the mobility number. Egmond aan Zee, the Netherlands.....	148
4.4. Nondimensional ripple height versus mobility number using all data with LWR field data (A) and without LWR field data (B); ripple steepness using all data with LWR field data (C) and without LWR field data (D). Lines denote the Grant and Madsen (1982) model curves.....	152
4.5. Nondimensional ripple height versus mobility number using all data with LWR field data (A) and without LWR field data (B); ripple steepness using all data with LWR field data (C) and without LWR field data (D). Lines denote the Van Rijn (1993) model curves.....	153
4.6. Nondimensional ripple height versus mobility number using all data with LWR field data (A) and without LWR field data (B); ripple steepness using all data with LWR field data (C) and without LWR field data (D). Lines denote the Nielsen (1981) model curves.....	154
4.7. Measured and computed values of η^2 / λ using computed ripple dimensions (lines) and measured ripple dimensions (symbols).....	158
4.8. Effect of bed roughness on predicted time-averaged concentration distribution. Delta Flume tests: A) $H_{1/3} = 1.0$ m, B) $H_{1/3} = 1.25$ m, C) $H_{1/3} = 1.0$ m, D) $H_{1/3} = 1.25$ m, E) $H_{1/3} = 1.5$ m. For all tests: $T_p = 5.0$, $h = 4.5$ m.....	161
4.9. Relative mean absolute errors ε_{ma} between measured and computed concentrations for Delta Flume experiments using four different k_s values.....	162
4.10. Effect of different bed roughness predictors on time-averaged concentration distribution. Delta Flume tests: A) $H_{1/3} = 1.0$ m, B) $H_{1/3} = 1.25$ m, C) $H_{1/3} = 1.0$ m, D) $H_{1/3} = 1.25$ m, E) $H_{1/3} = 1.5$ m. For all tests: $T_p = 5.0$, $h = 4.5$ m.....	163
4.11. Relative mean absolute errors between measured and computed concentrations for Delta Flume experiments using G&M, Van Rijn, Nielsen and modified Nielsen bed roughness predictors.....	164
4.12. Effect of bed roughness on predicted time-averaged concentration distribution for Egmond aan Zee field tests.....	166
4.13. Relative mean absolute errors between measured and computed concentrations for Egmond aan Zee field tests using four different bed roughness values.....	167
4.14. Effect of different bed roughness predictors on predicted time-averaged concentration distribution for Egmond aan Zee field tests, clustered for different values of ψ	168
4.15. Relative mean absolute errors between measured and computed concentrations for Egmond aan Zee field tests using G&M, Van Rijn, Nielsen and modified Nielsen bed roughness predictors....	169
4.16. Measured and predicted class-averaged current-related transport rates (absolute values) in cross-shore direction; effect of bed roughness; Egmond aan Zee field tests.....	170
4.17. Measured and predicted class-averaged current-related transport rates (absolute values) in cross-shore direction; effect of different bed roughness predictors; Egmond aan Zee field tests.....	170

4.18. Ensemble-averaged surface elevation (normalized) and concentration in relation to the phase of the wave cycle for a test with a plane sand bed (upper panel) and a rippled sand bed (lower panel)...	172
4.19. Measured and predicted wave-related suspended transport rates as a function of mobility number. The predictions are based on Equation (4.60) using measured velocities and measured concentrations.	176
4.20. Measured and predicted wave-related suspended transport rates as a function of mobility number and for varying roughness heights. The predictions are based on Equation (4.60) using measured velocities and predicted concentrations.	176
4.21. Measured and computed class-averaged wave-related transport rates in cross-shore direction ($k_{as} = 0.2$); effect of bed roughness; Egmond aan Zee.	178
4.22. Measured and computed class-averaged wave-related transport rates in cross-shore direction ($k_{as} = 0.2$); effect of different bed roughness predictors; Egmond aan Zee.	178
4.23. Bed level changes and resulting total net transport rates during 13.5 hours of testing with irregular waves, $H_{m0} = 1.25$ m, $h = 3.5$ m, $T_p = 5.9$ s, $D_{50} = 0.23$ mm.	183
4.24. Computed class-averaged bed-load transport rates in cross-shore direction; comparison of different bed-load transport models. The computations are based on wave height and velocity measurements near the coast of Egmond aan Zee, The Netherlands.	185
4.25. Vertical distribution of transport components; Egmond aan Zee field tests.	189
4.26. Relative contribution of measured current-related, high-frequency wave-related and low-frequency wave-related transport rates as a function of the mobility number. The error bars around each class-averaged value equal the standard error.	190
4.27. Relative contribution of bed-load to the total-load transport rate. A relative contribution of 0.5 would indicate equal bed-load and suspended load contributions.	190
4.28. Relative contribution of computed current-related and high-frequency wave-related transport rates as a function of the mobility number. The error bars around each class-averaged value equal the standard error.	191
4.29. Wave-related transport efficiency coefficient k_{as} as a function of mobility number, see Equation (4.76).	192
4.30. Relative contribution of computed current-related and high-frequency wave-related transport rates as a function of the mobility number, using the efficiency factor as described by Equation (4.76) The error bars around each class-averaged value equal the standard error.	192
4.31. Comparison of measured and computed transport rates.	193
4.32. Comparison of measured and computed transport rates.	194
5.1. Diagram of modules in morphological model.	199
5.2. Definition sketch of profile model.	200
5.3. Predicted bed profile development after 18 hours showing the effect of changing the current-related roughness $k_{s,c}$. LIPIID Delta Flume experiments, test 1B.	202
5.4. Predicted bed profile development after 18 hours showing the effect of changing the wave-related roughness $k_{s,w}$. LIPIID Delta Flume experiments, test 1B.	203
5.5. Predicted bed profile development after 18 hours showing the effect of changing the wave front slope β . LIPIID Delta Flume experiments, test 1B.	204
5.6. Predicted bed profile development after 18 hours showing the effect of changing the wave-related transport factor k_{as} . LIPIID Delta Flume experiments, test 1B.	204
5.7. Measured and predicted morphological changes after 18 hours for Test 1 B of the LIPIID experiments in the Delta Flume of Delft Hydraulics.	207
5.8. Measured and predicted morphological changes after 18 hours for Test 1 B of the LIPIID experiments in the Delta Flume of Delft Hydraulics.	207
5.9. Three-dimensional plot of the nearshore bathymetry near the coast of Egmond aan Zee, The Netherlands, 23 March 1998.	208
5.10. Wave height (A), wave period (B), wave direction (C) and tide level (D) versus time measured at 5 km from the shore at Egmond. Vertical dashed lines separate the selected periods.	209
5.11. Measured longshore-averaged profiles (solid lines) and standard error band (dashed lines) near Egmond.	210

5.12. Measured and predicted morphological changes near Egmond for period 1 between October 18 and October 24 (A), period 2 between October 24 and October 31 (B), and period 3 between October 31 and November 12 (C).....	213
5.13. Map of the Atlantic East coast of the USA showing the Duck field site.....	214
5.14. Wave height (A), wave period (B), wave direction (C) and tide level (D) versus time measured at 800 m from the shore at Duck, NC. Vertical dashed lines separate the selected periods.....	215
5.15. Measured longshore averaged profiles (solid lines) and standard error band (dashed lines) near Duck, NC, USA.....	216
5.16. Measured and predicted morphological changes near Duck for period 1 between September 21 and October 4 (A), period 2 between October 10 and October 14 (B), and period 3 between October 12 and October 20 (C).	218
5.17. Wave height (A), wave period (B), wave direction (C) and wind-driven water level setup (D) versus time measured during a 10 month period in 1998 at Egmond aan Zee.....	220
5.18. Probability of exceedance of H_{rms} during winter and summer period at Egmond.....	220
5.19. Measured longshore-averaged profiles (solid lines) and standard error band (dotted lines) versus cross-shore distance near Egmond.....	221
5.20. Measured and predicted medium-term morphological changes near Egmond for period 1 between 11 May 1998 and 24 October 1998 (A), and period 2 between 24 October 1998 and 25 February 1999 (B). See Figure 5.17 for wave conditions.....	222
5.21. Longshore-averaged cross-shore profiles before and after implementation of a shoreface nourishment in 1999 near the coast of Egmond aan Zee.	222
5.22. Wave height (A), wave period (B), wave direction (C) and wind-driven water level setup (D) versus time measured between September 1999 and September 2000 at Egmond. Vertical dashed lines separate the selected periods.	223
5.23. Longshore-averaged cross-shore profiles of the nearshore zone of Egmond aan Zee before (A) and after (B-F) the implementation of a shoreface nourishment on the seaward flank of the outer nearshore bar.....	225
5.24. Measured and predicted medium-term morphological changes after the implementation of a shoreface nourishment near Egmond aan Zee for period 1 between September 1999 and May 2000 (A) and period 2 between May 2000 and September 2000 (B).....	226
5.25. Effect of changing the wave chronology on the predicted short-term (A) and medium-term (B) morphological changes.	228
6.1. Principle sketch of measured and computed undertow velocities. The measurements generally reveal a shoreward shift of the body of the current profile that is not modelled.	237
6.2. Roller effect on vertical structure of undertow velocities.....	238

TABLES

2.1. Measurement accuracies.....	54
2.2. Experimental data from small-scale wave flume experiments done in 1994 at Delft University of Technology, The Netherlands.....	58
2.3. Experimental data from large-scale wave flume experiments done in 1997 in the Delta Flume of Delft Hydraulics, The Netherlands.....	60
2.4. Experimental data from large-scale wave flume experiments done in 1999 in the Grosser Wellenkanal of the Universities Hannover/Braunschweig, Germany.....	61
2.5. Parameters available from items (only items used in this thesis are given here) deployed during the EU-COAST3D measurements campaign near the coast of Egmond aan Zee.....	72
2.6. Maximum longshore current velocities due to tide, wind and wave driven processes near the coast of Egmond aan Zee, the Netherlands.....	74
2.7. Class-averaged experimental data from CRIS measurements.....	79
3.1. Overview of available data sets.....	90
3.2. Input parameters for all model runs.....	91
3.3. Qualification of error ranges of process parameters.....	97

3.4. Offshore conditions Egmond aan Zee, Netherlands, 28 October 1998, 08:00 h.....	110
3.5. Free model parameters, default values and range for sensitivity tests.....	110
4.1. Bed form types and dimensions as measured across a nearshore profile near the coast of Egmond aan Zee, the Netherlands.....	147
4.2. Relative mean absolute error between measured and predicted ripple dimensions.....	155
4.3. Relative mean absolute error between measured and predicted ripple dimensions.....	156
4.4. Basic experimental data of Delta Flume experiments.....	160
4.5. Predicted ripple roughness heights for Delta flume experiments from G&M, Van Rijn, Nielsen and modified Nielsen bed roughness predictors.....	162
4.6. Predicted ripple roughness heights (class-averaged values) for Egmond aan Zee field tests from G&M, Van Rijn, Nielsen and modified Nielsen bed roughness predictors.....	167
4.7. Measured depth-integrated suspended transport rates and computed bed-load transport rates.....	184
4.8. Comparison of transport rates measured in the Grosser Wellenkanal.....	184
4.9. Class-averaged bed-load transport rates computed with 1) Van Rijn model using $H_{1/3}$, 2) Van Rijn model using H_{rms} , 3) Ribberink model, 4) Bailard model.....	186
5.1 Qualification of error ranges.....	200
5.2. Applied range of model- and process parameters and default settings for sensitivity analysis based on LPIID model runs.....	201
5.3. Model runs, free model parameters, and Brier Skill Scores for LPIID, Test 1B, Delta Flume.....	206
5.4. Model runs and Brier skill scores on storm scale at Egmond.....	212
5.5. Model runs and Brier skill scores for Duck.....	217
5.6. Model settings and Brier skill scores for nourishment model runs Egmond aan Zee.....	227

VOORWOORD

Het schrijven van dit proefschrift was me niet gelukt zonder de hulp en steun van een groot aantal mensen die op de één of andere manier hebben bijgedragen aan de totstandkoming ervan. In onderstaande wil ik deze mensen bedanken voor hun bijdrage.

Ten eerste wil ik mijn eerste promotor en dagelijks begeleider *Leo van Rijn* bedanken. Ik heb de afgelopen jaren zeer plezierig met hem samen gewerkt. Ik heb mij op een vakgebied begeven waar zijn gedrevenheid mij soms tot wanhoop dreef, maar veel vaker zeer motiveerde om 'dat ook nog even uit te zoeken'. Leo, ik hoop dat de lijnen in de figuren dik genoeg zijn en ik ben met veel plezier je telefonische helpdesk geweest voor Word en Excel. De constructieve commentaren van mijn tweede promotor *Joost Terwindt* op de concept versies van dit proefschrift heb ik zeer gewaardeerd. Zijn nauwlettendheid in de beoordeling van de structuur van het proefschrift is de kwaliteit zeker ten goede gekomen. Ik heb veel profijt gehad van de inhoudelijke commentaren van mijn derde promotor *Piet Hoekstra*. Het is een voorrecht de eerste AIO te mogen zijn die onder zijn hoogleraarschap promoveert. Hij was een deskundig manager tijdens de veldcampagnes van het Europese COAST3D project.

Een belangrijk deel van de gegevens verwerkt in dit proefschrift is verzameld tijdens metingen bij de kust van Egmond aan Zee in het kader van het Europese COAST3D project. Het project werd gefinancierd door het onderzoeksprogramma MAST onder contractnummer MAS3-CT97-0086. Ik ben de deelnemers aan dit project dankbaar voor de gezellige sfeer en de goede en nauwe samenwerking. Alle veldmetingen heb ik uitgevoerd met mijn collega, veldpartner en kamergenoot *Arjan de Boer* met wie ik met erg veel plezier heb samengewerkt. Wanneer ik hem even een figuurtje liet zien leidde dat steevast tot discussies waarbij er meer vragen kwamen dan antwoorden. Ik wil speciaal de bestuurders van de WESP *Johan de Baare* en *Sjors Berepoot* van Rijkswaterstaat bedanken voor de prima samenwerking tijdens de meetcampagnes. We hebben heel wat uren doorgebracht boven de brekende golven. En natuurlijk *Luc Overmars*, *Gerard Kool*, *Evan Lont*, *Henk Halfweg*, *Albert Wittink*, *Jan Zwering* en *Chris Roosendaal* van Rijkswaterstaat voor de logistiek en management van de veldcampagnes en het operationeel maken en houden van de instrumentatie. *Tjip Vonk*, kustkenner en meetnestor, voor zijn grote inzicht en praktijkervaring die een zeer belangrijke spil in de veldcampagnes bij Egmond aan Zee zijn geweest. Van het Fysische Geografisch Laboratorium wil ik uiteraard *Bas van Dam*, *Henk Markies*, *Marcel van Maarseveen*, *Jaap van Barneveld* en *Theo Tiemissen* bedanken. Niet alleen voor het bedenken, ontwerpen en construeren van nieuwe meettechnieken zoals de beweegbare arm op de CRIS maar ook voor hun inzet bij het operationeel houden van de instrumentatie, in weer en wind, bij nacht en ontij. Koude overnachtingen zonder matras in een container op het strand werden niet geschuwd om de volgende dag weer op tijd te kunnen beginnen. En reken maar dat je nat en koud wordt als je in oktober de hele dag in de regen staat de sleutelen. *Baukje*, *Marc* en *Martijn* dank ik voor de bijdrage aan het onderzoek in het kader van hun onderwijsprogramma en *Roger*, *Arno* en *Daan* voor hun enthousiaste ondersteuning in het veld.

I would like to thank *Steve Elgar*, *Robert Guza* and *Falk Feddersen* for providing the Duck94 data.

Ik dank de vele collega's en oud-collega's van de vakgroep Fysische Geografie voor de gezellige atmosfeer die nodig is om dit werk te kunnen doen maar het vooral ook te kunnen relativeren. *Gerben Ruessink* voor de vele discussies over een breed scala aan onderwerpen die een belangrijke invloed hebben gehad op de koersbepaling in dit proefschrift en voor zijn uitvoerige commentaar op concepthoofdstukken. *Marlous van der Meer* voor haar lieve steun in alles, voor het aanhoren van mijn gemopper bij de laatste loodjes en voor het maken van figuren. *Aart Kroon* voor zijn motiverende begeleiding tijdens de KUST*2000 veldcampagnes en zijn constructieve commentaar op hoofdstuk 4 in dit proefschrift. *Klaas Houwman* voor zijn systematische opzet van data analyse waarvan ik dankbaar gebruik heb gemaakt en voor zijn hulp bij mijn programmeerwerk. Mijn lieve kamergenote *Susanne Quartel* voor de zin en onzin die we uitwisselen en voor de rode wijn. Voorts wil ik *Irene van Enckevort*, *Sandra Vermeer*, *Nicholas Grunnet*, *Ton Hoitink*, *Maarten Kleinhans*, *Bas van Maren* en *Pim van Santen* bedanken.

Mijn broer *Jeroen Grasmeijer* bedank ik voor zijn unieke vriendschap en steun. Wij hoeven nauwelijks woorden te spreken om elkaar te begrijpen. Ik bedank *Esther Grasmeijer* voor haar lieve betrokkenheid, *Aaron Grasmeijer* voor het samen zingen van poesje mauw voor de telefoon en *Sarah Grasmeijer* voor haar mooie lach.

Tot slot en boven iedereen wil ik mijn *ouders* bedanken. Zij hebben mij in staat gesteld de keuzes te maken dit geleid hebben tot dit proefschrift. Maar boven alles hebben ze mij de dingen geleerd die in wetenschap nooit te vinden zullen zijn. Dingen van veel grotere waarde dan er in een proefschrift vermeld zou kunnen worden. Want de wetenschap beschrijft slechts een beperkte aanblik, een klein aspect van de totale werkelijkheid.

1. INTRODUCTION

1.1. CENTRAL PROBLEM DEFINITION AND OBJECTIVE

The nearshore topography of a more or less dissipative beach is often characterized by the presence of one or more bars parallel to the shoreline. Waves break on these nearshore bars reducing the level of wave energy reaching the shore and in this way acting as a natural breakwater (Carter and Balsillie, 1983). Over long time spans (years), the bar systems often show a cyclic cross-shore behaviour, in which a bar is generated near the shoreline in water depths of 1-2 m, migrates offshore through the surf zone to depths of about 4-6 m and finally decays in the outer nearshore zone in depths of 5-7 m (Ruessink and Kroon, 1994; Wijnberg, 1995; Shand et al., 1999). Superimposed on these long-term changes are weekly and monthly fluctuations of the bar system (Van Enckevort, 2001). While the averaged yearly cross-shore migration rates are in the order of 0.01 m/day, the weekly fluctuations are in the order of 1 m/day. Offshore migration rates, related to storm events, are typically larger than onshore migration rates. Monthly fluctuations can be related to seasonal variations in the offshore wave climate (Van Enckevort, 2001). The trigger in the behavior of a nearshore bar system seems to be the outer bar (in the case of more than one bar). The degeneration of the outer bar is followed by the onset of offshore migration of the inner bar. Although much study has been done on the morphological behavior of a nearshore bar system (e.g. Sallenger et al., 1985; Lippmann et al., 1993; Ruessink et al., 2000), the hydrodynamic processes involved and the associated net sediment transport rates under the influence of wave action and wave- and tide-induced currents are still poorly understood. The generation and maintenance of longshore bars is commonly associated with the shoaling and breaking of high-frequency waves, possibly in combination with the generation of low-frequency wave effects in the surf zone. Much of the knowledge on these small-scale processes is incorporated in present day morphodynamic coastal profile models. Question is however, whether our present knowledge on driving processes and conditions is adequate to successfully predict the morphological changes on different time scales. Coastal profile models are commonly used for hind- and forecasting studies of nearshore bathymetry, often in response to human interference in the nearshore, for instance related to implementation of shoreface nourishments. They are developed to predict the short-term hydrodynamic and sediment transport processes on storm scale with time spans of days to weeks. On seasonal scale with time spans of months, process-based models are not expected to produce realistic results because of the build up of errors (De Vriend, 1997). However, to what extent and on which time scales process-based models can be used is not yet clear. It is therefore the central objective of this thesis to improve the understanding of hydrodynamic and sediment transport processes across a barred profile and how this knowledge can be incorporated in a state-of-the-art coastal profile model. The second objective that will be addressed is to what extent a coastal profile model is capable of predicting nearshore morphological changes on the time scale of storms and seasons, simplifying the coastal system to a longshore-averaged 2-D system.

1.2. NEARSHORE PROCESSES

Hydrodynamic and sediment transport processes that can be observed in the nearshore zone of a dissipative beach are shortly discussed here. Figure 1.1 illustrates the terminology used to describe the nearshore morphology, waves and currents herein. The nearshore zone is defined as the region from the beach to the location where waves start breaking on the outer nearshore bar (in case of more than one bar). The offshore is defined as the region seaward of the nearshore zone. The surf zone is defined as the region between the point where waves start breaking just seaward of the outer nearshore bar, and the beach. The swash zone is defined as the region where the waves run-up on the beach.

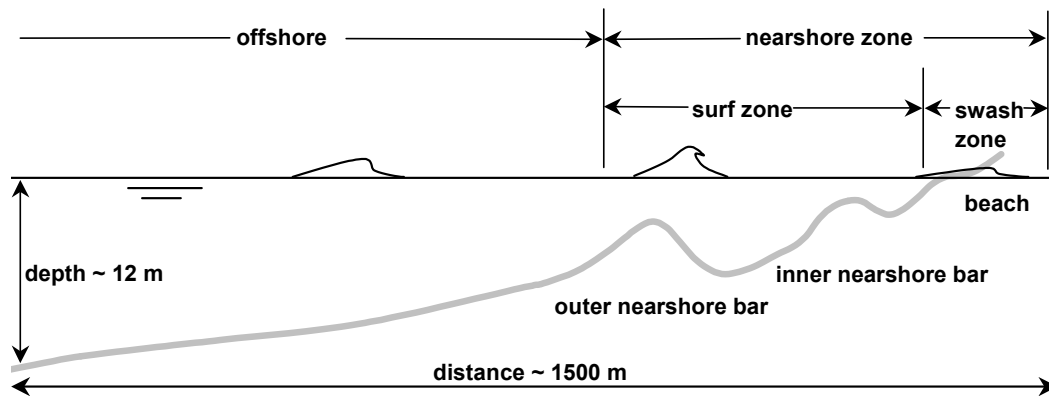


Figure 1.1. Terminology used to describe waves and currents in the nearshore (after Komar, 1998).

1.2.1. WAVES

Waves approaching the shore undergo a systematic transform. In the offshore region, the wave height decreases as a result of energy dissipation due to bottom friction (Figure 1.2).

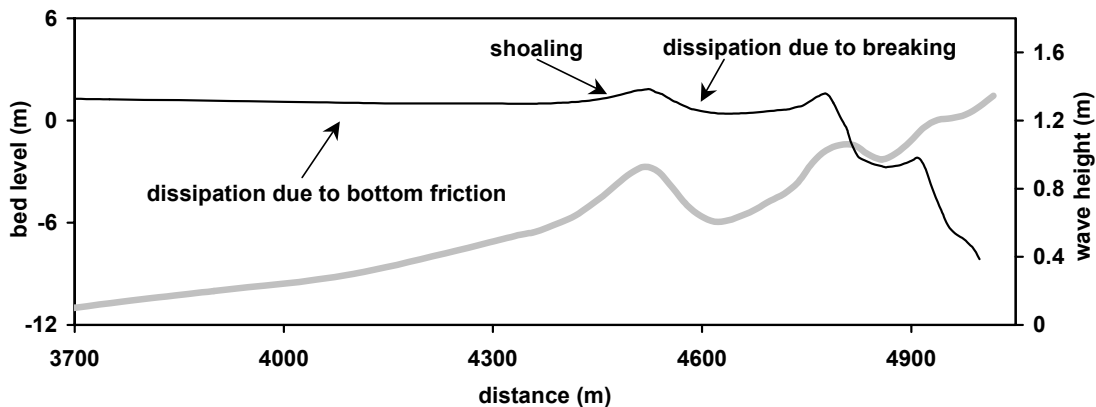


Figure 1.2. Shoaling and breaking of waves across a nearshore profile.

As waves propagate further shoreward, the wave celerity and wavelength decrease and wave height increases (shoaling), leading to an increase of wave steepness. Waves approaching the shore under an angle gradually reorient (refraction), near the beach eventually leading to the wave crest moving parallel to the shoreline ($\theta = 0^\circ$).

Besides the change in height and length, waves also undergo a change in form. Deep-water waves have a more or less sinusoidal shape (Figure 1.3). Reaching water depths not far beyond the surf zone the waveform becomes skewed with sharply peaked crests and broad, flat troughs. This is consistent with the theory of Stokes (1847), which predicts that the onshore velocity associated with the wave crest is stronger and of shorter duration than the offshore velocity associated with the wave trough. Shoaling and nearly breaking waves also show a vertical asymmetry or a tendency to become pitched forward, commonly referred to as wave asymmetry (Elgar and Guza (1985).

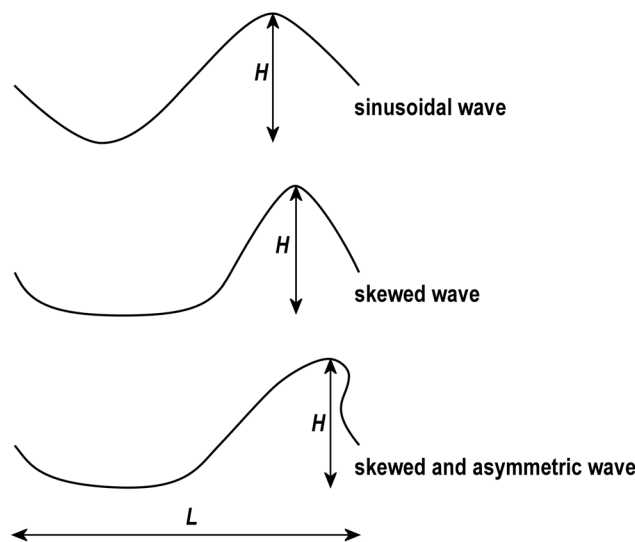


Figure 1.3. Schematic diagram of a sinusoidal (deep water) wave, a skewed (shoaling) wave, and a skewed and asymmetric (nearly breaking) wave.

Figure 1.3 shows the skewed and asymmetric waveform of a shoaling, nearly breaking wave. Generally the Stokes type theories or other wave theories with waves of permanent form such as cnoidal wave theory do not incorporate wave asymmetry because the harmonic components remain phase-locked and in phase with the primary component. The pitching forward of a wave represents a phase shifting of the harmonic components relative to the primary component and eventually leads to wave breaking. Battjes (1988) provides an excellent discussion of the onset of breaking (breaking criteria), types of breaking waves, and the transformation of waves in the surf zone and of the resultant motions. Waves propagating over a nearshore bar, break on the bar and cease breaking as the water depth increases again moving further shoreward in the bar trough. The process may repeat itself on an inner nearshore bar. After the start of wave breaking, the turbulent kinetic energy produced by wave breaking continues carrying momentum in the form of a roller over several wavelengths. This has an important effect on the mean flow forcing.

Besides the short wave motion, long or infragravity waves ($20 \text{ s} < T < 100 \text{ s}$) may also be manifest in the nearshore. The long wave motion is highly correlated to the short wave motion. Seaward of the surf zone, the grouped structure of short waves excites a secondary forced long wave that is bound to the wave groups and has a 180-degree phase difference with the short wave envelope (Figure 1.4). As the short waves propagate onshore into shallower water, the bound long wave progressively lags behind the wave groups (Elgar and Guza, 1985; Elgar and Guza, 1985). Eventually, as the short waves break, the bound long wave is released as a free wave (List, 1992; Ruessink, 1998a; Grasmeyer and Van Rijn, 1999). Long wave heights between 0.01 and 0.5 m have been measured in the nearshore of a dissipative beach (Ruessink, 1998a). The importance of the long wave motion relative to the short wave motion increases moving shoreward. Long wave heights of several decimeters up to a meter have been measured in wave run-up on the beach (Elgar and Guza, 1985; Ruessink, 1998a)

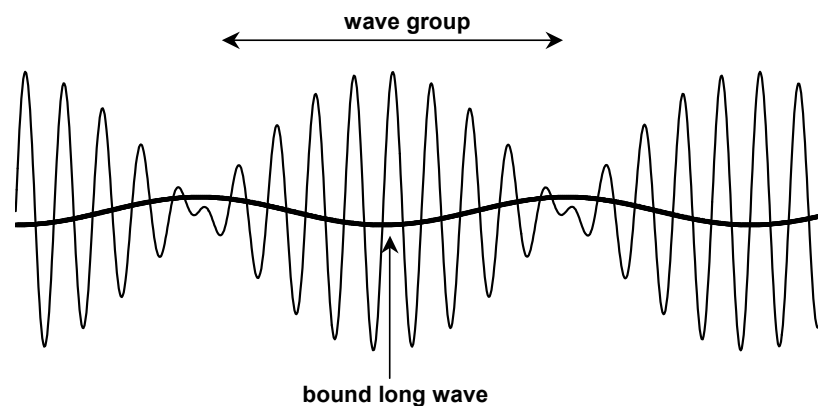


Figure 1.4. Wave groups and bound long waves.

The nearshore wave field can be modelled in different ways. Two classes of wave models can be distinguished, differing mainly in their formulations and the field of application. In the first, phase-averaged, class of models, the wave field is modelled in terms of the wave energy density, which can be based on a single representative wave height (parametric or single wave approach), or on discrete series of wave height classes (probabilistic, multi-wave or wave-by-wave approach). These models average the processes involved over at least one wave period. Examples of parametric models are those of Battjes and Janssen (1978) and Thornton and Guza (1983). Examples of probabilistic models are those of Mase and Iwagaki (1982), Dally (1992) and Van Rijn and Wijnberg (1996). Their computational efficiency makes them feasible for use in engineering models. However, they can include the effect of long waves and wave asymmetry only in an approximate manner. The second, phase resolving, class of models simulates the wave conditions across a coastal profile by a model based on the Boussinesq equations. It has been shown that a Boussinesq-based model can provide potentially accurate predictions of the wave skewness and asymmetry for shoaling and breaking waves (e.g. Eldeberky and Battjes, 1996). Examples of Boussinesq-based models are those of Madsen et al. (1997) and Rakha (1998). They can also incorporate nonlinear effects, such as the generation of bound long waves and resonant interactions.

However, these models are computationally intensive, and therefore difficult to employ in time-dependent nearshore morphodynamic models.

1.2.2. MEAN CURRENTS

When waves reach the shore and break, they generate currents that are superimposed on, for example, tide-induced currents.

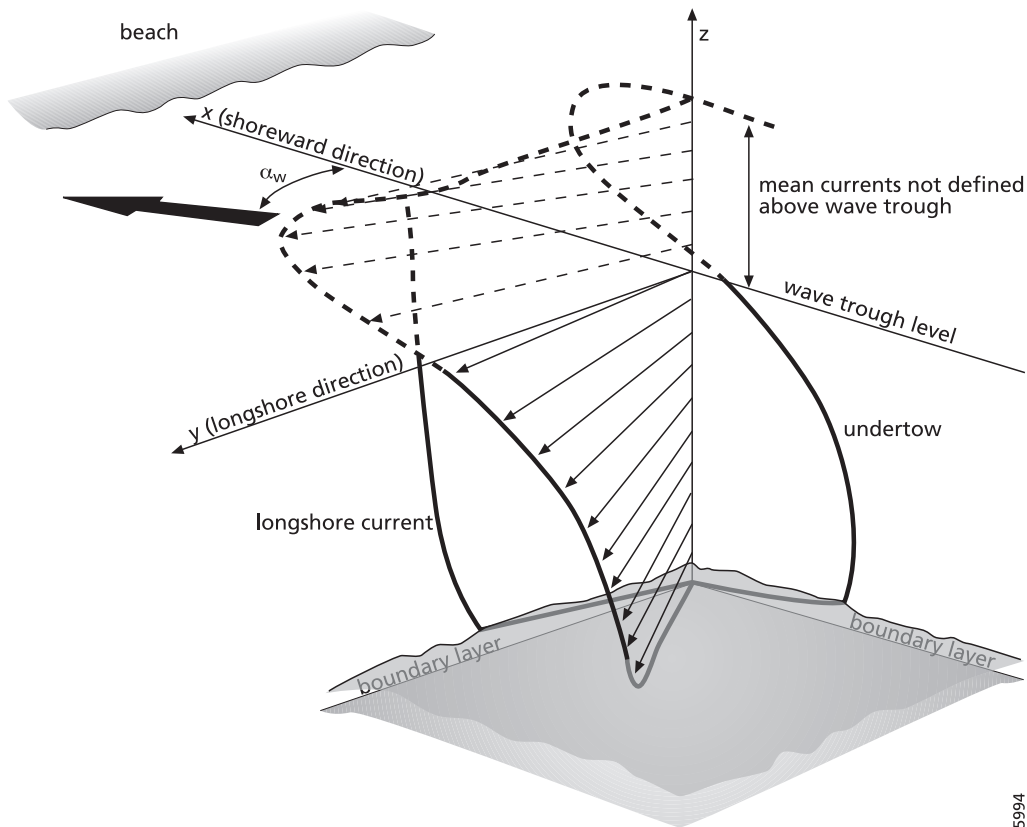


Figure 1.5. Schematic diagram of the vertical profile of the mean cross-shore and longshore current in the nearshore (after Svendsen and Lorenz, 1989).

Considering the 2D situation only, there are two wave-induced mean currents that dominate water movements in the nearshore: 1) cross-shore mean currents related to mass compensation under breaking waves, and 2) longshore mean currents generated by an oblique wave approach. These two mean current types can be considered as components of a continuum flow field. The resulting wave-induced mean current structure is illustrated in Figure 1.5. These nearshore currents in combination with the stirring action of the waves are important for transportation of sediment and are therefore significant factors in morphological changes.

Cross-shore current

Waves approaching the coast undergo changes due to refraction, shoaling and breaking. This affects the wave-induced contribution of horizontal momentum (radiation stress) to

the mean balance of momentum. Important factors determining the momentum balance are: 1) local conservation of mass over the vertical, 2) shear stress at the wave trough level, 3) shear stress at the bottom, 4) vertical variation of the eddy viscosity (turbulence). Of these, the local conservation of mass determines the magnitude of the undertow under breaking waves (Svendsen, 1984a; Svendsen, 1984b). Wave-induced onshore mass flux in the region between the wave crest and trough, including the contribution from breaking wave rollers is compensated by the net offshore undertow. The other three factors determine the vertical structure of the undertow profile.

Bagnold (1940) made the first documented observation of cross-shore currents. Dyhr-Nielsen and Sørensen (1970) gave a qualitative explanation of the generation of an onshore-directed current under shoaling waves and an offshore-directed current under breaking waves. Svendsen (1984b) has focused on the role of turbulence in undertow dynamics and parameterized this in the form of a wave roller. Since the wave roller in a breaking wave is advected with the wave front, its presence affects the mass transport. Moreover, the shear stress between the roller and the underlying wave surface acts upon the vertical undertow profile.

Davidson-Arnott and McDonald (1989) measured surface waves and nearshore water motion across the straight outer bars of a multiple parallel bar system at Wasaga Beach, Georgian Bay, Ontario. Mean cross-shore flows during storms, measured at 0.1 m above the bed, were offshore, with speeds of -0.04 to -0.10 m/s during moderate storms and -0.25 m/s during intense fall storms.

Greenwood and Osborne (1990) measured the waves, currents and mean water level set-up across a barred profile. Near the bed the cross-shore mean currents were offshore directed, ranging between -0.02 and -0.20 m/s. The currents decreased towards the water surface. Higher up in the water column both onshore and offshore directed currents were measured. The mean currents in the highest measurement point (1 m above the bed) ranged between +0.05 and -0.05 m/s.

Gallagher et al. (1998) measured waves and currents for about 2 months at nine locations along a cross-shore transect near the coast of Duck, NC, USA. The current meters were positioned at elevations between 0.4 and 1.0 m above the bed. The water depth ranged between 1 and 4 m. The significant wave height at 8 m water depth ranged between 0.1 and 4.0 m. The magnitude of the observed cross-shore mean current ranged between -0.05 and -0.70 m/s. The largest cross-shore currents occurred just shoreward of the bar crest and near the beach. It is noted that these velocities were measured at one elevation above the bed. No measurements of the vertical structure of the cross-shore flow were done.

Kuriyama and Nakatsukasa (1999) analyzed waves and currents measured along a field observation pier at the Kashima coast of Japan facing the Pacific Ocean. The current meters were positioned at about mid water depth, between 1 and 2 m above the bed. The water depth h in which the current meters were installed ranged between 2 and 4 m. The

significant wave height $H_{1/3}$ measured at 6 m water depth ranged between 0.8 and 2.6 m. The magnitude of the observed cross-shore mean current ranged between -0.05 and -0.40 m/s. The largest cross-shore current occurred on the bar crest or just shoreward of it. These velocities were measured at one or two elevations above the bed. No measurements of the vertical structure of the cross-shore flow were done.

Garcez Faria et al. (2000) examined the vertical and horizontal structure of the mean undertow across a barred beach, based on field data measured at Duck, NC, USA. Measured undertows were found to be maximum near the crest and the shoreward slope of the bar. The vertical structure was found to be the classic parabolic shape associated with strong wave-breaking turbulence (Svendsen, 1984a). In the inner trough region (shoreward of the bar), the undertow was found to be weak, and almost no vertical structure was seen. At the seaward slope of the bar, the vertical structure was found to be nearly uniform with depth.

Generally, the field observations of the undertow across a barred profile show strong undertow velocities near the bar crest or just shoreward of it (see also Smith et al., 1992; Haines and Sallenger, 1994). Largest value measured in the field in this region is about -0.70 m/s. The vertical structure of the undertow in this region of strong breaker waves often shows a parabolic shape with relatively large offshore-directed velocities in the lower part of the water column and small offshore-directed or even onshore-directed velocities in the upper part. Undertow velocities measured seaward of the bar and in the shoreward trough region are smaller than those near the bar crest and the vertical structure of the undertow velocities is more uniform. Many existing undertow models fail to predict correctly the mass flux under breaking waves and hence the magnitude of the undertow velocities just shoreward of a bar crest (Garcez Faria et al., 2000).

Longshore current

Breaking of obliquely incident waves results in excess longshore momentum flux, which drives a longshore current parallel to the coastline. For an irregular wave field, with waves breaking at different cross-shore locations, this momentum input is spread in the cross-shore, providing a natural smoothing of the forcing. Given the cross-shore distribution of the forcing due to the breaking waves, the longshore current velocity distribution can be computed from the wave-averaged and depth-integrated longshore momentum equation (see Figure 1.6). Excess longshore momentum flux induces a longshore force Rr on the water column. A shear force T brought about by a longshore-directed current velocity balances this force. Traditionally, it was assumed that the transfer of momentum from the waves to the current occurs instantaneously. However, it has been realized more recently that the turbulent kinetic energy produced by wave breaking continues carrying momentum in the form of a roller and that it is only with the dissipation of this kinetic energy (roller dissipation) that the mean flow forcing occurs. Svendsen (1984b) originally proposed the concept of a wave roller, a region of intense turbulence that lies on and is advected with the steep face of the breaking wave. Therefore, advection of the roller can cause shoreward shifts in current forcing patterns.

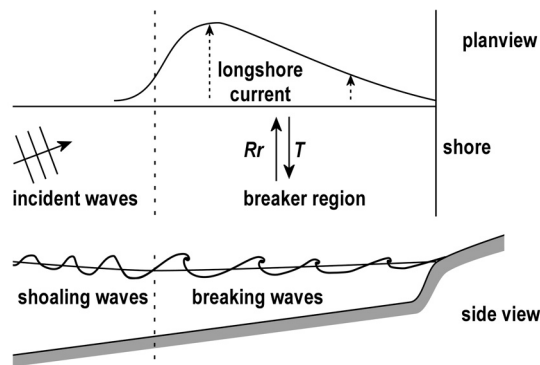


Figure 1.6. Schematic diagram of longshore momentum balance.

Besides waves, the tidally induced longshore gradient in the mean water level also generates a longshore current.

Greenwood and Sherman (1982) measured the horizontal and vertical structure of the longshore flow near the coast of Wendake Beach, Georgian Bay, Canada. Electromagnetic current meters were installed in water depths of 3-4 m at two locations across an inner nearshore bar, at three positions in the vertical. During a storm with an offshore significant wave height of 1.3 m and a peak period of 5 s, depth-averaged mean currents between 0.21 and 0.28 m/s were measured. The maximum mean variability between the three positions in the vertical was only about 10%, i.e. the profiles were fairly uniform.

Thornton and Guza (1986) measured waves at 14 locations and currents at 24 locations along a cross-shore transect near Leadbetter Beach, California, USA. The mean nearshore slope varied between 0.03 and 0.06. No nearshore bar was apparent. The winds were generally light during the measurement period. The incident waves were almost entirely derived from the deep ocean resulting in a narrow band swell. The H_{rms} wave height in 9 m depth ranged between 0.26 and 0.56 m. Plunging breakers were most often observed in the surf zone. The wave angles at breaking were moderately large ($\sim 5^\circ$) resulting in occasionally strong longshore currents (up to 0.50 m/s) depending on the wave height. Maximum longshore current was often located at 15-20 m shoreward of the mean breaker line and at 10-20 m from the shore in 1-2 m water depth.

Gallagher et al. (1998) measured waves and currents for about 2 months at nine locations along a cross-shore transect near the coast of Duck, NC, USA. The current meters were positioned at elevations between 0.4 and 1.0 m above the bed. The water depth ranged between 1 and 4 m. The significant wave height at 8 m water depth ranged between 0.1 and 4.0 m. Longshore currents between 0.05 and 1.20 m/s were measured. The maximum longshore current was often located close to the bar crest.

Kuriyama and Nakatsukasa (1999) analyzed waves and currents measured along a field observation pier at the Kashima coast of Japan facing the Pacific Ocean. The current meters were positioned at about mid water depth, between 1 and 2 m above the bed. The water depth h in which the current meters were installed ranged between 2 and 4 m. The significant wave height $H_{1/3}$ measured at 6 m water depth ranged between 0.8 and 2.6

m. Longshore currents between 0.05 and 0.60 m/s were measured. The maximum longshore current was often located close to the bar crest or just shoreward of it. The cross-shore distribution of the longshore current often showed a strong decrease in the bar trough and an increase again near the beach.

Houwman (2000) measured waves and currents at 6 locations along a cross-shore transect near the coast of Terschelling, The Netherlands. Two current meters were installed at each measurement location. The current meters were positioned at 0.25 and 0.75 m above the bed. The significant wave height $H_{1/3}$ at 17 m water depth ranged between 0.05 and 3 m. Longshore currents between 0.05 and 0.75 m/s were measured. Although the number of measurement locations was too few to get a good picture of the longshore current gradients, the maximum longshore current appeared to be located close to the bar crests.

Generally, field observations of the longshore current velocities across a barred profile show the current to be strongest near the bar crest or just shoreward of it. Although model predictions of the longshore current are generally in better agreement with observations than predictions of the undertow, there is still much discussion on the cross-shore distribution of the wave-driven longshore current velocity. Where the observations occasionally show a rather broad distribution with the maximum longshore current in the trough of the bar, models tend to predict narrow jets over the bar where momentum input is concentrated by breaking. Research has focused on four mechanisms to explain the large mixing and apparent shoreward shift of the forcing pattern. The first explanation lies in the presence of low-frequency instabilities of the longshore current (shear waves). These have been suggested to provide important mixing on barred coasts. Secondly, advection by the undertow may be important in the exchange of longshore flow momentum, broadening the longshore current profile (Houwman, 2000). Thirdly, dispersive mixing is caused by the interaction of the longshore currents and the undertow. According to Putrevu and Svendsen (1992) this mixing is an order of magnitude stronger than the direct turbulent mixing. It depends crucially on the vertical profile of the currents in the nearshore, in particular in the longshore direction. Finally, the importance of the wave roller has been investigated as a mechanism for spreading and delaying the input of momentum from the incident wave to the water column. This provides an effective mechanism for offsetting the current maximum into the bar trough (e.g. Ruessink et al., 2001).

1.2.3. OSCILLATORY FLOWS

Oscillatory flows in the nearshore are commonly subdivided into three main categories based on their period of oscillation: 1) short wave oscillatory motions with periods between 0 and 20 s, 2) infragravity wave oscillations with periods between 20 and 100 s, 3) shear instabilities with periods between 100 and 1000 s. Their main characteristics are briefly discussed here.

Short waves ($T < 20$ s)

The water particle displacement of short waves approaching the shore is shown schematically in Figure 1.7. In deep water the motion of the wave is not influenced by

the topography of the seabed. As waves enter shallow water near the shore, friction and interference from the seabed cause the circular path of the water particles to be squeezed into an ellipse. Eventually, the path is reduced to a simple back and forth motion.

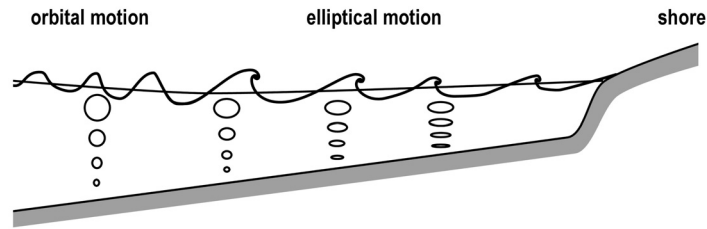


Figure 1.7. Orbital motion under waves approaching the shore.

The change in shape of the path of the water particles involves a change in the wave orbital velocities as well. In shoaling waves, the shoreward velocity associated with the wave crest is stronger and of shorter duration than the offshore velocity associated with the wave trough, known as wave skewness. This is consistent with the theory of Stokes (1847). The wave skewness S can be defined as

$$S = \frac{u_{on}}{u_{on} + u_{off}} \quad (1.1)$$

where u_{on} and u_{off} are the onshore and offshore peak orbital velocity, respectively. The wave skewness varies between 0.50 and 0.75. According to Isobe and Horikawa (1982) the maximum wave skewness takes the value of about 0.70, and decreases with beach slope. A maximum wave skewness of about 0.75 has been observed in the field (Van Rijn and Walstra, 2002).

Shoaling and nearly breaking waves also show a tendency to become pitched forward, commonly referred to as wave asymmetry (Elgar and Guza, 1985). As the water depth decreases, the waves evolve through a slightly skewed, somewhat asymmetrical shape, toward a highly asymmetrical, unskewed, sawtooth-like shape (Elgar and Guza, 1985); Doering and Bowen, 1987). Isobe and Horikawa (1982) parameterized a hybrid wave theory, which combines Stokes 5th order wave theory with cnoidal 3rd order wave theory to compute the wave orbital motion, and introduced two parameters to represent the skewness and asymmetry of the wave orbital motion. The hybrid wave theory has been adapted for use in process-based cross-shore profile models (Stripling and Damgaard, 1997; Grasmeijer and Van Rijn, 1998).

Infragravity waves (20 s < T < 100 s)

Short waves approaching the shore often have a grouped structure. It is well known that associated with this pattern of alternating high and low waves is a long wave forced by the radiation stress variations due to the change in wave height (Longuet-Higgins and Stewart, 1964). In case of shoaling non-breaking waves the bound long wave dominates the long wave motion. As the waves propagate onshore into shallower water, the bound long wave progressively lags behind the wave groups (Elgar and Guza, 1985). At wave breaking the bound long wave is gradually being released as a free long wave, but is

still correlated with the wave groups outside the surf zone. In this transition zone the long wave travels at bound long wave speed as long as wave grouping remains. In the zone of saturated breaking, where waves are poorly grouped, the bound long wave is fully released, traveling at $(gh)^{1/2}$ (Grasmeijer and Van Rijn, 1999). A second type of long wave motion in the nearshore is that of the breakpoint-forced long wave. The grouped structure of the short waves causes the breakpoint to vary with time. Only the high waves break in the deep water of the outer surf zone while all waves break in the shallow water of the inner surf zone. The intermittent breaking in the outer surf zone causes a variation in radiation stress that drives this breakpoint-forced long wave. During storm conditions, in the surf zone, the infragravity oscillations in current velocity may reach values of up to 1 m/s, accounting for up to 80% of the total spectral energy (Russell, 1993).

Shear instabilities ($100 \text{ s} < T < 1000 \text{ s}$)

Besides mean currents and oscillatory wave motions with periods between 0 and 100 seconds, a substantial level of energy in the nearshore velocity field can be found in oscillations with periods of the order 10^2 seconds. Oltman-Shay et al. (1989) made the first documented field observation of these oscillations in the longshore current inside the surf zone. Their field data showed a regular oscillation in the longshore current velocity, with a period of $\sim 200\text{-}400$ s. These shear instabilities in the wave driven longshore current are commonly referred to as shear waves. They are advected with the longshore current with a phase speed of one third to half the maximum longshore current velocity. The occurrence of shear instabilities is significantly influenced by the beach profile (Reniers et al., 1997). Shear waves occur on barred beaches but do not occur on non-barred beaches. Their root-mean-square horizontal velocities can exceed 0.30 m/s (Oltman-Shay et al., 1989). They can contribute up to 93% of the total velocity variance for long waves between 100 and 1000 s (Miles et al., 2002).

1.2.4. SEDIMENT TRANSPORT

The dynamics of sediment transport are complex under wave and current forcing. Hydrodynamic processes that have been identified as significant contributors to the cross-shore sediment transport in the nearshore zone include mean cross-shore currents, short waves, infragravity waves and shear waves (Jaffe et al., 1984; Huntley and Hanes, 1987; Osborne and Greenwood, 1992; Russell, 1993; Ruessink et al., 1998; Ruessink et al., 1999a; Miles et al., 2002). Most field studies on sediment transport show that the mean cross-shore currents and the short waves make the largest contributors to the total net sediment transport in the nearshore, inducing an on- and offshore transport, respectively. The skewness of the horizontal orbital motion (higher forward velocity and lower backward velocity) causes an onshore-directed oscillatory transport rate, while the undertow induced by breaking waves causes an offshore-directed mean transport rate.

Sediment transport rates by infragravity waves ($20 \text{ s} < T < 100 \text{ s}$) are often found to be of subordinate magnitude in the outer nearshore zone. However, as the other two components are about equal in magnitude and opposite sign, the transport rate by long

waves may not be ignored. It is often offshore directed, related to the presence of bound long waves that give a backward motion under the high waves, where the sediment concentrations are high. The presence of bound long waves could therefore change the direction of the net suspended transport from being onshore to being offshore directed (Ruessink et al., 1999a; Deigaard et al., 1999). During storm conditions, in the intertidal zone near the beach, the infragravity component may dominate the oscillatory transport rate and may, together with an offshore-directed mean transport component, be responsible for beach erosion (Russel, 1993).

Shear waves ($100 \text{ s} < T < 1000 \text{ s}$) may also contribute to the total cross-shore transport. In the intertidal zone, Miles et al. (2002) found the cross-shore transport due to shear waves to be directed offshore and to account for about 16% to the total cross-shore transport. The mean component dominated the cross-shore transport in this region, accounting for up to 69% of the total. Somewhat further offshore in the surf zone Aagaard and Greenwood (1995) found the cross-shore transport due to shear waves to account for up to 65% of the total.

Hydrodynamic processes that are of less importance to the net suspended transport in the nearshore zone are mean flows under non-breaking wave conditions and free infragravity waves (Ruessink et al., 1998).

As regards the height at which the sediment transport takes place, in deeper offshore waters outside the surf zone the sediment transport processes are generally concentrated in a layer close to the seabed because the mean currents and wave motion are relatively weak. The suspended load transport rate becomes increasingly important with increasing strength of the tide and wave-induced currents in shallow water. Sediment is being stirred up by the wave motion and transported by the mean currents. Ripple-related vortices or turbulent current mixing can intensify suspension of sediment. These mechanisms cause the suspended load to dominate in the surf zone.

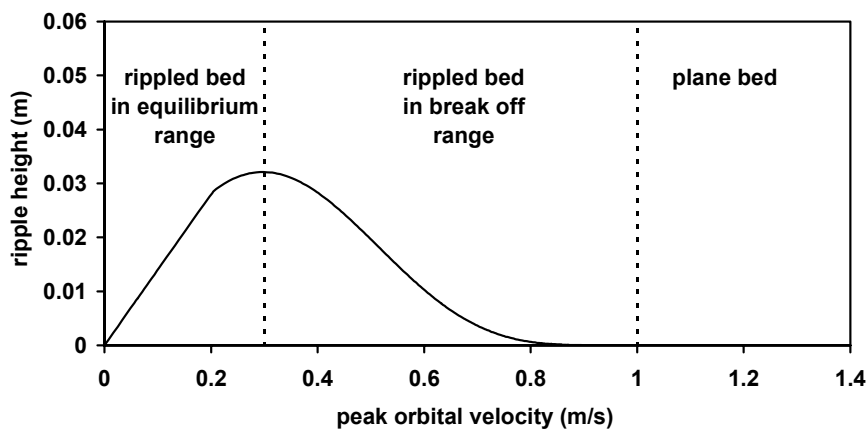


Figure 1.8. Ripple height versus peak orbital velocity for a sand bed with a grain diameter D_{50} of 0.24 mm and waves with a period T of 4 s; after the bed form model of Van Rijn (1993).

Besides the presence of mean currents, short waves, infragravity waves and shear waves, the magnitude and direction of the sediment transport rate also depends on the presence of bedforms (ripples) and their dimensions.

Ripples start to form as the friction of the seabed exceeds the threshold value for sediment movement. As waves and currents become stronger, ripples go through two distinct stages (Grant and Madsen, 1982). The first stage is known as the equilibrium range, in which flow is relatively slow and sediment transport is low (Figure 1.8). Both ripple height η and ripple length λ tend to increase until ripple steepness and ripple roughness reach their maximum. Within the equilibrium range, the length of the ripples scales with the near bed wave orbital diameter A (orbital ripples). As flow strength is further increased, ripples enter the second stage defined as the break-off range. When this break-off range is reached, ripple height will decrease while ripple length stays roughly constant or decreases slightly. This will lead to the decrease in ripple steepness and ripple roughness, and also the de-correlation between wave orbital diameter and ripple length (anorbital ripples). Finally, the ripples are washed out leaving a plane seabed.

The oscillatory wave motion over a sand bed in the equilibrium and break-off range causes strong vortex motions yielding suspended sediment clouds moving upward, forward and backward in the water column. The spatial sediment concentration variability is relatively large. Phase differences between the wave motion and sediment concentration peaks may result in offshore directed transport rates (Figure 1.9). The large oscillatory wave motion over a sand bed in the plane bed regime generates high concentrations in a thin layer near the bed (sheet flow layer). Under a skewed wave motion, the concentrations at the onshore stroke of the wave are generally larger than at the offshore stroke, resulting in an onshore-directed net sediment transport rate. The phase differences between the wave motion and the concentration peaks in case of a plane bed are generally small but may become important for fine sediment (<0.2 mm) and a strong skewed wave motion, which may result in net sediment transport against the wave direction at certain levels in the sheet flow layer (Dohmen-Janssen, 1999). Sediment concentrations above the sheet flow layer are generally relatively small, except in the presence of strong currents.

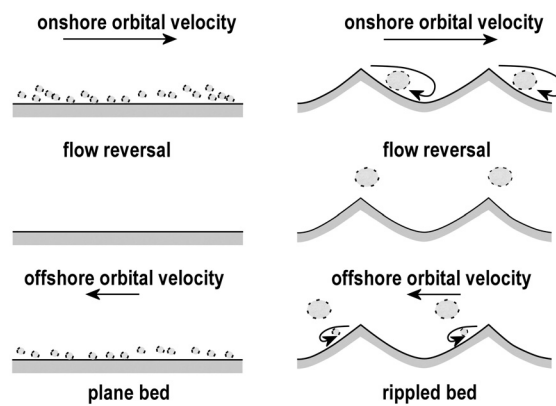


Figure 1.9. Transport processes in asymmetric wave motion over a plane bed (left) and a rippled bed (right).

1.3. NEARSHORE BAR FORMATION AND MIGRATION MECHANISMS

Various mechanisms have been proposed for the formation and migration of nearshore sand bars. Discussions and reviews of these concepts have been given by Greenwood and Davidson-Arnott (1979), Dally (1987), Sallenger and Howd (1989), Holman and Sallenger (1993), Van Rijn (1998), among others.

1.3.1. HARMONIC WAVE OVERTAKE CONCEPT

The harmonic wave overtake concept states that a periodic spatial pattern of wave energy transfer between a wave and its higher harmonics is responsible for bar formation and migration (Hulsbergen, 1974; Boczar-Karakiewicz and Davidson-Arnott, 1987; Boczar-Karakiewicz et al., 1995; Hulscher, 1996). Higher harmonics are generated by non-linear wave interactions when waves enter shallow water depths. Basically, the waveform can then be seen as the superposition of a base wave, a bound second order harmonic wave and a free second harmonic wave. The wave envelope of the base wave and the higher harmonics interfere causing a spatially varying pattern of the wave envelope amplitude. This leads to a spatially varying pattern of orbital velocities and near-bed mass transport velocities inside the wave boundary layer and hence to a variation of the near-bed sediment transport rates. Bars will form in regions where the wave envelope decreases from a maximum towards a minimum. These mechanisms have clearly been observed in a wave flume (Hulsbergen, 1974), and may be important in swell-dominated conditions when regular wave trains of low-amplitude waves approach the coast. However, in case of irregular waves, free harmonics over a wide range of frequencies exist, preventing the generation of a distinct spatial pattern of the wave envelope amplitude. The formation and migration of nearshore bars is therefore not likely to be due to the harmonic wave overtake concept but rather connected to wave breaking processes and the interaction between short and long waves (Hulscher, 1996). Moreover, the harmonic wave overtake concept assumes the bed-load to dominate the total net transport rate, whereas the suspended load transport rate has been shown to be very important in the nearshore zone. Therefore, this concept is not sufficient to explain and model nearshore sediment transport processes and morphological changes.

1.3.2. BREAKPOINT CONCEPT

The break point concept states that wave breaking is responsible for bar formation and migration (Dally, 1987; Sunamura and Maruyama, 1987).

Breaker vortex concept

The vortex motion under plunging breakers stirs up sediment in suspension. The mean offshore current then transports the suspended sediment offshore to form a bar (Zhang and Sunamura, 1994). In case of a relatively steep profile without bars or just a small swash bar near the shoreline, the plunging waves will first form a breaker bar near the shore in the initial stage of a storm event. This breaker bar may slowly move offshore by undertow-related transport processes, and in time the plunging breakers will change

into spilling breakers. Eventually, the distance from the shore to the breaker bar will be large enough for the spilling breakers to reform and plunging breaking waves will again be generated near the shore. The plunging breaking waves will create a new breaker bar, which will also proceed to move offshore and thus the cycle repeats itself (Kamphuis, 1995). Onshore bar migration is difficult to explain with the breaker vortex concept. The skewness concept and the asymmetry concept are more likely to be responsible for this.

Skewness concept

Nearshore sand bars may also be formed and maintained by a combination of shoaling waves and spilling breakers. The skewed wave motion under shoaling waves generates an onshore-directed transport that increases towards the breakpoint and decreases beyond it, thereafter grading into seaward transport by undertow currents. The seaward transport may also be caused by bound long waves (Doering and Bowen, 1988). In case of 3D circulation cells, longshore currents may maintain and deepen the trough by removing sediment that is subsequently transported offshore by rip currents. Multiple bars form when the larger waves of the spectrum break first at more offshore locations contributing to the formation of an outer bar while smaller unbroken waves and reforming broken waves propagate shoreward to break near the shoreline contributing to the formation of an inner bar. Offshore bar migration takes place under storm conditions with intense wave breaking on the bar crest and strong undertow currents just shoreward of the bar crest. Onshore migration takes place under calm conditions with a strongly skewed wave motion and small undertow currents (King and Williams, 1949; Greenwood and Davidson-Arnott, 1979; Douglas, 1995).

Asymmetry concept

Onshore migration of bars cannot always be explained with the skewness concept (Thornton et al., 1996; Gallagher et al., 1998). As waves shoal they also show a tendency to become pitched forward, referred to as wave asymmetry. The increase of the wave asymmetry eventually leads to a decrease of the wave skewness (Elgar and Guza, 1985; Doering and Bowen, 1987, 1988). Elgar et al. (2001) hypothesize this wave asymmetry to be responsible for net onshore sediment transport and sand bar migration. A spatial pattern of onshore transport related to wave asymmetry and offshore transport related to wave breaking might also be responsible for bar formation.

1.3.3. INFRAGRAVITY WAVE CONCEPT

The infragravity wave concept states that bar formation and migration is attributed to infragravity waves (Carter et al., 1973; Short, 1975; Wright et al., 1986; Sallenger and Holman, 1987; Aagaard, 1990). Sediment transport under low-frequency waves can be related to wave-induced mass transport velocities as well as to short-long wave interaction processes. Based on this, two different bar generation concepts can be distinguished: standing wave-mass transport concept and the short wave-long wave interaction concept.

Standing wave mass transport concept

Friction effects in the wave boundary layer induce mean mass transport velocities under low surface waves in shallow water (Longuet-Higgins, 1953). These mass transport velocities are superimposed on the basic orbital wave motion. In case of a standing wave field, the basic horizontal orbital velocities are maximal under the nodes and zero under the antinodes. The mean mass transport velocities are maximal midway between the node and anti-node while directed towards the nodes in the wave boundary layer and directed towards the antinodes above the wave boundary layer. For standing waves or partially standing waves, this causes sediment near the bed to be transported towards the nodes when bed-load is dominant and to the antinodes when suspended load is dominant. In case of progressive waves, mass transport is always in the wave propagation direction (Carter et al., 1973). Thus small spatial variations of the mass transport velocity may cause divergence and convergence of sediment and hence bar formation. The formation of one bar may result in resonant reflections and standing wave patterns shoreward of the bar leading to the formation of new bars shoreward of the existing bar (O'Hare and Davies, 1993; Dulou et al., 2000). The standing wave-mass transport concept requires the establishment of a well-defined and stable standing wave envelope (high reflection coefficient). This can only occur if the long-wave spectrum is narrow-banded in frequency. However, most field measurements reveal a broad-banded spectrum of long waves (e.g. Holman and Sallenger, 1993) for which nodal and antinodal points would be continuously changing and bar formation would be prevented. Moreover, mean return currents associated with breaking waves are neglected in the standing wave-mass transport concept, whereas the transport component related to this mean current is often found to be dominant in the nearshore zone under storm conditions (e.g. Aagaard et al., 1998). Consequently, the standing wave mass-transport concept may be less valid for strongly breaking waves under storm conditions in the surf zone (dissipative conditions).

Short wave – long wave interaction concept

Another mechanism for bar formation and migration may be the coupling between short waves and long waves that may lead to positions of sediment convergence or divergence (O'Hare and Huntley, 1994). Waves approaching the shore have a grouped structure. A radiation stress gradient due to this pattern of alternating high and low short waves induces a long wave that is bound to the short wave groups. Various studies indicate that the bound long waves are released from the wave groups in the outer surf zone and travel shoreward as free long waves (List, 1987; Ruessink, 1995; Grasmeijer and Van Rijn, 1999). Despite this release, there may still be a fixed phase relation between the short-wave envelope and the long wave motion, resulting in a net transport of sediment. The direction of the net transport rate depends on the phase relationship between the short-wave groups and the long-wave motion. If the phase coupling varies systematically over the profile, a convergence and divergence pattern of sediment fluxes may result in bar formation and migration. Past work has shown that multiple bars may form when so-called breakpoint-forced are dominant while bar migration may occur when bound long waves are dominant (O'Hare, 1994). However, model explorations and field studies point to the dominance of bound long waves in the long wave transport

component (Roelvink and Stive, 1989; Ruessink, 1998a), making bar formation unlikely to be related to mechanism proposed by O'Hare and Huntley (1994).

Edge wave trapping concept

Obliquely incident waves may generate long waves propagating along the shore with a cross-shore standing structure, commonly referred to as edge waves. Longshore currents may modify the structure of the edge waves, which may result in bar formation. Subsequently, edge waves trapped between the bar and the beach may have a significant contribution to the nearshore hydrodynamic forcing (Bryan et al., 1998) and may lead to migration of the bar. More strongly, past work has suggested that edge waves, trapped and amplified on longshore currents, may cause bars to form and migrate on plane beaches (e.g. Schönfeldt, 1995). On the other hand, field observations suggest that under most conditions, edge wave trapping is a subtle effect and is unlikely to produce significant morphological change unless the current is very strong (Bryan and Bowen, 1998).

1.3.4. CONCLUSIONS

Both the harmonic wave overtake concept and the standing wave mass transport concept require a wave spectrum that is narrow-banded in frequency, whereas field measurements reveal a broad-banded spectrum not only of the short waves ($T < 20$ s) but also of the long waves ($T > 20$ s). If these phenomena are at all present in the nearshore, they are a subtle effect and unlikely to produce significant morphological change. What is more, field measurements of sediment transport reveal that the short and long wave oscillatory motions as well as the mean motion dominate the transport fluxes and contribute to the total net transport rate. As such, the skewness concept and the asymmetry concept appear to be more credible theories to explain bar formation and migration in the nearshore zone of a dissipative beach. The breaker vortex concept is likely to play a role for steep beaches with plunging breakers. In addition, the short wave – long wave interaction concept, in particular the effect of bound long waves may play a role of importance as well. Trapping of edge waves may not be important as a direct sediment transport agent to form and migrate nearshore bars, but it may be relevant for the maintenance of 3-D rip cell circulations influencing longshore set-up and radiation stress variations.

1.4. NEARSHORE BAR MIGRATION MECHANISMS IN A SMALL-SCALE WAVE FLUME

1.4.1. INTRODUCTION

As an example and to identify the basic characteristics of the associated hydrodynamic processes and sand transport processes across a nearshore bar, a series of small-scale wave flume experiments with an artificial sand bar in the ripple regime are discussed in this section. This work has been published in Grasmeijer and Van Rijn (1999).

Field and laboratory measurements in the ripple regime indicate that flux contributions by the mean flow and the oscillatory wave motions at both high and low frequencies are

highly variable not only in magnitude, but also in direction. The fluxes also vary significantly with elevation above the bed (Vincent and Green, 1990; Osborne and Greenwood, 1992; Osborne and Vincent, 1996). These variations are largely related to the shape of the bed forms (steep vortex ripples or flatter post-vortex ripples) and the exact position of the instruments with respect to the bed form crest. The bed forms interacting with the near-bed currents impose distinct constraints on both the timing and magnitude of suspension events relative to the phase of the wave motion. Bosman and Steetzel (1986) and later Osborne and Vincent (1996) analysed sand concentration and velocity data at several positions along a rippled bed in laboratory conditions and found that the phase relationships between velocity and concentration are such that it could give completely opposite depth-integrated transport values at different positions along the bed form (on both flanks of the ripple). To determine an accurate value of the spatially-averaged depth-integrated transport, a large number of simultaneous measurements along the ripple surface is required. Another option is to use a measurement station moving slowly forwards and backwards over several ripples during sampling (ripple averaging). This latter procedure was introduced by Bosman and Steetzel (1986) and can be rather easily operated in laboratory conditions, as done by Van Rijn et al. (1993), Van Rijn and Havinga (1995) and in the present study.

The specific objectives of this small-scale wave flume study are:

- To get information of the mean and oscillatory (high and low frequency) sand transport processes across a barred profile in the ripple regime,
- To show the importance of the near-bed sand fluxes, which are not reflected in the measured suspended transport rates, but are revealed from bar migration data.

It must be realized that the sand bar and the selected wave conditions in the flume are supposed to represent a nearshore sand bar in a regime with breaking waves, but the experimental set up is no scale model of some specific field case. Furthermore, the bar in the flume was not moulded by long-term wave generation, but artificially constructed. Hence, the bar does not represent some kind of equilibrium bar. The objective of the experiments is no more than to create breaking wave conditions over a movable bed and to identify the basic characteristics of the associated hydrodynamic processes and sand transport processes. This may help to better understand similar processes in field conditions. Net transport rates and associated directions over a bar (onshore or offshore) depend critically on whether the bar is in some kind of equilibrium with the wave field or is well outside equilibrium. Most likely, the net transport rates measured in the flume are not representative for field conditions, but it is believed that the measured transport components are of interest in a qualitative sense. Furthermore, three-dimensional effects are absent in these flume tests.

Measurements of ripple-averaged sand transport rates in field conditions are extremely rare. Most field data refer to single point measurements at some unknown position along the ripple surface. Based on all these arguments, it will be difficult to compare the ripple-averaged transport rates of the present laboratory study to single-point field data. Despite interpretation problems using field data, two data sets (Vincent and Green, 1990; Osborne and Greenwood, 1992) have been selected for comparison to the results of the present small-scale laboratory study.

1.4.2. HYDRODYNAMICS ACROSS A NEARSHORE BAR

Herein, results will be presented of a small-scale wave flume test series simulating a moderate storm. Basic hydraulic parameters are presented in Figure 1.10 as a function of the location in the flume.

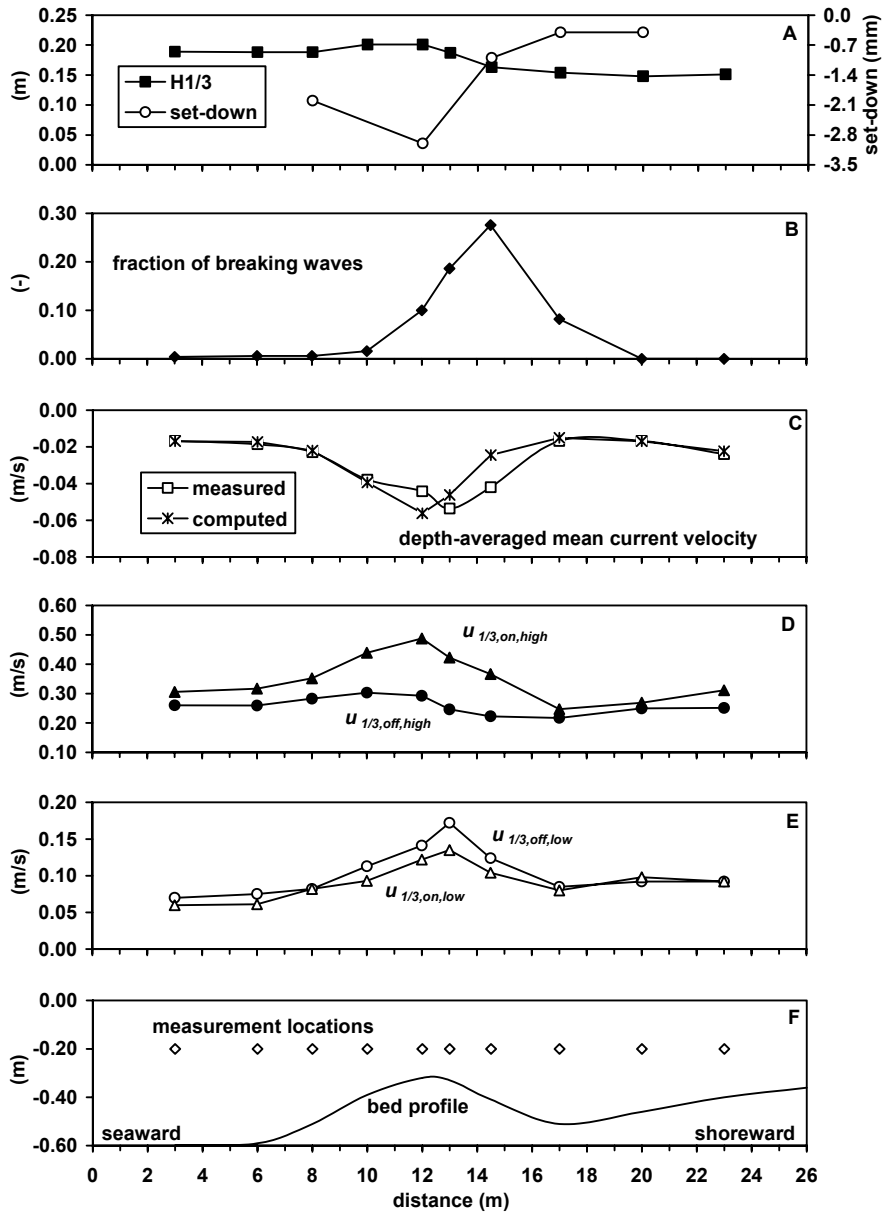


Figure 1.10. Hydraulic parameters across a barred profile in a small-scale wave flume. A) significant wave height and set-down, B) fraction of breaking waves, C) depth-averaged mean current, measured and computed based on Equation (1.2), D) onshore and offshore high-frequency peak near bed orbital velocities, E) onshore and offshore low-frequency peak near bed orbital velocities, F) bar profile.

It can be observed that waves are shoaling towards the bar crest (Figure 1.10A). Maximum wave height is found near the bar crest. Moving further shorewards, the wave

height decreases both due to the increasing water depth and due to energy dissipation caused by breaking of waves. Nearly all breaking waves were of the spilling breaker type. Occasionally near the bar crest, a plunging breaker occurred. This is in agreement with the breaker classification of Galvin (1968). It is interesting to note that the fraction of breaking waves is largest just shoreward of the bar crest (Figure 1.10B). Breaking waves of the spilling breaker type start breaking near the bar crest but continue breaking over several wave lengths while propagating further shorewards. Thus, waves initially breaking near the bar crest are also included in the fraction of waves breaking further shoreward from the crest. Set-down values are shown in Figure 1.10A. Maximum set-down is found near the bar crest and decreases rapidly further shoreward.

The depth-integrated mean current (Figure 1.10C) is found to be maximum in the measurement location just shoreward of the bar crest; this is likely caused by the relatively large fraction of breaking waves in this region. The measured mean current velocity can be approximated with the following expression:

$$\bar{u} = \frac{1}{8} \sqrt{\frac{g}{h}} \frac{H_{rms}^2}{h_t} \quad (1.2)$$

where H_{rms} is the root-mean-square wave height, h is the mean water depth, h_t is the water depth below the wave trough level defined as $h - \frac{1}{2}H_{rms}$. Equation (1.2) is based on linear mass flux ($\bar{u} h_t = 1/8 g H^2/c$), an effective depth equal to h_t and $c = (gh)^{0.5}$ is the wave propagation speed in shallow water.

The measured and estimated mean return flows are presented in Figure 1.10C. The measured mean return flows are estimated rather accurately using Equation (1.2), except in the region just shoreward of the bar crest, where the fraction of breaking waves is relatively large. In this region the mean return flow is significantly underestimated. It is believed that the mean return flow at a certain location is more strongly related to the wave height somewhat seaward of this location due to advection of kinetic wave energy (plunging effect). This may be an explanation for the ‘shift’ observed in Figure 1.10C between measured and calculated return flows. It can be observed from Figure 1.10A and Figure 1.10C that the maximum return flow coincides with a relatively large set-down gradient just shoreward of the bar crest.

Shoaling of waves leads to an increasing near-bed velocity skewness (in terms of peak orbital velocities), as shown in Figure 1.10D. The onshore-directed peak velocities (significant values) are larger than the offshore-directed peak velocities. It can also be observed that the largest high-frequency velocities are found near the bar crest. Further shorewards, the reduction in magnitude of the onshore-directed velocities is found to be less pronounced than the decrease of the offshore-directed velocities. This leads to a maximum velocity skewness just shoreward of the bar crest with onshore-directed high-frequency near-bed peak velocities that are 70% larger than the offshore-directed high-frequency near-bed peak velocities.

In addition to the short wave motion, long wave velocity fluctuations were found to be manifest in the flume, for a range of low-frequency significant wave heights between 0.02 and 0.04 m. From Figure 1.10E it can be observed that the long wave oscillatory velocities are largest just shoreward of the bar crest. In this region the offshore-directed

long-wave peak velocities (significant value) are found to be 20% larger than the onshore-directed long-wave peak velocities.

1.4.3. TRANSPORT PROCESSES OVER A NEARSHORE BAR

Time series of velocity and concentration were analyzed to determine the relative importance of the various transport processes across the bar (Figure 1.11). The depth-integrated transport rates calculated from velocity and concentration measurements are compared with transport rates measured from bed profile changes over short time intervals. In contrast with Van Rijn and Havinga (1995), the transport rates calculated from velocity and concentration measurements were not extrapolated to the unmeasured zone between the lowest measuring point and the mean bed level. Thus, the calculated depth-integrated values represent the suspended transport rather than the total transport rates (bed-load transport excluded).

From Figure 1.11A it can be observed that the net suspended transport rate, $q_{s,net}$, is directed offshore at all positions and increases in magnitude towards the bar crest. Decreasing transport rates are found further shorewards. Although the same trends can be observed for the current-related suspended transport rate (Figure 1.11A), occasionally small transport rates were found to be onshore directed in deeper water which may have been caused by onshore directed streaming effects near the bed (Longuet-Higgins drift/streaming) in combination with near-bed confined concentrations.

The high-frequency suspended transport rate ($q_{s,high}$) is found to be directed offshore at all locations (Figure 1.11B) and increases to a maximum towards the bar crest. Further shorewards a pronounced decrease in $q_{s,high}$ can be observed. The high-frequency suspended transport rate is found to be negligible in the measurement sections shoreward of the bar, where the fraction of breaking waves is largest. The offshore-directed transport by high-frequency oscillations is likely to be related to the mechanism of sand suspension over rippled bed forms. From the analysis of the concentration signals and from visual observations it appeared that, on the time scale of a single wave cycle, sediment was eroded from the bed at the onshore stroke of the wave and mobilized in vortices between the ripples. At flow reversal from on- to offshore, the vortex cloud was lifted and advected leading to large concentrations in phase with the offshore stroke of the wave. Similar, but less dominant processes were caused by separation vortices associated with the offshore phase of the wave cycle. This variation in timing of concentration maxima and minima results in a vertical distribution in which the high-frequency transport rate tends to be onshore directed near the bed and offshore directed at higher elevations above the bed. Measurements close to the bed could not be made. Hence, the transport rate in the near bed layer (bed-load transport) could not be estimated from the data, but this transport rate is believed to be onshore directed, as indicated by net transport rates derived from bed level changes (discussed hereafter).

From Figure 1.11B it can be observed that the low-frequency suspended transport rates seawards of the bar crest are extremely small and onshore directed. The onshore direction is probably related to the bound long wave being partly reflected by the

nearshore bar (Grasmeijer and Van Rijn, 1999), resulting in an onshore-directed long-wave velocity. In the measurement locations just shoreward of the bar crest, the low-frequency suspended transport rate is found to be relatively large and offshore directed. At these locations the low-frequency suspended transport rates may not only be caused by the bound long wave phenomenon. The undertow generated by irregular breaking waves may also show long-period velocity oscillations. Large concentration magnitudes under high-amplitude waves combined with the undertow oscillations induced by breaking waves (pulsating undertow) and low-frequency oscillations induced by bound long waves, result in a relatively large offshore-directed low-frequency suspended transport rate at locations just shoreward of the bar crest.

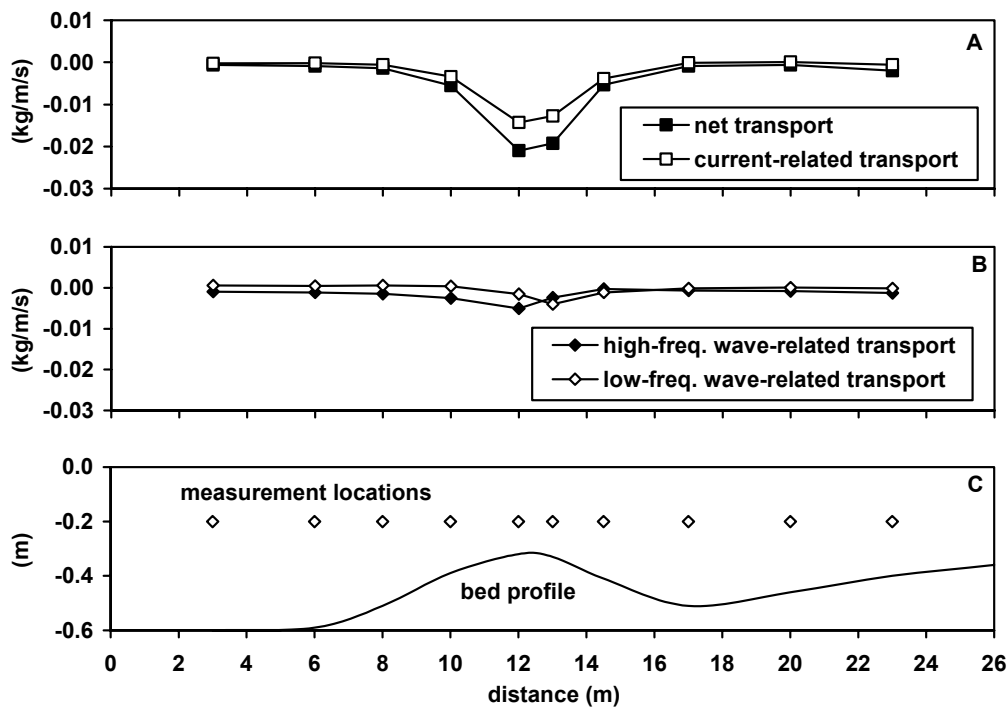


Figure 1.11. Transport rates in a small-scale wave flume based on velocity and concentration measurements across a barred profile. A) net and current-related transport rates, B) high- and low-frequency wave-related transport rates, C) bar profile.

The wave-related suspended transport is dominated by the high-frequency component in nearly all measurement locations seaward of the nearshore bar. At locations just shoreward of the bar crest, however, the low-frequency suspended transport rate exceeds the high-frequency component. It is interesting to note that the dominance of $q_{s,low}$ over $q_{s,high}$ occurs at locations where the fraction of breaking waves is relatively large.

Transport rates based on morphological changes were determined by measuring the bed level at the flume window every 0.25 m along the profile. After almost 3 hours of experiments the changes in morphology were determined.

In Figure 1.12A the initial bed level and the bed level after 9700 s of wave action are plotted for series B2. It can be observed that morphological changes take place

especially on the seaward slope of the bar (accretion) and on the shoreward slope of the bar (erosion). The bar crest is thus displaced seawards. Transport rates were calculated from the bed level changes assuming that the transport rates at deep water seaward of the bar are zero. Transport rates based on these morphological changes ($q_{morphology}$) are plotted in Figure 1.12B, as well as the time-averaged net suspended transport rates based on instantaneous velocity and concentrations measurements ($q_{s,net}$) and the difference between both curves (q_{rest}). The $q_{s,net}$ -value is the same curve as shown in Figure 1.11A. It can be observed from Figure 1.12B that $q_{morphology}$ is onshore directed shoreward of the bar and offshore directed near the bar crest. At locations near the bar crest $q_{s,net}$ and $q_{morphology}$ are both found to be offshore directed. The rest term, q_{rest} , is onshore directed in nearly all measurement locations. Largest values are found at locations near the bar crest, while q_{rest} is negligible in the measurement section where the fraction of breaking waves is largest.

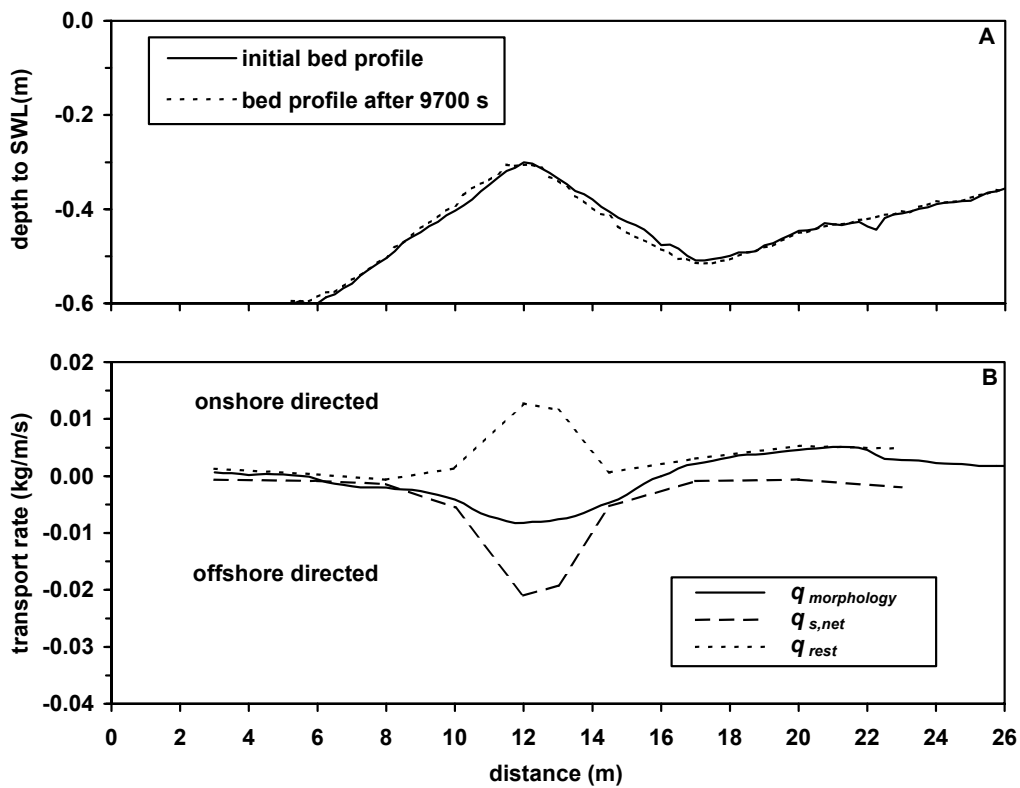


Figure 1.12. Transport rates and bed level changes across barred profile in small-scale wave flume. A) bed level changes, B) transport rates.

It is noted that the transport rates derived from the bed-level changes represents both the suspended and the bed-load transport rate, whereas the transport rates derived from the velocity and concentration measurements only represents the suspended transport.

The discrepancy between the transport rate based on morphology and that based on velocity and concentration measurements probably represents a combination of wave- and current-related transport in the unmeasured zone near the bed. From analysis of the vertical distribution of transport rates it appeared that in particular the high-frequency

wave-related transport rate near the bed tends to be onshore directed. The relatively large high-frequency velocities with onshore near-bed peak velocities larger than offshore near-bed peak velocities, together with the large concentrations magnitudes (and variation in concentration) may lead to large high-frequency transport rates in the onshore direction. It is expected that the high-frequency transport rate in the unmeasured zone near the bed will drastically change both the magnitude and the direction of the total net transport rate.

1.4.4. COMPARISON OF SMALL-SCALE WAVE FLUME DATA AND FIELD DATA

Vincent and Green (1990) used a shore-normal track covering a few ripples along which the sensor was moved forwards and backwards, to measure bed form profiles and suspended concentration profiles with a movable acoustical backscatter concentration meter (ACM at 0.5 m above bed) and one fixed electromagnetic current meter (ECM at 0.2 m above bed). The data set of Vincent and Green (1990) refers to the fine sand ripple regime on a macrotidal beach on the Norfolk coast of England. Tracking of the ACM was not performed when wave heights became too great. The data presented by Vincent and Green refer to fixed positions of the ACM and ECM. The measured data were used to drive a mathematical model to determine the vertical distribution of the sand fluxes over a layer of about 0.4 m above the bed. Their main findings are:

- The high-frequency oscillatory transport in the lowest 2 to 3 cm is strongly onshore, while between 5 and 15 cm the oscillatory transport is seaward; above 15 cm the oscillatory transport is almost zero (schematically shown in Figure 1.13);
- Without concentration values within a few centimeters of the bed, the depth-integrated flux estimates for the oscillatory flux component would have been offshore rather than onshore.

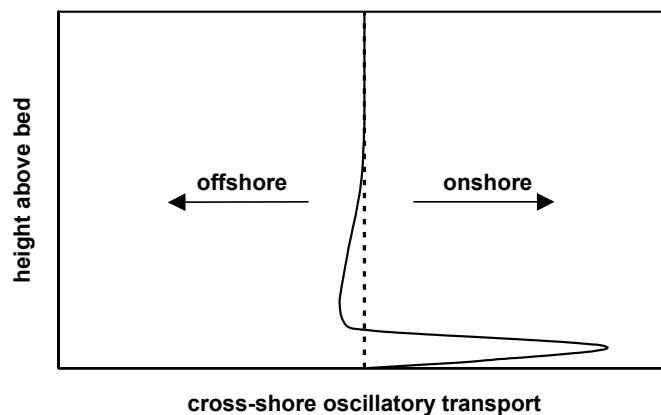


Figure 1.13. Schematic diagram of vertical distribution of oscillatory transport in field (after Vincent and Green, 1990).

These findings (onshore high-frequency suspended transport in near-bed layer and offshore high-frequency transport at higher elevations) are in line with the results of the present study.

Osborne and Greenwood (1992) performed a detailed field study of sand transport across a barred profile at the tideless Bluewater beach, Lake Huron, Ontario, Canada. Three bars were present on a mean nearshore slope of about 1 to 60 in fine to medium sand. The depth above the middle bar was about 1 m and the depth above the outer bar was about 2 m. Six sand transport monitoring stations were deployed across the barred profile. Each transport station consisted of two optical backscatter-sensors at nominal elevations of 0.04 and 0.1 m and two electromagnetic current meters at nominal elevations of 0.1 and 0.5 m.

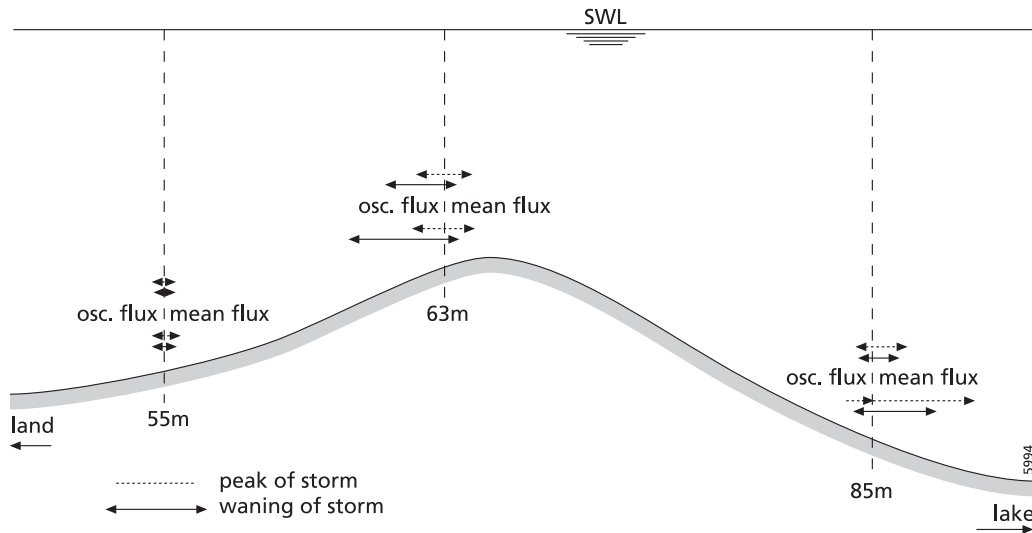


Figure 1.14. Schematic diagram of oscillatory and mean fluxes (at 0.04 m and 0.1 m above the bed) across a bar profile in the field (after Osborne and Greenwood, 1992)

The significant wave height was about 0.5 m (peak period of 4 s) at the toe of the middle bar (depth of about 2.3 m) during the peak of the storm. The bed was sandy with median particle sizes between 0.13 and 0.24 mm.

Plane bed sheet flow was observed on the bar crest during the peak of the storm event (peak orbital velocities of about 1 m/s). Post-vortex ripples were observed at the seaward slope of the bar at a depth of about 1.8 m during the storm event. Hereafter, results are given from three measurement stations along the middle bar during the rise, peak and decay of a minor storm event (schematically shown in Figure 1.14).

1. Lakeward bar slope:

- Under small shoaling waves relatively steep, three-dimensional vortex ripples are most commonly observed, showing a coupling between large near-bed concentrations and larger onshore velocities leading to a dominant net onshore oscillatory transport; significantly smaller low-frequency suspended transport is offshore-directed due to bound long waves;
- Under increasingly asymmetric waves associated with the onset of breaking, the steep vortex ripples change to less steep two-dimensional post-vortex ripples; as breaking is intensified, oscillation ripple steepness are decreased further and sediment concentrations become more uniform (vertically) and the direction of the net oscillatory transport is reversed to offshore (largest concentrations occur

during offshore phase of wave cycle); the oscillatory transport magnitudes remain small; the transition from dominant onshore oscillatory transport to weak offshore oscillatory transport coincides with changes in the local bed ;

- Under breaking waves there are maximum return currents (undertow) of about 0.1 m/s; the net fluxes are offshore-directed; the offshore-directed mean suspended fluxes associated with undertow currents are dominant over the oscillating fluxes.
2. Breaking zone at bar crest:
 - During the peak of the storm (breaking conditions) the larger waves are spilling ($H_s/h=0.4$); the undertow is relatively small (almost zero); the mean concentrations are relatively large; the net fluxes are almost zero; the mean transport is offshore-directed and of the same order as the oscillatory transport; the oscillatory transport is dominated by high-frequency suspended transport component; low-frequency transport component is small and offshore-directed;
 - During waning of storm the net fluxes are relatively large and onshore-directed; the net fluxes are dominated by onshore-directed high-frequency transport components; the offshore-directed mean transport component is relatively small (undertow is almost zero).
 3. Shoreward bar slope (near trough):
 - During all conditions (early, peak and waning phase of the storm) the net transport rates are small and offshore-directed; the net transport rate is dominated by the mean transport component (maximum undertow is about 0.1 m/s);
 - The oscillatory transport component is small and onshore-directed; it is dominated by onshore-directed low-frequency suspended transport; this low-frequency transport component is caused by a distinct low-frequency modulation of the velocity field, superimposed on the high-frequency oscillations of the breakers; the low-frequency oscillations most probably represent energy transferred from the group-bound long waves to long waves constrained by the presence of the bar crest and the time-varying position of the breaker line; the high-frequency transport component is negligibly small on the shoreward bar slope.

The results from the field study are quite different from the present laboratory results. In the flume the mean suspended transport rates are maximum in the bar crest zone with breaking waves, while the mean transport components in the crest zone are minimum (almost zero) for the field case. The high-frequency suspended transport component is maximum at the bar crest for both the laboratory and field case, but this transport component is offshore-directed in the laboratory and onshore-directed in the field. The low-frequency suspended transport components on the seaward flank of the bar are in good agreement; offshore-directed transport components due to group-bound long waves are present in the laboratory flume and in the field. The onshore-directed low-frequency transport component on the shoreward bar flank in the field due to varying breaking locations was not observed in the flume. The observed discrepancies are most probably related to three-dimensional cell circulations, which may have been present in the field (bars were sinuous-crescentic), while the laboratory bar is fully two-

dimensional. A striking feature in the field is the absence of the undertow at the bar crest, where most of the waves were found to be breaking (spilling). Hence, the onshore mass flux is not compensated locally, but probably carried away longshore to a rip channel.

1.4.5. CONCLUSIONS

The main findings of the small-scale wave flume study are summarized in the following conclusions:

- Besides the short wave motion, relatively large long wave velocity fluctuations are present in the small-scale wave flume, especially in the region just shoreward of the bar crest where the fraction of breaking waves is relatively large.
- Near the bar crest, the net transport in the measured zone is dominated by the time-averaged (current-related) transport rate due to the undertow.
- Outside the bar area, the net transport in the measured zone is dominated by the high-frequency (wave-related) transport rate which is offshore directed due to phase differences between peak orbital velocities and concentrations.
- With the exception of the region just shoreward of the bar crest, where the fraction of breaking waves is relatively large, the low-frequency transport rate is negligible.
- The morphological behavior of a nearshore bar and the associated net transport rates are strongly related to the wave-related transport rates in a rather thin layer near the sediment bed.
- Measurement of instantaneous velocities and concentrations in this layer are of crucial importance to determine the net transport rates and hence the net migration rate of the bar. It is, however, hardly possible to measure these transport rates with the available measurement techniques, not even in flume conditions.
- Measurements across a barred profile in a two-dimensional laboratory flume show large discrepancies with similar measurements in the field, which may have been caused by three-dimensional effects and stresses the importance of three-dimensional measurements in the field.

1.5. MODELLING NEARSHORE BAR BEHAVIOR

Morphodynamic process-based coastal profile models are commonly used for hind- and forecasting studies of nearshore bathymetry, often in response to human interference in the nearshore, for instance related to implementation of shoreface nourishments (e.g. Hoekstra et al., 1996; Shelden et al., 1999). They not only provide a means of determining the most effective location for the nourished sediments, but also give information on the behavior of the nourishment during the design life of the project. The

location of the nourishment, which may form an artificial bar, should be carefully determined so that the sediment is transported shoreward or at least stays in the nourished area. However, whether or not the present understanding of the physics of coastal processes justifies the use of process-based profile models is subject to some debate (Stive and De Vriend, 1995; Van Rijn et al., 2002b).

1.5.1. MODELLING OF HYDRODYNAMICS

Process-based profile models consist of various sub modules, predicting the cross-shore wave transformation, and the cross-shore evolution of wave orbital velocities and of the mean cross- and longshore currents. Examples of process-based models are those by Bowen (1980), Dally and Dean (1984), Stive and Battjes (1984), Roelvink and Stive (1989), Southgate and Nairn (1993), O'Connor and Nicholson (1999), and others. In all models, the wave field is modelled in terms of the wave energy density, which can be based on a single representative wave height (parametric or single wave approach), or on discrete series of wave height classes (probabilistic, multi-wave or wave-by-wave approach). In the parametric approach the wave orbital velocities, mean currents and sediment transport rates are computed directly based on a single representative wave height (often the root-mean square value, under the assumption of a Rayleigh distribution) and the peak period. In the probabilistic approach the hydrodynamics and sediment transport rates are computed for each wave class separately, after which the integrated values are determined based on the weighted sum. Van Rijn and Wijnberg (1996) argue that the probabilistic approach is better suited for profile modelling because of the strong non-linear dependence of the sediment transport on wave height, which would not be captured correctly with the single-wave parametric approach. Whether the probabilistic approach indeed outperforms the parametric approach both regarding hydrodynamics and sediment transport is however unknown.

All models include the effect of the undertow and skewness of the wave orbital velocities. In order to derive the undertow, in most models the water column is divided in three layers, i.e. a surface layer above the wave trough level, a middle layer, and a bottom layer. The onshore-directed mass flux in the surface layer determines the magnitude of the undertow in the middle layer. Models differ in describing the vertical structure of the undertow in the middle layer and the mean currents in the bottom layer. Roelvink and Stive (1989) and Southgate and Nairn (1993) solve the horizontal momentum balance equation after De Vriend and Stive (1987) to determine the vertical structure of the undertow in the middle layer. O'Connor and Nicholson (1999) use an assumed shape of the undertow velocity profile (see O'Connor et al., 1998), in which the undertow velocity consists of two parts: a parabolic distribution representing the upper part of the flow and a logarithmic distribution representing the lower part of the flow. Rattanapitikon and Shibayama (2000) suggest a similar approach as O'Connor et al. (1998) for the middle layer. The vertical structure of the undertow velocities in the middle layer is an important difference between the models. The presence of a surface roller influences the undertow profile significantly. No roller is present at the onset of breaking, which results in a rather uniform velocity profile (Figure 1.15). A fully

developed surface roller causes an onshore-directed shear stress on the water column at the wave trough level. This leads to a decrease of the offshore-directed velocities in the upper part of the velocity profile and mass balance results in an increase of the velocities in the lower part of the profile under these conditions. The velocity profiles in Figure 1.15 are based on the undertow model of Rattanapitikon and Shibayama (2000) and are consistent with observations by Garcez Faria et al. (2000).

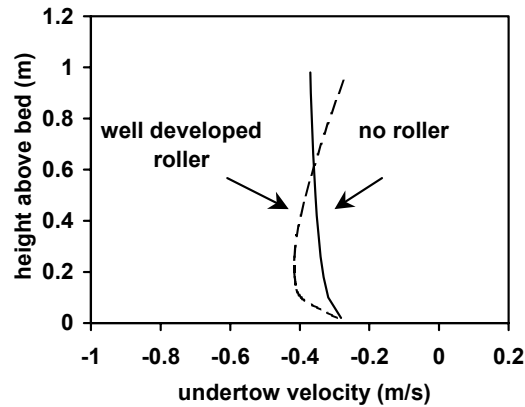


Figure 1.15. Roller effect on vertical structure of undertow velocities

The condition at the lower boundary between the middle and the lower layer depends on whether or not waves are breaking. For non-breaking waves the so-called conduction solution of Longuet-Higgins (1953) is applied and for breaking waves no shear stress is assumed. In some models the no-slip condition is applied (that is, velocity equal to zero in lower layer). The undertow velocities are almost independent of the way in which the steady streaming in the lower layer is calculated (Svendsen et al., 1987).

Various approaches are used to compute the wave orbital velocities. Roelvink and Stive (1989) adopt the Fourier approximation of the stream function method as developed by Riencker and Fenton (1981), which they apply only for the non-breaking waves. Southgate and Nairn (1993) use the non-linear Viscous wave theory of Swart (1978). Stripling and Damgaard (1997) improved the Southgate and Nairn (1993) model by applying the hybrid wave theory of Isobe and Horikawa (1982), which combines Stokes 5th order wave theory with cnoidal 3rd order wave theory. Besides the short wave orbital motion, Roelvink and Stive (1989) incorporate the additional role of short wave – long wave interaction in their cross-shore profile model. They state that the long wave effect gives an important contribution.

Wave, wind and tidal currents in the longshore direction are determined from the longshore time-averaged momentum balance after Longuet-Higgins and Stewart (1964). Most models include the effect of the surface roller. Inclusion of the surface roller causes a lag in the transfer of momentum to the longshore current velocity, thereby shifting the location of the maximum longshore velocity in the onshore direction compared to a no-roller model, consistent with laboratory (Reniers and Battjes, 1997) and field observations (Ruessink et al., 2001). There is still much discussion on the magnitude and distribution of lateral mixing of the longshore current. In the models lateral mixing is included as a diffusion term. Important sources for lateral mixing in the

surfzone are breaking-induced turbulence (Battjes, 1975), depth variation in the cross-shore and longshore velocities (Putrevu and Svendsen, 1992) and shear waves (Özkan-Haller and Kirby, 1999).

1.5.2. MODELLING OF SAND TRANSPORT

Modelling the sediment transport rate in the nearshore zone with different kinds of bed forms basically requires the simultaneous numerical solution of both the time-dependent momentum equation for the fluid flow and the time-dependent advection-diffusion equation for suspended sediment particles. The latter reads as:

$$\frac{\partial c}{\partial t} + \frac{\partial}{\partial x} \left(uc - \varepsilon_{s,x} \frac{\partial c}{\partial x} \right) + \frac{\partial}{\partial z} \left((w - w_s) c - \varepsilon_{s,z} \frac{\partial c}{\partial z} \right) = 0 \quad (1.3)$$

where c is the concentration, x is the horizontal coordinate, z is the vertical coordinate, t is time, w is the vertical velocity, w_s is the fall velocity of the sediment, $\varepsilon_{s,x}$ is the horizontal mixing coefficient, $\varepsilon_{s,z}$ is the vertical mixing coefficient. However, the oscillatory flow over a rippled bed is rather complicated due to the generation, advection and diffusion of the near-bed vortices including the effect of sediment particles carried by these vortices. Numerical simulation of this vortex motion requires detailed modelling of the instantaneous fluid flow and suspended sediment concentrations. Furthermore, the shape and dimension of the bed form should be known a priori. This approach requires relatively large computation times making it unsuitable for application in a numerical morphological model with feedback to the changing bathymetry. Moreover, the detailed modelling of vortex formation and shedding over different bed forms is still at an early stage. Therefore, in many morphological models, a simpler 1-DV approach is used, in which the presence of bed forms is represented by simply increasing the bed roughness k_s in the standard one-dimensional vertical formulations. Equation (1.3) is reduced to (1.4) for a plane bed assuming that the effects of the ripples on the flow and sediment concentrations can be represented by an effective bed roughness and effective sediment diffusivity:

$$\frac{\partial c}{\partial t} + \frac{\partial}{\partial z} \left(-w_s c - \varepsilon_{s,z} \frac{\partial c}{\partial z} \right) = 0 \quad (1.4)$$

In these models, Equation (1.4) is further simplified by time averaging over several wave periods. The time-averaged suspended sediment concentrations are then computed based on the time-averaged wave- and current-related bed shear stresses. Field and laboratory measurements have shown that the oscillatory (time-dependent or intra-wave) component cannot be neglected (e.g. Vincent and Green, 1990; Osborne and Greenwood, 1992; Ruessink et al., 1998; Grasmeyer and Van Rijn, 1999). The oscillatory component can be accounted for by means of a quasi-steady approach as done by Houwman and Ruessink (1996). Quasi-steady models are based on the assumption that the instantaneous sediment transport within a wave cycle is proportional to some power of the instantaneous near-bed orbital velocity. Houwman and Ruessink (1996) applied a quasi-steady model approach to develop an expression

for the oscillatory (wave-related) transport rate based on the time-averaged suspended sediment concentrations.

In contrast to this 1-DV approach, in some morphological models the transport formulation proposed by Bailard (1981) is adopted. This approach is based on the idea that a portion of the fluid energy is expended in maintaining a sediment transport load. The energetics approach is originally due to Bagnold (1966) who pursued this approach for the prediction of sediment transport in unidirectional streams (rivers). Bailard (1981) developed the energetics approach for longshore and cross-shore sediment transport on a nearshore profile. Roelvink and Stive (1989) extended the formulation with the additional effect of stirring due to wave breaking. Based on measured hydrodynamics, the Bailard (1981) approach has been shown not able to predict onshore bar migration (Thornton et al., 1996; Gallagher et al., 1998). This is likely due to the vertically integrated instantaneous response of the transport according the Bailard (1981) approach (Roelvink and Stive, 1989; Gallagher et al., 1998)

A comparison between the 1-DV approach and the Bailard (1981) approach will be made in Chapter 4 of this thesis.

1.5.3. MODELLING OF MORPHODYNAMICS

Three types of cross-shore profile models can be found in the literature, i.e. descriptive models, equilibrium profile models and process-based models (Roelvink and Brøker, 1993).

Descriptive models are based on observations of beach profile and beach profile changes for a range of environments and on different time scales. Beaches and beach states are classified according to parameters that determine the transition from one beach state to another. An example of a descriptive model is the one by Wright and Short (1984), which describes the transitions of beaches through several stages, based on an environmental parameter including the breaking wave height, wave period and sediment fall velocity. Descriptive models are useful in pointing out typical beach topographies and transitional regimes in beach morphology. However, the quantitative and/or predictive capabilities of these models are limited and the effects of changes caused by human interference cannot be treated.

Equilibrium profile models are based on empirical correlations between a scale parameter and the sediment size or fall velocity. The most often used form is $h(x) = Ax^{2/3}$ in which h is the water depth at a distance x from the shoreline and A is the sediment-dependent scale parameter (see e.g. Dean, 1991). The equilibrium profile concept has proven to be useful in areas where longshore transport gradients can be neglected, and where the profile is able to reach equilibrium. Equilibrium profile models have also been used to predict profile behavior in time. In this view, changes in beach profile shape can be regarded as adjustments of the profile from the course of one equilibrium to another as the forcing conditions change. An example of such a model is the one by Larson et al. (1999). Although the theoretical equilibrium profile model produces a shape that is in agreement with field data, the physical justification for the equilibrium condition is not clear and the assumptions made are rather ad hoc. The

empirical relations are so crude and cover so many processes that these models always have to be calibrated for a given site. Moreover, this type of models does not account for the presence of permanent nearshore bars. Advantage of this type of models is the limited computing capacity required. They may be used in combination with the more generally applicable process-based models, in this way suppressing erroneous developments resulting from over-extrapolating from short to long-term time scales.

The “state of art” on the present knowledge of morphodynamic processes is reflected by the current generation of mathematical, process-based models. These models integrate and synthesize theoretical knowledge based on experiences gained during many field and laboratory experiments. Examples of process-based models are those by Bowen (1980), Dally and Dean (1984), Stive and Battjes (1984), Roelvink and Stive (1989), Southgate and Nairn (1993), Nairn and Southgate (1993), Thornton et al. (1996), Rakha et al. (1997), O'Connor and Nicholson (1999), and others.

The process-based models have a common structure, consisting of sub modules, representing: 1) the hydrodynamics such as wave propagation, tide-, wind- and wave-driven currents, 2) the associated sediment transport patterns and 3) bed level changes, implemented in a loop system to ensure feedback and dynamic interaction of the elements of the morphodynamic system. Coastal profile models reflect the physical processes in a cross-shore direction, assuming longshore uniformity. Van Rijn et al. (2002b) describe and compare five process-based profile models. Most relevant transport components in the cross-shore direction such as wave skewness and the presence of mean cross-shore currents are included in the models. Bed level changes follow from numerical solution of the mass conservation balance. Longshore wave-driven and tide-driven currents and the resulting sediment transport are included in most models.

The process-based models typically operate on short-term and medium-term time scales up to 5 years, corresponding with tidal, storm and seasonal events. The spatial scales involved vary from a few meters and larger with a total area coverage of several hundred meters to a few square kilometers.

The quality and use of coastal profile models is still seriously affected by a number of limitations. Shortcomings may be found in the description of the randomness and directionality of the waves, the near-bed wave velocity skewness, the wave breaking processes, the wave-induced streaming in the boundary layer, the wave-induced cross-shore and longshore currents, the generation of low-frequency processes and the wave-induced sand transport components. The sand transport module generally is a critical key element and still requires a substantial input of information from empirical data sets; these data sets usually do not cover the total range of conditions and processes. Furthermore, the sand transport models generally are transport capacity models, which means that the spatial phase lags effects between hydrodynamics and sediment transport are not taken into account. As a consequence of all these shortcomings, the predictive capability of the process models generally is rather low in quantitative sense. Actually, these models are still in their infancy. In the best cases, models are useful qualitative tools that can be operated to compare relative performance of one solution versus another. Much in the behavior of these models is still poorly understood. One of the

reasons for this is the uncertainty in the values and variability of the free model parameters, such as e.g. the bed roughness. Another reason is that it is unclear for which time scales these models are applicable. Both aspects will be addressed in this thesis.

Process-based coastal area models are 2 or 3-dimensional horizontal models consisting of, and linking, the same set of sub modules of the wave field, the tide-, wind- and wave-driven flow field, the sediment transport fluxes and the bed evolution. De Vriend et al. (1993) give an overview of coastal area models. Fully 3D-models describing the currents on a three-dimensional grid are in a very early stage of development, and require excessive computer memory and power at present.

1.6. RESEARCH OBJECTIVES AND OUTLINE

The central aim of this thesis is to improve the understanding of the short to long-term behavior of barred profiles. The central hypothesis is that nearshore bar behavior can be represented by the break-point concept and that a parametric process-based cross-shore profile model can accurately describe the mechanisms involved. Based on this hypothesis, the following research objectives and questions are formulated.

Hydrodynamics

- Can the nearshore hydrodynamic processes be represented sufficiently accurate by a parametric (single-wave) model or is a probabilistic (multi-wave) approach considering the full wave spectrum required to accurately predict nearshore wave and current conditions?
- Is it acceptable to ignore long-wave oscillations in predicting the wave and flow field in the nearshore zone?
- What are the most important parameters determining model performance?

Sediment transport

- Can the nearshore sediment transport rate be predicted with a relatively simple engineering approach based on a parametric (single-wave) approach or is a probabilistic (multi-wave) approach required?
- What is the relative contribution of the wave-related (high- and low-frequency) and current-related suspended transport component to the net suspended transport rate?
- What is the relative contribution of the bed-load and suspended load component to the total depth-integrated transport rate?
- What are the key parameters in the prediction of suspended sediment concentrations and current- and wave-related suspended sediment transport rates?
- Is it for morphodynamic purposes acceptable to ignore the long wave component of the sediment fluxes?

Morphodynamics

- Is a cross-shore profile model capable of predicting nearshore morphological changes on the time scale of storms and seasons (weeks to years), simplifying the coastal system to a longshore-averaged 2-D system?
- Can the nearshore morphological changes be predicted using a single-wave approach or is a multi-wave approach required?
- What are the most influential parameters for nearshore bar behavior?
- Can a cross-shore profile model be used for simulation of a shoreface nourishment?

These research questions are addressed based on analysis of field and laboratory data and comparison with model predictions. The field data comprise a rather unique set of sediment transport measurements in the nearshore zone of Egmond aan Zee in the Netherlands, which are described in Chapter 4 of this thesis.

The outline of the thesis is presented in the following section and is intended as a guideline to the reader.

- Chapter 2 describes the set-up of the laboratory and field experiments, the measurement techniques and gives an estimate of the accuracy of measured parameters.
- Chapter 3 presents the hydrodynamic module of the cross-shore profile model. The hydrodynamic processes are directly relevant for the modelling of sediment transport rates and include cross-shore wave transformation (shoaling, refraction, dissipation), orbital motion and time-averaged cross-shore and longshore currents. A specific question that will be addressed is whether and to what extent a probabilistic approach is necessary to accurately predict nearshore hydrodynamics.
- Chapter 4 presents the sediment transport module of the cross-shore profile model and compares measured and predicted transport rates. The specific question that will be addressed is with what accuracy the sediment transport in the nearshore zone can be predicted using the relatively simple process-based (parametric) transport model of Van Rijn (2000). A comparison is made with the often applied Bailard (1981) approach. In addition, the relative contribution of transport components is studied.
- Chapter 5 addresses the question whether and to what extent a cross-shore profile model is capable of predicting nearshore morphological changes on the time scale of storms and seasons, simplifying the coastal system to an longshore-averaged 2-D system. Cross-shore profile changes predicted by the model are compared to observed profile changes on storm and seasonal scale. The use of the profile model for simulation of a shoreface nourishment will be explored.

2. EXPERIMENTAL DATA

2.1. INTRODUCTION

This chapter serves as a description of how the experimental data were obtained and to give an estimate of the confidence of measured parameters (error band). The scales involved range from small-scale laboratory tests to large-scale field experiments.

The advantage of small-scale laboratory experiments is that they provide an accurate description of the hydrodynamic and sediment transport processes involved. Conditions are perfectly controlled and instruments are precisely placed in position, reducing measurement errors to a minimum, in this way providing highly reliable data. This also accounts for large-scale laboratory experiments while these provide information on proto-type scale comparable with field conditions. Field measurements provide information on hydrodynamic and sediment transport processes under natural conditions. Large-scale field measurements on sediment transport processes have hardly been performed. Most field campaigns focus on hydrodynamic processes. It appears to be rather difficult to measure sediment concentrations in surf zone conditions with a constantly changing bed level and different bed forms making it rather troublesome to determine the exact height of the instruments above the seabed. Besides, instruments suitable for measuring in the field are still in a developing stage. This thesis presents a rather unique set of measurements of horizontal velocity and suspended sediment concentration (arrayed vertically) at a number of locations across a nearshore bar near the coast of Egmond aan Zee in the Netherlands. The instruments could be adjusted accurately at a given elevation above the seabed. Together with high-quality laboratory data, these measurements are compared with model results in the chapters hereafter.

Herein, first a description is given of the applied measuring techniques and their accuracy. Then, the experiments themselves are described. Experimental procedures are explained and basic experimental data are given. First, a description is given of small-scale flume experiments done in a wave flume of the Delft University of Technology in the Netherlands. Second, large-scale flume experiments performed in the Delta Flume of Delft Hydraulics in the Netherlands are described. Then, the experimental set-up of large-scale flume tests done in the Grosser Wellenkanal of the Universities Hannover/Braunschweig in Germany will be given. Finally, field experiments near the coast of Egmond aan Zee in the Netherlands are described.

It is noted that apart from the present data, data from earlier experiments have also been used in this thesis. Laboratory data from the LIPIID experiments in the Delta Flume and field data from experiments near Duck, NC, USA, are used in Chapter 3 and 5. A description of the set-up of these earlier experiments will not be repeated here. The reader is referred to earlier publications where necessary.

2.2. INSTRUMENTS AND MEASUREMENT ERRORS

Van Rijn, Grasmeijer and Ruessink (2000) give a description of instruments used in the field and in a laboratory to measure waves, currents and sediment concentrations. They compare different measurement techniques under controlled conditions thus providing information on the measurement errors involved. The instruments described are: 1) pressure sensor, electromagnetic flow meter (EMF), a 5-fold acoustic sediment transport meter (5F-ASTM), optical backscatter sensor (OBS) and a pump sampler. Conclusions on measurement accuracies are summarized in Table 2.1 and described below.

Table 2.1. Measurement accuracies.

Parameter	Instrument	Accuracy
Wave heights	Pressure sensor	10-15% with 0.10 m minimum
Current velocities	EMF	10% with 0.05 m/s minimum
	5F-ASTM	15-20% for $\bar{c} > 0.5 \text{ kg/m}^3$
Sand concentrations	Pump sampler	10%
	5F-ASTM	30% for $\bar{c} > 0.1 \text{ kg/m}^3$
	OBS	30% for $\bar{c} > 0.5 \text{ kg/m}^3$

Under non-breaking wave conditions, wave heights derived from converted pressure data using linear wave theory may differ up to 10% from the wave heights derived from direct measurements of water surface elevation. Under breaking wave conditions, this difference increases to about 15% with a minimum of 0.10 m. This suggests that wave heights in the field can rather accurately be determined from pressure data using linear wave theory and that nonlinear effects are small.

Peak near-bed orbital EMF velocities were found to be accurate within 10% of those measured with a Laser Doppler current meter. Time-averaged EMF velocities were found to be accurate within about 10% of the measured value with a minimum of 0.05 m/s. Inaccuracies of the EMF can be attributed to zero drift stability, air bubbles in the water, wearing and fouling.

The accuracy of 5F-ASTM velocities depends on the amount of sediment in suspension. The velocity is not entirely recorded if the time-averaged concentration drops under a level of about 0.5 kg/m^3 . Still, data satisfying this requirement showed peak near-bed 5F-ASTM velocities to be about 15% smaller than those measured with an EMF. Time-averaged 5F-ASTM velocities were up to 20% smaller than those measured with an EMF. These inaccuracies, together with the fact that the 5F-ASTM measures the velocity of the suspended sediment particles rather than the fluid velocity, make the 5F-ASTM less suitable for measuring instantaneous and time-averaged fluid velocities.

OBS sensors are highly sensitive to the grain size of the suspended sediment. This implies that the OBS concentrations should be calibrated for the smaller size of the sediment in suspension rather than using the bed material in the calibration procedure. This requires sampling of suspended sediment during field and laboratory experiments.

The effective concentration range for OBS sensors is 0.5 to 100 kg/m³. Concentrations measured within this range have an accuracy of about 50%. The OBS sensors show a relatively steady offset concentration that can be related to the presence of relatively fine sediments (silt and mud). The offset can be defined as the minimum value of the data record (burst).

The 5F-ASTM appeared to be much less sensitive to sediment grain size. One calibration curve could be used for sediments with a D_{50} between 0.16 and 0.33 mm. The effective measurement range is between 0.1 and 10 kg/m³. On an average, the 5F-ASTM concentrations differed about 30% from concentrations measured with a pump sampler, in agreement with manufacturer specifications.

2.3. SMALL-SCALE LABORATORY EXPERIMENTS

Small-scale laboratory measurements of horizontal velocity and suspended sediment concentration (arrayed vertically) were done at a number of locations across a simulated shallow water bar built in fine sands ($D_{50} = 0.10$ mm) and subjected to irregular waves of varying significant wave height, but with a constant spectral shape (JONSWAP spectrum). The specific objectives of the experiments were: 1) to get information of the mean and oscillatory (high and low frequency) sand transport processes along a barred profile in the ripple regime, 2) to investigate the importance of the near-bed sand fluxes, which are not reflected in the measured suspended transport rates, but are revealed from bar migration data.

The sand bar and the selected wave conditions in the flume are supposed to represent a nearshore sand bar in a regime with breaking waves, but the experimental set up is no scale model of some specific field case. Furthermore, the bar in the flume was not moulded by long-term wave generation, but artificially constructed. Hence, the bar does not represent some kind of equilibrium bar. The objective of the experiments is no more than to create breaking wave conditions over a movable bed and to identify the basic characteristics of the associated hydrodynamic processes and sand transport processes. This may help to better understand similar processes in field conditions. Net transport rates and associated directions over a bar (onshore or offshore) depend critically on whether the bar is in some kind of equilibrium with the wave field or is well outside equilibrium. Most likely, the net transport rates measured in the flume are not representative for field conditions, but it is believed that the measured transport components are of interest in a qualitative sense. Furthermore, three-dimensional effects are absent in these flume tests.

The experiments were conducted in 1995 in a small-scale wave flume of the Laboratory of Fluid Mechanics of the Faculty of Civil Engineering (Delft University of Technology). The flume has a length of 45 m, a width of 0.8 m and a depth of 1.0 m. The flume is equipped with a remote controlled rail guided carriage. Irregular waves (following a JONSWAP spectrum) were generated with a peak spectral period of $T_p = 2.3$ s (± 0.2 s). When attempting to reproduce natural wave conditions in a laboratory flume it is important to prevent the reflection of the free long waves traveling offshore toward the wave generator. This was achieved by active wave absorption. At the end of the

flume wave energy was absorbed by a wave dampening structure. The wave dampening structure consisted of a curved (convex shape) panel with a roughened surface. The higher waves were spilling over the top of the panel into a stilling basin; return flow was possible underneath the panel. Sand with the following grain size characteristics was used: $D_{10} = 0.076$ mm, $D_{50} = 0.100$ mm and $D_{90} = 0.131$ mm; the representative (50%) settling velocity of the sediment is $w_s = 0.008$ m/s.

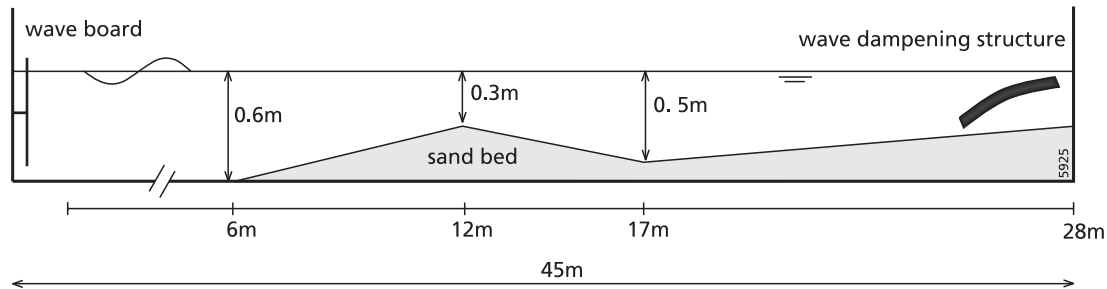


Figure 2.1. A conceptual view of the small-scale wave flume of Delft University of Technology

An artificial sand bar of the form shown in Figure 2.1 was constructed in the flume. The bed profile varies in depth from 0.60 m seaward of the bar to 0.30 m at the bar crest. The water depth in the trough shoreward of the bar crest is 0.50 m. The sand bar has a steep seaward slope of 1 to 20 and a steep shoreward slope of 1 to 25. The bed slope shoreward of the bar trough is 1 to 63.

Two test series were performed (series B1 and B2) with incoming H_{rms} wave heights of 0.11 and 0.13 m respectively. Measurements were performed at 10 different locations across the sand bar. Experimental conditions are presented in Table 2.2. The measurements are identified with respect to the appropriate location across the profile. Complete velocity and concentration measurements are presented by Grasmeijer and Van Rijn (1999).

Time-averaged concentrations were measured using a pump sampling system. The pump sampler consisted of a vertical array of 10 intake tubes of 3 mm internal diameter connected to the pumps by plastic hoses. The height of the intake tubes ranged from 0.01 m to 0.26 m above the crest level of the bed forms, with the intake openings placed in a direction transverse to the plane of orbital motion. The intake velocity was about 1 m/s, satisfying sampling requirements. The 10-liter samples were collected in calibrated buckets. The pump sampler was operating for 15 minutes giving an average concentration over the measuring time.

Instantaneous concentrations were measured using an acoustic sediment transport meter (1F-ASTM, see Figure 2.2). The 1F-ASTM measures the horizontal sand particle velocity and particle concentration using the principles of Doppler frequency shift and intensity variation of reflected sound waves, respectively. The response frequency of the transducers is 4.5 MHz ($\pm 10\%$). The velocities and concentrations were measured at the same elevations above mean bed as those of the concentrations with the pump sampler starting at the lowest measuring point and working upward. The output voltage of the 1F-ASTM is linearly proportional to the sediment concentration. Using linear regression on the time-averaged output of the 1F-ASTM (time-averaging period of 5

minutes) and the concentrations measured simultaneously with the pump sampler, a calibration relationship was determined with a regression coefficient of $r^2 = 0.96$.

Surface elevations were measured by conductivity-type wave gauges. Specifications for level stability and linearity deviations, namely, $< 0.5\%$ of immersion depth and $< 0.5\%$ of full scale deflection, respectively, were confirmed by referencing and calibration.

Horizontal orbital velocities were measured using an electromagnetic velocity meter (EMF) consisting of a 2-axis, 4 cm diameter, ellipsoid probe with an inaccuracy of $0.01 \text{ m/s} \pm 1\%$ of the measured value and a zero stability of less than 5 mm/s . The instantaneous EMF-velocities were measured at the same elevations above the mean bed level as those of the pumped concentrations. As with the 1F-ASTM signals a time-averaging period of 5 minutes was applied.

Morphological changes of the barred profile were determined by measuring the bed level at the flume window every 0.25 m along the profile before and after each test. Mean bed level and ripple dimensions like ripple height η and ripple length λ were determined using a so-called profile follower (PROFO). The instrument consists of a vertical gauge with a conductivity sensor at the bottom tip. The gauge moves vertically by means of a servo system to maintain a constant distance close to the sediment bed. The inaccuracies of the instrument are negligible compared to the statistical inaccuracies associated with the natural variability of the bed. The PROFO was not used for determining morphological changes of the barred profile because of the small range of the instrument.

Except for a reference wave gauge, all instruments were installed on the carriage: the intake tubes, a wave gauge, a profile follower, an electromagnetic velocity meter and the 1F-ASTM. A sampling frequency of 20 Hz was used. To eliminate small-scale ripple-related variations in velocity and concentration, the measurement carriage was moved forward and backward over four to five ripple lengths during the sampling period (5 minutes). The velocity of the moving carriage was small (approximately 0.01 m/s) compared to the fluid velocity and large compared to the bed-form migration velocity. Waves were run 15 minutes prior to initial sampling.



Figure 2.2. Photo showing instruments used in the small-scale wave flume of Delft University of Technology. The instruments are: acoustic sediment transport meter (left), electro magnetic current meter (middle), and pump sampler (right). The profile follower and wave gauge are not shown.

Table 2.2. Experimental data from small-scale wave flume experiments done in 1994 at Delft University of Technology, The Netherlands. The depth-integrated suspended sand transport rates are defined between 0.001 m above the ripple crests and mean water depth.

cross-section	distance	wave height	water depth	fraction breaking waves	onshore orbital velocity	offshore orbital velocity	ripple height	ripple length	$q_{s,net}$	$q_{s,w,high}$	$q_{s,w,low}$	$q_{s,c}$
	$H_{1/3}$	h	Q_b	$u_{1/3,on}$	$u_{1/3,off}$	η	λ	(m)	(kg/m/s)	(kg/m/s)	(kg/m/s)	(kg/m/s)
B1												
1	3.0	0.160	0.60	0	0.256	0.243	0.007	0.068	-0.00009	-0.00059	0.00023	0.00027
2	6.0	0.156	0.59	0	0.251	0.239	0.010	0.047	-0.00057	-0.00094	0.00046	-0.00009
3	8.0	0.156	0.50	0	0.276	0.253	0.007	0.050	-0.00102	-0.00084	0.00019	-0.00036
4	10.0	0.165	0.39	0.4	0.359	0.284	0.012	0.048	-0.00230	-0.00193	0.00021	-0.00058
5	12.0	0.177	0.32	6.3	0.411	0.300	0.008	0.051	-0.00792	-0.00216	0.00017	-0.00593
6	14.5	0.149	0.42	14.9	0.291	0.216	0.007	0.061	-0.00138	-0.00018	-0.00037	-0.00082
7	17.0	0.140	0.50	2.7	0.223	0.229	0.010	0.046	-0.00072	-0.00086	0.00001	0.00013
8	20.0	0.134	0.45	0	0.281	0.269	0.005	0.047	-0.00043	-0.00021	-0.00011	-0.00011
9	23.0	0.137	0.41	0	0.283	0.251	0.011	0.053	-0.00220	-0.00115	-0.00052	-0.00052
10	26.0	0.132	0.36	0	0.316	0.278	0.013	0.073	-0.00211	-0.00095	-0.00030	-0.00087
B2												
1	3.0	0.189	0.60	0.4	0.295	0.280	0.011	0.083	-0.00062	-0.00095	0.00057	-0.00024
2	6.0	0.188	0.59	0.6	0.304	0.282	0.006	0.044	-0.00086	-0.00112	0.00043	-0.00018
3	8.0	0.188	0.51	0.6	0.320	0.315	0.007	0.045	-0.00141	-0.00147	0.00061	-0.00056
4	10.0	0.201	0.39	1.6	0.412	0.340	0.005	0.038	-0.00554	-0.00254	0.00036	-0.00337
5	12.0	0.201	0.31	10.0	0.471	0.335	0.006	0.069	-0.02099	-0.00503	-0.00157	-0.01431
5a	13.0	0.187	0.33	18.6	0.432	0.293	0.011	0.054	-0.01922	-0.00241	-0.00398	-0.01276
6	14.5	0.163	0.40	27.6	0.361	0.240	0.007	0.055	-0.00531	-0.00031	-0.00114	-0.00387
7	17.0	0.154	0.51	8.2	0.248	0.239	0.010	0.054	-0.00090	-0.00067	-0.00014	-0.00009
8	20.0	0.148	0.46	0	0.276	0.277	0.006	0.038	-0.00066	-0.00078	0.00002	0.00010
9	23.0	0.151	0.40	0	0.310	0.274	0.008	0.049	-0.00199	-0.00128	-0.00013	-0.00059

2.4. LARGE-SCALE LABORATORY EXPERIMENTS: DELTA FLUME

Large-scale laboratory measurements of horizontal velocity and suspended sediment concentration (arrayed vertically) were done in 1997 on a horizontal sand bed subjected to irregular waves of varying significant wave height, but with a constant spectral shape (JONSWAP spectrum). The specific objective of the experiments was to get information on the oscillatory (high- and low-frequency) suspended sand transport processes under prototype conditions in the ripple regime. Dang Huu Chung and Grasmeyer (1999) give an extensive description of the experiments. Grasmeyer et al. (1999) used the data to make a comparison with a wave-related suspended transport formulation.

The experiments were done in the Delta Flume of Delft Hydraulics, the Netherlands (Figure 2.3). The flume has a total length of 233 meters, a depth of 7 meters and a width of 5 meters. A piston activated wave board generates the (irregular) waves. A horizontal sand bed with a height of 0.5 m was placed in the flume over a length of about 40 m (Figure 2.4). Two measurement series were made, one with sand with a median diameter of $D_{50} = 0.33$ mm and the second with $D_{50} = 0.16$ mm. The water depth at the test section was $h = 4.5$ m for all tests.



Figure 2.3. Photo of the Delta Flume of Delft Hydraulics.

The experiments were two-dimensional, in the sense that the waves were normal to the sand bed (cross-shore experiment with no longshore component) but local processes might have been three dimensional due to the generation of bed forms (ripples). A 5-fold acoustic sediment transport meter (5F-ASTM) was used to measure the instantaneous fluid velocities and sand concentrations at five points simultaneously between 0.065 m and 1.0 m above the bed. Other instruments were used to obtain additional data of velocities and concentrations. The instruments were mounted in a tripod, which was placed on the sand bed at location $x = 125$ m. During each test the instruments were operated for about 15 minutes to sample over a representative wave record.

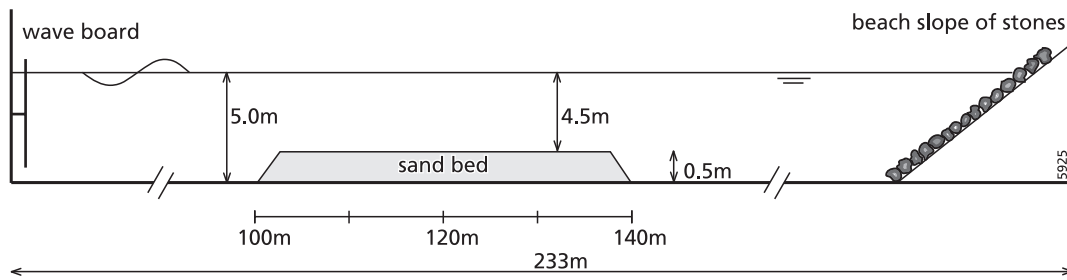


Figure 2.4. A conceptual view of the Delta Flume of Delft Hydraulics.

For comparison with the 5F-ASTM data, five EMF sensors and a pump sampling system were installed in the wave flume. The EMF sensors were attached to the flume wall at $x = 121$ m. The pump sampling unit was used to obtain time-averaged sand concentrations. It was attached to the flume wall at distance $x = 123$ m during the tests with coarse sand. As the turbulence around the supporting structure made a scour hole, which resulted in undersampling of sediment, it was decided to move the pump sampling unit away from the flume wall and closer to the 5F-ASTM for the series of tests with fine sand. The intake nozzles of the pump sampling unit were within 2 m of the 5F-ASTM sensors for these tests. Basic experimental data of the Delta Flume experiments are given in Table 2.3.

Table 2.3. Experimental data from large-scale wave flume experiments done in 1997 in the Delta Flume of Delft Hydraulics, The Netherlands. The sediment transport rates are based on measurements between 0.065 and 1.0 m above the sand bed. A negative sign means that the transport rates are offshore directed.

test	grain size D_{50} (mm)	wave height $H_{1/3}$ (m)	wave period T_p (s)	water depth h (m)	ripple height η (m)	ripple length λ (m)	$q_{s,net}$ (kg/m/s)	$q_{s,w,high}$ (kg/m/s)	$q_{s,w,low}$ (kg/m/s)	$q_{s,c}$ (kg/m/s)
A	0.33	1.00	5.0	4.5	0.053	0.38	0.0028	0.0027	-0.0003	-0.0004
B	0.33	1.25	5.0	4.5	0.055	0.39	0.0033	0.0049	-0.0015	-0.0011
C	0.16	1.00	5.0	4.5	-	0.94	0.0002	0.0016	0.0002	-0.0016
D	0.16	1.25	5.0	4.5	n.m.	n.m.	0.0002	0.0035	-0.0004	-0.0030
E	0.16	1.50	5.0	4.5	n.m.	n.m.	0.0017	0.0042	-0.0004	-0.0022

2.5. LARGE-SCALE LABORATORY EXPERIMENTS: GROSSER WELLENKANAL

Large-scale laboratory measurements of horizontal velocity and suspended sediment concentration (arrayed vertically) were done in 1999 on a horizontal sand bed subjected to irregular waves (JONSWAP spectrum) with $H_{1/3} = 1.25$ m, $T_p = 6$ s. The specific objective of the experiments were: 1) to get information on the oscillatory (high- and low-frequency) suspended sand transport processes under prototype conditions in the ripple regime, and 2) to show the importance of the near-bed sand fluxes, which are not

reflected in the measured suspended transport rates, but are revealed from bed level changes.

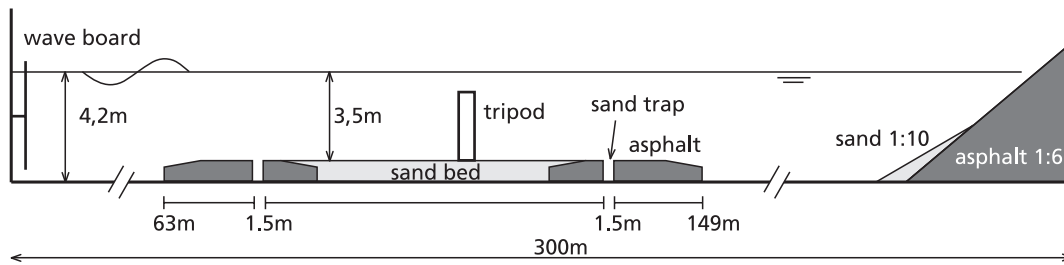


Figure 2.5. A conceptual view of the Grosser Wellenkanal of the University of Hannover and the Technical University of Braunschweig.

The Grosser Wellenkanal (GWK) is a joint research facility of the University of Hannover and the Technical University of Braunschweig, Germany. The wave flume is the largest in the world. It has a length of about 300 m, a depth of 7 m and a width of 5 m. The piston-type wave generator allows prototype experiments with regular or irregular waves with periods between 1 and 15 s and heights up to 2.5 m. The wave reflections from the beach are compensated directly at the wave paddle (Schmidt-Kopenhagen et al., 1997).

Table 2.4. Experimental data from large-scale wave flume experiments done in 1999 in the Grosser Wellenkanal of the Universities Hannover/Braunschweig, Germany. Transport rates are averaged values over 12 tests (standard error between brackets). The suspended sediment transport rates are based on measurements between 0.02 and 1.0 m above the sand bed. The bed-load transport rate is derived from measured bed level changes. A negative sign means that the transport rates are offshore directed.

Grain size D_{50} (mm)	wave height $H_{1/3}$ (m)	wave period T_p (s)	water depth h (m)	$q_{s,net}$ (kg/m/s)	$q_{s,w,high}$ (kg/m/s)	$q_{s,w,low}$ (kg/m/s)	$q_{s,c}$ (kg/m/s)	q_b (kg/m/s)
0.23	1.25	6.0	3.5	0.008	0.019	-0.002	-0.008	-0.009
				(± 0.002)	(± 0.002)	(± 0.000)	(± 0.000)	(± 0.001)

A sand bed with a length of approximately 50 m was constructed in the flume (Figure 2.5). Sand was used with grain size characteristics: $D_{10} = 0.14$ mm, $D_{50} = 0.23$ mm, $D_{90} = 0.34$ mm. The sand bed was bordered by asphalt constructions on both sides in which sand traps were built. The sand traps were intended for determining the sediment transport rates based on volumetric changes. Previous experiments by Dohmen-Janssen (1999, personal communication) showed that this approach was unsuccessful. In the present experiments it was therefore decided not to use the sand traps but to use bed profile changes to get a rough estimate of the sediment transport rate. Bed profiles were measured along the centerline of the flume using a mobile carriage (Figure 2.6). The system is described in detail by Berend et al. (1997). The bed level was recorded with a horizontal grid spacing of 0.025 m. The vertical resolution is approximately 0.01 m.

For the present experiments irregular waves were generated with a $H_{1/3}$ of 1.25 m ($H_{rms} = 0.89$ m) and a wave spectrum peak period of $T_p = 6.0$ s. The water depth was kept constant at a value of 4.2 m in front of the wave generator. The water depth at the test section was about 3.5 m. Sediment transport measurements were done with an instrumented tripod (Figure 2.6) in which three OBS sensors at 0.02, 0.04 and 0.10 m, an EMF at 0.10 m, and 5F-ASTM sensors between 0.10 and 1.0 m above the bed were mounted. The three lowest 5F-ASTM sensors are shown in Figure 2.6. Basic experimental data are given in Table 2.4.

Difference between these experiments and those in the Delta Flume is the minimum height at which the suspended transport rates were measured (0.065 m in Delta Flume and 0.020 m in Grosser Wellenkanal) and measurements of bed level changes in the Grosser Wellenkanal from which net total transport rates could be determined.

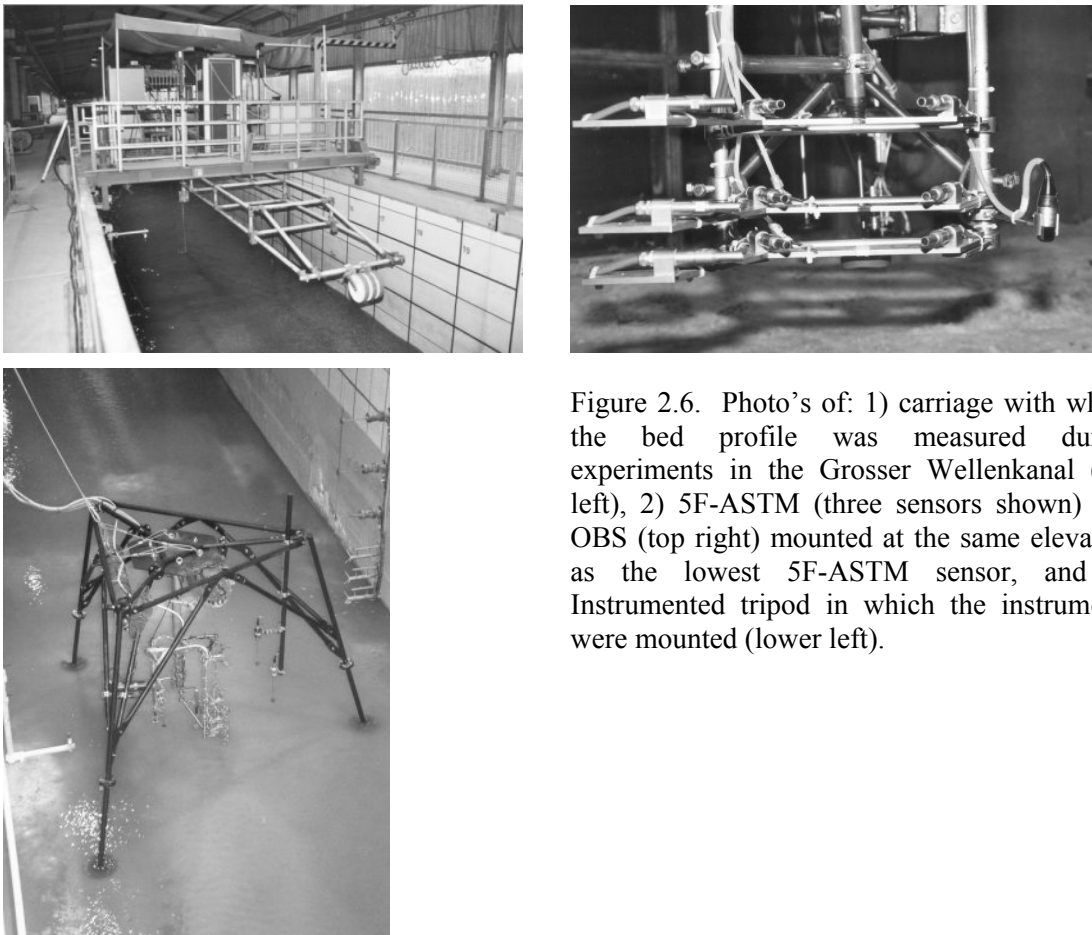


Figure 2.6. Photo's of: 1) carriage with which the bed profile was measured during experiments in the Grosser Wellenkanal (top left), 2) 5F-ASTM (three sensors shown) and OBS (top right) mounted at the same elevation as the lowest 5F-ASTM sensor, and 3) Instrumented tripod in which the instruments were mounted (lower left).

2.6. LARGE-SCALE FIELD EXPERIMENTS: EGMOND AAN ZEE

2.6.1. FIELD SITE

The field site was located at approximately 1 km south of Egmond aan Zee, The Netherlands. It forms part of the 120 km long inlet free, wave dominated central Netherlands coast, consisting of sandy beaches and multiple barred nearshore zones (Short, 1992; Wijnberg, 1995). The orientation of the slightly curved coastline is essentially NNE-SSW (Figure 2.7).

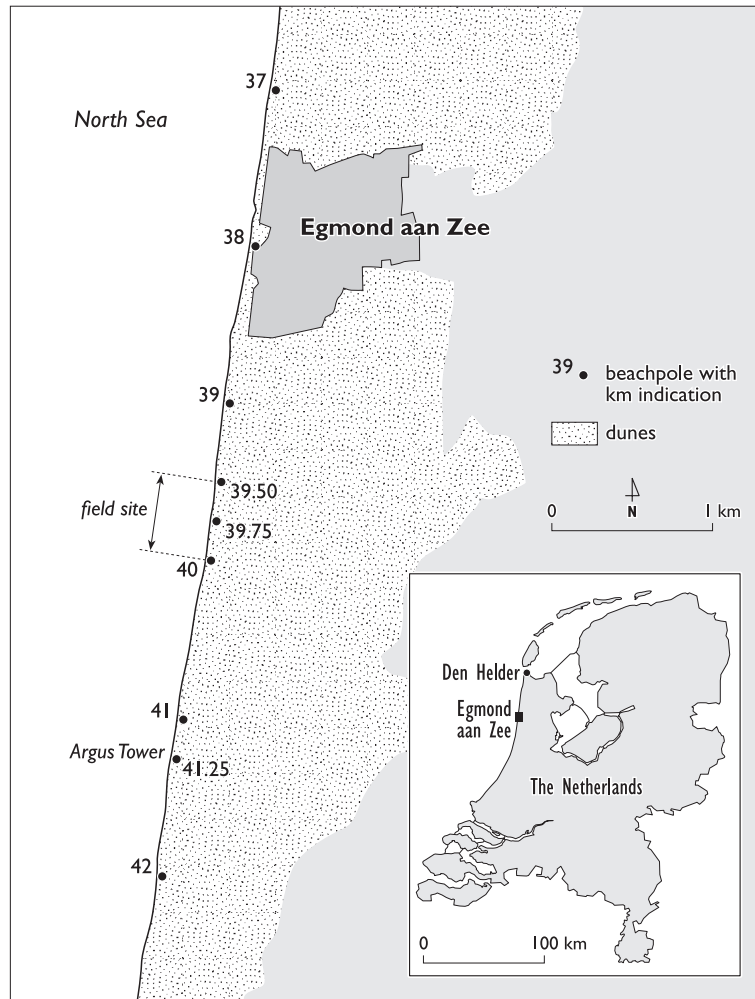


Figure 2.7. Map of the Holland coast showing the Egmond field site. Note that the beach-pole numbering corresponds to the distance in km from Den Helder.

The nearshore subtidal morphology is characterized by a shore-parallel double sandbar system. The inner bar often contains longshore variations with longshore wavelength varying between 350 and 900 m (Short, 1992). The outer bar is either straight or contains rhythmic features with length well in excess of 1 km (Short, 1992). On the whole, the Egmond aan Zee bar system can be classified as a 2.5 D coastal system. On a decadal time scale the bars show an offshore migration cycle with decay of the outer bar at the edge of the nearshore zone and generation of a new bar in front of the beach

(Wijnberg, 1995). The beach slope at the field site is about 1:30 (see also Kroon, 1994). The average beach width is about 80 m. The beach shows ridge and runnel systems during low-wave periods but these systems are eroded during storms. The modal beach state is of the ridge-runnel/low tide terrace type (Short, 1992).

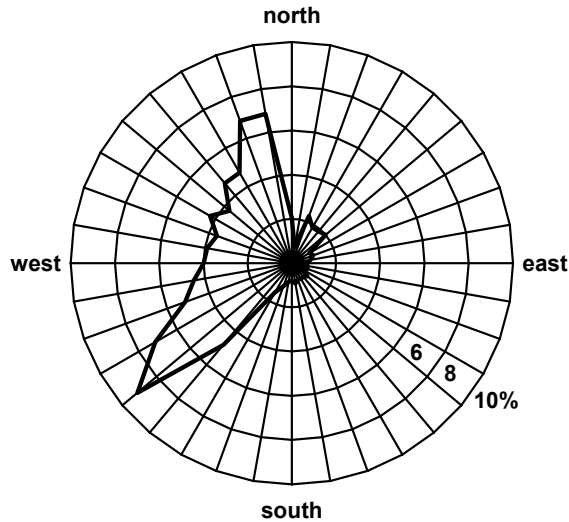


Figure 2.8. Average wave directions of offshore wave fields based on data from wave buoy YM6 at about 21 m water depth, 30 km from the shore, between 1 January 1990 and 1 January 2000.

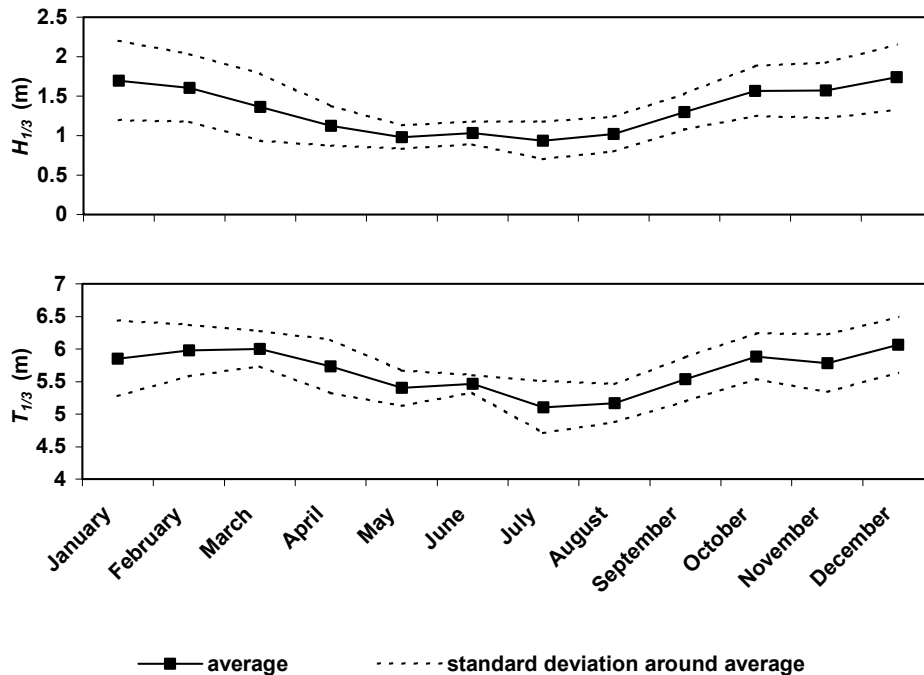


Figure 2.9. Monthly-averaged significant wave height and period based on data from wave buoy YM6 at about 21 m water depth, 30 km from the shore, between 1 January 1990 and 1 January 2000.

The wave climate is dominated by sea waves with a mean annual significant offshore wave height $H_{1/3}$ and period $T_{1/3}$ of about 1.3 m and 5.7 s, respectively. Waves mainly approach the coast from southwesterly (9%) and north-northwesterly (7%) directions (Figure 2.8). The seasonal variation in the storminess of the wind climate is clearly reflected in the wave climate. In the stormy winter months (November through January), the monthly mean $H_{1/3}$ is about 1.7 m, while in the summer season (April through August) the monthly mean $H_{1/3}$ is about 1.0 m (see Figure 2.9). Longshore differences in the offshore wave climate are small due to the short length and the relatively uniform orientation of the central Netherlands coast.

The central Netherlands coast is a micro-tidal coast. The mean tidal range is about 1.6 m. The tidal range at the field site varies between 1.4 m (neap) and 2 m (spring). The peak tidal currents in the offshore zone are about 0.5 m/s; the flood current to the north is slightly larger than the ebb current to the south. The sediments along the central Netherlands coast are well sorted and composed of fine to medium sand. The median grain size at the field site is 0.2-0.25 mm. Further northward, the sediments tend to be somewhat coarser getting into the 0.25-0.5 mm class, while south of the field site the sediments are within the 0.125-0.25 mm range (Stolk, 1989).

2.6.2. EXPERIMENTAL SETTING

The EU-COAST3D project

The EU-COAST3D project was carried out in the framework of the European Commission's research program MAST-III. The objectives of the EU-COAST3D experiments have been formulated as follows:

1. to improve understanding of the physics of coastal sand transport and morphodynamics,
2. to remedy the lack of validation data of sand transport and morphology suitable for testing numerical models of coastal processes,
3. to test a representative sample of numerical models for predicting coastal sand transport and morphodynamics against this data,
4. to develop validated modelling tools and methodologies in a form suitable for coastal zone management.

Two field sites representative of a large proportion of the coastline of Europe, were chosen, the first near Egmond aan Zee in the Netherlands (Figure 2.7) and the second near Teignmouth in the United Kingdom. Herein attention is focused on the experiments near Egmond aan Zee.

Two measurement campaigns were conducted near the coast of Egmond aan Zee. The pilot campaign was held from 16 March till 9 May 1998 and the main campaign took place from 12 October till 20 November 1998. The activities during the measurement campaigns included bathymetric surveys of the beach and the nearshore, measurements of near-bed wave- and current driven processes, measurements of offshore wave

conditions, tides and meteorological conditions and various other activities including sediment sampling, tracer experiments, bed form mapping, and video and radar imaging of the nearshore region. Soulsby (1998) and Van Rijn et al. (2002a) give more details on the objectives and experimental design of the EU-COAST3D experiments.

Morphology

During the EU-COAST3D experiments bathymetric surveys were performed with the WESP, an approximately 15 m high, motorized amphibious vehicle (Figure 2.10). The longshore extent of the survey area was 500 m between beach poles 39.500 and 40.000. Each survey was carried out along cross-shore profiles with 50 m spacing from the dune foot to a maximum water depth of about 7 m at about 750 m from the shoreline. All surveys covered the inner bar area, whereas only about 50% of the surveys also contained the outer bar. The error in the vertical coordinate z is estimated to be around 0.10 m. This error does not account for unresolved bed forms having lengths less than $O(1\text{ m})$ and amplitudes less than $O(0.10\text{ m})$. The horizontal coordinates were, for the purpose of this study, transformed to a local coordinate system, which has a directional wave buoy at about 5 km offshore as its origin. Positive x is onshore directed, while positive y is directed to the north. The vertical z coordinate was evaluated with respect to NAP (Dutch reference level, about mean sea level). After the EU-COAST3D experiments, surveys were done on a regular basis over a longshore distance of 750 m for monitoring purposes.



Figure 2.10. The Water and Beach Profiler (Water and Strand Profiler (WESP) in Dutch).

Two subtidal bars characterized the nearshore morphology of the field site (Figure 2.11). The outer nearshore bar, a longshore uniform, straight bar, oriented parallel to the shoreline, was located at about 480 m offshore. The inner nearshore bar, a non-straight longshore bar, was located at about 200 m offshore.

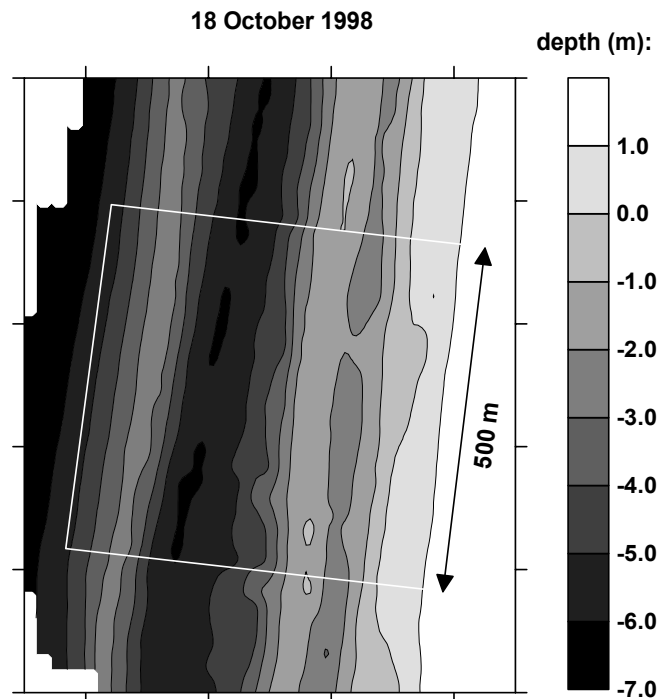


Figure 2.11. Nearshore bathymetry of the field site near Egmond aan Zee measured on 18 October 1998. The box marks the field site.

Ruessink et al. (2000) studied the two- and three-dimensional variability of the bar crest positions at Egmond using complex empirical orthogonal function (CEOF) analysis. The first complex mode, containing about 85% of the variance in the data set, corresponded to the amplitude growth and longshore migration of an approximately 600 m long longshore non-uniformity. The longshore migration rate varied between 0 and 150 m/day and was found to be well related to the longshore component of the offshore wave energy flux. The second complex mode explained about 10% of the variance and largely described the longshore-averaged cross-shore bar migration.

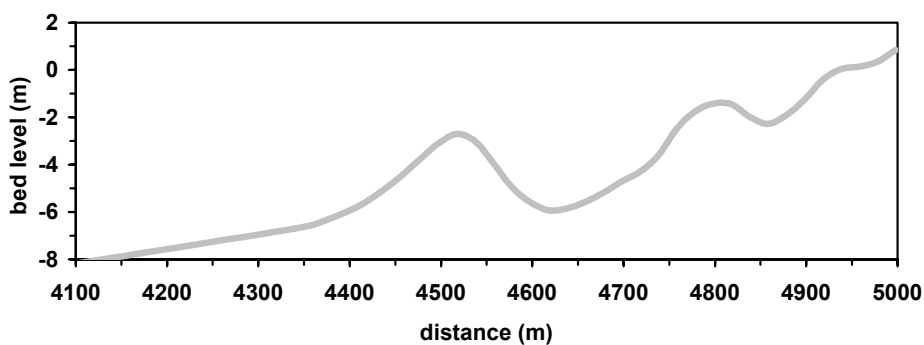


Figure 2.12. Longshore-averaged (over 500 m) cross-shore profile based on 11 profiles measured near the coast of Egmond aan Zee on 18 October 1998. The nearshore bathymetry of the entire field site is shown in Figure 2.11.

Ruessink et al. (2000) suggest that short-term variability in bar-crest position is largely due to changes in the quasi-regular topography and not to longshore-uniform

on/offshore oriented behavior. Because of this longshore variability of the bar position, the available (interpolated) cross-shore profiles were longshore averaged over 500 m for the time span of the EU-COAST3D experiments. For larger time spans (several months), this longshore distance was extended to 750 m. An example of a longshore-averaged cross-shore profile is shown in Figure 2.12. The local beach width of the field site was about 80 m and the beach slope varied around 1:30.

Offshore wave conditions

Offshore wave conditions were measured by Rijkswaterstaat with a directional Waverider buoy, located approximately 5 km from the shoreline in the main measurement transect in 15-m depth.

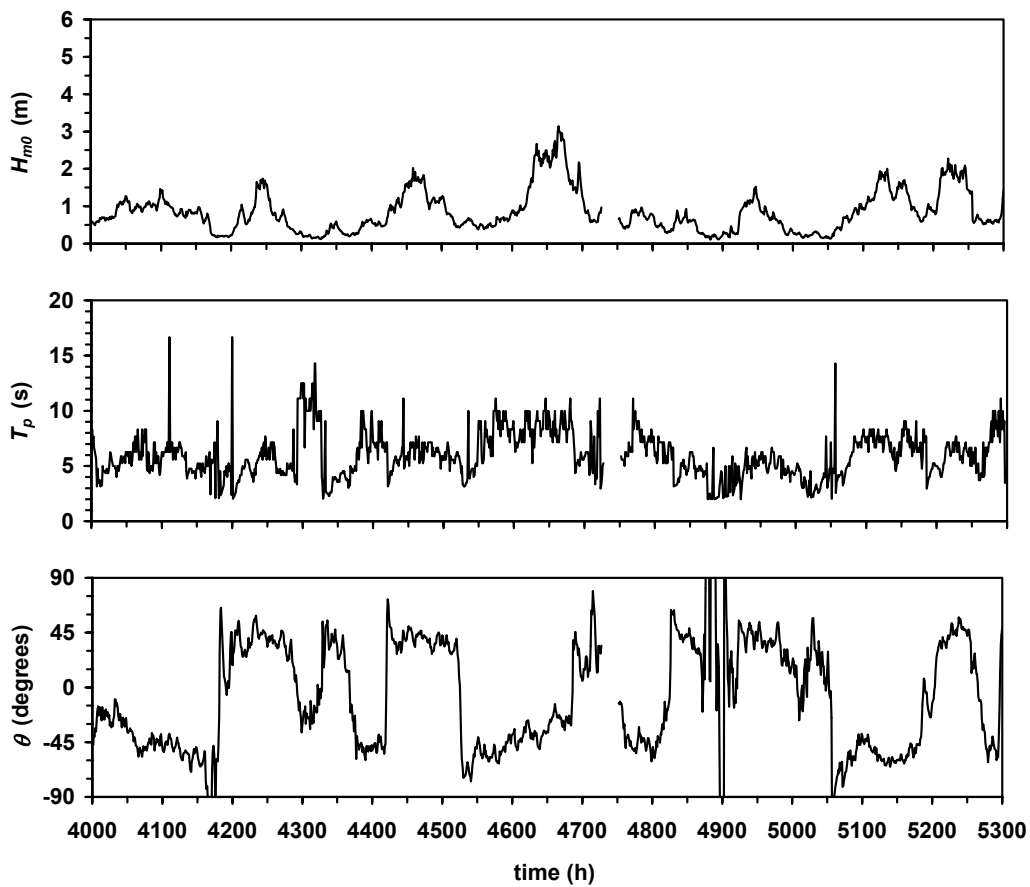


Figure 2.13. Offshore wave conditions during EU-COAST3D pilot campaign; 16 March – 9 May 1998.

Hourly values of the significant wave height H_{m0} , the wave spectrum peak period T_p and the incident wave direction θ during the pilot campaign and the main campaign are presented in Figure 2.13 and Figure 2.14, respectively. Waves incident from the southwest quadrant result in a positive value for θ , whereas waves incident from the northwest result in a negative θ . The x-axis in the figures contains EU-COAST3D burst numbers, where burst number 1 corresponds to 1 October 1997 01:00 Mean European

Time. Each hour (= each burst) has been numbered consecutively since. The burst numbers of the Egmond pilot campaign range from 4000 to 5300. The burst numbers of the main campaign range from 9000 to 10000. The Waverider malfunctioned for about 20% of the time during the main campaign. Missing data were replaced by data gathered by an identical buoy located approximately 20 km to the north, near Petten, in 18-m water depth. Overlapping Egmond and Petten data were virtually identical. It can be observed from Figure 2.13 that during the pilot campaign the offshore H_{m0} ranged between 0.2 and 3.1 m. The wave spectrum peak period T_p ranged between 2.4 and 14.4 s. During the main campaign, H_{m0} ranged between 0.2 and 5.5 m, while the wave spectrum peak period ranged between 4 and 11 s (Figure 2.14).

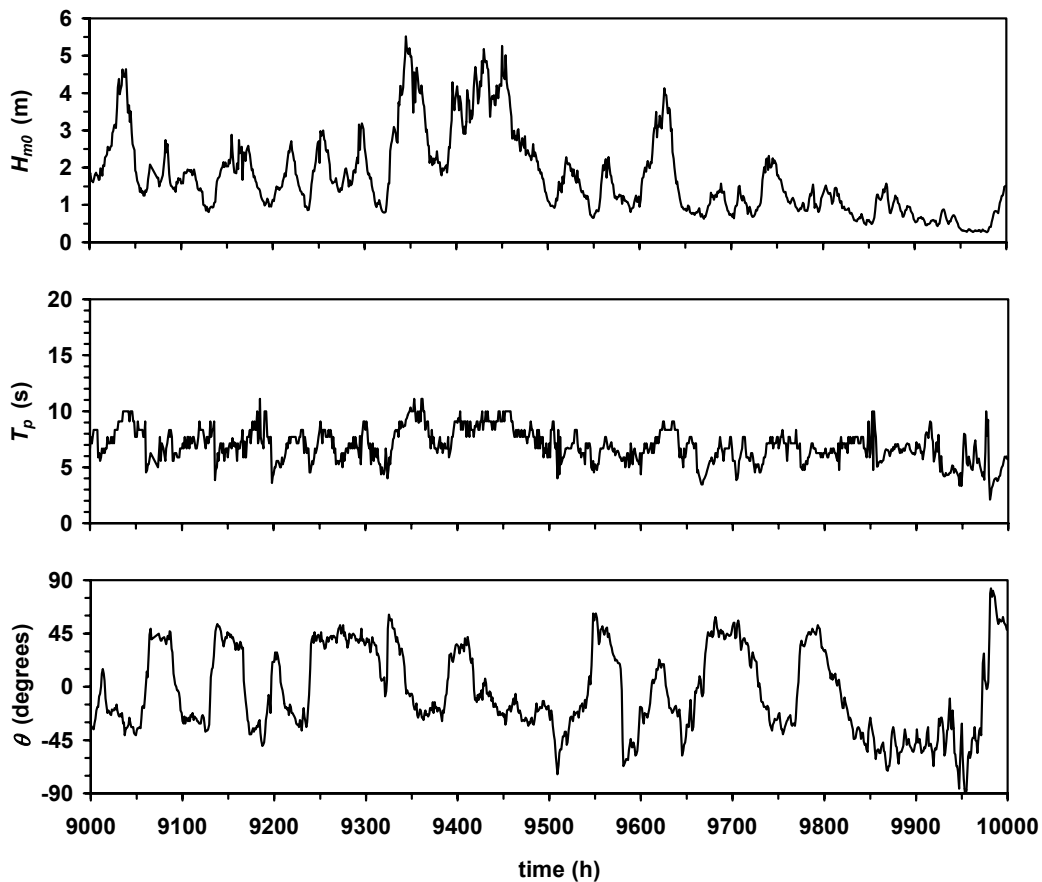


Figure 2.14. Offshore wave conditions during EU-COAST3D main campaign; 12 October – 20 November 1998.

2.6.3. PROCESS MEASUREMENTS

Sediment transport measurements were done at four to five locations in a cross-shore array over the inner nearshore bar using the Coastal Research Instrumented Sledge (CRIS). The CRIS is a 3.5 m square and 2.5 m high vehicle on which a pressure sensor, three EMF sensors, the 5F-ASTM, three OBS sensors and a sand ripple profiler were mounted. Most instruments were attached to a vertically movable arm with which the

height of the instruments could be adjusted at a given elevation above the seabed with an accuracy of 0.01 m (Figure 2.15). The CRIS was being towed to its position by the WESP (Figure 2.16). In order to minimize the influence of settling of the CRIS into the seabed, measurements were started 25 minutes after the CRIS was placed in position (Figure 2.17). Dependent on the conditions, 8.5 or 17.1 minute long records were obtained.



Figure 2.15. Instruments attached to vertically movable arm on the CRIS. The instruments shown are: three OBS sensors at 0.02, 0.04 and 0.10 m above the bed and an EMF at 0.10 m (lower foreground), 5F-ASTM sensors between 0.10 and 1.0 m above the bed (background) and bed sensor (middle). The pressure sensor mounted at $z = 0.60$ m, two other EMF sensors mounted at $z = 2.0$ and 3.0 m, and the sand ripple profiler are not shown.



Figure 2.16. CRIS being towed by WESP

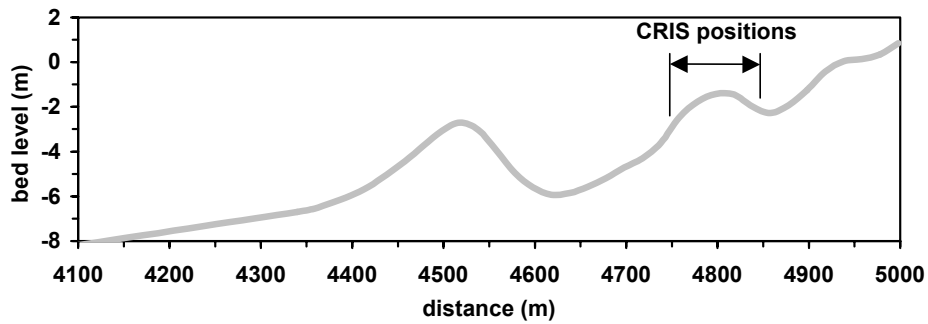


Figure 2.17. Range of positions at which sand transport measurements were done with the CRIS during the EU-COAST3D pilot and main campaigns.

Detailed measurements of hydrodynamics were also done with instrumented tripods placed in a cross-shore transect, thus providing information on the gradients in hydrodynamics over the bars. The tripods were deployed with the WESP as shown in Figure 2.18. The data from seven of these tripods (items E1-E7) are used in this thesis (Figure 2.19). Items E2-E6 were all equipped with at least two EMF sensors and a pressure sensor.



Figure 2.18. WESP deploying instrumented tripod

Items E1 and E7 were equipped with an S4 current meter. Items E2, E4 and E5 were also equipped with two OBS sensors. Data from the latter are not used in this thesis. Tilt meters were used to assess whether the tripods were positioned approximately level to the horizontal plane. A compass was installed to obtain information on the orientation of the EMF sensors relative to the magnetic north. All items were stand alone in the sense that they had their own power supply and data storage. Van Rijn et al. (2002a) give an extensive description of the EU-COAST3D field experiments near the coast of Egmond aan Zee. A list of parameters available from the various items is presented in Table 2.5.

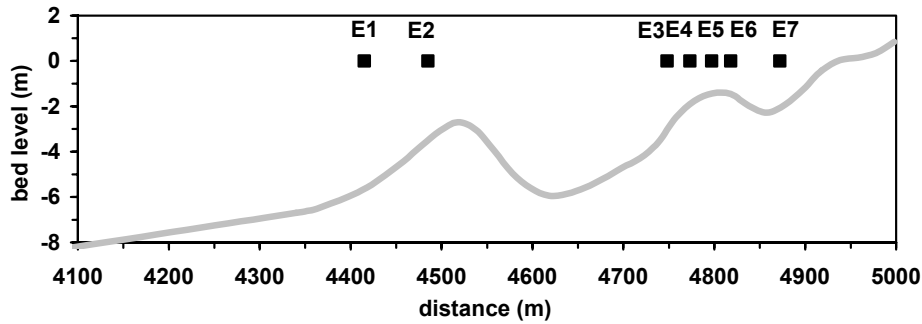


Figure 2.19. Depth relative to mean sea level versus cross-shore distance on 18 October 1998 at Egmond, and locations of instruments.

Measurements with the instrumented tripods were performed in a burst-sampling mode. Background parameters of interest are the water temperature, which varied between 9 and 12 degrees Celsius and the salinity, which varied between 20 and 25 pro mille. The maximum wind speed was about 20 m/s (Beaufort 8) from western directions (normal to shore) on 29 October. The wind and waves generally were in the same directions.

Table 2.5. Parameters available from items (only items used in this thesis are given here) deployed during the EU-COAST3D measurements campaign near the coast of Egmond aan Zee.

Item	distance (m)	description	parameters
E1	4415	S4	\bar{u} , \bar{v}
E2	4485	pressure sensor, EMF, OBS	H , \bar{u} , \bar{v} , u_{on} , u_{off}
E3	4748	pressure sensor, EMF	H , \bar{u} , \bar{v} , u_{on} , u_{off}
E4	4773	pressure sensor, EMF, OBS	H , \bar{u} , \bar{v} , u_{on} , u_{off}
E5	4797	pressure sensor, EMF, OBS	H , \bar{u} , \bar{v} , u_{on} , u_{off}
E6	4818	pressure sensor, EMF	H , \bar{u} , \bar{v} , u_{on} , u_{off}
E7	4872	S4	\bar{u} , \bar{v}

2.6.4. BASIC EXPERIMENTAL DATA

Hydrodynamics

The basic features of the hydrodynamics in the surf zone of Egmond aan Zee during the EU-COAST3D experiments are shortly described here. Van Rijn et al. (2002a) give a more extensive description. Here only a summary of their analysis on the wave height variation, the wave breaking process, the skewness of the wave orbital velocities, the longshore current velocity, and the cross-shore current velocity near the coast of Egmond is given.

Based on the measured wave data, Van Rijn et al. (2002a) found that during major storm events with offshore $H_{1/3}$ of 4 to 5 m, the nearshore $H_{1/3}$ at the crest of the inner nearshore bar ($h \sim 1.5$ m) is reduced to about 50% of the offshore value due to refraction, bottom friction and wave breaking. The wave height distribution across the

nearshore profile could rather well be described with a Rayleigh distribution at each location. According to this distribution, the significant wave height is related to the root-mean-square wave height by $H_{1/3}/H_{rms} = 1.41$. At all measurement locations, the $H_{1/3}/H_{rms}$ ratio varied between 1.45 and 1.30. The mean value of $H_{1/3}/H_{rms}$ was about 1.40 for calm conditions with $H_{1/3}/h < 0.3$ and about 1.35 for storm conditions with $H_{1/3}/h \geq 0.4$ (breaking waves). Thornton and Guza (1983) also observed that the initially Rayleigh wave height distributions offshore were modified by breaking and shoaling into new distributions which were again nearly Rayleigh distributed but with some energy loss.

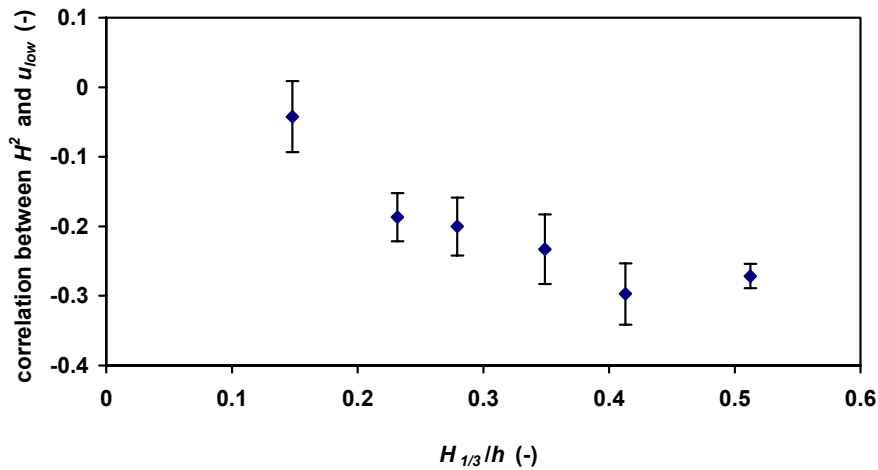


Figure 2.20. Correlation between H^2 and u_{low} as a function of the relative wave height $H_{1/3}/h$. Each data point is the average of 10 or more tests and the error bars denote the standard error.

The relative wave height of the low frequency waves $H_{1/3,low}/h$ was 0.10-0.15 for locations E2 and E3 under storm conditions. This ratio was 0.10-0.35 for locations E4-E6. The largest low-frequency waves ($H_{1/3,low}/h = 0.35$) occurred during low tide. Cross-shore low-frequency velocity oscillations were negatively correlated to the short wave energy as shown in Figure 2.20, which is an indication of the presence of bound long waves, though the correlations are relatively small. The tendency shown in Figure 2.20 was also observed by Ruessink (1998b) based on measurements near the coast of Terschelling, The Netherlands.

The breaking process in an irregular wave field can be expressed through the fraction of breaking waves (Battjes and Janssen, 1978). This was determined during the EU-COAST3D experiments based on observation with the WESP and the CRIS. The fraction of breaking waves increases with relative wave height (Figure 2.21). No waves are breaking for relative wave heights $H_{1/3}/h < 0.25$ and 50% of the waves are breaking at $H_{1/3}/h \sim 0.5$. Van Rijn et al. (2002a) found the maximum or saturated value of $H_{1/3}/h$ at locations E2-E5 to be about 0.8 and at location E6 about 0.4. This latter value is smaller because of its location on the shoreward flank of the inner nearshore bar where the water depth is somewhat deeper and waves are still breaking.

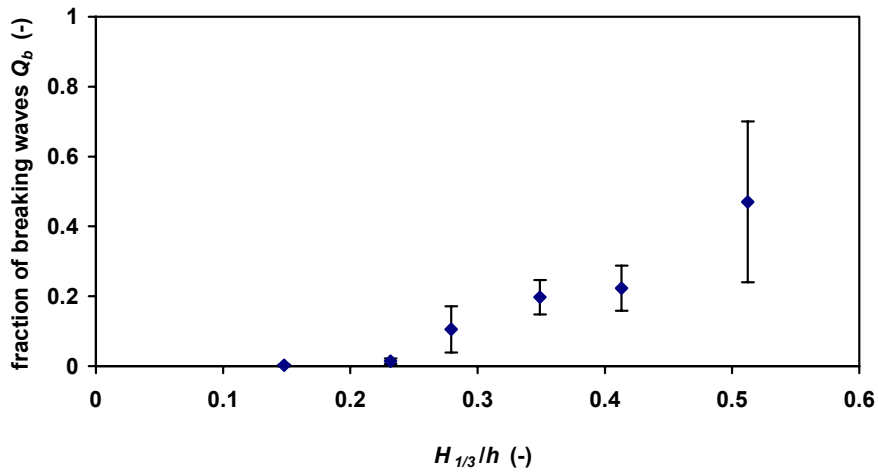


Figure 2.21. Fraction of breaking waves Q_b as a function of the relative wave height $H_{1/3}/h$. Each data point is the average of 10 or more tests and the error bars denote the standard error between the tests.

Van Rijn et al. (2002a) show that the skewness of the peak orbital velocities increases with relative wave height at all measurement locations and reaches its maximum of $u_{1/3,on}/(u_{1/3,on} + u_{1/3,off}) \sim 0.6$ for $H_{1/3}/h \sim 0.35$ at the inner nearshore bar. Maximum skewness on the outer nearshore bar is reached for $H_{1/3}/h \sim 0.7$. Larger breaking waves in shallow water do not produce larger skewness values. Small skewness values between 0.47 and 0.53 are found for the low-frequency waves at all measurements locations.

Table 2.6. Maximum longshore current velocities due to tide, wind and wave driven processes near the coast of Egmond aan Zee, the Netherlands. See Figure 2.19 for locations.

Location	Initial depth (to MSL)	Maximum longshore currents due to tide		Maximum longshore currents due to tide, wind and waves	
		flood	ebb	flood + waves from SW	ebb + waves from NW
	(m)	(m/s)	(m/s)	(m/s)	(m/s)
	18 October				
E2	-3.5	0.50	-0.35	2.0	-1.10
E3	-3.0	0.35	-0.25	1.0	-0.75
E4	-1.7	0.35	-0.25	1.1	-0.90
E5	-1.6	0.30	-0.20	1.2	-1.15
E6	-1.9	0.30	-0.20	1.3	-1.15
E7	-2.5	0.40	-0.35	1.1	-1.10

The maximum tidal currents in the nearshore of Egmond aan Zee vary in the range of 0.3 – 0.5 m/s (Table 2.6). These values occur during calm weather conditions. Storms from the southwest enhance the flood currents to the north, but reduce the ebb currents

to the south. Storms from the northwest show the opposite effect. Generally, the wind and wave-induced longshore currents on the inner nearshore bar are between 0.5 and 0.8 m/s for offshore wave heights up to 3 m (from southwest) and up to 1.3 m/s for offshore waves larger than 3 m. The wind and wave-induced longshore currents on the outer nearshore bar are between 0.6 and 1.2 m/s for offshore wave heights up to 3 m (from southwest) and up to 2.0 m/s for offshore waves larger than 3 m. Storms from the northwest show the opposite behavior. Roughly, it can be said that the peak tidal flood (ebb) currents are increased by a factor 3 to 4 due to wind and wave-driven processes during major storm events from southwest (northwest) direction. Longshore velocities generally are maximum near the bar crests.

The velocity data also show regular oscillations in the longshore current velocity, with a period of ~200-400 s. These shear instabilities in the wave driven longshore current are commonly referred to as shear waves. They are advected with the longshore current with a phase speed of one third to half the maximum longshore current velocity. The standard deviation of the velocity oscillations is of the order of about 0.3 m/s near the inner bar during storm conditions, which is about 25% of the mean longshore current velocity of about 1.2 m/s (Ruessink et al., 1999b). Near the beach, this variation is up to 50% of the mean value of 0.8 m/s. The low-frequency velocity oscillations near the beach are not well correlated to the low-frequency water surface elevations (Miles et al., 2002).

Van Rijn et al. (2002a) show that the cross-shore current velocities on the outer nearshore bar are almost zero during calm conditions with offshore significant wave heights ($H_{1/3,0}$) smaller than 1 m. Minor storms with $H_{1/3,0}$ up to 3 m enhance the cross-shore current velocities to maximum values of -0.1 m/s. Major storms with $H_{1/3,0}$ larger than 3 m strongly enhance the cross-shore current velocities to maximum values of -0.4 m/s at the outer bar crest.

Maximum cross-shore current velocities on the inner nearshore bar are -0.2 m/s during calm conditions with $H_{1/3,0}$ smaller than 1 m. Minor storms with $H_{1/3,0}$ up to 3 m strongly enhance the offshore current velocities to maximum values of -0.4 m/s. Major storms with $H_{1/3,0}$ larger than 3 m strongly enhance the offshore current velocities to maximum values of -0.6 m/s. Though offshore-directed velocities prevail, onshore-directed velocities up to 0.1 m/s do also occur during major storm events.

The cross-shore velocities strongly depend on the local wave height, water depth, tide level and the presence of a rip channel. The largest cross-shore current velocities (up to -0.6 m/s offshore-directed) have been observed at location E2 on the seaward flank of the outer nearshore bar during storm conditions with an offshore significant wave height of about 4.5 m. Similar values have been observed at the crest of the inner nearshore bar inside a rip channel during major storm events. Offshore-directed velocities generally prevail, but onshore-directed velocities up to 0.1 m/s do also occur during major storm events. Relatively large rip current velocities were present at low wave conditions at low tide. The rip current velocities at the inner nearshore bar exhibit a pulsating behavior related to low and high tide levels. The offshore-directed current velocities can be as large as -0.6 m/s during fair weather conditions with a local $H_{1/3}$ of 0.5 to 1 m during low tide. These conditions frequently occur during normal summer conditions.

The maximum velocities of about -0.6 to -0.7 m/s observed in the rip channel through the inner nearshore bar near the coast of Egmond aan Zee are comparable to those measured in rip channels near Duck in the USA (Gallagher et al., 1998) and at Palm Beach, Sydney, Australia (Ranasinghe et al., 2000; Brander, 2000).

Grain size of bed material

Samples of the bed material were taken from the WESP with a Van Veen grabber at different locations across the main transect on 7 April and 10 November 1998 (Figure 2.22). Generally the D_{10} of the bed material ranges between 0.15 and 0.20 mm. The D_{50} ranges between 0.20 and 0.25 mm except for locations just shoreward of the inner and outer nearshore bar crest where the D_{50} increases to about 0.4 mm. The D_{90} ranges between 0.22 and 0.35 mm with a maximum of about 0.70-0.80 mm just shoreward of the inner and outer nearshore bar crest. It is noted that the relatively large grain sizes just shoreward of the bars are partly caused by the presence of shell fragments in the samples. These shell fragments were not present in the samples taken at other locations.

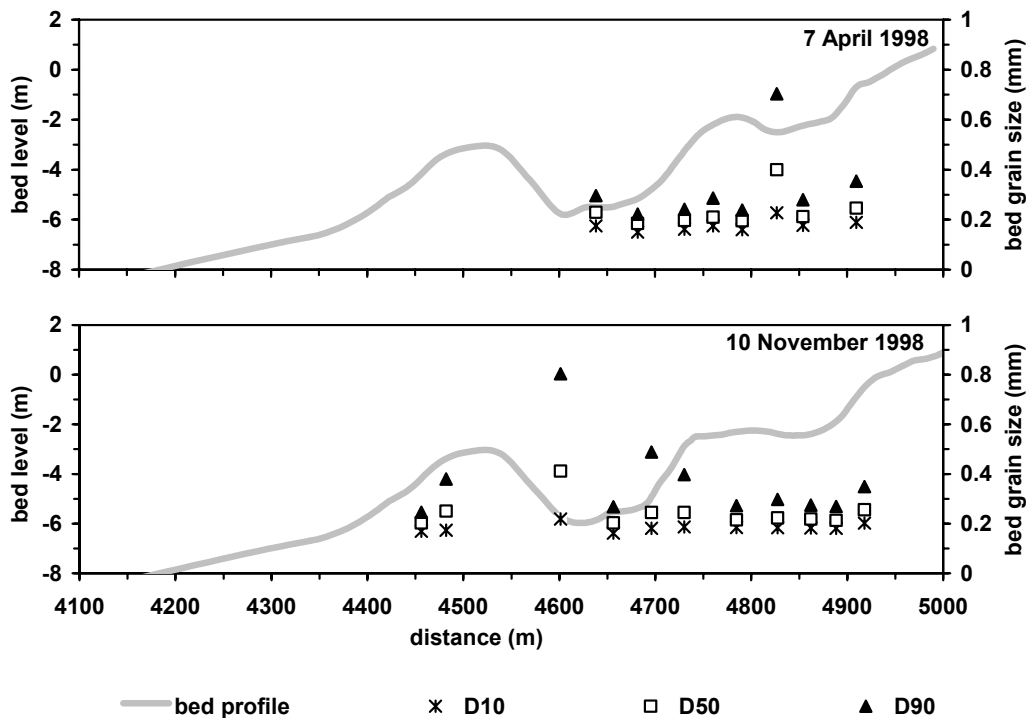


Figure 2.22. Sediment grain sizes of bed material versus cross-shore distance on 7 April and 10 November 1998 at Egmond aan Zee.

Grain size of suspended material

Samples of suspended sediment were taken at about 0.10 m above the seabed with the pump sampler on the CRIS during the EU-COAST3D pilot campaign. Figure 2.23 shows the grain sizes for all tests at different locations across the inner nearshore bar. Note the different y-scales between Figure 2.22 and Figure 2.23. The grain size of the suspended sediment increases moving shoreward, which is likely due to increasing

wave action since the grain size of the bed material does not show this trend. Figure 2.24 shows that there is a slight tendency for the suspended sediment grain size to increase with mobility number, which is a measure for the wave action. On an average, the D_{50} of the suspended sediment is about 85% of that of the bed material.

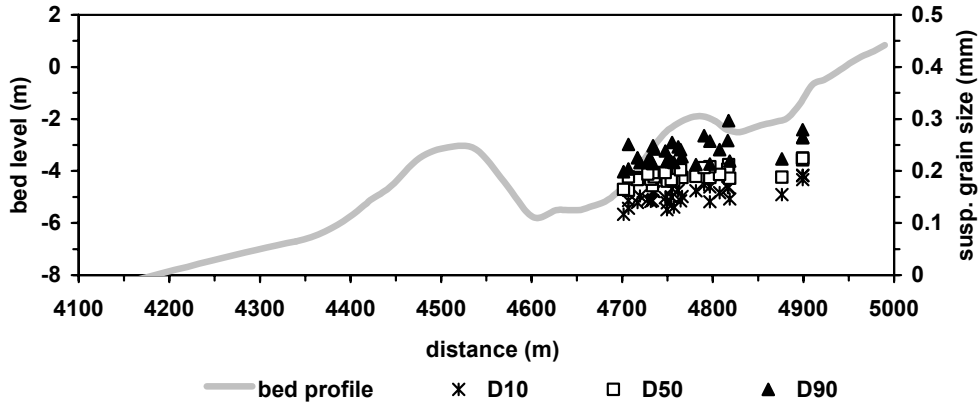


Figure 2.23. Depth relative to mean sea level and sediment grain sizes of suspended material versus cross-shore distance during the EU-COAST3D pilot measurement campaign at Egmond aan Zee. The bed profile measured on 7 April 1998 is shown as a reference.

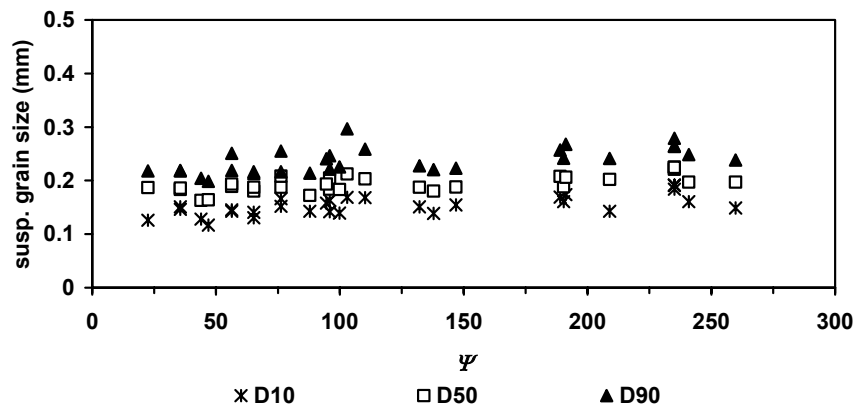


Figure 2.24. Grain size of suspended sediment versus mobility number during the EU-COAST3D pilot campaign at Egmond aan Zee.

Sediment transport rates

Altogether, about 60 CRIS data-bursts have been analyzed. The water depth for these bursts ranges between 1 and 5 m, and the significant wave height between 0.5 and 1.5 m. The relative wave height $H_{1/3}/h$ ranges between 0.06 and 0.5. The largest depth-averaged long- and cross-shore currents measured are 0.5 and 0.3 m/s, respectively. The measured data has been clustered into classes based on hydrodynamic conditions. Each class contains about 10 tests and is represented by the mobility number:

$$\psi = \frac{u_{1/3}^2}{\Delta g D_{50}} \quad (2.1)$$

where Δ is the relative sediment density in water (~ 1.65) [-], g is the acceleration of gravity [m/s^2], $u_{1/3}$ is the peak orbital velocity defined as the mean of $u_{1/3,on}$ and $u_{1/3,off}$ [m/s], and D_{50} is the median grain diameter [m].

This yields six hydrodynamic classes with mobility numbers $\psi = 25, 54, 94, 152, 215$ and 298 , corresponding to orbital velocities $u_{1/3} = 0.30, 0.44, 0.59, 0.75, 0.89$ and 1.05 m/s . For each class, the mean values of all parameters are computed (mean wave height, mean flow velocity, mean transport etc.) and to obtain an indication of the variations around the mean, the standard error is computed also.

$$\sigma = \frac{s}{\sqrt{n}} \quad (2.2)$$

where n is the number of observations and s the standard deviation in the class. Basic data for each class are given in Table 2.7. It should be noted that this procedure has been applied only to reveal the general trend in the data. To take account of non-linearities and interdependencies between parameters, all sediment transport computations have been based on the non-clustered measured hydrodynamic data. The clustering method only serves to simplify the interpretation of the results.

Table 2.7. Class-averaged experimental data from CRIS measurements near the coast of Egmond aan Zee, Netherlands; Ψ = mobility number [m], h = water depth [m], $H_{1/3}$ = significant wave height [m], T_p = wave spectrum peak period [s], θ = angle between waves and current (angles between brackets are based on absolute values) [deg], $u_{1/3, on}$ and $u_{1/3, off}$ = significant peak onshore and offshore orbital velocity near bed [m/s], η and λ = ripple height and length [m], \bar{v} = depth-mean longshore velocity (based on absolute values) [m/s], \bar{u} = depth-mean cross-shore return velocity (negative = offshore directed) [m/s], $q_{s,c, long}$ and $q_{s,c, cross}$ = depth-integrated current-related suspended transport in longshore and cross-shore direction (based on absolute values) [kg/m/s], $q_{s,w, cr, high}$ and $q_{s,w, cr, low}$ = depth-integrated high- and low-frequency wave-related suspended transport in cross-shore direction (negative = offshore directed) [kg/m/s]. The depth-integrated suspended transport rates are defined between 0.02 and 1.0 m above the seabed.

Class	Ψ	h	$H_{1/3}$	T_p	θ	\bar{u}	\bar{v}	$u_{1/3, on}$	$u_{1/3, off}$	η	λ	$q_{s,c, cross}$	$q_{s,c, long}$	$q_{s,w, cr, high}$	$q_{s,w, cr, low}$
1	ave	25	3.14	0.46	6.84	-10 (15)	0.01	0.10	0.32	0.29	0.026	0.328	0.008	0.000	0.000
	stderror	3	0.30	0.06	0.39	4 (3)	0.01	0.02	0.01	0.003	0.073	0.002	0.000	0.000	0.000
2	ave	54	2.71	0.58	6.50	6 (18)	-0.03	0.10	0.50	0.39	0.027	0.571	-0.002	0.000	0.000
	stderror	4	0.27	0.04	0.44	5 (3)	0.01	0.02	0.01	0.004	0.087	0.001	0.003	0.000	0.000
3	ave	94	2.87	0.80	6.17	3 (19)	-0.07	0.17	0.67	0.51	0.033	0.658	-0.006	0.013	0.000
	stderror	5	0.25	0.07	0.37	6 (3)	0.01	0.02	0.01	0.002	0.008	0.136	0.002	0.003	0.001
4	ave	152	2.54	0.86	6.77	-3 (19)	-0.08	0.16	0.89	0.61	0.040	0.917	-0.019	0.037	0.004
	stderror	6	0.17	0.05	0.26	5 (2)	0.02	0.03	0.01	0.002	0.009	0.141	0.005	0.011	0.001
5	ave	215	2.70	1.08	6.62	-8 (19)	-0.15	0.28	1.08	0.70	0.046	1.043	-0.040	0.072	0.017
	stderror	6	0.25	0.08	0.32	5 (2)	0.02	0.04	0.01	0.003	0.022	0.206	0.010	0.015	0.006
6	ave	298	2.13	1.10	7.18	-13 (13)	-0.28	0.28	1.26	0.85	-	-	-0.128	0.148	0.035
	stderror	24	0.27	0.23	1.96	3 (3)	0.01	0.14	0.04	0.06	-	-	0.027	0.050	0.002

2.7. DATA FROM EARLIER EXPERIMENTS

Besides data from experiments described in the previous sections, also data from earlier experiments are used in the present work. Hydrodynamic and morphological data collected during the LIPIID tests in the Delta Flume of Delft Hydraulics (Roelvink and Reniers, 1995) and during the Duck94 field experiment in September and October 1994 (Gallagher et al., 1998) are used in Chapters 3 and 5.

3. MODELLING OF WAVES AND CURRENTS IN THE NEARSHORE

3.1. INTRODUCTION

Morphodynamic coastal profile models aim at predicting cross-shore bathymetric evolution by accounting explicitly for the various hydrodynamic and sediment transport processes involved (Roelvink and Brøker, 1993). With the increase in process knowledge and computing power, profile models have become standard tools in coastal management and are used for hind- and forecasting studies of nearshore bathymetry, often in response to human interference in the nearshore, for instance related to implementation of a shoreface nourishment. The models generally consist of three main modules. In the hydrodynamic module, the cross-shore evolution of wave height, orbital velocities and time-averaged (over many wave periods) cross-shore and longshore currents are predicted. These are then used as input in the sediment transport module. From the cross-shore gradients in the sediment transport rates, morphological changes are computed in the bed-update module, after which the whole procedure is repeated.

Two main approaches in process-based profile modelling can be distinguished. In the first approach, known as parametric, the natural random wave field is assumed to be narrow banded in frequency and direction. Its description is then reduced to a single representative wave height, period and direction. All subsequent computations of hydrodynamics and sediment transport are then based on this single wave approach. Examples of parametric morphodynamic models are Roelvink and Stive (1989), Nairn and Southgate (1993). Roelvink and Brøker (1993) review profile models. In the second, probabilistic approach the computation of hydrodynamics and sand transport is based on a discrete number of wave classes. The method is probabilistic in the sense that each wave class has a certain probability of occurrence. The hydrodynamic and sediment transport computations are performed separately for each wave class. In the bed-update module, the transport rates are then combined using the probability density function of the wave classes to yield bathymetric change. Van Rijn and Wijnberg (1996) argue that the probabilistic approach is better suited for profile modelling because of the strong non-linear dependence of the sediment transport on wave height, which would not be captured correctly with the single-wave parametric approach.

Previous probabilistic modelling studies have mainly focussed on modelling histograms of wave height and associated statistics and on longshore currents (Mase and Iwagaki, 1982; Mizuguchi, 1982; Dally and Dean, 1986; Van Rijn and Wijnberg, 1996). A comparison between measured and computed orbital velocities and undertow has not been made. Furthermore, whether the probabilistic approach indeed outperforms the parametric approach both regarding hydrodynamics and sediment transport is unknown. The probabilistic approach is rather time-consuming because all wave classes (generally 10-12) are propagated shoreward separately and independently. In contrast, the parametric approach transforms only one representative wave shoreward. Therefore, if the same accuracy can be reached, the computationally quicker parametric approach would be better suitable for long-term morphological computations than the computationally intensive probabilistic approach.

A process-based cross-shore profile model is presented in the following chapters, of which this is the first. The aim is to present a modelling concept of the main wave, current, sediment transport and morphodynamic processes in the surf zone. The second objective is to provide a link between measurements at individual points to obtain a full synoptic view of the conditions in the nearshore and get more insight in the processes involved. The present chapter concentrates on the modelling of wave and current processes.

In this chapter the hydrodynamic module of the process-based morphodynamic profile model is presented that can be used in both parametric and probabilistic mode. The described hydrodynamic processes are directly relevant for the modelling of sediment transport rates and include cross-shore wave transformation (shoaling, refraction, dissipation), orbital motion and time-averaged cross-shore and longshore currents. In the probabilistic mode, the present model is an extension of the work by Van Rijn and Wijnberg (1996). The specific question addressed in this chapter is whether and to what extent a probabilistic approach is necessary to accurately predict nearshore hydrodynamics. The wave transformation model used here is based on the work of Van Rijn and Wijnberg (1996). The present model is different in this respect that it can be used in parametric (single wave) as well as in probabilistic (wave-by-wave) mode. Other model improvements were achieved by better representation of physical processes or inclusion of additional processes, decreasing the number of free variables. The wave model drives local models for the longshore and cross-shore velocity distributions, where also wind and tidal influence are included. Combined with models for the near-bed orbital velocity this information is used in the prediction of longshore and cross-shore sediment transport rates.

Herein, first a brief summary of the theoretical background of the hydrodynamic model is given. Formulae for wave heights, cross-shore and longshore currents, as well as wave skewness in the surf zone are given in Section 3.2. The formulae are tested using small-scale and large-scale laboratory data as well as data from two field measurement campaigns. Results are compared using a simple parametric approach with results from the computationally intensive probabilistic approach in Section 3.3. This section concludes that the parametric approach suffices with respect to the description of hydrodynamic phenomena. In Section 3.4, the sensitivity of the parametric model is assessed for the free model parameters, i.e. bed roughness, breaker criterion, horizontal mixing and wave front slope. The effect of changing these free model parameters on the predicted waves and currents is studied using data from field experiments near Egmond aan Zee in the Netherlands. The present model ignores long-wave oscillations in predicting the wave and flow field in the nearshore zone. Therefore, the relative importance of low-frequency waves is discussed in Section 3.5 on the basis of a series of small-scale wave flume experiments to verify whether this assumption is justified. Finally, the results are discussed and conclusions are drawn in Section 3.6.

Part of the work in this chapter has been published in Grasmeyer and Van Rijn (1998), Grasmeyer and Van Rijn (1999) and Van Rijn et al. (2001). The work in Section 3.3 on the comparison of the parametric and probabilistic approach has been submitted to the Coastal Engineering journal.

3.2. MODEL DESCRIPTION

3.2.1. WAVE TRANSFORMATION

The wave model consists of two coupled differential equations describing the time-averaged wave and roller energy balances. With the assumption of longshore uniform bathymetry, the former reads:

$$\frac{\partial}{\partial x} \left(\frac{1}{8} \rho g H^2 c_{g,r} \cos \theta \right) + D_{br} + D_{bf} = 0 \quad (3.1)$$

in which x is the cross-shore direction, positive onshore, H is the wave height, $c_{g,r}$ the relative wave group velocity, θ is the angle of incidence, g is acceleration of gravity, ρ is the water density, D_{br} and D_{bf} are the wave energy dissipation by breaking and bottom friction, respectively.

Breaking-induced dissipation is given by (Van Rijn and Wijnberg, 1996):

$$D_{br} = 0.25 \alpha \rho g \left(\frac{H^2 - H_{max}^2}{T} \right) \text{ if } H > H_{max} \quad (3.2)$$

in which α is a calibration coefficient ($= 1.5$, see Van Rijn and Wijnberg, 1996), T is the relative wave period and H_{max} is the maximum wave height following from $H_{max} = \text{minimum}[\gamma h, 0.14 L \tanh(kh)]$. Waves are assumed to break only if H is larger than H_{max} . γ is a breaker parameter, which, based on earlier calibrations, depends on the ratio of local bottom slope ($\tan \alpha$) and local wave steepness (H/L). The breaker criterion is presented in Figure 3.1. L , h and k are the wavelength, water depth and wave number, respectively. Dissipation by bed friction D_{bf} , modelled according to Van Rijn and Wijnberg (1996), is of subordinate magnitude inside the surfzone where wave breaking dominates the dissipation.

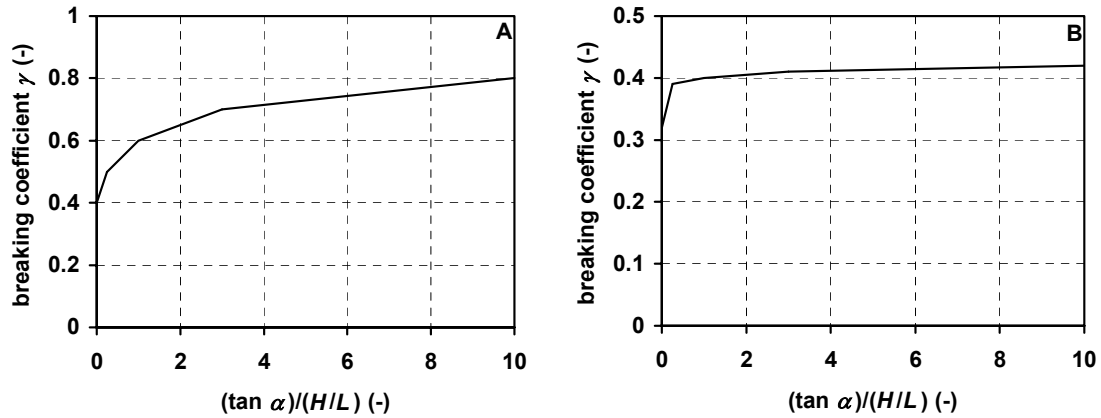


Figure 3.1. Breaking criterion probabilistic mode (A) and parametric mode (B), where $\tan \alpha =$ bed slope.

In probabilistic mode, H is the height H_i of the i -th wave class. The period of each wave class can be given as an input by the user but can also be computed using

$$T_i = \left(\tanh \left(1.7 \frac{H_i}{H_{rms}} + 0.2 \right) \right) T_p \quad (3.3)$$

where H_i and T_i are the wave height and wave period for the i -th wave class, respectively, and T_p is the wave spectrum peak period. Equation (3.3) was derived from measurements in a small-scale wave flume with irregular waves based on a JONSWAP spectrum.

Although the wave direction θ can also be varied for each class, it was kept constant at the energy weighted mean value. The breaker parameter γ takes a value of 0.4 for a horizontal bed and increases with beach slope and with wave period for sloping beds (Figure 3.1A). These breaking coefficients are 10-15% smaller than the values presented by Van Rijn and Wijnberg (1996).

In parametric mode, H in Equation (3.2) is H_{rms} , the wave period is the peak period T_p , and the angle of incidence θ is the energy-weighted mean angle, determined from offshore measurements. The breaker parameter γ takes a value of 0.32 for a horizontal bed and increases to a value of 0.42 for a steep sloping bed (Figure 3.1B). These values are based on calibration using data from the small-scale wave flume tests described in Section 2.3 and the large-scale wave flume data described by Roelvink and Reniers (1995).

At wave breaking, part of the organised wave energy is first converted into forward momentum flux to the roller. This region of aerated water appears as a wave makes the transition from nonbreaking to fully broken state. Svendsen (1984a) accounted for this roller influence in the energy balance by means of a term:

$$E_r = \frac{\rho A c^2}{2L} = \frac{\rho A c}{2T} \quad (3.4)$$

where A is the roller area, L is the wave length, c is the wave phase speed and T the wave period.

The energy balance for rollers is (Stive and De Vriend (1994):

$$\frac{\partial}{\partial x} (2E_r c \cos \theta) = -\tau_r c + D_{br} \quad (3.5)$$

where E_r is the roller energy density, D_{br} is energy dissipation by breaking as computed from Equation (3.2), and τ_r is the shear stress exerted by the moving roller on the wave surface below it. By this shear stress, energy is withdrawn from the roller and converted to turbulent kinetic energy. The term $\tau_r c$ denotes the roller dissipation D_r . The shear stress can be modelled as (Duncan, 1981; Deigaard, 1993):

$$\tau_r = \frac{2gE_r \sin \beta}{c^2} \quad (3.6)$$

The wave front slope β is usually assumed to be 0.1 or less (e.g. Reniers and Battjes, 1997; Ruessink et al., 2001). The time-averaged wave set-up and set-down follows from the time-averaged cross-shore momentum balance, including contributions due to waves, rollers and the cross-shore wind stress. Equations (3.1) and (3.5) can be solved in the onshore direction on a simple forward stepping scheme for given bathymetry and

offshore values of H_{rms} , T_p , θ and tide level. In probabilistic mode the offshore H_{rms} is schematized into a number (10-12) of wave classes with the probability of each class given by the Rayleigh distribution. Linear wave theory is used to compute c_r and c_{gr} , and $\theta(x)$ is determined using Snell's law.

3.2.2. CROSS-SHORE FLOW

Probably the most important mechanism causing profile adaptation during strong wave conditions is the offshore-directed steady current near the seabed, commonly referred to as undertow. Here, the time-averaged and depth-averaged undertow velocity \bar{u} is derived from the mass flux due to the wave motion (Q_w) and the mass flux due to the surface roller (Q_r).

$$\bar{u} = -\frac{Q_w + Q_r}{h_{trough}} \quad (3.7)$$

where $h_{trough} = h - H/2$.

Using linear theory, Q_w is computed as:

$$Q_w = \frac{E}{\rho c} = \frac{1}{8} \left(\frac{g}{c_r} \right) H^2 \cos \theta \quad (3.8)$$

Using Equation (3.4), the roller contribution Q_r is computed as (Svendsen, 1984a):

$$Q_r = \frac{2E_r}{\rho c} \cos \theta \quad (3.9)$$

In probabilistic mode, the mass transport is computed for each wave class individually, after which the undertow velocities are computed weighted over all wave classes. In parametric mode, the mass transport is based on the total wave energy represented by the root-mean-square wave height.

3.2.3. LONGSHORE FLOW

The depth- and time-averaged longshore current velocity \bar{v} is obtained from the 1-D depth-integrated and time-averaged longshore momentum balance between wave, wind and tidal forcing, and bottom stress and lateral mixing

$$\frac{\partial S_{xy}}{\partial x} + \rho g h \frac{\partial h}{\partial y} - \tau_{s,y} = -\rho f_c \bar{v} |\bar{v}| + \rho \varepsilon \frac{\partial}{\partial x} \left(h \frac{\partial \bar{v}}{\partial x} \right) \quad (3.10)$$

in which S_{xy} is the off-diagonal component of the radiation stress tensor (Longuet-Higgins and Stewart, 1964), h is the total water depth, $\tau_{s,y}$ is the longshore wind stress, f_c is the current-related friction coefficient, \bar{v} is the time- and depth-averaged longshore current velocity, ε is a lateral mixing coefficient, x is the cross-shore coordinate, y is the longshore coordinate.

The wave forcing is the cross-shore gradient of S_{xy} . Using linear theory and assuming waves to be narrow banded in direction, S_{xy} is

$$S_{xy} = \frac{1}{8} \rho g H^2 c_{g,r} \cos \theta \sin \theta + 2E_r \cos \theta \sin \theta \quad (3.11)$$

where the terms on the right-hand side are the wave and roller contribution, respectively.

Using (3.1) with $D_{bf} \ll D_{br}$, Equations (3.5) and (3.11) yield (Reniers and Battjes, 1997; Ruessink et al., 2001)

$$\frac{\partial S_{xy}}{\partial x} = -\frac{D_r \sin \theta}{c} \quad (3.12)$$

Inclusion of the surface roller in Equation (3.12) causes a lag in the transfer of momentum to \bar{v} , thereby shifting the location of the maximum \bar{v} in the onshore direction compared to a no-roller model, consistent with laboratory (Reniers and Battjes, 1997) and field observations (Ruessink et al., 2001).

The longshore-surface gradient is estimated from tide driven longshore velocities at the offshore boundary

$$\frac{\partial h}{\partial y} = -\frac{\bar{v}_0^2}{C^2 h} \quad (3.13)$$

in which C is the Chezy coefficient,

$$C = \frac{18 \log(12h)}{k_a} \quad (3.14)$$

with k_a the apparent roughness as given by Van Rijn (1993).

The current-related friction coefficient f_c is given by

$$f_c = \frac{g}{C^2} \quad (3.15)$$

Lateral mixing is included in Equation (3.10) as a diffusion term (Longuet-Higgins, 1970). Important sources for lateral mixing in the surfzone are breaking-induced turbulence (Battjes, 1975), depth variation in the cross-shore and longshore velocities (Putrevu and Svendsen, 1992) and shear waves (Özkan-Haller and Kirby, 1999). However, the cross-shore distribution of ε is not well understood, and for simplicity, a cross-shore constant and time-independent ε is assumed.

3.2.4. ORBITAL VELOCITIES

Skewness of the near-bed cross-shore orbital velocity plays a central part in many cross-shore profile models. Waves in shallow water produce an onshore velocity associated with the wave crest that is stronger and of shorter duration than that due to a wave trough. This onshore velocity is more effective at moving coarser sediment than the offshore velocity. This effect is essential in predicting the shoreward transport of sediment during periods of beach recovery. It may be of equal importance as other

cross-shore mechanisms such as the undertow (e.g. Elfrink et al., 1999; Ruessink et al., 1998).

A variety of wave theories have been devised to deal with the skewness of the wave orbital motion in deep or shallow water, all with their own range of application. In the present model Isobe and Horikawa's (1982) parameterisation of a hybrid wave theory is used, which combines fifth-order Stokes wave theory and third-order cnoidal wave theory. The method by Isobe and Horikawa (1982) was originally formulated in terms of offshore wave conditions, but was later on modified by Grasmeijer and Van Rijn (1998) for local wave conditions. The method starts by computing the sum of the near-bed onshore and offshore peak velocity \hat{u} as

$$\hat{u} = 2 r u_{linear} \quad (3.16)$$

where u_{linear} is the peak near-bed velocity computed using linear wave theory and r is an empirical coefficient. In the present modified formulation the near-bed value of \hat{u} is derived from the local wave conditions following Grasmeijer and Van Rijn (1998). The near-bed onshore peak orbital velocity u_{on} now follows from (Isobe and Horikawa (1982):

$$\left(\frac{u_{on}}{\hat{u}}\right) = 0.5 + \left(\left(\frac{u_{on}}{\hat{u}}\right)_{\max} - 0.5\right) \tanh\left(\frac{\left(\frac{u_{on}}{\hat{u}}\right)_a - 0.5}{\left(\frac{u_{on}}{\hat{u}}\right)_{\max} - 0.5}\right) \quad (3.17)$$

where the maximum skewness is given by

$$\left(\frac{u_{on}}{\hat{u}}\right)_{\max} = 0.62 + \frac{0.003}{\text{bed slope}} \quad (3.18)$$

and $\left(\frac{u_{on}}{\hat{u}}\right)_a$ by

$$\left(\frac{u_{on}}{\hat{u}}\right)_a = \lambda_1 + \lambda_2 \left(\frac{\hat{u}}{\sqrt{gh}}\right) + \lambda_3 \exp\left(-\lambda_4 \left(\frac{\hat{u}}{\sqrt{gh}}\right)\right) \quad (3.19)$$

with

$$\lambda_1 = 0.5 - \lambda_3 \quad (3.20)$$

$$\lambda_2 = \lambda_3 \lambda_4 + \lambda_5 \quad (3.21)$$

$$\lambda_3 = \frac{(0.5 - \lambda_5)}{\lambda_4 - 1 + \exp(-\lambda_4)} \quad (3.22)$$

$$\lambda_4 = \begin{cases} -15 + 1.35 \left(T \sqrt{\frac{g}{h}}\right), & T \sqrt{\frac{g}{h}} \leq 15 \\ -2.7 + 0.53 \left(T \sqrt{\frac{g}{h}}\right), & T \sqrt{\frac{g}{h}} > 15 \end{cases} \quad (3.23)$$

$$\lambda_s = \begin{cases} 0.0032 \left(T \sqrt{\frac{g}{h}} \right)^2 + 0.000080 \left(T \sqrt{\frac{g}{h}} \right)^3, & T \sqrt{\frac{g}{h}} \leq 20 \\ 0.0056 \left(T \sqrt{\frac{g}{h}} \right)^2 - 0.000040 \left(T \sqrt{\frac{g}{h}} \right)^3, & T \sqrt{\frac{g}{h}} > 20 \end{cases} \quad (3.24)$$

It is noted that Equation (3.24) contains a typing error in the paper of Isobe and Horikawa (1982). This equation is continuous for $T(gh)^{1/2} = 20$ and not 30 (see Equation 19 in Isobe and Horikawa (1982)).

The laboratory and field data used in this study showed that the influence of bed slope on the maximum skewness is small. Instead, the maximum skewness was found to depend on h/L as (Figure 3.2):

$$\left(\frac{u_{on}}{\hat{u}} \right)_{\max} = -2.5 \frac{h}{L} + 0.85 \quad (3.25)$$

with:

$$0.62 \leq \left(\frac{u_{on}}{\hat{u}} \right)_{\max} \leq 0.75 \quad (3.26)$$

Note that Equations (3.25) and (3.26) do not compute the skewness but are used to limit the skewness values computed with Equation (3.17). The offshore peak orbital velocity is determined by $u_{off} = \hat{u} - u_{on}$.

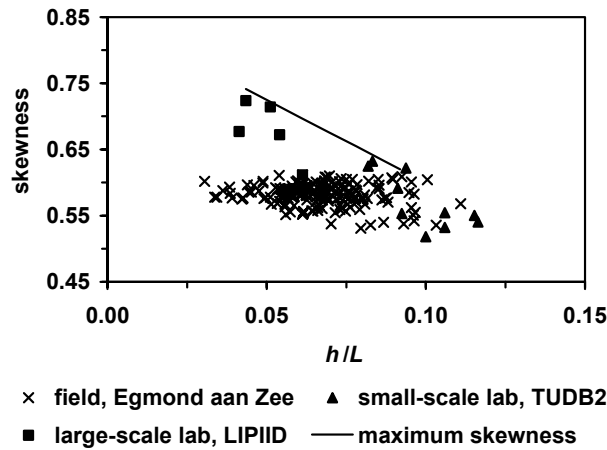


Figure 3.2. Orbital velocity skewness u_{on}/\hat{u} as a function of h/L , based on small-scale wave flume data (TUDB2), large-scale wave flume data (LIPIID) and field data (Egmond aan Zee).

The present model includes a sinusoidal distribution of the instantaneous velocities during the forward and backward phase of the wave cycle. The duration period of each phase is corrected to obtain zero net flow over the full cycle. This sinusoidal shape is different from the original approach of Isobe and Horikawa who accounted also for the asymmetry (pitching forward) of a wave.

In the probabilistic approach the peak orbital velocities are computed for each wave class separately, after which the significant on- and offshore values are determined statistically. In parametric mode the significant on- and offshore orbital velocities are computed directly based on the significant wave height (assuming $H_{1/3} = \sqrt{2} H_{rms}$) and peak period.

3.2.5. INPUT PARAMETERS; FIXED AND FREE PARAMETERS

The model input consists of so-called fixed and free model parameters. The fixed model parameters include the physical boundary conditions i.e. offshore wave height, offshore tidal current, tide level, storm-induced water level set-up, and grain size of bed material. Most of these parameters are often directly measured during field campaigns and these measurements can be used as an input in the model. For example, for the incident wave conditions often the conditions measured by a directional wave buoy are used. Averaged tidal gauge data from tidal stations are used as an input for the tidal water level variations and wind input often consists of wind data obtained from a meteorological station. For the model runs in this thesis always the measured values are used for the boundary conditions described above.

However, tide driven longshore velocities at the offshore boundary are often not measured. In that case, the tidal velocity input for the cross-shore profile models has to be obtained from larger tide models or, if velocities measured in the outer nearshore zone are available, these can be low-pass filtered and used as an input. The filtering has to be done to eliminate wave driven longshore currents from the measured signal. This latter procedure was adopted for the storm scale model runs in this thesis. For the seasonal scale morphological runs in Chapter 5, the offshore tidal current was simply related to measured water level variations.

The sensitivity of the model for different longshore current boundary conditions was tested by taking 50% and 200% of the original tidal velocity as an input, respectively. This affected the longshore currents at the seaward flank of the outer nearshore bars, but hardly had an effect on the velocities in the inner nearshore region. The effect on the morphological runs was found negligible. It has to be considered though, that longshore current model performance as discussed in Section 3.4.3, is influenced by uncertainties of the longshore current boundary condition for locations in the outer nearshore region. On the other hand, there is no need for a detailed description of the longshore tidal currents if the cross-shore profile development is the main interest, as is the case in Chapter 5 of this thesis. In contrast, if an accurate description of the longshore transports is required the tidal schematization is important.

Free model parameters include the breaker criterion γ , the horizontal mixing ε , the wave-related roughness height $k_{s,w}$, the current-related roughness height $k_{s,c}$, and the wave front slope β . These parameters are uncertain to a large extent and are used to calibrate the model for a specific site. Herein, the free model parameters are varied between physically realistic limits to reflect uncertainties in the model and evaluate the influence on the model results. The range of predictions based on these different settings also provides insight in the overall strength and limitations of the model independent of the values of the free model parameters. From a comparison of the different model runs

it should become clear whether the model behavior is caused by a change of the free model parameters or whether it is related to the representation (parameterization) of the physical processes. A sensitivity analysis for the free model parameters is done in Section 3.4.

3.3. PARAMETRIC VERSUS PROBABILISTIC APPROACH

3.3.1. INTRODUCTION

The previous sections presented formulae for wave heights, cross-shore currents and longshore currents, as well as wave skewness in the nearshore zone. These formulae can be applied using a parametric as well as a probabilistic approach. Van Rijn and Wijnberg (1996) argue that the probabilistic approach is better suited for profile modelling because of the strong non-linear dependence of the sediment transport on wave height, which would not be captured correctly with the single-wave parametric approach. Whether the probabilistic approach indeed outperforms the parametric approach both regarding hydrodynamics and sediment transport is however unknown.

In this section, the model is tested using small-scale and large-scale laboratory data as well as data from two field experiments. Results are compared using the simple parametric approach with results from the computationally intensive probabilistic approach.

Table 3.1 Overview of available data sets

Type	Source	Parameters
Small-scale lab.	Grasmeijer and Van Rijn (1999)	$H, \bar{u}, u_{on}, u_{off}$ and pdf of H
Large-scale lab.	Roelvink and Reniers (1995)	$H, \bar{u}, u_{on}, u_{off}$
Field, Egmond	Ruessink et al. (2001)	H, \bar{u}, \bar{v} and pdf of H
Field, Duck	Gallagher et al. (1998)	H, \bar{u}, \bar{v}

An overview of the applied data sets, including a list of parameters available from the data, is provided in Table 3.1. In all data sets, the parameters were collected at several cross-shore locations across one or two nearshore bars.

The following questions are addressed:

- 1) Is it possible to give an accurate description of the hydrodynamic processes in the nearshore including a correct representation of the wave height distribution using a wave-by-wave model?
- 2) Is it necessary to use a wave-by-wave approach to compute the wave heights, undertow velocities and longshore currents across a nearshore profile, or in other words;
- 3) Can the hydrodynamic processes be described accurately using a single representative wave height for the total wave energy?

The (range of) input parameters for all model runs are given in Table 3.2. The effect of changing the free model parameters on the results from the parametric model is discussed in more detail in Section 3.4.

Table 3.2. Input parameters for all model runs. $H_{rms,o}$ = offshore wave height, T_p = wave period, h_0 = offshore water depth, θ = wave direction relative to shore normal, D_{50} = median grain size of sediment, \bar{v}_0 = tidal current, n = number of wave classes for probabilistic mode, $k_{s,w}$ = wave-related roughness height, $k_{s,c}$ = current-related roughness height, γ = breaker criterion (see Figure 3.1), ε = horizontal mixing, β = wave front slope (parametric mode/probabilistic mode).

Type	fixed model parameters					free model parameters						
	$H_{rms,0}$ (m)	T_p (s)	h_0 (m)	θ (deg)	D_{50} (mm)	\bar{v}_0 (m/s)	n (-)	$k_{s,w}$ (m)	$k_{s,c}$ (m)	γ (-)	ε (m ² /s)	β (-)
Small-sc. lab.	0.13	2.5	0.6	0	0.10	0	12	0.01	0.01	func.	n.a.	0.06/0.1
Large-sc. lab.	0.97	5.0	4.1	0	0.22	0	12	0.02	0.03	func.	n.a.	0.06/0.1
Field, Egmond	1.2-3.3	5.9-10.0	15.0	-29-42	0.24	-0.3-0.7	12	0.02	0.03	func.	2.0	0.06/0.1
Field, Duck	0.4-2.0	3.4-16.0	7.7	-22-5	0.15	< 0.05	12	0.02	0.03	func.	2.0	0.06/0.1

3.3.2. COMPARISON WITH SMALL-SCALE LABORATORY DATA

Two tests with irregular waves were carried out in a small-scale wave flume of Delft University of Technology, Netherlands. The waves were propagated over a shallow sand bar followed by a deep trough (Figure 3.3). The bed consisted of fine sand with a median diameter of 0.1 mm. Small-scale ripples with a height of 0.01 m and a length of 0.07 m were present at all locations.

The predictions based on the probabilistic mode show good agreement with the measurements at locations shoreward and seaward of the bar crest (Figure 3.3). Discrepancies are less than 5% in these regions. However, the shoaling near the bar crest is under-predicted, causing wave heights to be underestimated with about 10%. Agreement between measured and computed H_{rms} is slightly better for the parametric mode.

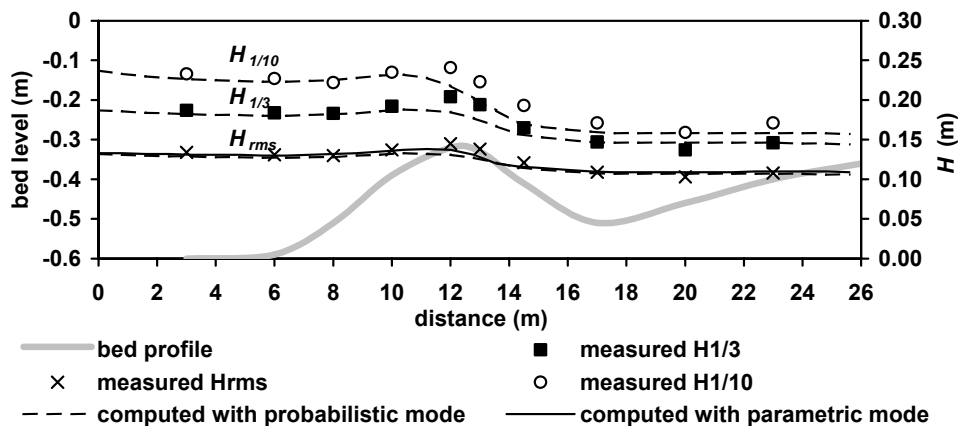


Figure 3.3. Measured and computed wave heights, TUD B2.

To investigate the degree to which the probabilistic mode is capable of reproducing the wave height distribution correctly, measured and predicted wave height distributions were compared (Figure 3.4).

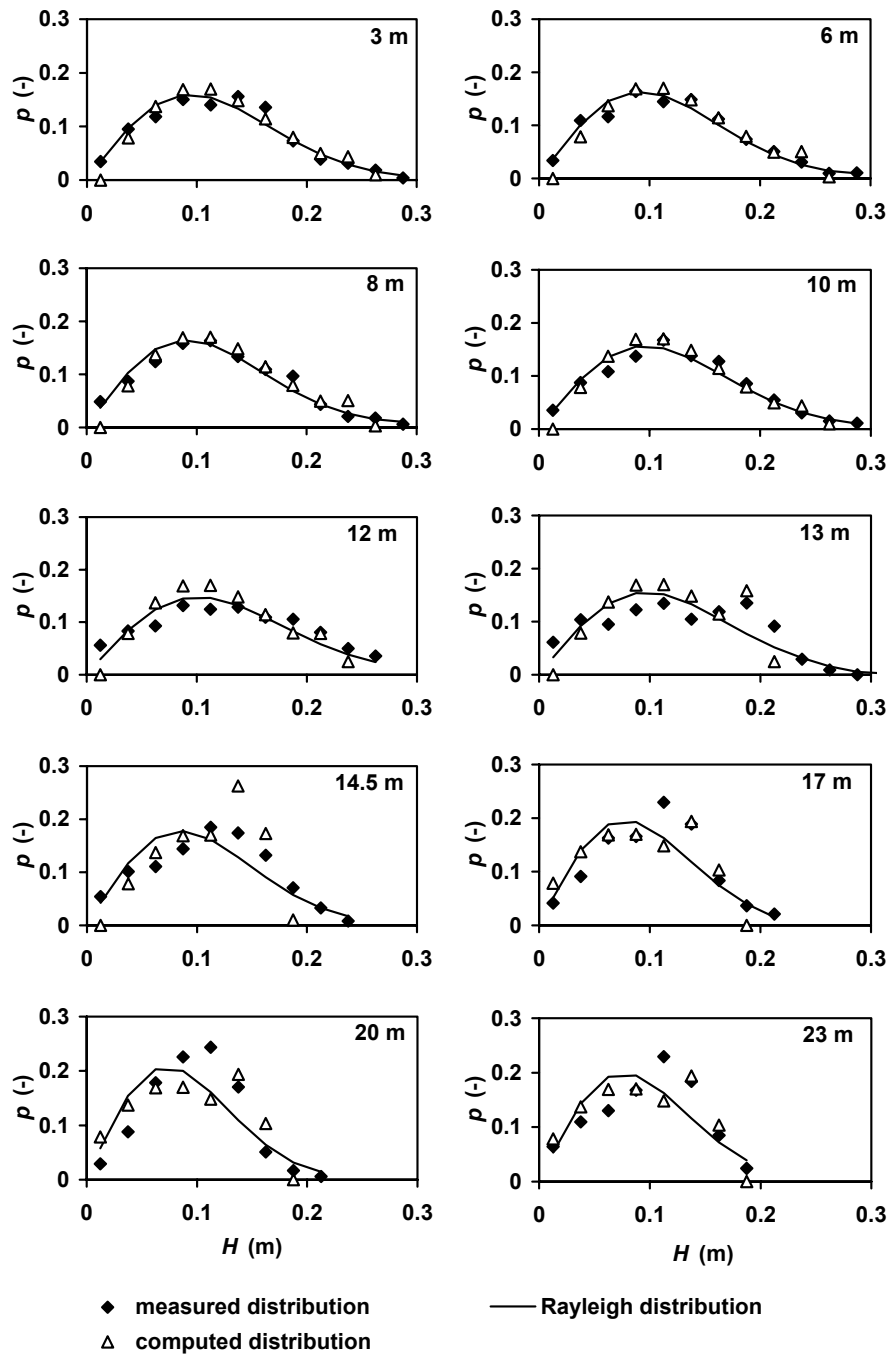


Figure 3.4. Wave height distributions at all measurement locations for small-scale laboratory TUB2 tests. For locations see Figure 3.3.

Both the measured and predicted wave height distribution become narrower in the onshore direction, caused by the breaking of the largest waves. However, the shapes of the measured and predicted distributions differ at locations just shoreward of the bar

crest ($x > 12$ m). The upper tail of the measured distribution extends to values greater than predicted. For example, at location $x = 13$ m, the largest wave height in the predicted distribution is 0.21 m while the maximum measured wave height is 0.29 m. Moreover, at locations shoreward of the bar crest (breaking waves), the predicted wave height distribution is too peaked with large probability density values in the upper tail of the distribution. This effect is most pronounced at location $x = 14.5$ m, where the fraction of breaking waves was observed to be largest. It is interesting to see that the Rayleigh distribution represents the measured wave height distributions reasonably, consistent with findings by Thornton and Guza (1983) under field conditions and by Baldock et al. (1998) for small-scale laboratory tests.

Measured and predicted \bar{u} are compared in Figure 3.5. The predicted location of maximum \bar{u} is near the bar crest, whereas the measured maximum is located more shoreward. The difference between the two modes is small, although maximum \bar{u} is located somewhat more shoreward for the parametric mode. The effect of the roller was tested by running the model with the same $k_{s,w}$ but without roller (results not shown here). Neglecting the roller causes an immediate transfer of energy from organized wave motion to the undertow, resulting in smaller undertow velocities shoreward of the bar crest. However, the roller influence was found to be relatively small in this test case. A comparison between the two approaches for u_{on} and u_{off} is shown in Figure 3.6. As can be seen the difference between the two methods is again small (less than 10%).

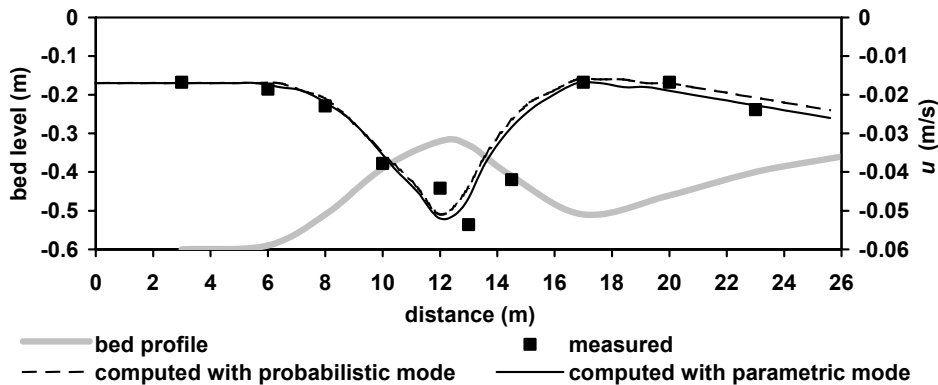


Figure 3.5. Measured and predicted undertow velocities; TUD B2.

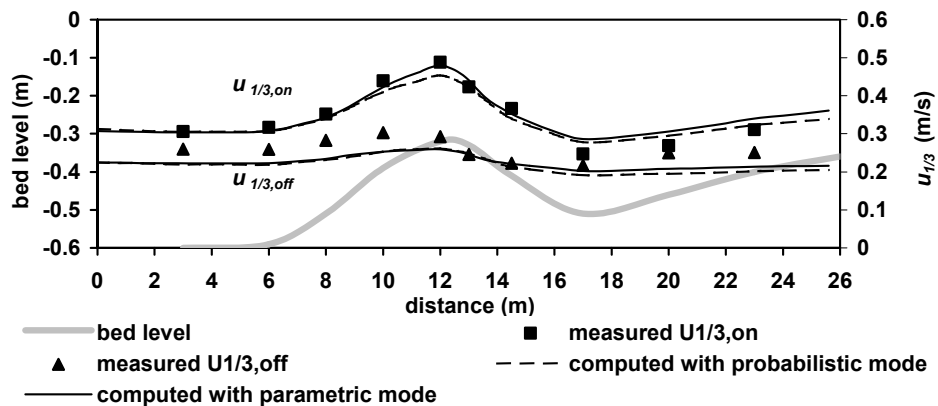


Figure 3.6. Measured and predicted onshore and offshore near bed peak orbital velocities; TUD B2.

3.3.3. COMPARISON WITH LARGE-SCALE LABORATORY DATA

The large-scale laboratory data used here were collected during the LIPII 1B test in the Delta Flume of Delft Hydraulics, described in Roelvink and Reniers (1995). Test 1B represents erosive short-period ($T_p = 5$ s) storm waves with an offshore H_{rms} of 1.0 m. A small bar was present at the start of the experiment (Figure 3.7). Median sediment grain size was 0.22 mm.

Figure 3.7 shows the measured and predicted wave heights along the profile. In parametric mode, H_{rms} values seaward of the bar crest are quite accurately predicted. Further shorewards however, H_{rms} is underestimated by about 20%. In probabilistic mode, the model predicts the significant wave heights quite accurately while the root-mean-square wave height is generally overestimated by about 20%, especially at locations near the bar crest, which is partly caused by the fact that the probabilistic model was calibrated focusing on the significant wave heights (Van Rijn and Wijnberg (1996). The measured ratio $H_{1/3}/H_{rms}$ remains about 1.4 throughout the surf zone whereas the probabilistic mode results in a decrease of this ratio because of breaking of only the highest waves. It is noted that the accuracy of wave heights measured with a pressure sensor as used in these experiments is about 10% (see Table 2.1 in Section 2.2).

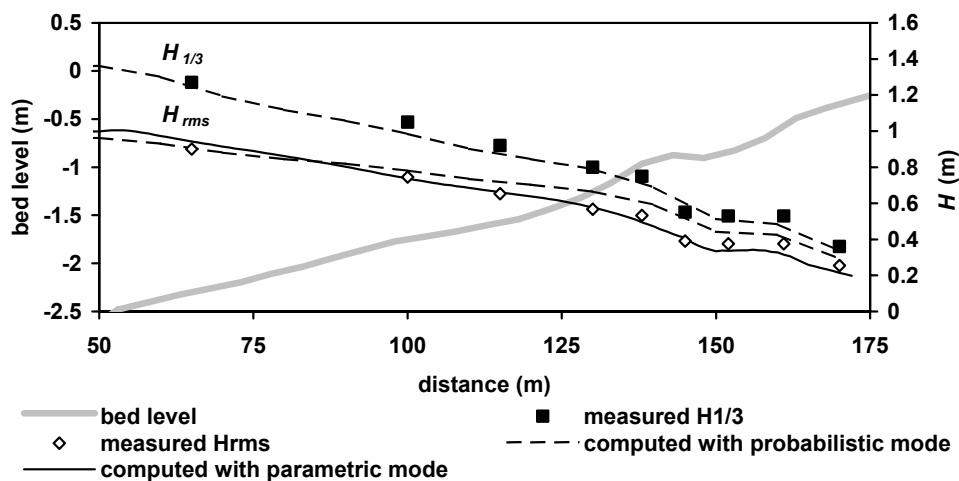


Figure 3.7. Measured (symbols) and predicted (lines) wave heights using model in parametric and probabilistic mode; Delta Flume LIPII, test 1B.

Cross-shore mean currents near the bar crest are modelled fairly well (Figure 3.8). The model slightly overestimates cross-shore mean currents seaward of the bar. The parametric mode produces slightly larger cross-shore currents at locations seaward of the bar and slightly smaller values near the bar crest than the probabilistic mode but the difference between the two modes is generally less than 10%. It is noted here that the accuracy of velocities measured with an EMF as used in these tests is about 10% or 0.05 m/s (see Table 2.1 in Section 2.2).

The model also reproduces the peak near bed orbital velocities $u_{1/3,on}$ and $u_{1/3,off}$ fairly well (Figure 3.9). The difference between measured and computed values near the bar and further seaward is generally less than 10%. Offshore orbital velocities are

underestimated by about 20% at locations shoreward of the bar. The parametric mode produces slightly larger orbital velocities at locations seaward of the bar than the probabilistic mode but the difference between the two modes is generally less than 10%.

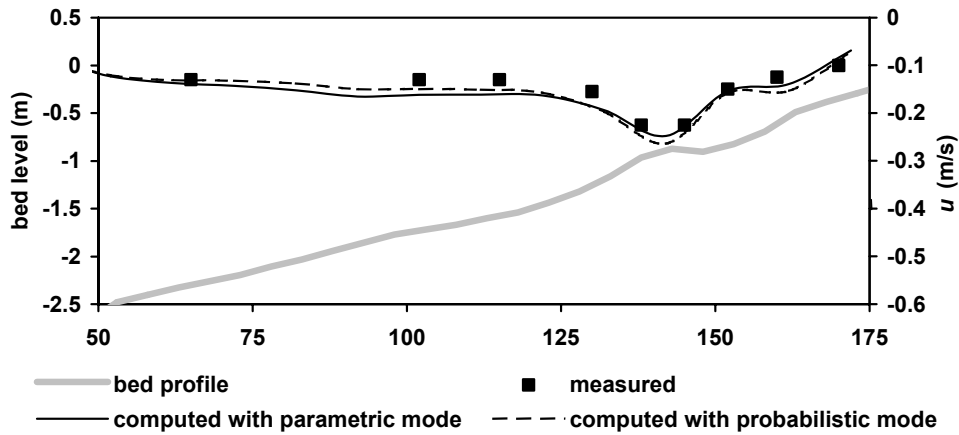


Figure 3.8. Measured and predicted undertow velocities using the model in parametric mode and probabilistic mode; Delta Flume LIPII, Test 1B.

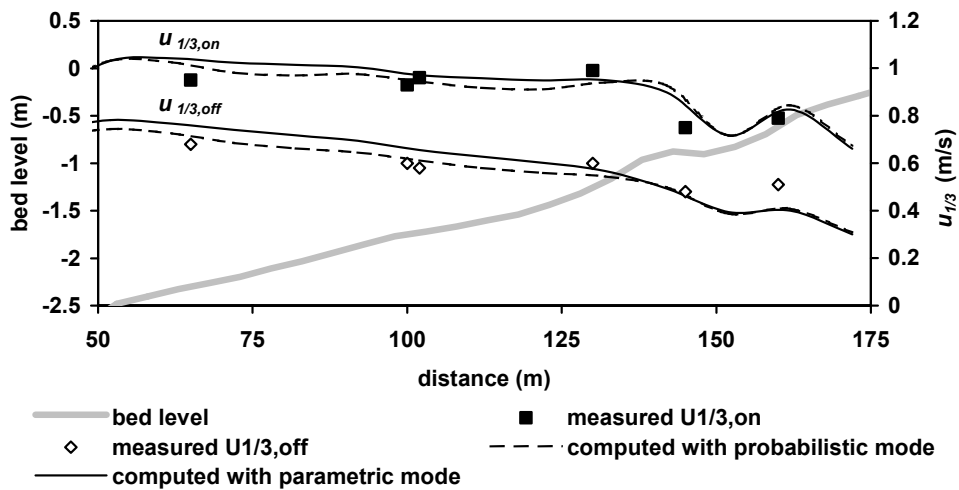


Figure 3.9. Measured and predicted near bed peak orbital velocities using the model in parametric mode and probabilistic mode; Delta Flume LIPII, Test 1B.

3.3.4. COMPARISON WITH FIELD DATA, DUCK, NC, USA

The data from the field site near Duck, NC, USA, were obtained during the Duck94 field experiment in September and October 1994. The Duck field site is situated on the east Atlantic coast of the USA. The tidal range is about 1 m and the tidal currents are weak (0.1 to 0.3 m/s). The winter period is dominated by storm waves and the summer period is dominated by long-period swell. The bed profile generally shows a single bar in the surf zone (Figure 3.10) and sometimes a low outer bar is present. Pressure and velocity observations were obtained at 13 cross-shore positions of which 6 were

selected for the present comparison (Figure 3.10) extending from the shoreline across a sandbar to 4.5-m depth. Gallagher et al. (1998) give a description of the experimental set-up and of the nearshore bar behaviour during the Duck94 measurement campaign. The mean grain size along the transect varied between 0.15-0.29 mm. Bathymetric surveys were obtained with an amphibious vehicle. Longshore non-uniformities in the bar were small in September and the first half of October 1994. A broad cross-shore channel (rip channel) developed between 10 and 20 October 1994.

Herein the model computations are compared with measurements based on a time series of 48 hours between 21 and 23 September 1994 at six representative positions (Figure 3.10). In 8-m depth, 750 m from shore, H_{rms} ranged between 0.5 and 1.9 m, peak periods between 4 and 10 s, θ between $\pm 20^\circ$, and wind speed between 4 and 20 m/s. Longshore current maxima reached values up to 1.2 m/s, and the largest velocities were located near the bar crest (Feddersen et al. (1998)). The location of the maximum was tidally modulated, shifting from near the bar crest at low tide to 30-m farther shoreward at high tide. Undertow currents reached values up to 0.5 m/s, and the largest velocities were located near the bar crest or just shoreward of it (Gallagher et al. (1998)). The tidal range was about 1m and tidal currents were weak (<0.05 m/s).

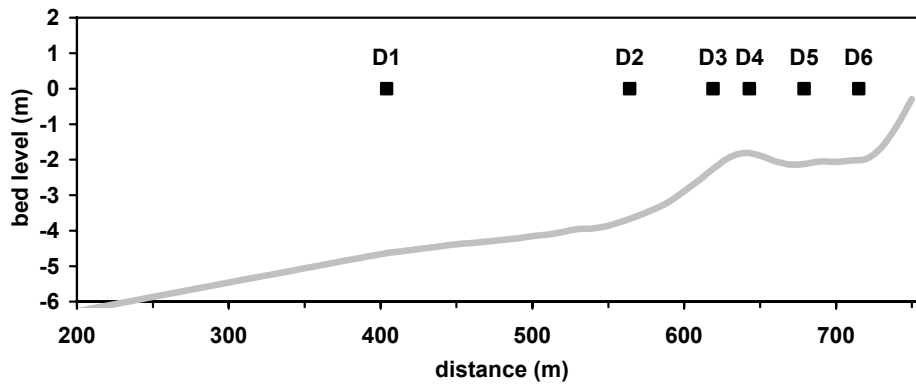


Figure 3.10. Locations of co-located current meters and pressure sensors during the measurement campaign in 1994 near Duck, NC, USA. The bed profile measured on September 21, 1994 is shown as a reference.

The model performance was judged based on a number of complementary error statistics, quantified for each measurement location. The first is the relative mean absolute error ε_{rma} , given by

$$\varepsilon_{rma} = \frac{\overline{|X_{predicted} - X_{measured}|} - X_{error}}{\overline{|X_{measured}|}} \quad (3.27)$$

where X is the parameter of interest, the overbar represents an average and X_{error} is a constant measurement error based on Table 2.1 (see also Van Rijn et al., 2002a), for the wave heights estimated at 0.1 m and for the time-averaged current velocities at 0.05 m/s. The qualifications for ε_{rma} values used in this thesis, based on Van Rijn et al. (2002b), are listed in Table 3.3.

The second is the root mean square error:

$$\varepsilon_{rms} = \sqrt{\left(|X_{predicted} - X_{measured}| - X_{error} \right)^2} \quad (3.28)$$

In Equations (3.27) and (3.28) the value $|X_{predicted} - X_{measured}| - X_{error} < 0$ was set to 0. Additional error statistics were the slope of the best-fit linear line between predicted and measured values ($m < 1$ corresponds to model under-predictions) and the corresponding skill r^2 . Cross-shore constant m values imply that the cross-shore distribution of the parameter in question is predicted correctly.

Table 3.3 Qualification of error ranges of process parameters

Qualification	Wave height	Velocity
	ε_{rma} (-)	ε_{rma} (-)
Excellent	<0.05	<0.1
Good	0.05-0.1	0.1-0.3
Reasonable/fair	0.1-0.2	0.3-0.5
Poor	0.2-0.3	0.5-0.7
Bad	>0.3	>0.7

Figure 3.11 shows measured and computed H_{rms} wave heights at six locations across the nearshore profile. Wave height variations across the profile are small for the relatively calm conditions at the start and end of the selected period, which is represented correctly by both the parametric and the probabilistic mode. During the more energetic stage ($t = 24-36$ h, where t is time), wave height decreases from about 1.8 m at the most offshore measurement location D1 to about 0.8 m shoreward of the nearshore bar at D6.

The parametric mode accurately represents this strong wave decay across the nearshore profile, although the wave heights at D6 are somewhat overestimated. The probabilistic mode overestimates the wave height at locations D3-D6 on the nearshore bar and shoreward of it.

Wave height model statistics are given in Figure 3.14A. The ε_{rma} is 0.02 or smaller for the parametric model, which is excellent, and varies between 0.01 and 0.08 for the probabilistic mode (between excellent and good). Errors for the probabilistic mode were smaller when comparing measured and computed $H_{1/3}$ instead of H_{rms} (not shown), which is partly due to an inaccurate modelling of the wave height distribution.

Comparison of measured and computed wave height distributions (not shown here) revealed that at locations shoreward of the bar crest, the computed wave height distribution is too peaked, with large probability density values in the upper tail of the distribution. This means that the probabilistic mode underestimates breaking of the smaller waves.

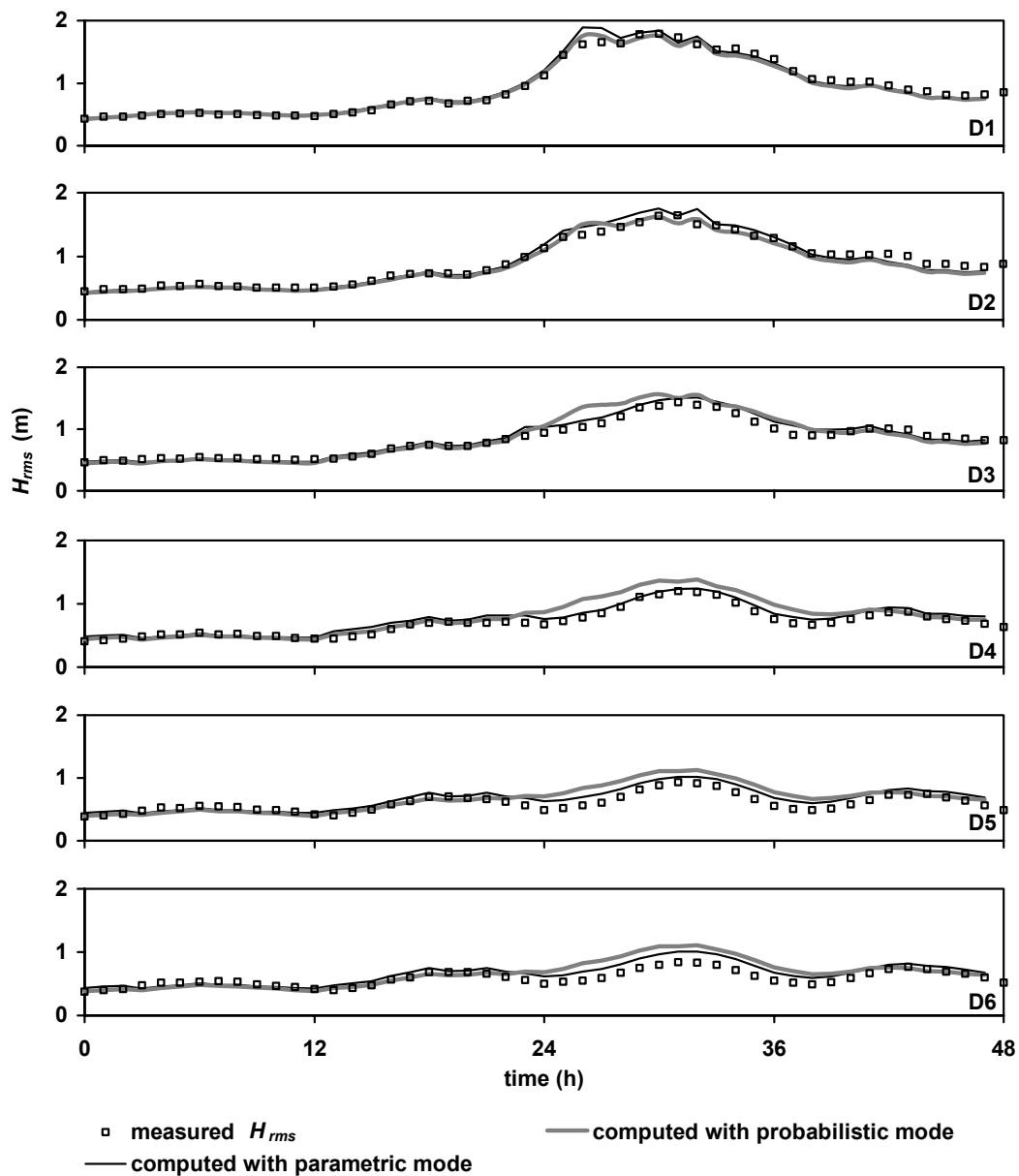


Figure 3.11. Measured and predicted H_{rms} from offshore (top panel) to onshore (bottom panel) versus time; 21-23 September 1994, Duck, NC, USA; for measurement locations see Figure 3.10.

Measured and computed \bar{u} are shown in Figure 3.12. Measured cross-shore velocities are smallest at location D1 with values between 0.06 and -0.18 m/s and largest at D5 just shoreward of the inner nearshore bar with values between -0.08 and -0.55 m/s. The model accurately predicts the relatively small cross-shore velocities at D1 but generally underestimates the values measured at more shoreward locations. Both modes significantly underestimate the measured \bar{u} of up to -0.5 m/s under storm conditions in the trough region at locations D5 and D6 ($x = 679$ and 715 m). It is noted that the measured currents are defined at about 0.5 m above the bed, whereas the computed values represent the depth-averaged currents. This could at least cause some of the

differences. Figure 3.14B gives the \bar{u} model statistics for Duck, showing that errors are small at location D1 but increase when moving shoreward. The difference between the parametric and probabilistic mode is generally less than 10%.

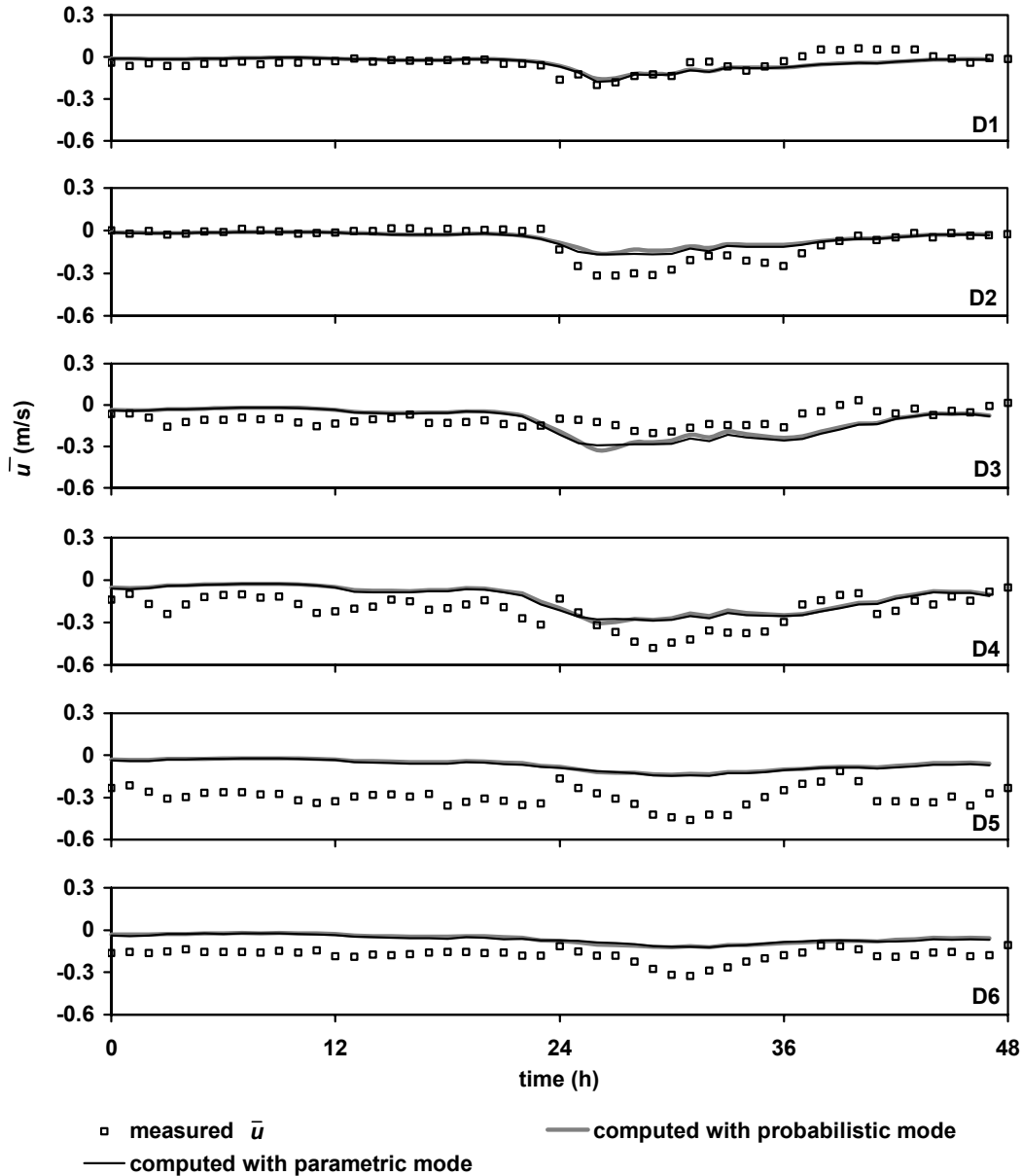


Figure 3.12. Measured and predicted cross-shore mean current \bar{u} from offshore (D1, top panel) to onshore (D6, bottom panel) versus time; 21-23 September 1994, Duck, NC, USA; for measurement locations see Figure 3.10.

Measured and computed \bar{v} are shown in Figure 3.13. The measured longshore mean currents at location D1 range between 0.28 and -0.66 . The wave-driven longshore currents are largest at D4 with a maximum value of -1.16 m/s. Generally, reasonable to good agreement between measured and computed longshore currents is obtained in the nearshore (Figure 3.13). However, the model gives bad \bar{v} predictions (underestimated)

at the most seaward measurement location D1 ($x = 404$ m). The difference between the computations in parametric and probabilistic mode is generally less than 10%. The ε_{rma} varies between about 0.29 and 0.73 for the parametric mode and between 0.25 and 0.74 for the probabilistic mode (Figure 3.14C). The parametric mode produces slightly better results than the probabilistic mode but both modes underestimate the longshore currents at all measurement locations to some extent.

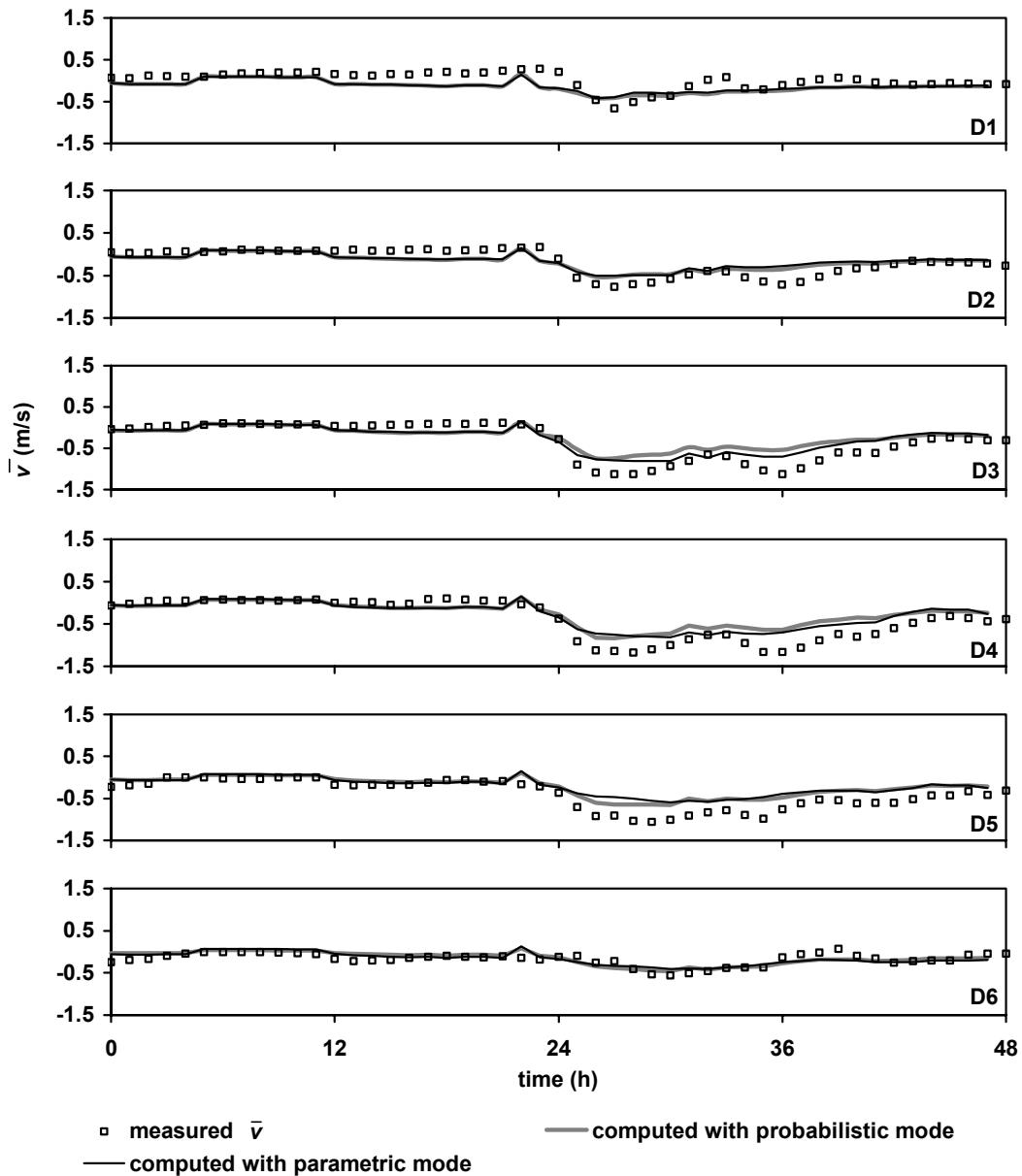


Figure 3.13. Measured and predicted longshore mean current \bar{v} from offshore (D1, top panel) to onshore (D6, bottom panel) versus time; 21-23 September 1994, Duck, NC, USA; for measurement locations see Figure 3.10.

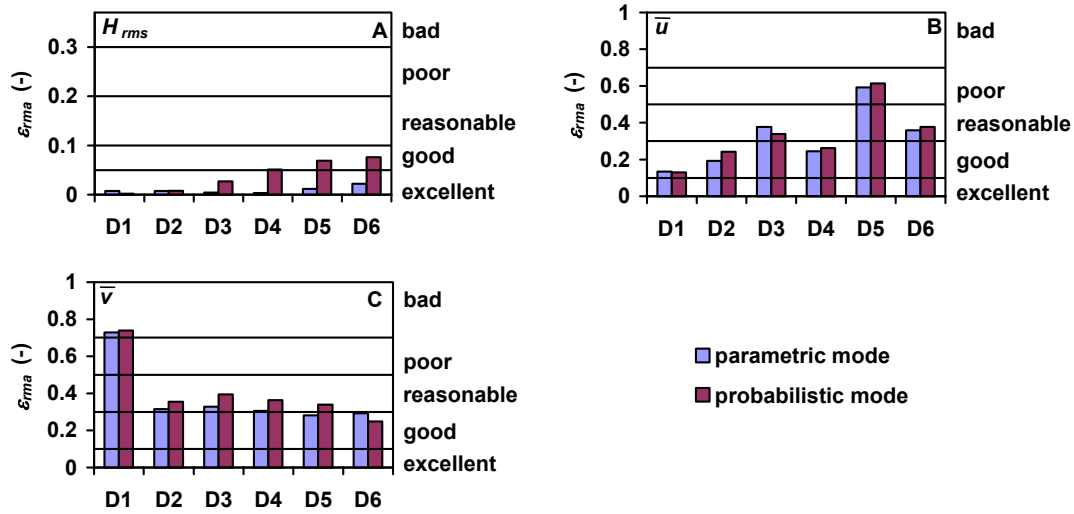


Figure 3.14. Model error statistics for waves (A), cross-shore currents (B) and longshore currents (C); 21-23 September 1994, Duck, NC, USA.

3.3.5. COMPARISON WITH FIELD DATA, EGMOND AAN ZEE, THE NETHERLANDS

The data used here were obtained during a large field campaign in 1998 near the coast of Egmond aan Zee, The Netherlands (Section 2.6). The main transect is shown in Figure 3.15. The stations E1-E7 are assumed to be representative for the processes in the main transect, although not all stations (E1, E7) were located in the main transect. A directional wave buoy, located in 16-m water depth, 5 km offshore, measured offshore wave conditions.

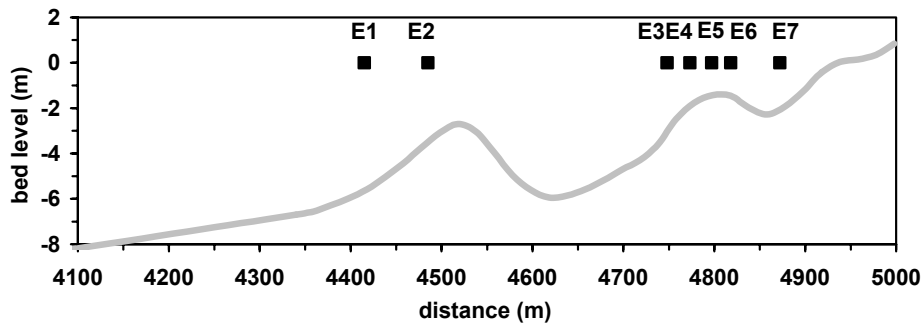


Figure 3.15. Locations of instruments during the measurement campaign in 1998 near Egmond aan Zee, the Netherlands. The bed profile measured on October 26, 1998 is shown as a reference.

Spatially extensive nearshore bathymetric surveys were obtained every few days with an amphibious vehicle. Bathymetric longshore nonuniformities were always detectable, but were most pronounced during the second half of the campaign when a cross-shore rip channel developed close to the measurement transect. Herein the model computations are compared with measurements based on a time series of 48 hours between 26 and 28 October 1998, when longshore nonuniformities were small. In 16-m

depth, H_{rms} ranged between 1.2 and 3.3 m, significant periods between 6.2 and 9.7 s, and θ between -30° and $+40^\circ$, where positive θ indicates waves from the southwest.

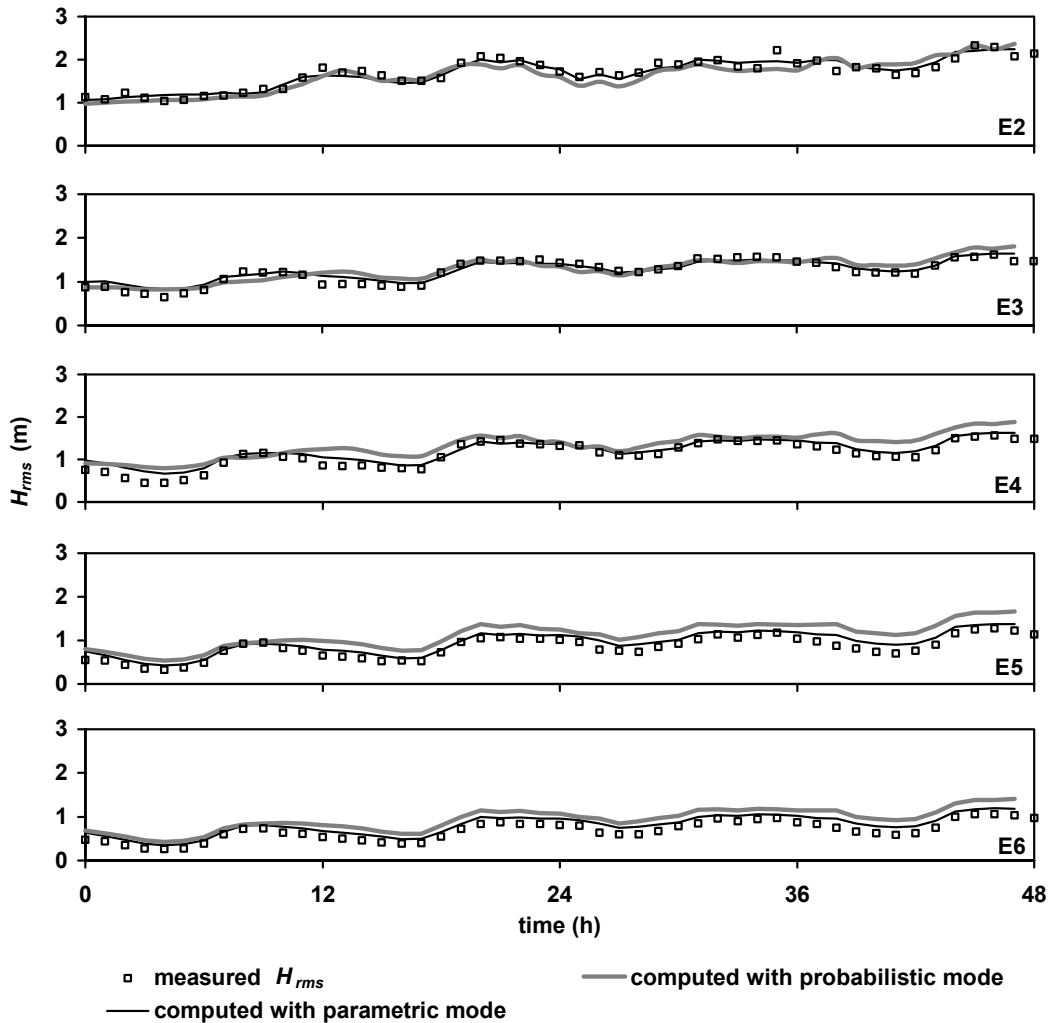


Figure 3.16. Measured (symbols) and modelled (curves) wave height H_{rms} from offshore (E2, top panel) to onshore (E6, bottom panel) versus time; 26-28 October 1998, Egmond aan Zee, the Netherlands.

Figure 3.16 shows measured and computed H_{rms} wave heights for the 48-hour period at different locations across the nearshore of Egmond aan Zee. The offshore H_{rms} (at 5 km offshore) increases from 1.2 to 3.3 m during the selected period. Wave heights at location E2 are smaller and range between about 1.0 to 2.2 m. The wave heights at location E2 are correctly represented by both modes. However, the two modes differ with respect to the wave height decay across the nearshore zone. The parametric mode accurately predicts H_{rms} at all measurement locations, whereas the probabilistic mode overestimates H_{rms} , especially in the inner nearshore at locations E4-E6. Wave model error statistics for Egmond aan Zee are shown in Figure 3.19A. The parametric mode shows excellent agreement with the measurements ($\epsilon_{rma} \leq 0.05$). The probabilistic mode shows good to excellent agreement for locations E2 and E3 seaward of the inner bar ($\epsilon_{rma} \leq 0.05$) but predictions are reasonable to poor for the more shoreward locations

E4-E6 ($\epsilon_{rma} = 0.11-0.23$). Errors for the probabilistic mode were smaller when comparing measured and computed $H_{1/3}$ instead of H_{rms} , which indicates an inaccurate modelling of the wave height distribution.

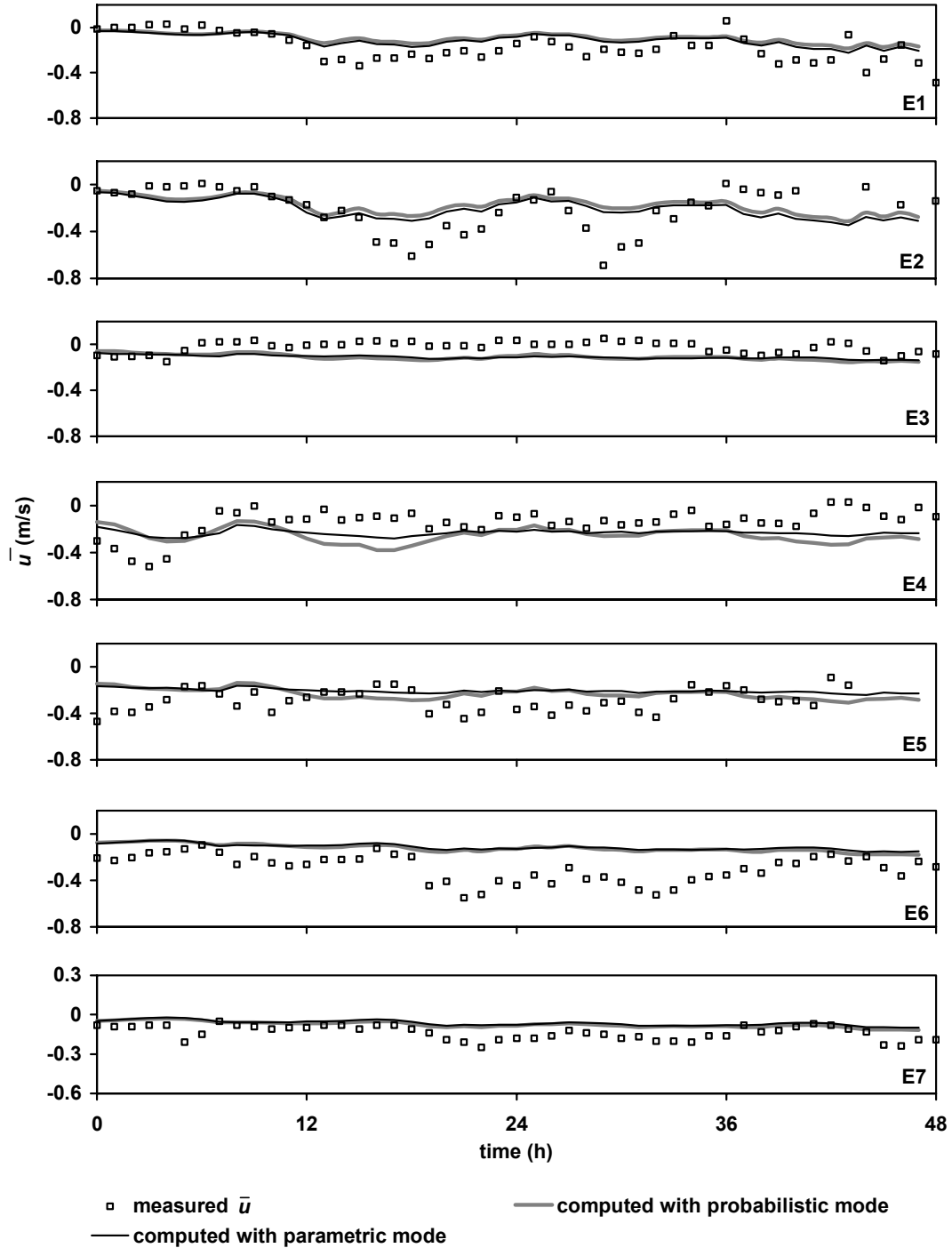


Figure 3.17. Measured (symbols) and modelled (curves) cross-shore current \bar{u} from offshore (E1, top panel) to onshore (E7, bottom panel) versus time; 26-28 October 1998, Egmond aan Zee, the Netherlands.

Measured and computed \bar{u} are shown in Figure 3.17. Measured cross-shore velocities at location E1 on the outer bar range between 0.05 and -0.3 m/s. The measured values at location E2 show two large peaks of -0.6 and -0.7 m/s at $t = 18$ and 29 h that coincide with low tide. Moving further shoreward, cross-shore currents are small at the seaward flank of the inner nearshore bar (E3 and E4) with values that are nearly zero, increase on the bar crest and shoreward flank (E5 and E6) with values from -0.10 to -0.55 m/s, and decrease again in the trough shoreward of the inner bar (E7).

Generally, the model underestimates \bar{u} on the seaward flank of the outer bar (E1, E2), especially the peaks in the cross-shore current at E2. The model overestimates \bar{u} on the seaward flank of the inner bar (E3, E4) and underestimates the values again on the crest and shoreward flank of the inner bar (E5-E7).

The \bar{u} error statistics are shown in Figure 3.19B. Model predictions are reasonable to good for locations E1 and E2 on the outer bar ($\varepsilon_{rma} = 0.25-0.41$) and locations E5-E7 on the crest and shoreward flank of the inner bar ($\varepsilon_{rma} = 0.17-0.45$). Agreement between measured and computed \bar{u} is poor to bad at E3 and E4 on the seaward flank of the inner nearshore bar ($\varepsilon_{rma} = 0.53-1.17$), where the model overestimates the cross-shore currents. Reason for this might be the presence of a local rip channel.

Although disparities between measured and computed cross-shore currents are large, the parametric mode and the probabilistic mode show comparable results. The difference between the two modes is generally less than 10%.

Figure 3.18 shows the measured and computed longshore mean currents \bar{v} . The measured longshore mean current is largest at the most offshore measurement location (E1), ranging between -0.5 and 1.4 m/s during the selected period. Smaller velocities are observed at locations further shoreward. The measured longshore mean current at the most shoreward location (E7) ranges between -0.3 and 1.0 m/s. Generally, reasonable to good agreement between measured and computed \bar{v} is obtained. Figure 3.19C shows the longshore currents model error statistics. Both modes give reasonable predictions for locations E1 and E2 on the outer nearshore bar (ε_{rma} between 0.39 and 0.45) and reasonable to good predictions on the inner nearshore bar (ε_{rma} between 0.18 and 0.33). The model slightly underestimates longshore currents at all locations. Generally, the parametric mode gives slightly better predictions of the longshore mean current than the probabilistic mode.

Error statistics for computed peak orbital velocities are given in Figure 3.19D and E. Both modes show good to excellent agreement between measured and computed orbital velocities. The u_{on} errors increase and u_{off} errors decrease when moving shoreward from E2 to E6. Difference between the two modes is small (less than 10%), both for the onshore and offshore directed orbital velocities, although the probabilistic mode predicts u_{on} slightly better than the parametric mode.

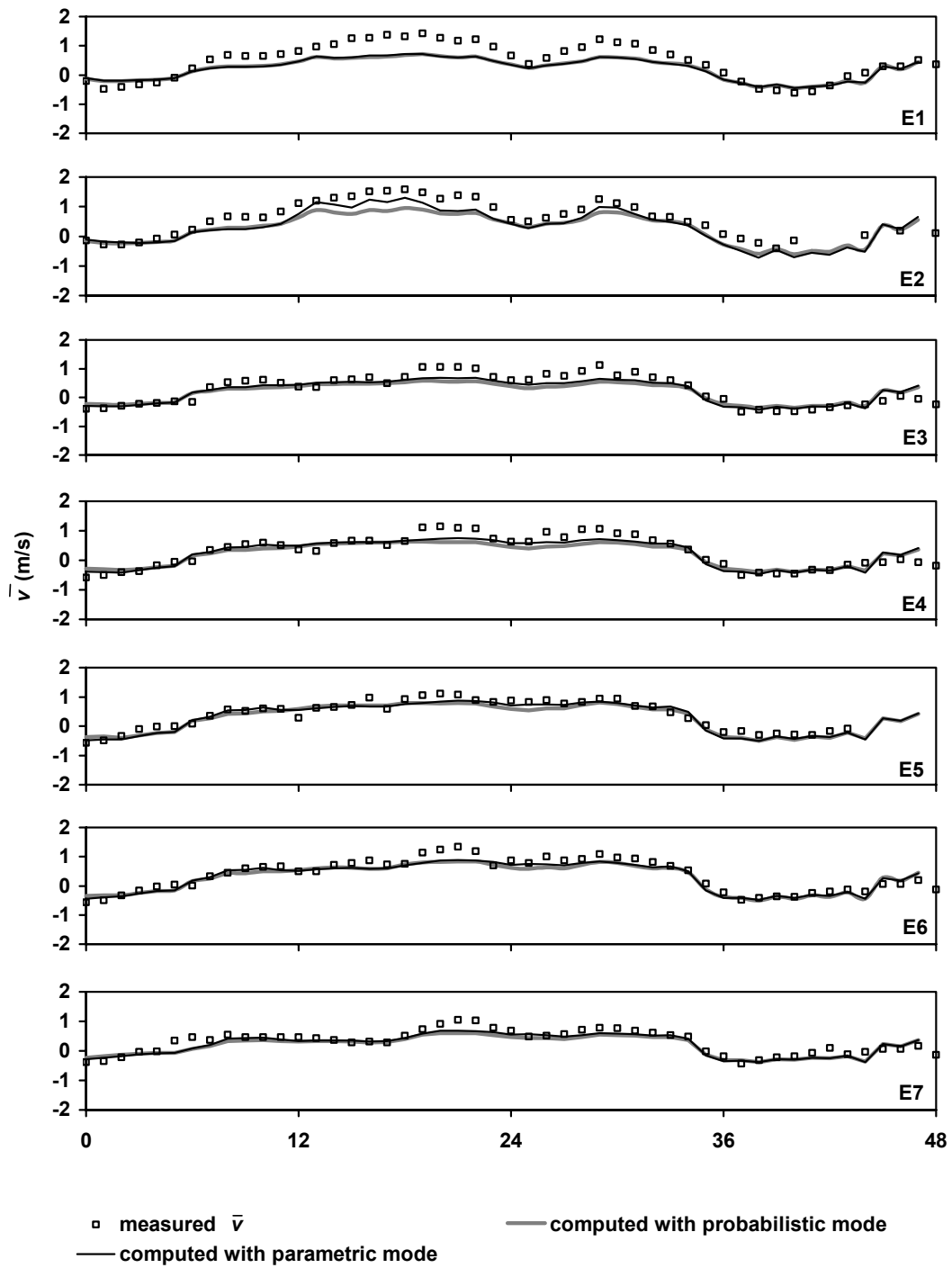


Figure 3.18. Measured (symbols) and modelled (curves) longshore current \bar{v} from offshore (E1, top panel) to onshore (E7, bottom panel) versus time; 26-28 October 1998, Egmond aan Zee, the Netherlands.

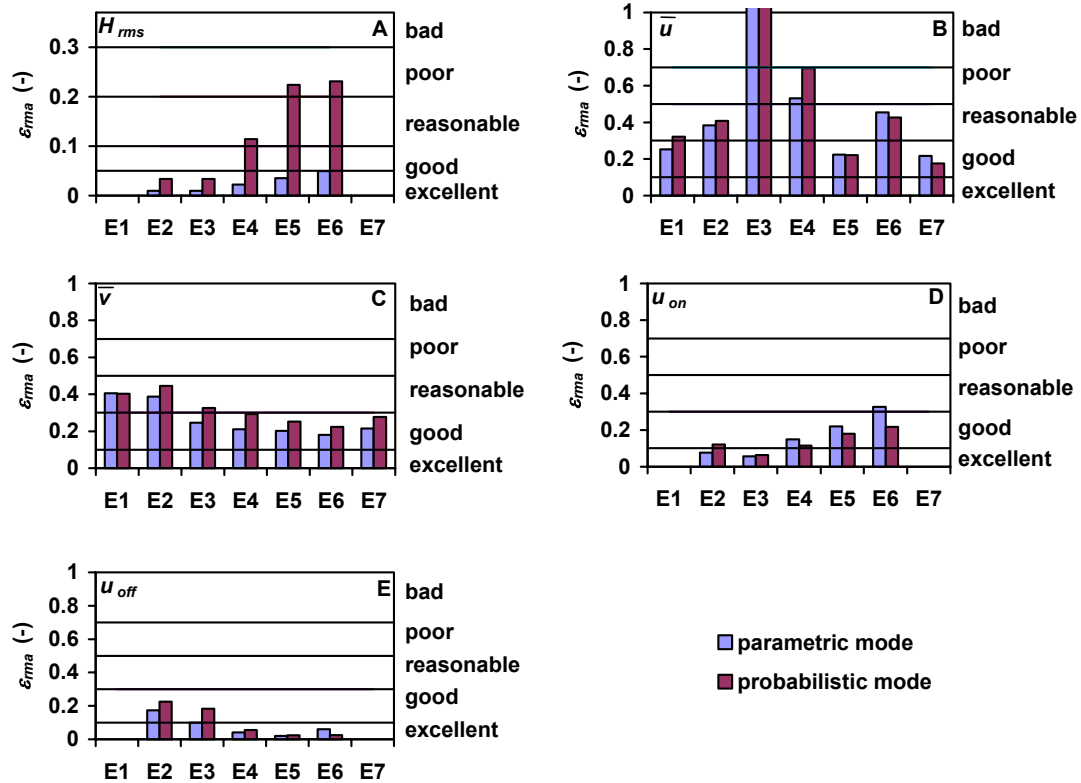


Figure 3.19. Model error statistics for waves (A), cross-shore currents (B), longshore currents (C), onshore orbital velocity (D) and offshore orbital velocity (E); 26-28 October 1998, Egmond aan Zee, the Netherlands.

3.3.6. DISCUSSION

Predictions of nearshore hydrodynamics in probabilistic mode may rely, at least partly, on the accuracy of the computed wave-height probability density function (pdf). Both the small-scale laboratory experiments and the Egmond field data indicated that the present model predicts measured pdfs that are too broad and thus extend to too large wave heights, in particular within the surf zone. Interestingly, a Rayleigh wave-height distribution appears to fit the measured pdfs reasonably well, both in the laboratory (Figure 3.4) and in the field (Figure 3.20), consistent with earlier laboratory (Baldock et al. (1998) and field observations (Thornton and Guza (1983)). The major cause of the discrepancy between the measured and computed wave-height pdf is likely to be the assumption that all waves approach exactly the same height as saturation is attained in the surf zone. In contrast, the measurements suggest that there is certain variability in breaker criterion that leads to a smoothing of the wave height distribution. This variability in the breaker criterion may be caused by wave-wave interactions. Visual observations by the present author in a small-scale laboratory flume showed that a wave smaller than the stable wave height may break when it is preceded by a large breaking wave. The small wave may be pushed over by the large undertow velocities induced by the preceding breaking wave. Other causes for a varying breaker criterion include wave reflection and interaction with surf beat (Dally (1992)).

Goda (1975) and Mase and Iwagaki (1982) included surf beat in their models by varying the still water level in a random fashion, which is basically the same as varying the breaker criterion around a mean γ . Dally (1992) adopted a Gaussian distribution for each γ value, which served to smooth the peak in the wave height distribution. To test the effect of a varying breaker criterion in the present model, a similar approach as the one by Dally (1992) was adopted. The wave model was run five times, each with a different breaker criterion. These breaker criteria, each representing 20% probability, were $\gamma - 0.1$, $\gamma - 0.05$, γ , $\gamma + 0.05$ and $\gamma + 0.1$. Wave height distributions were then calculated using the combined results of all five runs. As expected, use of the probabilistic breaker criterion improves the shape of the distribution as compared to the measured data (not shown). The variable breaker criterion only reduces the magnitude in the peak of the wave height distribution but does not affect the prediction of H_{rms} , $H_{1/3}$ and $H_{1/10}$ and of the orbital motion and time-averaged currents, consistent with the findings of Dally (1992). This means that if only the hydrodynamic statistics are required, the deterministic breaker criterion as shown in Figure 3.1 suffices. However, using a probabilistic breaker criterion increases the computation time of the model with a factor 5, which makes this approach rather unsuitable for long-term (months to years) morphodynamic computations. What is more, the present data suggest that the wave height distribution can very reasonably be approximated with a Rayleigh distribution, which is represented by a single wave height H_{rms} and period T_p .

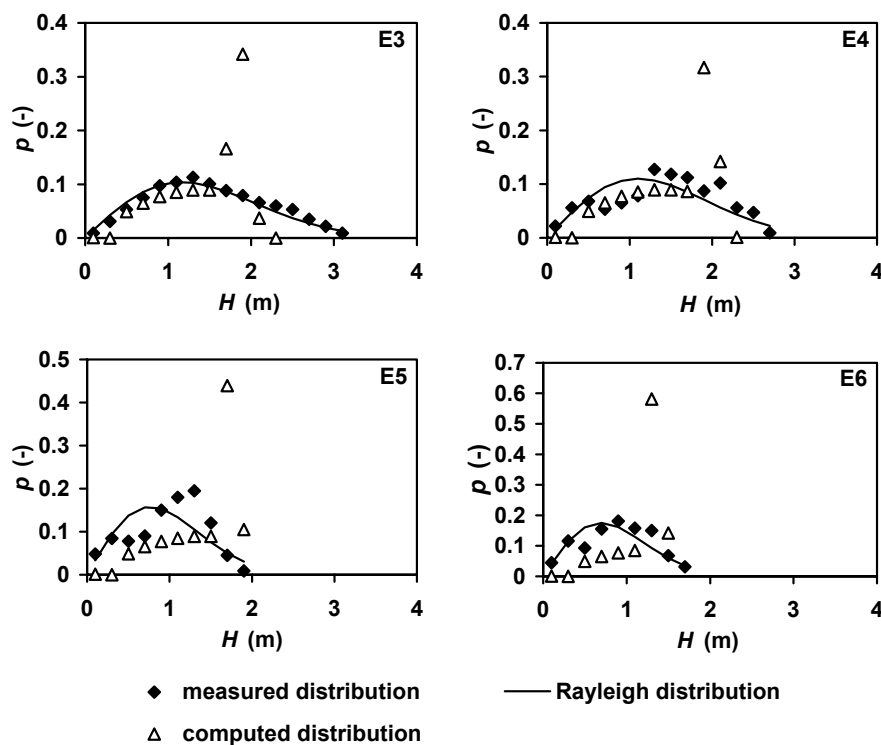


Figure 3.20. Measured, computed and Rayleigh wave height distributions at four locations near the coast of Egmond aan Zee. For locations see Figure 3.15.

Although modelled \bar{u} compare favourably with measured \bar{u} in the large-scale laboratory, the computed cross-shore currents in the field near Duck and Egmond show rather poor agreement with the measurements. Generally, cross-shore currents are overestimated at locations seaward of a nearshore bar and underestimated at locations more shoreward.

This might be caused by the choice of a fixed wave front slope β . Walstra et al. (1996) suggested that β varies in the cross-shore. To test whether a varying wave front slope would improve the predictions, the β function as proposed by Walstra et al. (1996) was applied in the present model. Generally, this led to the same results as when using $\beta = 0.1$ and did not improve the predictions of the cross-shore mean currents.

Bad predictions of the cross-shore mean currents might also be related to horizontal cross-shore mixing, which is not explicitly considered in the present model. Including this might improve the predictions, which seems to be supported by comparisons with small-scale laboratory data in which the measured mean cross-shore currents distribution is somewhat broader than the computed one.

A third way of improving the cross-shore mean current predictions may be to change parameters in the wave model. A larger wave energy dissipation rate shoreward of the nearshore bars produces a steeper decay in wave height, which not only gives better agreement with the wave heights measured in the field but would also move the cross-shore current profile shoreward.

The fourth reason for the discrepancies between measured and computed \bar{u} under field conditions is that currents measured in the field were defined at about 0.5 m above the bed (depth-averaged values were used from the lab data), whereas the computed values represent the depth-averaged currents. No roller is present at the onset of breaking, which results in a rather uniform velocity profile. A fully developed surface roller causes an onshore-directed shear stress on the water column at the wave trough level. This leads to a decrease of the offshore-directed velocities in the upper part of the velocity profile and mass balance results in an increase of the velocities in the lower part of the profile under these conditions. In the field, the velocities were measured in this lower part of the profile. Assuming these to be the depth-averaged velocity exaggerates the roller effect. The velocities measured in the field at 0.5 above the bed are therefore larger than the actual depth-averaged velocity, which leads to larger discrepancies with the model predictions. Under breaking waves, the difference between the velocity measured at a single height and the depth-averaged value may reach a factor 2; see e.g. Houwman (2000).

Overestimation of the undertow velocities on the seaward flank and near the crest of a nearshore bar may be caused by the use of linear wave theory to compute the mean mass transport associated with the organized wave motion in the present model. Dally and Brown (1995) have shown that the use of stream function wave theory leads to more accurate predictions of the undertow velocities compared to linear wave theory.

Finally, observations may depart from the computations because of the presence of 3-dimensional circulations. It is needless to say that the predictive performance of the present 2D model is poor for cases where 3D circulations are important.

The rather poor model performance with respect to the prediction of the cross-shore mean currents is not specific for the present model. Within the EU-COAST3D project, five process-based cross-shore models, including the present, were tested against the Egmond aan Zee field data set. All five models showed a poor performance in predicting the cross-shore mean currents (Van Rijn et al. (2002b)).

3.3.7. CONCLUSIONS

In this section a hydrodynamic model has been presented that can predict the cross-shore transformation of wave height, on- and offshore orbital motion, and time-averaged cross-shore and alongshore currents in a parametric and probabilistic mode. In the parametric mode, the computations are based on the root-mean-square wave height, the peak period and the energy-weighted mean angle of incidence, while in the probabilistic mode a discrete number of classes with their own wave height, period, and angle of incidence is prescribed. Predictions of the two modes differ marginally and result in about the same error statistics when compared to data from laboratory and field experiments. Consistent with other probabilistic wave models, measured wave height distributions inside the surf zone were not reproduced accurately by the present probabilistic model. Although this could be remedied by introducing some variability around the breaker parameter, predictions of the other hydrodynamic parameters did not improve as a result. The present work suggests that the modelling of hydrodynamic parameters commonly used to predict nearshore sediment transport does not require a rather time-consuming probabilistic approach, as the same accuracy can be reached with a computationally quicker parametric approach. The root-mean-square wave height, peak period and energy-weighted angle of incidence can thus be considered as representative single-wave parameters for hydrodynamic computations in natural random wave fields. Whether the parametric mode is also sufficient to accurately reproduce sediment transport and morphological change (compared to the probabilistic mode) is a topic in Chapters 4 and 5, respectively.

3.4. EFFECT OF CHANGING FREE MODEL PARAMETERS ON MODEL RESULTS

3.4.1. INTRODUCTION

The effect of changing the free model parameters on the predicted waves and currents (sensitivity test) has been studied in detail using data for a wide range of hydrodynamic conditions collected during the EU-COAST3D main campaign near Egmond aan Zee in 1998.

In this section, the results from one event (Table 3.4) and a time series of 48 hours are compared to the model estimates. Other events generally showed the same results. The differences between the probabilistic and parametric approach were found to be small in the previous section, therefore the parametric approach was used to study the effect of changing the free model parameters.

A large number of hydrodynamic simulations were done to account for uncertainties in the input parameters and measurement variations. Parameters such as wave-related

roughness, current-related roughness, breaker criterion, horizontal mixing and the wave front slope were varied between physically realistic limits. The free model parameters, their default values and the range over which they were varied for the sensitivity test are given in Table 3.5.

Table 3.4. Offshore conditions Egmond aan Zee, Netherlands, 28 October 1998, 08:00 h.

$H_{rms,0}$	T_p	h_0	θ	η_{tide}	\bar{v}_0
(m)	(s)	(m)	(deg)	(m)	(m/s)
2.23	8.3	15.0	24	1.41	0.70

The wave-related roughness height $k_{s,w}$ influences the wave-energy dissipation by bed friction and is related to the grain size of the bed material or the ripple dimensions. This parameter can be used to optimize the wave height results. Higher values result in larger wave energy dissipation and hence smaller waves. The current-related roughness height $k_{s,c}$ influences the roughness ‘felt’ by a mean current and is also related to the grain size of the bed material or the ripple dimensions. This parameter can be used to optimize velocity results. Higher values result in larger bed shear stresses and hence lower velocities. In general, the $k_{s,w}$ value should be lower than the $k_{s,c}$ value. Default values for $k_{s,w}$ and $k_{s,c}$ are 0.02 m and 0.03 m, respectively. The breaker criterion γ influences the wave breaking process and can be used to calibrate the wave model. This parameter has a significant influence on the predicted wave heights. A smaller γ value results in ‘easier’ breaking of waves. Default value for γ is the function shown in Figure 3.1. The horizontal mixing ε influences the cross-shore distribution of the longshore velocity. A higher ε value results in smaller velocity gradients and hence a ‘flatter’ cross-shore distribution of the longshore velocity. Default value for ε is 2.0 m²/s for field conditions. The wave front slope β influences the roller model. Higher values of β reduce the lag effect and result in a lower persistence of wave breaking behind a bar while lower values increase the lag of energy transfer from waves to the underlying water. This parameters can be used to calibrate the water levels and the flow module as it determines the transfer of momentum from the waves to the current. Default value for β is 0.06.

Table 3.5. Free model parameters, their default values and the range over which they were varied for sensitivity tests.

free model parameter	default value	Range of values
wave-related roughness, $k_{s,w}$ (m)	0.02	0.01-0.04
current-related roughness, $k_{s,c}$ (m)	0.03	0.01-0.04
breaker criterion, γ (-)	function (Figure 3.1)	0.32-0.42
horizontal mixing, ε (m ² /s)	2.0	0.5-2.5
wave front slope, β (-)	0.06	0.04-0.1

First, the sensitivity of the cross-shore profile model is assessed for the free model parameters. Seven events were studied (Van Rijn et al., 2002b). Herein, the results are presented of one exemplary event on 28 October 1998, 08:00 h of which the offshore wave conditions are given in Table 3.4.

Second, the model is verified by systematically varying the main input parameters. This verification is done by comparing measured and computed quantities based on measured time series of 48 hours. Model performance is expressed in terms of the relative mean absolute error (ϵ_{rma}).

3.4.2. EFFECT ON MODEL RESULTS: QUALITATIVELY

Wave-related bed roughness

The wave-related bed roughness height determines the wave dissipation by bottom friction. This roughness parameter, which is actually a schematization of several physical processes in a thin layer close to the bed, is difficult to determine in field conditions, because it is influenced by the presence of grains on the seabed, the formation of bed forms, and large sediment concentrations creating additional friction effects. Although several formulations are available to compute the bed roughness from the ripple height and the ripple length (e.g. Grant and Madsen, 1982; Nielsen, 1992), there still is much uncertainty about their accuracy. Therefore, in the present cross-shore profile model, the user gives the bed roughness as an input.

To get some insight in the influence of the bed roughness height on the computations, the sensitivity of the profile model for different bed roughness heights was tested. For these computations, the wave-related bed roughness height was varied between $k_{s,w} = 0.01$ and 0.04 m. The roughness was kept constant across the profile. Figure 3.21 shows the influence of the wave-related bed roughness on the computed wave heights. For comparison, the measured wave heights are shown also.

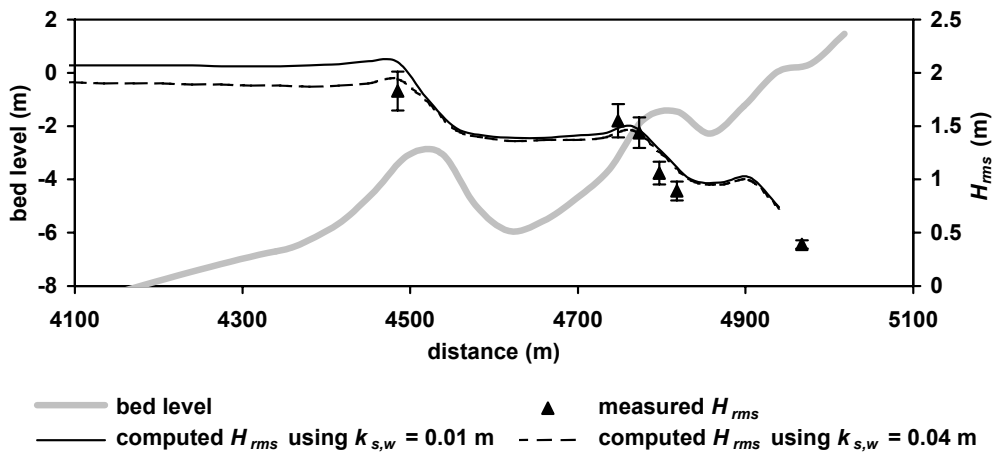


Figure 3.21. Effect of wave-related bed roughness on the predicted wave height variation across a nearshore profile near the coast of Egmond aan Zee, the Netherlands.

A larger wave-related bed roughness leads to more wave energy dissipation by bottom friction (Figure 3.21). This takes place over a relatively long distance and therefore has a profound effect. For example, energy dissipation by bottom friction decreases the H_{rms} with 10-20% over a distance of about 4000 m between the offshore boundary and the outer nearshore bar. Consequently, increasing $k_{s,w}$ results in smaller wave height gradients across the profile (Figure 3.21). Changing $k_{s,w}$ hardly affects the wave height distribution shoreward of the outer nearshore bar ($x > 4500$ m). In this region wave energy dissipation is dominated by wave breaking.

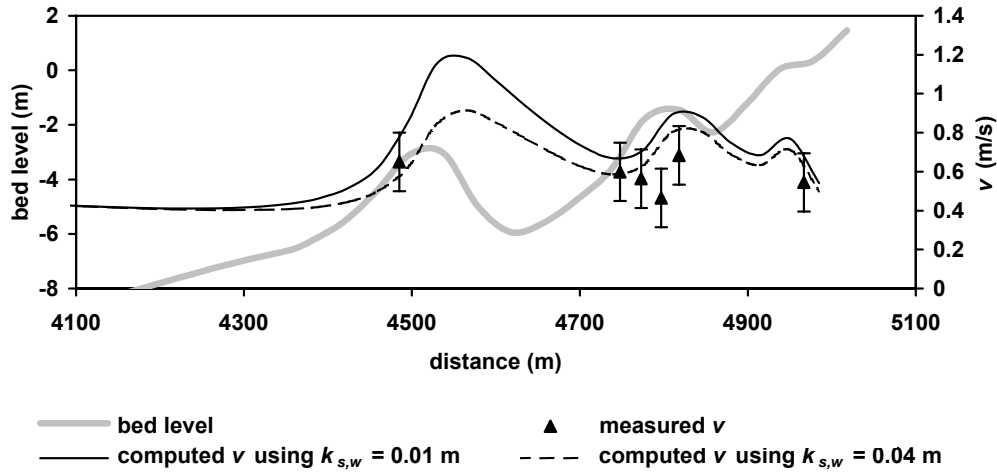


Figure 3.22. Effect of wave-related bed roughness on the predicted longshore current variation across a nearshore profile near the coast of Egmond aan Zee, the Netherlands.

As the gradient of the longshore component of the radiation stress is the driving force of the longshore current, the magnitude and gradient of the latter also decreases with increasing wave-related bed roughness. With a small $k_{s,w}$ the computed longshore velocity is very peaked with maximum velocities of 1.2 m/s on the outer bar (Figure 3.22). The distribution is more uniform using larger wave-related roughness heights.

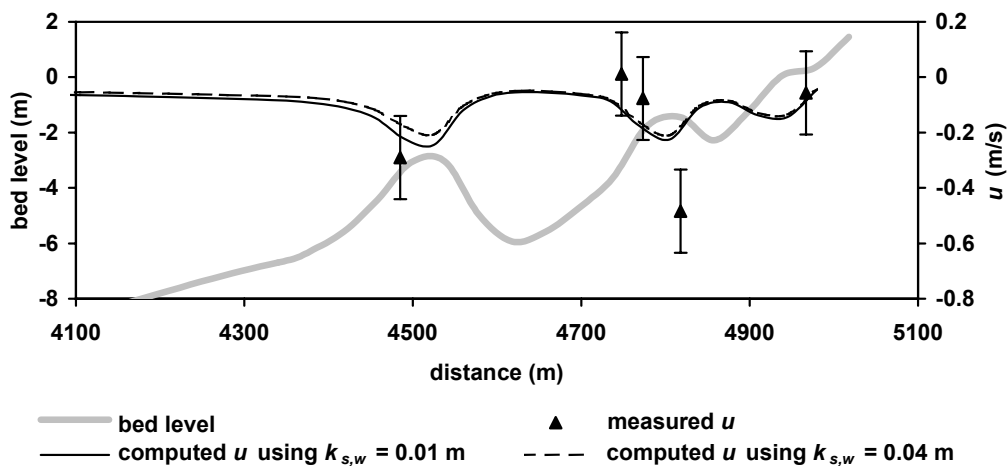


Figure 3.23. Effect of wave-related bed roughness on predicted cross-shore current variation across a nearshore profile near the coast of Egmond aan Zee, the Netherlands.

The undertow decreases with increasing roughness height (Figure 3.23) but the effect is less pronounced compared to effect on the longshore velocities. The undertow velocities near the bar crests are about 20% smaller using $k_{s,w} = 0.04$ m compared to using $k_{s,w} = 0.01$ m. In general, the model tends to overestimate the undertows on the seaward flank of the inner nearshore bar and underestimate the velocities on the shoreward flank. It is noted that the measurements of the currents were done at about 0.5 m above the bed, whereas the computed values represent the depth-averaged currents. However, this does not sufficiently explain the large discrepancies between the model and the measurements. Other causes for the discrepancies between the measured and predicted undertows are discussed in Section 3.3.6.

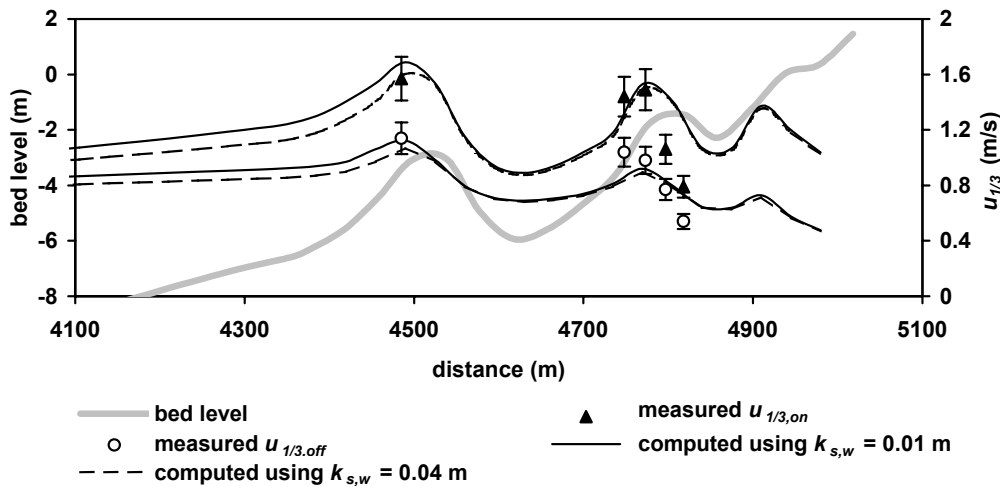


Figure 3.24. Effect of wave-related bed roughness on predicted peak near-bed orbital velocities across a nearshore profile near the coast of Egmond aan Zee, the Netherlands.

Following the wave height, an increase in $k_{s,w}$ decreases the magnitude of both the on- and offshore directed peak orbital velocities, without significantly altering the skewness (Figure 3.24). An increase of $k_{s,w}$ from 0.01 to 0.04 m results in a decrease of the peak orbital velocities on the outer bar crest with about 10%; that is consistent with the decrease in wave height.

Current-related bed roughness

The model needs the current-related bed roughness to determine the bottom boundary conditions for the flow Equations (3.10) - (3.12). Similar as for the wave-related roughness, the current-related roughness also can be considered to consist of a grain-related part, a form-related part, and a transport-related part. The grain-related roughness is often assumed equal to $3D_{90}$. This grain roughness is always present and therefore represents the minimum value for the current-related roughness in case of a plane bed. The form roughness, related to the presence of bed forms, and the transport-related roughness, associated with a higher viscosity of the fluid-sediment mixture near the bed, are less well known. For this reason, the current-related roughness is also given as an input in the model.

The wave-current interaction is computed using the method proposed by Van Rijn (1993). In this formulation, the increase of the (apparent) roughness k_a experienced by a current in the presence of waves depends on the ratio of the peak orbital velocity and the mean flow velocity. To give an idea of the magnitude, for the case presented here this results in a k_a ranging between about 0.15 m on the bar crests to 0.30 m in the troughs between the bars.

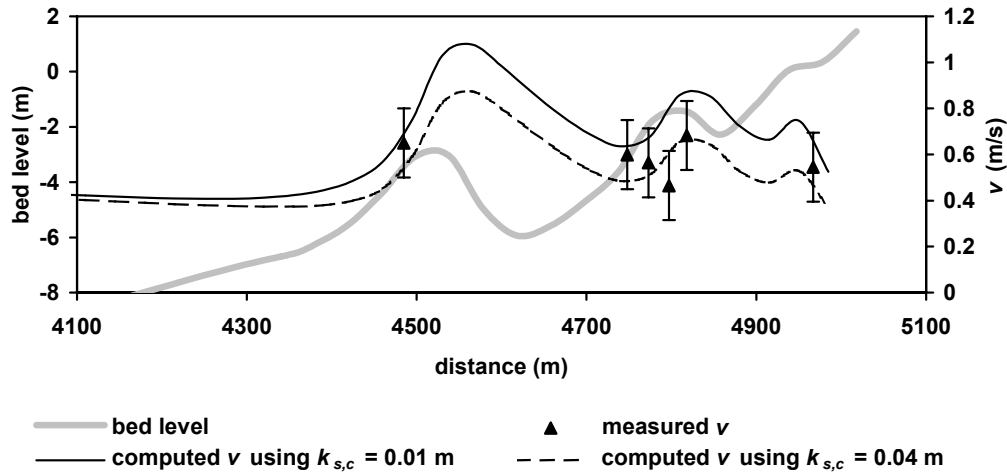


Figure 3.25. Effect of varying the current-related bed roughness on predicted longshore current variation across a nearshore profile near the coast of Egmond aan Zee, the Netherlands.

Changing the current related roughness only affects the longshore current velocities (Figure 3.25). An increase in $k_{s,c}$ decreases the magnitude of \bar{v} without altering the cross-shore shape of \bar{v} . An increase of $k_{s,c}$ from 0.01 m to 0.04 m results in a decrease of the longshore velocities with about 20-30%.

Breaker criterion

The effect of breaking on wave properties and dimensions is important in predicting cross-shore profile changes, not only because the cross-shore undertow and the longshore current are directly related to the wave height gradient across the profile, but also because the sediment transport depends non-linearly on the wave height. Random waves of root-mean-square height H_{rms} break on a beach in water of depth h given to a first approximation by $H_{rms} = \gamma h$ where the coefficient γ takes the value of about 0.4. The breaker criterion increases with beach slope and with wave period for sloping beds (Weggel, 1972). However, there is still uncertainty about the exact condition for wave breaking. Dally (1992) uses a Gaussian distribution for the breaker criterion with values between 0.31 and 0.49. Thornton and Guza (1983) use a fixed value of 0.42 based on a wide range of field data. Van Rijn and Wijnberg (1996) suggest a breaker criterion as a function of the local bed slope and wave steepness.

Two options are available in the present model, the first is to use a fixed breaker criterion that can be given by the user, and the second option is to use a breaker function, following the approach of Van Rijn and Wijnberg (1996). The breaker criterion was varied between physically realistic values to evaluate the influence on the

model results. Figure 3.26 shows the modelled wave height variation across the profile using a fixed breaker criterion of 0.32 and 0.42, respectively, and using the breaker function as shown in Figure 3.1. It is noted that the parametric mode was used here.

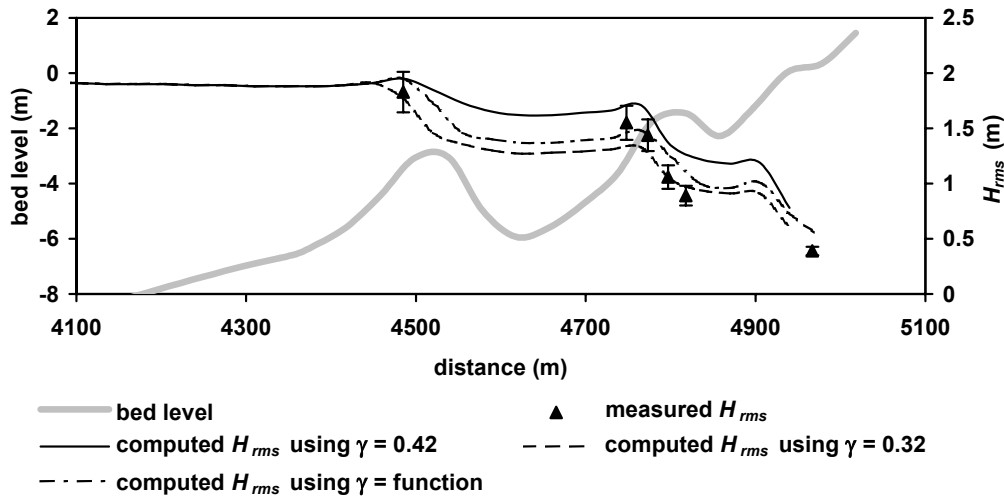


Figure 3.26. Effect of varying the breaker criterion on predicted wave height variation across a nearshore profile near the coast of Egmond aan Zee, the Netherlands.

As can be seen, compared to bottom friction, the wave energy dissipation by the breaking of waves takes place over a shorter distance and nearer to the shore. The same amount of energy that is being dissipated by bottom friction over a distance of 4 km is dissipated by wave breaking over a distance of 200 m across the outer bar, resulting in relatively large wave height gradients in this region. Decreasing the breaker criterion leads to larger wave height gradients near the outer bar and, consequently, smaller wave heights further shoreward because much of the wave energy has been dissipated on the outer bar. Figure 3.26 shows that the wave heights are reasonably predicted using the breaker function although the waves just shoreward of the inner nearshore bar are somewhat over-predicted (about 10%).

Since the longshore currents are calculated directly from the wave energy dissipation rate, the change in breaker criterion has a substantial effect on the magnitude of the longshore currents. The results are shown in Figure 3.27. No waves are breaking on the outer bar when using $\gamma = 0.42$, resulting in a solely tidally induced longshore current at this location. The current velocities decrease slightly on the outer bar crest due to an increased bed friction. On the inner nearshore bar the longshore current is very peaked with a maximum of 1.0 m/s just shoreward of crest, which is significantly larger than the measured values. Using $\gamma = 0.32$ causes waves to start breaking just shoreward of the outer bar crest. This leads to a predicted maximum of about 1.1 m/s located at the outer bar crest. The longshore current decreases gradually moving shoreward and reaches a maximum of about 0.8 m/s again at the inner nearshore bar crest. Longshore flow velocities on the beach are in the same range as measured. Using the breaker function results in a shoreward shift of the breaker dissipation and thus a shoreward shift of the maximum longshore current.

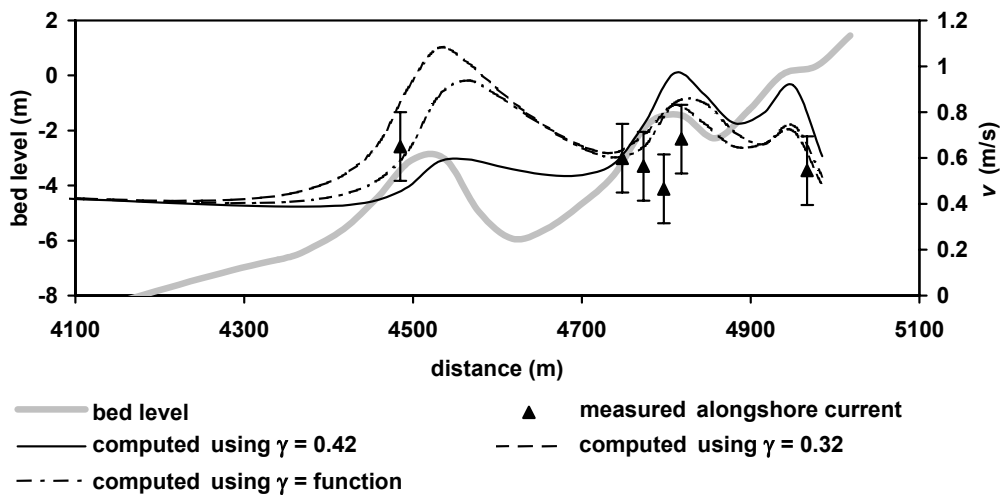


Figure 3.27. Effect of varying the breaker criterion on predicted longshore current variation across a nearshore profile near the coast of Egmond aan Zee, the Netherlands.

The predicted time- and depth-averaged cross-shore currents are derived from the mass flux due to the wave motion Q_w and the mass flux due to the surface roller Q_r . The first depends on the wave energy and the second on the roller energy according to Equations (3.8) and (3.9), respectively, which on their turn depend on the wave height variation and the dissipation by wave breaking. Therefore, smaller wave heights as a result of a smaller breaker criterion lead to smaller cross-shore currents (Figure 3.28).

The effect of the breaker criterion on the cross-shore currents is stronger than that of the bed roughness. Varying the breaker criterion in the model between physically realistic values results in a 100% variation of the undertow predictions on the inner nearshore bar and the beach.

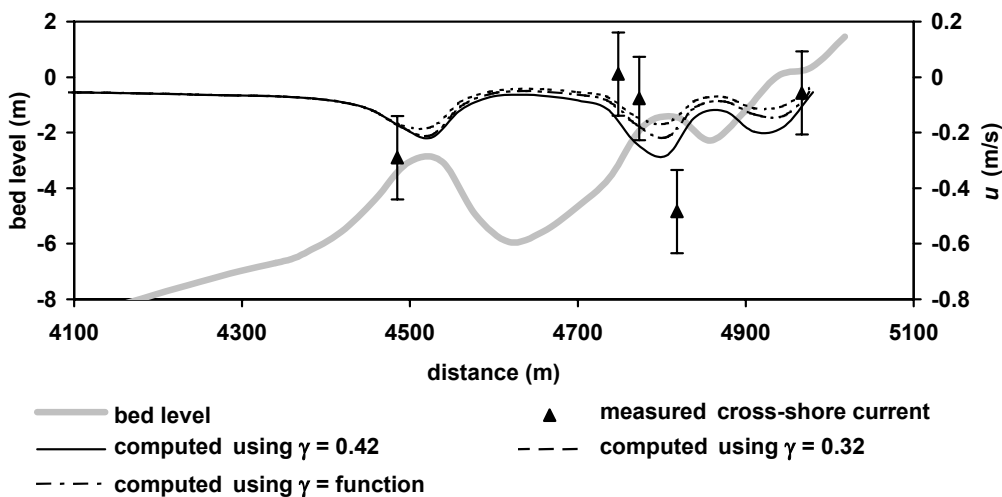


Figure 3.28. Effect of varying the breaker criterion on predicted cross-shore current variation across a nearshore profile near the coast of Egmond aan Zee, the Netherlands.

Horizontal mixing

In the model, the large-scale horizontal mixing coefficient ε controls the cross-shore exchange of longshore momentum and has no effect on the wave heights and cross-shore currents (Figure 3.29).

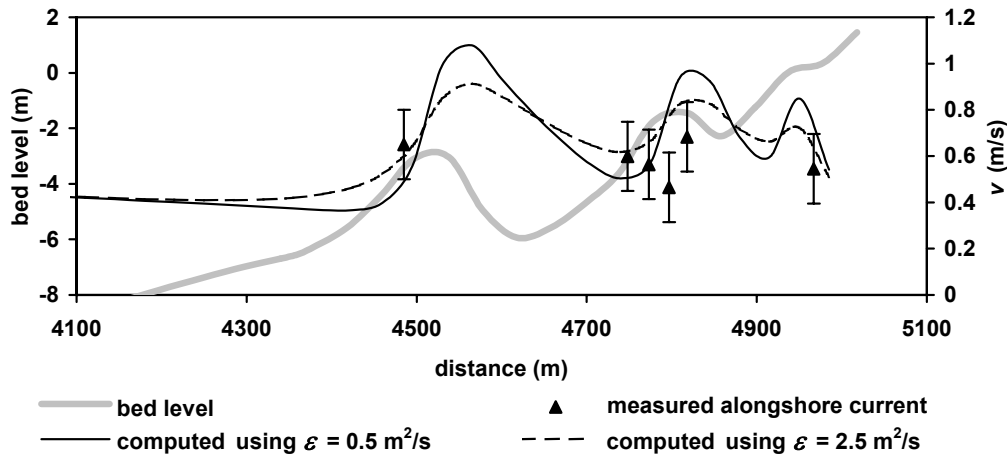


Figure 3.29. Effect of varying the horizontal mixing coefficient on predicted longshore current variation across a nearshore profile near the coast of Egmond aan Zee, the Netherlands.

Horizontal exchange of momentum mixes water particles having different longshore velocities, thereby smearing the current profile. This smoothing of the longshore current profile in the surf zone is expected because of the intense turbulence created by breaking waves, which is advected back and forth by oscillatory wave motion. Shear waves may be another mixing mechanism. Bowen and Holman (1989) note that the greater cross-shore length scale of a shear wave (order of 50 m) as compared with the depth-limited orbital wave motion of a short wave in the surf zone (order of 5 m) suggests that shear waves may be a dominant mixing mechanism. Horizontal mixing smooths the cross-shore distribution of the longshore current without shifting the location of the maximum. Based on the parameterization of Özkan-Haller and Kirby (1999) with $M = 0.5$, mixing coefficients between 0.1-0.9 m^2/s are expected for the Egmond field site under the present conditions.

For the present sensitivity test, the horizontal mixing coefficient was varied between 0.5 - 2.5 m^2/s . As can be seen, with little mixing the computed longshore velocity distribution is rather peaked with maximum velocities of about 1.0 m/s on the bars where most of the waves are breaking. More uniform distributions are obtained using a larger mixing coefficient.

Wave front slope (roller)

The wave front slope β controls the advection length of the roller in the model (Equation (3.6)). A decreasing β increases the advection length, which results in shoreward shift of the maximum cross-shore and longshore currents, and a smoothing of the longshore current profile. The influence of the wave front slope is examined by varying β between 0.03 and 0.1.

The effect of changing the wave front slope on the time-averaged cross-shore currents is shown in Figure 3.30. Undertow velocities at the outer nearshore bar are hardly influenced by changing β from 0.03 to 0.1. Predictions on the inner nearshore bar differ with about 30%. Largest influence is observed on the beach where the undertow velocities change with almost a factor 2. A wave front slope of $\beta = 0.03$ leads to high undertow velocities in this region. The β function as proposed by Walstra et al. (1996) produces almost the same results as when using $\beta = 0.1$.

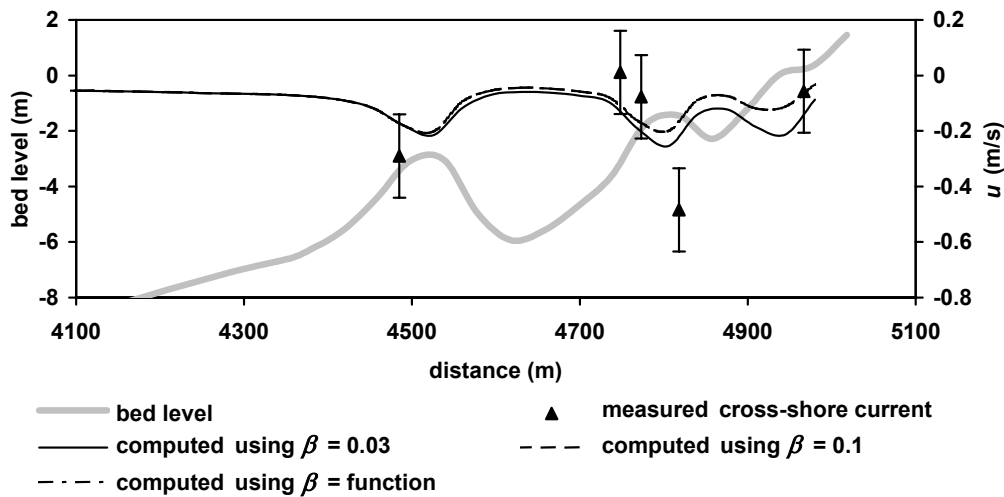


Figure 3.30. Effect of varying the wave front slope on predicted cross-shore current variation across a nearshore profile near the coast of Egmond aan Zee, the Netherlands.

With a large wave front slope, narrow longshore current jets are located just shorewards of the bar crests and near the shoreline (Figure 3.31). Decreasing β shifts the maximum longshore current shoreward and broadens the current jets by increasing the velocities in the troughs and decreasing the velocities just shoreward of the bar crests.

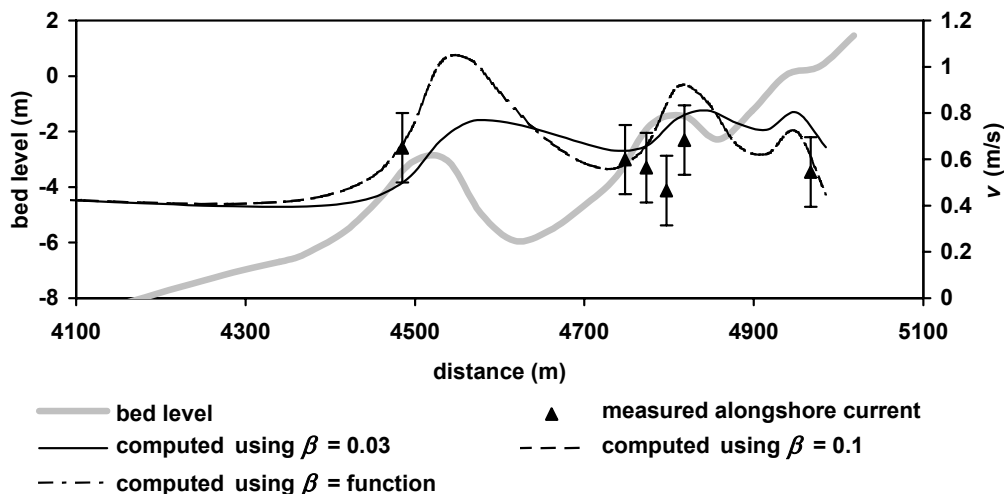


Figure 3.31. Effect of varying the wave front slope on predicted longshore current variation across a nearshore profile near the coast of Egmond aan Zee, the Netherlands.

The effect of the roller on the time-averaged longshore velocities can be explained from the changes in magnitude and direction of the wave and roller-induced forces on the water column. The cross-shore distribution of the breaker dissipation D_{br} is shown in Figure 3.32. Significant peaks are present near the two bar crests. Energy losses due to wave breaking are converted to roller energy. Subsequently, the roller dissipation D_r drives the longshore current. Figure 3.32 shows the roller dissipation term computed with a wave front slope of $\beta = 0.03$ (dashed line) and 0.1 (dash-dot line). The roller shifts the peak in the energy dissipation about 30 m shoreward.

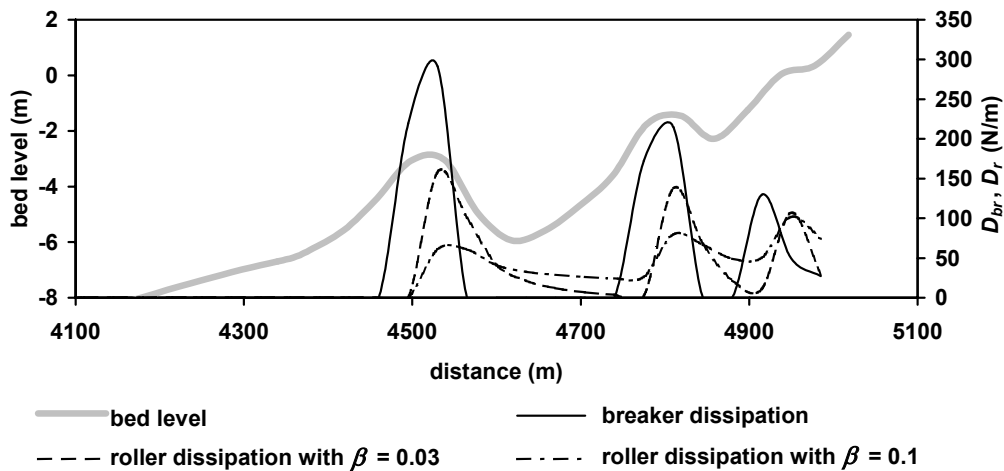


Figure 3.32. Cross-shore distribution of the breaker dissipation D_{br} and roller dissipation D_r with $\beta = 0.03$ and $\beta = 0.1$.

Figure 3.32 also shows that decreasing the wave front slope β does not so much shift the energy dissipation peak further shoreward but results more in a broadening of the energy dissipation distribution across the entire profile. A small wave front slope results in a more or less continuous build-up of the dissipation term resulting in a continuous increase of the longshore current across the entire profile. Under the conditions presented here this is not realistic because waves were not observed to persist breaking between the outer and inner nearshore bar.

3.4.3. EFFECT ON MODEL RESULTS: QUANTITATIVELY (MODEL PERFORMANCE)

To define the model performance in a more quantitative manner, the model computations are compared with measured time series of 48 hours at 7 locations across a nearshore profile (Figure 3.33) near the coast of Egmond aan Zee in the Netherlands between 26 and 28 October 1998. The relative mean absolute error (ϵ_{rma} , see Equation (3.27) in Section 3.3.4) is used for evaluation and qualification of the model performance with respect to time series of waves and currents.

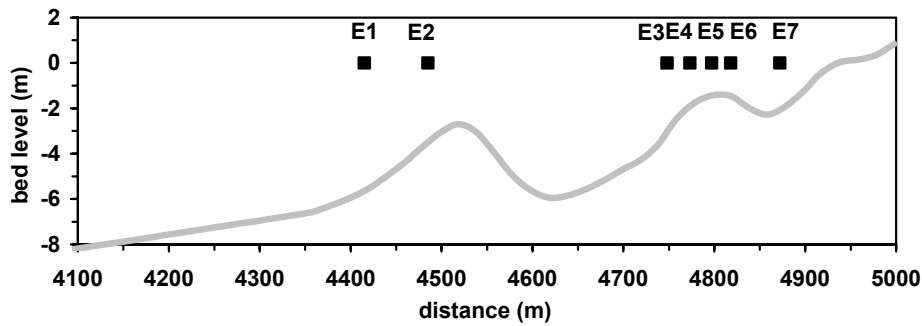


Figure 3.33. Locations of instruments during the measurement campaign in 1998 near Egmond aan Zee, the Netherlands. The bed profile measured on September 26, 1998 is shown as a reference.

Waves

The breaker criterion has the most pronounced effect on the model results because it not only influences the wave energy dissipation in the nearshore and thus the wave height variation across the nearshore profile but also significantly affects the magnitude and distribution of the cross-shore and longshore currents. In general, the γ function in Figure 3.1 is expected to give best results as it includes the influence of the local bed slope and the local wave steepness on the breaker criterion (Van Rijn and Wijnberg, 1996; Raubenheimer et al., 1996). The effect of changing the breaker criterion was tested by running it 3 times using $\gamma = 0.32$, 0.42 and the function in Figure 3.1. The ϵ_{rma} values for each model run are given in Figure 3.34. Good to excellent agreement is obtained using a relatively small breaker criterion of 0.32 . The wave heights are somewhat underestimated at E2 on the outer nearshore bar (see also Figure 3.26). Using $\gamma = 0.42$ leads to excellent predictions of the wave heights on the outer bar (E2) but leads to significant overestimation of the wave heights on the inner bar (E3-E6).

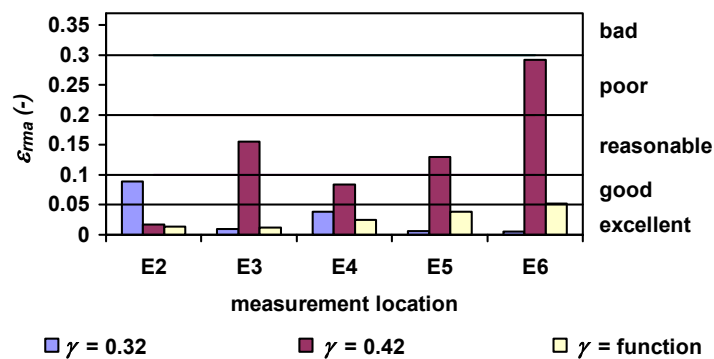


Figure 3.34. Wave model error statistics at Egmond showing the effect of changing the breaker criterion γ . For measurement locations see Figure 3.33.

The model was run 3 times, using different wave-related bed roughness heights $k_{s,w}$. The ϵ_{rma} values for each model run are given in Figure 3.35. Clearly, the runs with a relatively large wave-related bed roughness compare best with the measurements. The model provides an accurate description of the wave height variation across the outer bar

and the seaward flank of the inner bar (items E2, E3 and E4). The model performance can be qualified as excellent in this region, irrespective of the roughness height used. Larger ε_{rma} values are found closer the shore at locations just shoreward of the inner nearshore bar crest. Generally, the estimated wave heights over the trough of the inner nearshore bar (E5 and E6) are too large. Using a bed roughness height of $k_{s,w} = 0.04$ m results in excellent agreement ($\varepsilon_{rma} < 0.05$) between measured and computed wave height at all measurement locations.

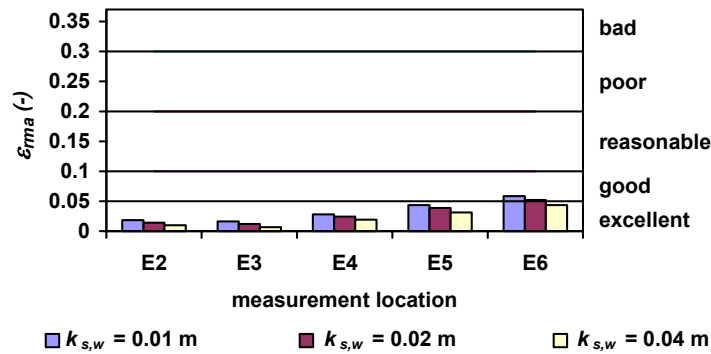


Figure 3.35. Wave model error statistics at Egmond showing the effect of changing the wave-related roughness height $k_{s,w}$. For measurement locations see Figure 3.33.

Cross-shore currents

The effect of changing the breaker criterion on the predicted cross-shore currents was also tested (Figure 3.36). Again three different breaker criteria are used, i.e. $\gamma = 0.32$, 0.42 and the γ -function in Figure 3.1. Using $\gamma = 0.32$ leads to model predictions more or less comparable to using the γ -function. Increasing the fixed γ makes undertow predictions worse, in particular at locations just seaward of the inner nearshore bar crest (E3 and E4). The γ -function is preferred as it gives excellent wave height predictions.

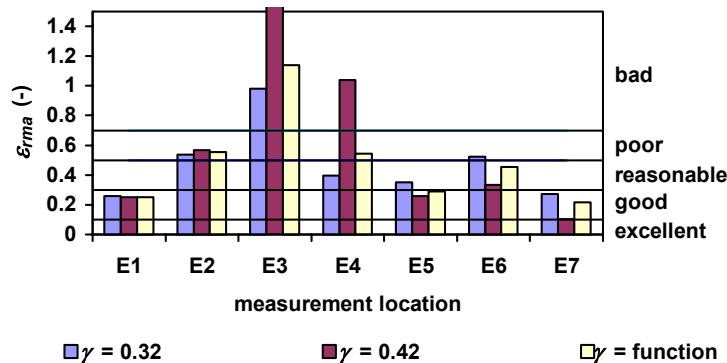


Figure 3.36. Cross-shore current model error statistics at Egmond showing the effect of changing the breaker criterion γ . For measurement locations see Figure 3.33.

Changing the wave-related roughness height $k_{s,w}$ has a relatively small effect on the cross-shore current model error statistics (Figure 3.37). Model performance for location E3 on the seaward flank of the inner bar slightly improves with increasing wave-related

roughness height but predictions remain bad for this location. Overall best agreement is obtained using a $k_{s,w}$ of about 0.02 m.

Generally, cross-shore current velocities are overestimated at locations seaward of the inner nearshore bar (E3 and E4), whereas the velocities on the bar crest and just shoreward (E5-E7) are underestimated, see also Figure 3.28 and Figure 3.30. This might have to do with the advection length of the roller.

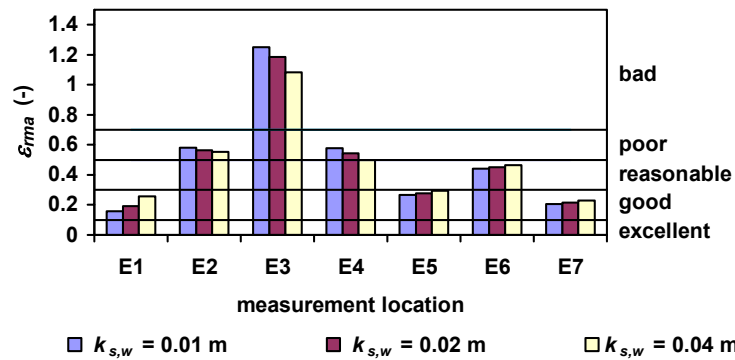


Figure 3.37. Cross-shore current model error statistics at Egmond showing the effect of the wave-related roughness height $k_{s,w}$. For measurement locations see Figure 3.33.

Besides an accurate estimate of the wave height variation across the nearshore profile, the prediction of the time-averaged cross-shore current velocities also depends on one additional parameter, i.e. the wave front slope β , which regulates the lag between the production and dissipation of turbulent kinetic energy. A decreasing β increases the advection length of the roller shifting the maximum mean cross-shore current shoreward and broadening the distribution. The model was run 3 times using different wave front slopes. Other parameters were kept constant. A wave-related bed roughness height of $k_{s,w} = 0.04$ m was used. Error statistics are shown in Figure 3.38.

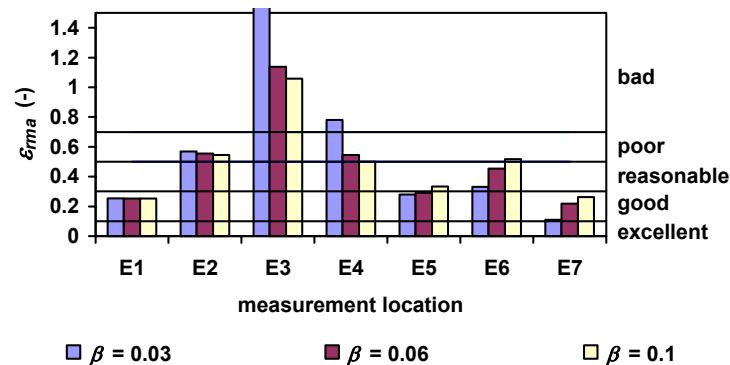


Figure 3.38. Cross-shore current model error statistics at Egmond showing the effect of changing the wave front slope β . For measurement locations see Figure 3.33.

It can be seen that varying the wave front slope hardly influences the cross-shore currents on the outer nearshore bar (E1 and E2). In contrast, changing β has a rather large influence on the predicted undertows just shoreward of the inner nearshore bar

crest. Using $\beta = 0.03$ results in large model errors on the seaward slope of the inner nearshore bar (E3 and E4). Undertow velocities are significantly over-predicted at these locations. Errors ε_{rma} decrease with increasing β , although predictions remain bad to poor.

Shoreward of the inner nearshore bar crest (E6 and E7), ε_{rma} increases with increasing wave front slope. Cross-shore velocities are under-predicted here. Best overall agreement is obtained using $\beta = 0.06$, which is close to the value used by Ruessink et al. (2001) and about mid-range of values cited by Walstra et al. (1994). Although based on ε_{rma} predictions are reasonable at locations shoreward of the inner nearshore bar crest, the root-mean-square error ε_{rms} ranges between 0.12 and 0.18 m/s for item E6. The cross-shore current is significantly under-predicted at this location.

The present results suggest that the roller delays the maximum undertow velocity insufficiently, even with a rather small wave front slope. The measured maximum undertow velocities are located more shoreward than those computed with the model, a phenomenon that was observed also under small-scale laboratory conditions (see Section 3.3.2). Artificially computing the undertow velocities using wave conditions smoothed over a distance of 0.1, 0.2 and 0.4 wavelengths seaward did not improve the predictions. The discrepancy is probably also related to other factors not included in the model or the presence of 3D circulations.

Longshore currents

The effect of changing the breaker criterion is most pronounced for the longshore current predictions on the outer neashore bar (Figure 3.39). Using $\gamma = 0.32$ causes waves to start breaking just shoreward of the outer bar crest. This leads to improved predictions compared to using the γ -function from Figure 3.1. No waves break on the outer bar when using $\gamma = 0.42$, resulting in a solely tidally induced longshore current at this location. Changing the breaker criterion has a minor effect on the model performance in the inner nearshore zone (E4-E7). Although using $\gamma = 0.42$ leads to poor wave height predictions at location E6, longshore current predictions are good. Using a different cross-shore model, Ruessink et al. (2001) also accurately predicted the longshore currents in the inner nearshore region despite an overestimation of the wave heights.

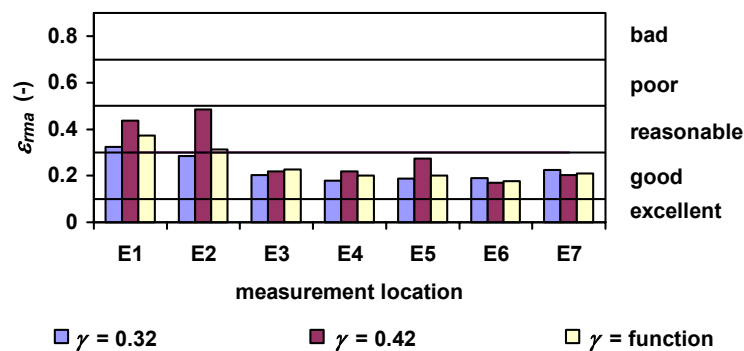


Figure 3.39. Longshore current model error statistics at Egmond showing the effect of changing the breaker criterion γ . For measurement locations see Figure 3.33.

The wave-related roughness height $k_{s,w}$ also has a minor effect on the longshore current model performance in the inner nearshore region (E3-E7) but does affect model predictions on the outer bar (E1 and E2). Model predictions in this region become worse when using a larger wave-related roughness height. A larger $k_{s,w}$ leads to more wave energy dissipation by bottom friction. Consequently, increasing this bed roughness height results in waves reaching the shore being smaller. This leads to smaller wave height gradients across the outer nearshore bar and thus smaller longshore currents.

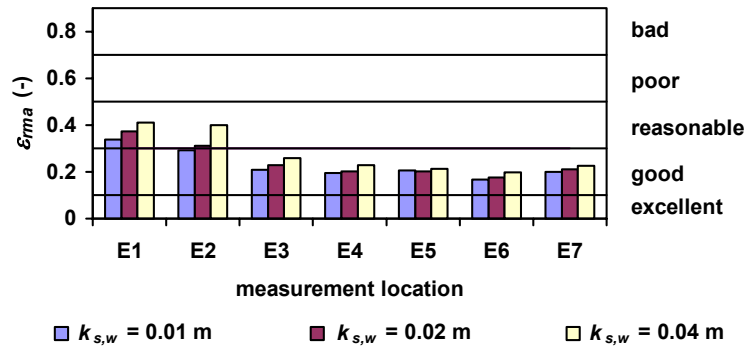


Figure 3.40. Longshore current model error statistics at Egmond showing the effect of changing the wave-related roughness height $k_{s,w}$. For measurement locations see Figure 3.33.

Based on an excellent prediction of the wave heights, the prediction of the longshore current velocities depends on three additional parameters, i.e. the current-related roughness $k_{s,c}$, the horizontal mixing coefficient ε and the wave front slope β . This increases the degrees of freedom considerably.

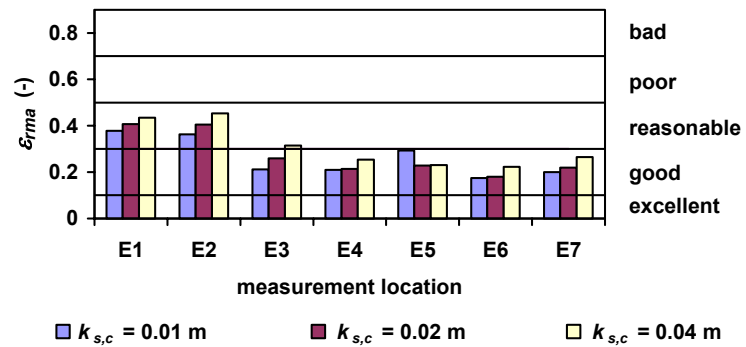


Figure 3.41. Longshore current model error statistics at Egmond showing the effect of changing the current-related roughness height $k_{s,c}$. For measurement locations see Figure 3.33.

First, the model was run 3 times using different current-related roughness heights. Other parameters were kept constant. It can be seen from Figure 3.41 that changing the current-related roughness height has a relatively small effect on model performance. Using a $k_{s,c}$ between 0.01 and 0.02 m gives slightly better agreement compared to a larger roughness height. The model agrees reasonably with the longshore currents measured on the outer nearshore bar (E1 and E2), with ε_{rma} between 0.4 and 0.5 (Figure 3.41). Good agreement is obtained for locations more shoreward, with ε_{rma} between 0.2 and 0.3.

Secondly, the horizontal mixing ε_0 was varied between 0.5 and 2.0 m²/s while other parameters were kept constant. Results are shown in Figure 3.42. Although not pronounced, model performance improves with increased mixing. Model performance is however less sensitive to the horizontal mixing than to the current-related roughness. Best overall agreement is obtained using $\varepsilon_0 = 2.0$ m²/s.

It is interesting to see that this relatively large horizontal mixing coefficient is not capable of improving the model performance at measurement locations on the outer bar crest.

Generally, the longshore current velocities were under-predicted by the present model in the outer bar region, which might be caused by too small longshore current imposed at the offshore boundary. Unfortunately, no information was available to verify this. The underprediction of the longshore currents seaward of the outer nearshore bar might have also been caused by the rather abrupt transition from shoaling to breaking waves when using the model in parametric mode (single wave approach), which leads to a sudden increase of the breaker dissipation at the location where waves start to break. This results in a rather peaked longshore current distribution.

Using the model in probabilistic mode (wave-by-wave approach) might be expected to result in a more gradual distribution of the breaker dissipation and consequently a more gradual longshore current distribution. However, this would require an accurate prediction of the wave height distribution, which can only be achieved when using a varying breaker criterion. Moreover, it has been shown in Section 3.3 that the parametric and probabilistic mode produce comparable results with respect to longshore current predictions.

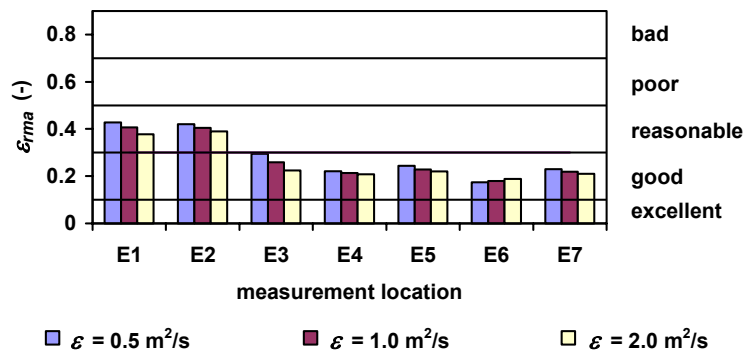


Figure 3.42. Longshore current model error statistics at Egmond showing the effect of changing the horizontal mixing coefficient ε . For measurement locations see Figure 3.33.

Thirdly, the wave front slope β was varied between 0.03 and 0.1 while other parameters were kept constant. Results are shown in Figure 3.43. For locations on the outer bar, model performance slightly improves with increasing β . Generally, best predictions for locations on the inner nearshore bar are obtained using a wave front slope of 0.06.

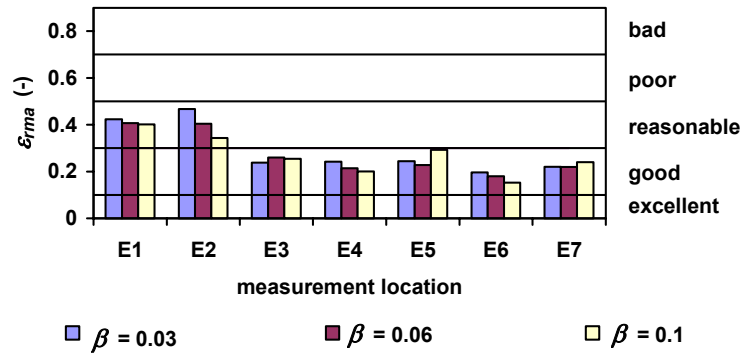


Figure 3.43. Longshore current model error statistics at Egmond showing the effect of changing the wave front slope β . For measurement locations see Figure 3.33.

3.4.4. CONCLUSIONS

The most pronounced effect on the model results is the breaker criterion γ . This parameter not only influences the wave energy dissipation in the nearshore and thus the wave height variation across the nearshore profile but also significantly affects the magnitude and distribution of the cross-shore and longshore currents. Good to excellent wave height predictions are obtained using a locally varying breaker criterion dependent on local wave steepness and local bottom slope (standard wave breaking function in the model).

Of second importance is the wave-related roughness height $k_{s,w}$ that influences the wave energy dissipation further offshore and thus the amount of wave energy that reaches the shore. This also significantly affects the cross- and longshore currents in the nearshore. Best overall agreement for waves, cross-shore currents and longshore current was obtained using a $k_{s,w}$ of about 0.02 m.

The current-related roughness height $k_{s,c}$ only affects the longshore current. Generally, best results were obtained using a $k_{s,c}$ value of 0.01 or 0.02 m.

The wave front slope β affects the cross-shore and longshore current model predictions. Increasing β from 0.03 to 0.1 generally improved both the cross-shore and longshore current predictions for locations on the seaward slope of a nearshore bar but made results worse for locations on the landward slope. Best overall agreement was obtained using $\beta = 0.06$, although cross-shore current predictions remained rather poor. A discussion on the discrepancy between measured and computed cross-shore currents is held in Section 3.3.6 of this thesis.

The horizontal mixing coefficient ε only affects the longshore current distribution across a nearshore profile. Compared to the other free model parameters, ε has a minor effect on the model results. Model predictions slightly improved when increasing ε from 0.5 to 2.0 m^2/s .

3.5. IMPORTANCE OF LOW-FREQUENCY WAVES

3.5.1. INTRODUCTION

The previous sections showed a comparison between measured and predicted wave heights, cross-shore currents, longshore currents and near-bed orbital velocities. However, in addition to the short wave motion and time-averaged currents, long wave velocity fluctuations are often found to be manifest. For example, the observed low-frequency significant wave heights in the small scale wave flume tests discussed in Section 3.3.2 ranged between 0.02 and 0.04 m. The present model neglects these long wave oscillations. To see whether this assumption is justified, the origin and magnitude of the long wave motion and the relative contribution of these oscillations to the total water motion is studied here based on small-scale wave flume tests.

3.5.2. MAGNITUDE AND ORIGIN OF LOW-FREQUENCY WAVES

The data used here are obtained from a series of small-scale laboratory measurements of surface elevation, horizontal velocity and suspended sediment concentration at a number of locations across a simulated shallow water bar built in fine sands ($D_{50} = 0.10$ mm) and subjected to irregular waves with an incident significant wave height $H_{1/3}$ of 0.19 m and a wave spectrum peak period of $T_p = 2.3$ s.

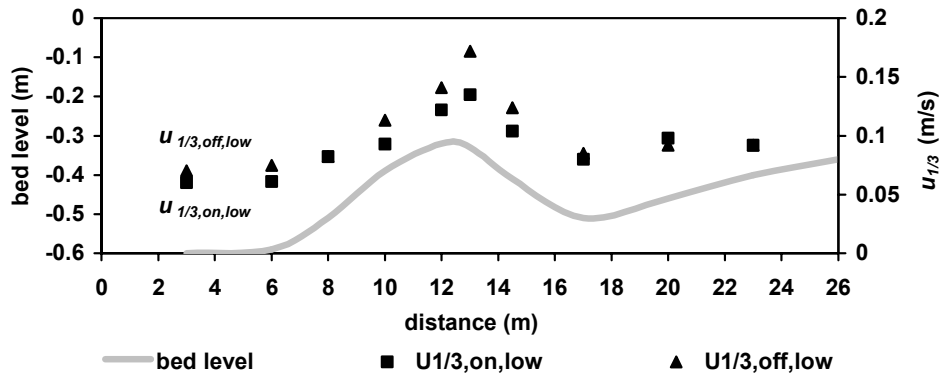


Figure 3.44. Measured onshore and offshore low-frequency near-bed peak orbital velocities. Flume test TUD B2.

Herein the measured surface elevation and velocity time series are used to demonstrate the relative importance of low-frequency oscillations across a barred profile. For this purpose, the surface elevation and velocity time series are analyzed in terms of instantaneous and time-averaged quantities. This is done by decomposing the time series as follows:

$$u = \bar{u} + \tilde{u}_{high} + \tilde{u}_{low} \quad (3.29)$$

where \bar{u} is the mean component, \tilde{u}_{high} is the high-frequency oscillatory component and \tilde{u}_{low} is the low-frequency oscillatory component. High- and low-frequency oscillations are separated (by filtering) at a period of 5 s ($\sim 2T_p$) based on spectral analysis.

Figure 3.44 shows the on- and offshore significant low-frequency orbital velocities $u_{1/3,on,low}$ and $u_{1/3,off,low}$ at different location across the bar profile. It can be observed that the long wave oscillatory velocities are largest just shoreward of the bar crest. In this region the offshore-directed long-wave peak velocities (significant value) are found to be 20% larger than the onshore-directed long-wave peak velocities.

The origin of the long-wave phenomena in the flume was analyzed using a cross-correlation technique. The cross-correlation function is a measure of the degree of linear relationship between two instantaneous signals in the time domain. For each measurement location the correlation function between the short wave energy ($\propto H^2$) and the co-located long-wave surface elevation (η_{low}) was determined, in order to differentiate between group-related long-wave components traveling shoreward, and those either reflected or generated by the wave board. The maximum time lag used is 50 seconds. Details of the computations are given by Grasmeyer and Van Rijn (1999). As an example, the cross-correlation function at a location just seaward of the bar crest ($x = 10$ m) is presented in Figure 3.45. It can be observed that a positive correlation peak occurs at a positive time lag (3 s) and a negative correlation peak occurs at a small negative time lag (1 s) as may be expected for bound long waves. The bound long wave shows the typical shallow water modification (asymmetric positive/negative form) as described by List (1992). In Figure 3.46, the negative peaks of the cross-correlation functions are presented as a function of the location in the flume. It can be observed that the bound long wave correlation increases slightly when moving from seawards towards the bar crest and decreases significantly when moving from the bar crest further shorewards.

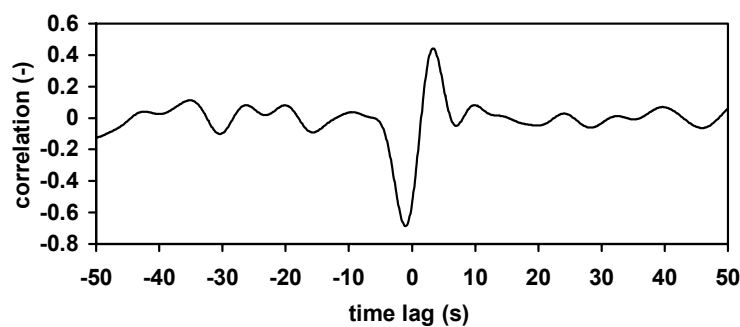


Figure 3.45. Correlation function between short wave energy H^2 and co-located long-wave surface elevation η_{low} at $x = 10$ m (for location see Figure 3.44).

The decrease in the negative correlation peak shoreward of the bar crest may be due to a decrease in the amplitude of the bound long wave, but may also have other explanations. Small cross-correlations between short-wave energy and long-wave surface elevation may well be due to long-wave effects from such sources other than the bound long wave mechanism, thus decreasing the coherence. Such effects include long waves generated by the wave board because of first order wave generation, long waves

generated by the temporal and spatial shifts of the break point on the time scale of wave groups (break-point-forced long waves), (standing-) long waves caused by reflection against the end of the flume or against the wave generator, and long period fluctuations of the undertow due to the variable breaking of short waves. Besides these effects, decreasing cross-correlations may also be due to the release of the bound long wave from the wave groups during the breaking of short waves, or to the interaction of short waves with long-wave depth or current modulations. The latter effect is expected to occur only in very shallow water being of the same order of magnitude as the long-wave height.

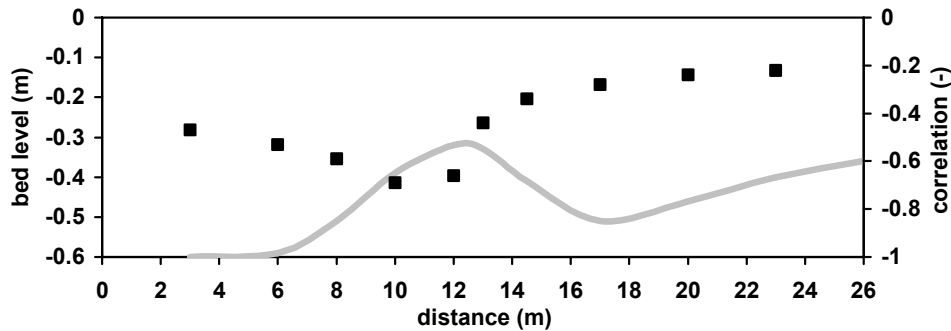


Figure 3.46. Minimum cross-correlation values across the bar profile

Because of first order wave generation, the wave paddle generated a secondary free long wave, initially 180° out of phase with the bound long wave. In principle, the incident long wave behaves as a linear superposition of the two. However, this free long wave is expected to be of secondary importance in these experiments, since the growth of the bound long wave due to short wave shoaling is expected to exceed the growth of the free long wave due to shoaling (Roelvink and Stive, 1989; Dally, 1987). Moreover, a significant correlation peak with increasing positive time lag between the wave group and the free long wave (traveling with a speed of $(gh)^{1/2}$) was not observed in the present cross-correlation functions, also suggesting that the free long wave generated by the wave board is of minor importance.

The presence of break-point-forced long waves and reflected long waves in the flume was examined by splitting the long-wave signal into an onshore- and an offshore-propagating signal (Guza et al., 1984; Ruessink, 1995) in order to discriminate between ingoing (bound) long waves and the outgoing long waves. In the measurement sections seaward of the bar crest a negative peak occurred in the cross-correlation function between H^2 and the offshore propagating long wave. An example of such a cross-correlation function for a measurement location just seaward of the bar crest ($x = 10$ m) is presented in Figure 3.47. The observed and calculated time lag between the wave group and the long wave trough appeared to agree reasonably well when assuming that the offshore propagating long wave trough originates from a bound long wave (traveling with c_g) that is reflected by the nearshore bar and travels seaward as a free long wave (traveling with $(gh)^{1/2}$). The difference between the calculated and the observed time lags was found to be less than 8%. The offshore propagating long wave trough in Figure 3.47 might also be related to a break-point-forced long wave. It is however difficult to

predict exactly how a break-point forced long wave affects the cross-correlations (List, 1987).

The presence of reflected long waves will have its effect on the (direction of) low-frequency wave-related transport rate because a long wave trough propagating in the offshore direction is related to an onshore directed long wave particle velocity. Reflection against the wave paddle was prevented by active wave absorption.

The cross-correlations shoreward of the nearshore bar show no clear evidence for the presence of reflected long waves. However, standing-long waves, caused by reflection against the end of the flume, may not be identified by significant peaks in the cross-correlation function. In order to examine the presence of standing long waves in the flume, coherence and phase spectra between the different locations shoreward of the bar crest were analyzed. Increasing phase with frequency was found, indicating the presence of a propagating (non-standing) long wave, with a squared coherence well above the 95% confidence level. Apparently long waves were damped sufficiently by the wave damper at the end of the flume.

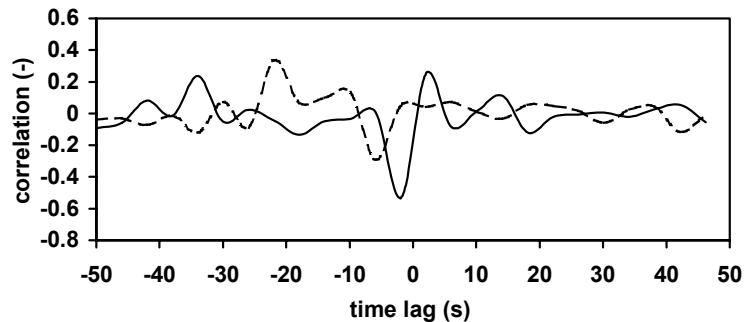


Figure 3.47. Cross-correlation between H^2 and onshore, respectively offshore propagating long wave at $x = 10$ m. For location see Figure 3.44.

Various studies indicate that bound long waves are released from the wave groups in the outer surf zone and travel shoreward as free long waves (List, 1987; Ruessink, 1995). Decreasing cross-correlations, as shown in Figure 3.46, may be due to this release of the bound long wave from the wave groups during the breaking of short waves near the bar crest. To test this idea, the cross-correlations between short wave energy in a measurement section seaward of the bar ($x = 10$ m) and the long-wave surface elevation in the sections shoreward of the bar ($x = 14.5$ m, 17 m, 20 m) were determined. The data (not presented here) show the same trend as in Figure 3.46. However, the negative cross-correlation peaks were found to be 40% to 50% larger than the negative peaks of the co-located cross-correlation functions, which indicates that the long-wave surface elevation in the measuring sections shoreward of the bar are more strongly correlated to the wave groups seaward of the bar than to the co-located wave groups. This suggests that near the bar crest the bound long wave is being released from the wave groups. However, the propagation time between the various measurement locations was best predicted using the group velocity c_g at which the bound long waves travel, while free long waves travel at $(gh)^{1/2}$. At locations shoreward of the bar trough, the long wave appeared to precede the wave group only very slightly. No clear evidence for a bound

long wave being fully released as a free long wave was found. These findings suggest a transition zone in which the bound long wave is being released as a free long wave. In case of shoaling non-breaking waves the bound long wave probably dominates the long wave motion. In the case of increasingly breaking waves, the bound long wave is gradually being released as a free long wave, but is still correlated with the wave groups outside the surf zone. In this transition zone the long wave travels at bound long wave speed as long as wave grouping remains. In the zone of saturated breaking, where waves are poorly grouped, the bound long wave is fully released, traveling at $(gh)^{1/2}$.

3.5.3. CONCLUSIONS

Relatively large low-frequency velocity oscillations were found to be manifest in a small-scale wave flume at measurement sections just shoreward of the bar crest. These long-wave phenomena could not be explained satisfactorily by the presence of bound long waves, break point related long waves or free long waves. The data used here suggest that in the measurement sections just shoreward of the bar crest, where the fraction of breaking waves is relatively large, low-frequency velocity oscillations are induced by long period fluctuations of the undertow (pulsating return flow), in addition to the bound long-wave effect. The pulsating undertow is likely to be driven by measured set-down fluctuations across the bar profile (low-frequency variation in water level gradient).

Significant low-frequency oscillations were also found to be manifest at the field site of Egmond aan Zee (Van Rijn et al., 2002a). The relative wave height $H_{1/3}/h$ of the low-frequency waves (periods longer than 20 s) was between 0.1 and 0.15 at the seaward flank of the bars and between 0.2 and 0.35 on the crest and the shoreward flank of the inner nearshore bar. These relatively high values occurred during low tide and were considerably smaller during high tide.

The processes described in this section are not incorporated in the present cross-shore profile model. Modelling of long-wave effects is still at an early stage. Roelvink (1993) developed a predictive model describing the propagation of normally incident short wave trains and their associated long-wave motion (see also Roelvink and Stive, 1989; Nairn et al., 1990). Shin-ichi Aoki and Yasumi Yamamura (2000) developed a method to estimate the bound long-wave component in irregular wave trains with directional spreading. Further study is required.

3.6. DISCUSSION AND CONCLUSIONS

In this chapter the hydrodynamic module of the cross-shore profile model has been presented including an evaluation of the predicted wave heights and currents using the model in probabilistic (multi-wave) and parametric (single-wave) mode. Wave heights H_{rms} were predicted more accurately using the model in parametric mode. The present probabilistic approach was not able to reproduce wave height distributions measured under small-scale laboratory and large-scale field experiments. Better agreement was obtained using a probabilistic breaker criterion similar to the approach of Dally (1992). However, the variable breaker criterion only served to reduce the magnitude in the peak

of the wave height distribution and had a negligible effect on the wave statistics. Moreover, the probabilistic breaker criterion increased the computation time of the model with a factor 5, which makes this approach rather unsuitable for long-term (months to years) morphodynamic computations. What is more, the present data suggest that the wave height distribution can very reasonably be approximated with a Rayleigh distribution, which is represented by a single wave height H_{rms} and period T_p .

At present, the lack of knowledge on the breaking process of individual waves makes it difficult to provide an accurate description of the wave height distribution in the nearshore. Moreover, based on the present results it may be concluded that, as regards the other hydrodynamic parameters, there is no advantage of a multi-wave approach above a single-wave approach. Waves and currents in the nearshore were predicted with at least the same accuracy. Differences were generally less than 10%. A major advantage of the single-wave approach is the relatively small computation time.

Low-frequency oscillations are neglected in the present cross-shore model. Small-scale laboratory experiments were used to verify whether this assumption is justified. Relatively large low-frequency oscillatory velocities were found just shoreward of the bar crest where the fraction of breaking wave was relatively large. This could not satisfactorily be explained by the presence of bound long waves, break point related long waves or free long waves. Low-frequency velocity oscillations appeared to be induced by long period fluctuations of the undertow (pulsating return flow), in addition to a bound long-wave effect. The pulsating undertow is likely to be driven by measured set-down fluctuations across a barred profile (low-frequency variation in water level gradient). These processes are not included in the model.

The model was applied in parametric mode to predict wave heights and currents near the coast of Egmond aan Zee in the Netherlands. The aim of this evaluation was to verify the model concepts, clarify the processes incorporated, to reveal the sensitivities of the model and determine the model performance in a quantitative manner.

The predicted wave heights were most sensitive to the breaker criterion applied. Excellent agreement between measured and predicted H_{rms} wave heights was found using a breaker criterion depending on the ratio of the bed slope and the wave steepness.

Predicted longshore current showed reasonable to good agreement with the measurements. The longshore currents were not much influenced by input parameters. It was found necessary to use a relatively large horizontal mixing coefficient ($\varepsilon = 2.0 \text{ m}^2/\text{s}$) to reproduce current profiles as measured in the field. The optimum cross-shore constant value for the mixing coefficient was approximately the same for two contrasting field sites. Although this mixing coefficient is physically realistic, it is large compared with the parameterization of Özkan-Haller and Kirby (1999), which for field conditions used here yielded a range of cross-shore averaged mixing coefficient between 0.1-0.9 m^2/s . The necessity for the large mixing coefficient may be related to factors not included in the model.

One of these factors might be a roller dissipation rate that varies across the bar profile. The roller dissipation rate depends on the advection length of the roller, which decreases with decreasing wave front slope β and increasing wave phase speed c . The wave front

slope is usually assumed to be 0.1 or less. In the present model best results were obtained using a cross-shore averaged β value of 0.06 and 0.1 for the parametric and probabilistic mode, respectively. Walstra et al. (1994) found that the β factor is not constant across a nearshore profile. They suggested an expression in which this factor depends on the wave height H , the water depth h and the wave number k . However, the roller effect occurs only in case of wave breaking whereas the larger current velocities are needed in a region (seaward of outer bar crest) where waves were observed to be non-breaking under the conditions used here. A wave front slope varying across the nearshore profile is therefore not expected to be the solution for an accurate prediction of the longshore current velocities seaward of the outer nearshore bar.

A possible resolution of the discrepancies found between measured and computed longshore currents on the outer nearshore bar may also lie in the presence of shear waves with increasing cross-shore length scales from the shoreline seaward. This is supported by the assumption of a horizontal mixing coefficient that increases with distance from the shoreline as suggested by Longuet-Higgins (1970):

$$\varepsilon_0 = Nx\sqrt{gh} \quad (3.30)$$

where N denotes a non dimensional parameter with a typical approximation of about 0.016 (Greenwood and Sherman, 1986), x is the distance from the shoreline [m], g is acceleration of gravity [m/s^2] and h is the water depth [m]. This relationship predicts ε_0 as equal to about $55 \text{ m}^2/\text{s}$ at locations seaward of the outer bar with a water depth of 5 m. This value is close to the one determined by Greenwood and Sherman (1986) based on field experiments on a barred beach, but significantly larger than according to the parameterization of Özkan-Haller and Kirby (1999). It is yet unclear whether these large mixing values are physically justifiable. Equation (3.30) is an approximation of the eddy viscosity, which is described as:

$$\varepsilon_0 = l^2 \frac{\delta v}{\delta x} \quad (3.31)$$

in which v is the longshore current velocity [m/s] and l denotes a mixing length [m]. Using (3.31) with a mixing coefficient of $55 \text{ m}^2/\text{s}$ typical length scales would become in the order of 100 m at locations seaward of the outer bar. The presence of shear waves may be a cause for these large mixing lengths. Indicative computations (results not shown) with the present model revealed a horizontal mixing coefficient of $55 \text{ m}^2/\text{s}$ to be somewhat too large. A mixing coefficient of about $10 \text{ m}^2/\text{s}$, with length scales in the order of tens of meters, gave good estimates ($\varepsilon_{rma} < 0.3$) of the time-averaged longshore velocities on the outer nearshore bar and on the seaward slope of the inner nearshore bar. Further study is necessary.

Although comparison with large-scale laboratory data was good, the modelled cross-shore currents in the field near Egmond aan Zee showed rather poor agreement with the measurements. The predicted undertow velocities were affected by the wave front slope β , especially at locations on the inner nearshore bar crest. As with the longshore currents, predictions might improve using a wave front slope depending on the wave conditions. Furthermore, horizontal cross-shore mixing generated inside the surf zone is

not explicitly considered in the present model. Including this might improve the predictions, which seems to be supported by comparisons with small-scale laboratory data in which the measured time- and depth-averaged cross-shore velocity distribution was found to be somewhat broader than the predicted one. Another way of improving the predictive capability of the current model is to adapt parameters in the wave model. A larger wave energy dissipation rate shoreward of the nearshore bars would produce a steeper decay in wave height, which would give slightly better agreement with the wave heights measured in the field and would move the body of the current profile shoreward accordingly (Figure 3.48). This might be achieved by adapting the breaker criterion.

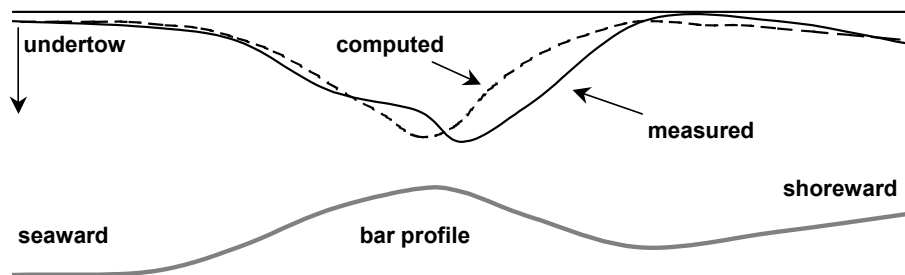


Figure 3.48. Principle sketch of measured and computed undertow velocities. The measurements generally reveal a shoreward shift of the body of the current profile that is not modelled.

Battjes and Stive (1985) assumed the breaker criterion to be cross-shore constant and only weakly dependent on the deep-water wave steepness. Wave height predictions using this breaker criterion are generally in good agreement with observations on planar beaches. However, agreement on barred beaches is usually less fair (e.g. Ruessink et al., 2001). Various approaches to remedy the model overprediction shoreward of a nearshore bar have been proposed of which that proposed by Southgate and Wallace (1994) seems the most physically realistic. They separated the fraction of breaking waves in a fraction of newly breaking waves and a fraction of breaking waves that persisted from seaward locations. The cross-shore length that a newly breaking wave was allowed to persist, referred to as the persistence length l_p , was assumed to be proportional to the breaker height H_b . Depending on the value of proportionality b between l_p and H_b , breaking wave persistence may vary from persistence across the entire trough ($b = \infty$) to no persistence ($b = 0$). Various tests against single bar, large-scale laboratory data showed improved predictions of the fraction of breaking waves shoreward of the bar crest using $b = 38$. In multiple bar systems the Southgate and Wallace (1994) approach will lead to a stronger wave height decay in the most seaward trough of the outer nearshore bar than in the more shoreward trough of an inner nearshore bar because of the increase of l_p with H_b , and thus h . This is in contrast with observations that wave height predictions in especially inner nearshore zones need to be improved.

Roelvink et al. (1995) introduced the concept of breaker delay, which is based on the assumption that waves need a distance in the order of one wavelength to actually start or stop breaking. They suggest taking into account the water depth some distance seaward

of the computational point when determining the water depth to be applied in the breaker criterion. To that end they define a reference depth, obtained from weighting water depths seaward of the computational point via a weighting function. This approach has the effect of shifting the wave height decay by breaking and thus the body of the current profile shoreward.

In the present model the breaker criterion depends on the ratio of local bottom slope and local wave steepness (Figure 3.1) and is therefore not constant across the nearshore profile. Waves break more easily on the shoreward slope of a bar than on the seaward slope. This approach has more or less the same effect as the breaking wave persistence approach of Southgate and Wallace (1994) or the breaker delay approach of Roelvink et al. (1995). However, it also shows the same discrepancy with observations in multiple bar systems as the Southgate and Wallace (1994) approach, though with a different cause. In the present model, the breaker criterion is smaller (waves break more easily) on the outer nearshore bar than on the inner nearshore bar because of the larger wave steepness H/L in the outer nearshore zone, whereas in the Southgate and Wallace (1994) approach this is caused by larger water depth h in the outer nearshore zone.

Generally it may be concluded that a cross-shore varying breaker criterion is needed to obtain accurate wave height and current predictions. Observations suggest that the breaker criterion is smaller on an inner nearshore bar than on an outer nearshore bar in a multiple bar system. A breaker criterion that increases with decreasing wave steepness and/or water depth as in the present approach or that of Southgate and Wallace (1994) are therefore contradictory to observations. Better agreement between measured and predicted wave heights variations across a multiple bar system might be obtained using a breaker criterion that varies with the h/L ratio, for example.

However, this does not seem to be the most important reason for a bad prediction of the undertow. The present results suggest that the roller delays the maximum undertow velocity insufficiently, even with a rather small wave front slope. The measured maximum undertow velocities are located more shoreward than those computed with the model.

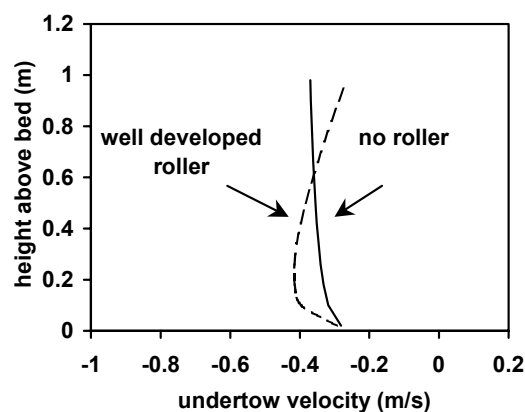


Figure 3.49. Roller effect on vertical structure of undertow velocities

Most important reason for the overestimation of the undertow velocities on the seaward flank and near the crest of a nearshore bar is likely to be the use of linear wave theory to

compute the mean mass transport associated with the organized wave motion, i.e. Stokes drift. Dally and Brown (1995) have shown that the use of stream function wave theory leads to more accurate predictions of the undertow velocities compared to linear wave theory.

Another cause for the discrepancies between measured and computed undertow velocities under field conditions is that currents measured in the field were defined at about 0.5 m above the bed (depth-averaged values were used from the lab data), whereas the computed values represent the depth-averaged currents. The presence of a surface roller influences the vertical profile significantly (Figure 3.49). No roller is present at the onset of breaking, which results in a rather uniform velocity profile. A fully developed surface roller causes an onshore-directed shear stress on the water column at the wave trough level. This leads to a decrease of the offshore-directed velocities in the upper part of the velocity profile and mass balance results in an increase of the velocities in the lower part of the profile under these conditions. In the field, the velocities were measured in this lower part of the profile. Assuming these to be the depth-averaged velocity exaggerates the roller effect. The velocities measured in the field at 0.5 above the bed are therefore larger than the actual depth-averaged velocity, which leads to larger discrepancies with the model predictions. Under breaking waves, the difference between the velocity measured at a single height and the depth-averaged value may reach a factor 2; see e.g. Houwman (2000).

In addition, observations may depart from the computations because of the presence of 3-dimensional circulations. Needless to say, the predictive performance of the present 2D model is poor for cases where 3D circulations are important.

The rather poor model performance with respect to the prediction of the cross-shore mean currents is not specific for the present model. Within the EU-COAST3D project, five process-based cross-shore models, including the present one, were tested against the Egmond aan Zee field data set. All five models showed a poor performance in predicting the undertow velocities (Van Rijn et al., 2002b).

An important process not included in the present model is the hydrodynamics of the swash zone. Further experimental and theoretical investigations on this subject are desirable.

This chapter was concerned with the hydrodynamic module of a cross-shore process-based profile model. In the next chapter the sediment transport module will be described and evaluated. Chapter 5 compares measured and computed profile changes on the time scale of storms (days to weeks) and seasons (weeks to months).

4. MODELLING OF SEDIMENT TRANSPORT IN THE NEARSHORE

4.1. INTRODUCTION

This chapter represents the second of three chapters describing a process-based cross-shore profile model. The hydrodynamic module hereof was described and evaluated in the previous chapter. In this chapter the sediment transport module is presented. The described transport rates are directly relevant for the modelling of morphological changes, which will be discussed in Chapter 5. In this chapter, a comparison is made between measured and predicted sediment transport rates. The predicted transport rates are based on a single representative wave. The basic data of the measurements are given in Chapter 2. Specific questions that will be addressed are:

- Can the nearshore sediment transport rate be predicted with a relatively simple engineering approach based on a single-wave approach or is a multi-wave approach required?
- What is the relative contribution of the wave-related (high- and low-frequency) and current-related suspended transport component to the net suspended transport rate?
- What is the relative contribution of the bed-load and suspended load component to the total depth-integrated transport rate?
- What are the key parameters in the prediction of suspended sediment concentrations and current- and wave-related suspended sediment transport rates?
- Is it for morphodynamic purposes acceptable to ignore the long-wave component of the sediment fluxes?

In this chapter, first a description of the transport model is given. Bed forms have a profound effect on the transport of suspended sediment. Therefore, bed form measurements obtained from the field measurements near the coast of Egmond aan Zee are used to evaluate the applicability of various bed-roughness predictors (Section 4.3). Modelling of the current-related, the wave-related and the bed-load transport components is then treated in Sections 4.4, 4.5 and 4.6, respectively. The relative contribution of the various transport components is discussed in Section 4.7. Discussion and conclusions are given in Section 4.8. Part of the work presented in this chapter has been published in Grasmeijer and Van Rijn (2001).

4.2. DESCRIPTION OF TRANSPORT MODEL

4.2.1. INTRODUCTION

The net total sediment transport is obtained as the sum of the net bed load (q_b) and net suspended load (q_s) transport rates. The bed-load transport is defined as the transport of sand particles in the wave boundary layer in close contact with the seabed. The suspended load transport is the transport of sand particles above the bed-load layer up to the water surface.

The definition of bed load is not universally agreed upon. For example, sheet flow may be considered as a type of bed-load transport but it may also be seen as near-bed suspended load transport. Some researchers regard bed-load transport as occurring in the region where grain-grain interactions are important and grains are not supported purely by the fluid forces. For practical reasons, the bed-load transport is herein regarded as the transport rate below the lowest measurement point, which is about 0.02 m above the sand bed for the experimental data used here.

4.2.2. SUSPENDED LOAD TRANSPORT

In the present model, the net suspended load transport (q_s) is obtained as the sum of the current-related ($q_{s,c}$) and the wave-related ($q_{s,w}$) suspended transport components.

Current-related suspended load transport

The time-averaged current-related suspended load transport ($q_{s,c}$) is defined as the transport of sediment particles by the time-averaged current velocities:

$$q_{s,c} = \rho_s \int_{z_a}^h cu \, dz \quad (4.1)$$

where ρ_s is the sediment density [kg/m^3], c is the time-averaged concentration [m^3/m^3], u is the time-averaged current velocity [m/s], z is the height above the bed [m], z_a = reference height [m], h = water depth [m].

The time-averaged concentration profile is computed from the standard convection-diffusion equation according to:

$$w_s c(z) + \varepsilon_s(z) \frac{dc(z)}{dz} = 0 \quad (4.2)$$

where w_s is the sediment fall velocity [m/s], ε_s = sediment mixing coefficient [m^2/s].

The sediment-mixing coefficient is computed as (Van Rijn, 1993):

$$\varepsilon_s(z) = \sqrt{\varepsilon_{s,c}^2 + \varepsilon_{s,w}^2} \quad (4.3)$$

The current-related mixing ($\varepsilon_{s,c}$) is derived from the standard expressions for turbulent flow but also depends on the fall velocity of the suspended sediment (Van Rijn, 1993):

$$\begin{aligned} \varepsilon_{s,c} &= \kappa \beta u_* z \left(1 - \frac{z}{h}\right) \quad \text{for } 0 < z < 0.5 h \\ \varepsilon_{s,c} &= 0.25 \kappa u_* h \beta \quad \text{for } z \geq 0.5 h \end{aligned} \quad (4.4)$$

with

$$\beta = 1 + 2 \left(\frac{w_s}{u_*} \right)^2 \quad (4.5)$$

$$u_* = \frac{\sqrt{g}}{C} v_r \quad (4.6)$$

$$C = 18 \log \frac{12h}{k_{s,c}} \quad (4.7)$$

where z is the height above the bed [m], h is the water depth [m], κ is the Von Karman constant ($= 0.4$) [-], v_r is the time- and depth-averaged velocity vector resulting from current and wave action [m/s], $k_{s,c}$ is the current-related roughness height [m].

The wave-related mixing ($\varepsilon_{s,w}$) is described by an empirical expression based on data analysis (Van Rijn, 2000).

$$\varepsilon_{s,w} = \varepsilon_{b,w} + (\varepsilon_{\max,w} - \varepsilon_{b,w}) \left(\frac{z - d_s}{0.5h - d_s} \right) \quad \text{for } d_s < z < 0.5 h \quad (4.8)$$

$$\varepsilon_{s,w} = \varepsilon_{\max,w} \quad \text{for } z > 0.5 h$$

with

$$\varepsilon_{\max,w} = 0.035 \gamma_{br} h \frac{H_{1/3}}{T_p} \quad \text{and} \quad \varepsilon_{b,w} \leq \varepsilon_{\max,w} \leq 0.05 \text{ m}^2/\text{s} \quad (4.9)$$

$$\gamma_{br} = 1 + \sqrt{\frac{H_{1/3}}{h} - 0.4} \quad \text{for } \frac{H_{1/3}}{h} > 0.4 \quad (4.10)$$

$$\gamma_{br} = 1 \quad \text{for } \frac{H_{1/3}}{h} < 0.4$$

$$\begin{aligned} d_s &= 10 \gamma_{br} k_{s,w} & \text{for } 5 \gamma_{br} \delta_w > 10 k_{s,w} \\ d_s &= 5 \gamma_{br} \delta_w & \text{for } 5 \gamma_{br} \delta_w < 10 k_{s,w} \end{aligned} \quad (4.11)$$

where $H_{1/3}$ is the significant wave height [m], T_p is the wave spectrum peak period [s], δ_w is the wave boundary layer thickness [m], $k_{s,w}$ is the wave-related roughness height [m], $u_{b,w}$ is the mean of on- and offshore peak near-bed orbital velocity, $(u_{1/3,on} + u_{1/3,off})/2$ [m/s].

The wave-related sediment mixing near the bed ($\varepsilon_{b,w}$) depends on the near bed orbital velocity ($u_{b,w}$), the bed roughness, and is related to the height of breaking waves:

$$\varepsilon_{b,w} = 0.018 \beta_w d_s u_{b,w} \quad (4.12)$$

with

$$\beta_w = 1 + 2 \left(\frac{w_s}{u_{*w}} \right)^2 \quad (4.13)$$

$$u_{*w} = \sqrt{\frac{\tau_w}{\rho_w}} \quad (4.14)$$

where ρ_w is the density of water [kg/m³], τ_w is the wave-related bed shear stress [N/m²]. The near-bed reference concentration c_a is computed as (Van Rijn, 2000):

$$c_a = 0.015 \frac{D_{50}}{z_a} \frac{T_a^{1.5}}{D_*^{0.3}} \quad (4.15)$$

with

$$T_a = \frac{\tau_{cw} - \tau_{cr}}{\tau_{cr}} \quad \text{for } \tau_{cw} \geq \tau_{cr} \quad (4.16)$$

$$T_a = 0 \quad \text{for } \tau_{cw} < \tau_{cr}$$

$$D_* = D_{50} \left(\frac{(s-1)g}{\nu^2} \right)^{1/3} \quad (4.17)$$

where c_a is the time-averaged near-bed reference concentration [m³/m³], D_{50} is the median grain diameter [m], T_a is the time-averaged nondimensional bed shear stress due to currents and waves [-], D_* is a nondimensional particle parameter [-], z_a is the reference height above the bed [m], τ_{cw} is the time-averaged combined current- and wave-related bed shear stress [N/m²], τ_{cr} is the time-averaged critical bed shear stress [N/m²], s is the relative sediment density ($= \rho_s/\rho_w$) [-], g is the acceleration of gravity [m/s²], ν is the kinematic viscosity [m²/s].

The time-averaged combined current- and wave-related bed shear stress τ_{cw} is computed following Van Rijn (1993). The time-averaged critical shear stress τ_{cr} is computed as:

$$\tau_{cr} = (\rho_s - \rho) g D_{50} \theta_{cr} \quad (4.18)$$

where θ_{cr} is computed according to the classical Shields curve (Van Rijn, 1993).

Wave-related suspended load transport

The time-averaged wave-related suspended sediment transport ($q_{s,w}$) is defined as the transport of sediment particles by the oscillating velocity components. In the present model this transport component is based on a formulation by Houwman and Ruessink (1996). The formulation is derived from the velocity moments approach of Bailard (1981).

$$q_{s,w} = k_{as} \rho_s \frac{u_{on}^4 - u_{off}^4}{u_{on}^3 + u_{off}^3} \int_{z_a}^h c \, dz \quad (4.19)$$

where z_a is the reference height above the bed [m], k_{as} is an efficiency factor [-], u_{on} is the peak onshore orbital velocity [m/s], u_{off} is the peak offshore orbital velocity [m/s].

The efficiency factor k_{as} is a free adjustable parameter in the model. Theoretically this parameter has an upper limit of 0.44 (Grasmeijer et al., 1999).

The sand transport model can be used in the single fraction mode as well in the multi-fraction mode. The computations in this thesis are based on a single representative particle diameter (D_{50}).

4.2.3. BED-LOAD TRANSPORT

In the present model, the net bed-load transport rate is obtained by time averaging (over the wave period) of the instantaneous transport rate using (Van Rijn, 2000):

$$q_b(t) = 0.5 \frac{\beta_s D_{50} \rho_s u_* T(t)}{D_*^{0.3}} \quad (4.20)$$

where β_s is a slope factor, D_{50} is the median grain diameter of the sediment [m], ρ_s is the sediment density [kg/m^3], u_* is the bed shear velocity based on the near-bed velocity vector [m/s], $T(t)$ is the nondimensional instantaneous bed shear stress [-] and D_* is a nondimensional particle parameter according to Equation (4.17) [-].

In case of a sloping bed the transport induced by gravity has to be taken into account when the grains have been set in motion. For this reason the Bagnold parameter β_s is introduced which increases the transport rates in case of downslope transport and decreases the transport in case of upslope transport:

$$\beta_s = \left(1 + \frac{\frac{dz_b}{ds}}{\tan \varphi} \right) = \frac{\tan \varphi}{\tan \varphi + \frac{dz_b}{ds}} \quad (4.21)$$

where

$$\frac{dz_b}{ds} = \frac{u_{bx}}{|u_b|} \frac{dz_{bx}}{dx} \quad (4.22)$$

and φ the angle of repose.

4.2.4. BED SHEAR STRESS FORMULATIONS

The bed shear stress formulations are given here to be complete.

Wave-related bed shear stress

The time-averaged wave-related bed shear stress can be written as:

$$\tau_w = 0.25 \rho f_w u_{b,w}^2 \quad (4.23)$$

with:

$$f_w = \exp \left(-6 + 5.2 \left(\frac{A_{b,w}}{k_{s,w}} \right)^{-0.19} \right) \quad (4.24)$$

$$f_{w,\max} = 0.3$$

where $A_{b,w}$ is the near-bed orbital excursion, and $k_{s,w}$ is the wave-related roughness height, which is a user defined value between about 0.01 and 0.04 m.

Current-related bed shear stress

The time-averaged current-related bed shear stress is modelled as

$$\tau_c = 0.125\alpha_r\rho f_c v_r^2 \quad (4.25)$$

with

$$f_c = 0.24 \left[\log \left(\frac{12h}{k_{s,c}} \right) \right]^{-2} \quad (4.26)$$

$$\alpha_r = \frac{\left[\ln \left(\frac{30\delta}{k_a} \right) \right]^2}{\left[\ln \left(\frac{30\delta}{k_{s,c}} \right) \right]^2} \frac{\left[-1 + \ln \left(\frac{30h}{k_{s,c}} \right) \right]^2}{\left[-1 + \ln \left(\frac{30h}{k_a} \right) \right]^2} \quad (4.27)$$

where δ is the wave-boundary layer thickness defined as $0.072A_{b,w}(A_{b,w}/k_{s,w})^{-0.25}$, $k_{s,c}$ is the current-related roughness height, which is a user defined value between about 0.01 and 0.04 m, and k_a is the apparent roughness, which is computed using the following relationship (Van Rijn, 1993):

$$\frac{k_a}{k_{s,c}} = \exp \left(\gamma \frac{u_{b,w}}{v_r} \right) \quad (4.28)$$

with

$$\left(\frac{u_{b,w}}{v_r} \right)_{\max} = 5$$

$$k_{a,\max} = 10k_{s,c}$$

where $u_{b,w}$ is the near-bed orbital velocity (mean of $u_{1/3,on}$ and $u_{1/3,off}$). The coefficient γ depends on the wave-current angle α (rad) and is given by (Van Rijn, 1993):

$$\gamma = 0.8 + \alpha - 0.3\alpha^2 \quad (4.29)$$

Combined current- and wave-related bed shear stress for suspended load

The current- and wave-related bed shear stresses are total shear stresses. However, in the presence of waves, the total shear stresses are not fully effective in transporting

sediment (e.g. Nielsen, 1992). Therefore, they have to be multiplied by efficiency factors to obtain the effective bed shear stress.

The efficiency factor for waves μ_w is likely to depend on the bed roughness but the functional relationship is not yet known. Van Rijn (2000) used the μ_w factor as a calibration parameter for the near-bed concentrations. Based on analysis of experimental data, Van Rijn (2000) suggests the following relationship:

$$\mu_w = 0.125 \left(1.5 - \frac{H_{1/3}}{h} \right)^2 \quad (4.30)$$

The efficiency factor for currents is given by (Van Rijn, 1993):

$$\mu_c = \frac{f'_c}{f_c} \quad (4.31)$$

with

$$f'_c = 0.24 \log \left(\frac{12h}{3D_{90}} \right)^{-2} \quad (4.32)$$

and f_c as given by Equation (4.26).

The time-averaged bed shear stress under currents and waves combined τ_{cw} now becomes:

$$\tau_{cw} = \mu_c \tau_c + \mu_w \tau_w \quad (4.33)$$

and the time-averaged nondimensional bed shear stress is:

$$T_a = \frac{\tau_{cw} - \tau_{cr}}{\tau_{cr}} \quad \text{for } \tau_{cw} \geq \tau_{cr} \quad (4.34)$$

$$T_a = 0 \quad \text{for } \tau_{cw} < \tau_{cr}$$

Combined current- and wave-related bed shear stress for bed load

The combined current- and wave-related bed shear stress for bed load yields (Van Rijn, 1993):

$$\tau_{b,cw}(t) = 0.5 \rho f'_{cw} |u_{r,\delta}| u_{r,\delta} \quad (4.35)$$

with

$$f'_{cw} = \alpha \beta f'_c + (1 - \alpha) f'_w \quad (4.36)$$

$$\alpha = \frac{v_{r,\delta}}{v_{r,\delta} + u_{w,\delta}} \quad (4.37)$$

$$\beta = 0.25 \left(\frac{-1 + \ln\left(\frac{30h}{k_{s,c}}\right)}{\ln\left(\frac{30\delta}{k_{s,c}}\right)} \right)^2 \quad (4.38)$$

$$f'_w = \exp\left(-6 + 5.2 \left(\frac{A_{b,w}}{3D_{90}}\right)^{-0.19}\right) \quad (4.39)$$

where $v_{r,\delta}$ is the mean near-bed velocity in the main current direction at the top of the wave boundary layer, $u_{w,\delta}$ is the peak near-bed orbital velocity without mean current and $u_{r,\delta}$ is the resulting instantaneous velocity vector.

The nondimensional bed shear stress for the bed-load transport then becomes:

$$T(t) = \frac{\tau_{b,cw}(t) - \tau_{cr}}{\tau_{cr}} \quad (4.40)$$

4.3. MODELLING THE BED ROUGHNESS

4.3.1. INTRODUCTION

In the previous section the sediment transport model was described. There is however one parameter that needs to be specified before the model can be applied to field conditions namely the bed roughness. The bed roughness can be described by a single roughness scale k_s , in which the ripple roughness is an important component. The use of this roughness length is analogous to the Nikuradse (1933) equivalent sand grain roughness. Whereas Nikuradse's sand grain roughness is a constant for a given grain diameter, k_s may vary as a function of the skin friction in the flow. Various models have been derived to predict ripple roughness for wave or combined flows (Nielsen, 1992; Grant and Madsen, 1982). However, these models are mostly based on laboratory data and are derived for waves only. They have not been tested adequately against field data under combined wave and current conditions.

In this section, ripple measurements obtained from the field experiments near Egmond aan Zee are used to evaluate the applicability of three ripple predictors to combined wave and current field conditions. The model described in Section 4.2 is then used to calculate the suspended sediment concentrations and transport rates under variable wave-current conditions. Correlations between the flow dynamical parameters and the computed sediment parameters are then analyzed to understand the bed-form response to the change of wave-current dynamics and how the bed-form controls the suspended sediment concentration profiles and transport rates.

4.3.2. PRINCIPLES OF BED ROUGHNESS

When waves and currents exert force on a movable bed, ripples start to form as the friction of the seabed exceeds the threshold value for sediment movement. As waves and currents become stronger, ripples go through two distinct stages (Grant and Madsen, 1982). The first stage is known as the equilibrium range, in which flow is relatively slow and sediment transport is low. Both ripple height η and ripple length λ tend to increase until ripple steepness and ripple roughness reach their maximum. Within this equilibrium range, the length of the ripples scales with the near-bed wave orbital diameter A (orbital ripples). As flow increases, ripples enter the second stage defined as the break-off range. When this break-off range is reached, ripple height will decrease while ripple length stays roughly constant or decreases slightly. This will lead to a decrease in ripple steepness and ripple roughness, and also to a de-correlation between wave orbital diameter and ripple length (anorbital ripples). Many investigators have tried to quantitatively predict ripple height and length. The most widely used concepts are those of Nielsen (1992), Grant and Madsen (1982) and Van Rijn (1993).

Once the ripple height and ripple length are estimated, ripple roughness is here predicted as:

$$k_s = \alpha \eta \frac{\eta}{\lambda} \quad (4.41)$$

where η is the ripple height, λ the ripple length and α an empirical coefficient. The experimental values for α are 8, 20 and 27.7 according to Nielsen (1992), Van Rijn (1993) and Grant and Madsen (1982), respectively.

4.3.3. MEASURED BED ROUGHNESS

Bed forms are described and characterized most simply by their crest-to-trough height and their length between crest or troughs. Such a description is only accurate for two-dimensional bed forms with similar shapes. Real bed forms exhibit a wide variety of shapes and patterns that in some cases cannot be completely described by height and length alone. Nonetheless, it is useful to describe bed forms by their characteristic dimensions, particularly in applications that require the parameterized effect of the bed form on the suspension of sediment. Herein the bed forms are described by their height and length determined from a cross-shore profile of the seabed measured with a Sand Ripple Profiler (SRP) during the EU-COAST3D measurement campaigns near Egmond aan Zee. Bell et al. (1998) explain the working of the SRP and the analysis procedure to obtain profiles of the seabed from the SRP-data. Average bed-form height and length were determined from cross-shore profiles of 2-m length of the seabed.

It is stressed here that the present data does not contain information on the three-dimensional character of the bed forms nor on the effect of preceding wave conditions (history effect) on the bed form dimensions. Lanckneus et al. (1999) measured bed forms in the nearshore area of Egmond aan Zee during calm weather conditions using a side scan sonar. They found the bed to be generally plane at the crest of a nearshore bar

and in areas shallower than 2.2 m, where wave activity is most intense. Lunate mega ripples with wing points in the onshore direction occurred on the seaward flank of the inner nearshore bar in the lee of a rip channel depression. Irregular bed forms were present in the throat of the rip channel. Bifurcated symmetrical ripples with crests parallel to the shore were present in the trough between the inner and outer nearshore bar (deeper than 5.5 m). The bed forms recorded by Lanckneus et al. (1999) in depths up to 3 m are typical for relatively calm weather conditions. The bed forms in larger water depths may be relict features generated during a minor storm preceding the sonar measurements. These 3-dimensional characteristics and history effects are neglected in the present analysis, which strongly restricts general applicability of the present results. Nonetheless, for the parameterized effect of the bed forms on the stirring up of sediment it might be enough to characterize the bed form dimensions by their cross-shore height and length scales.

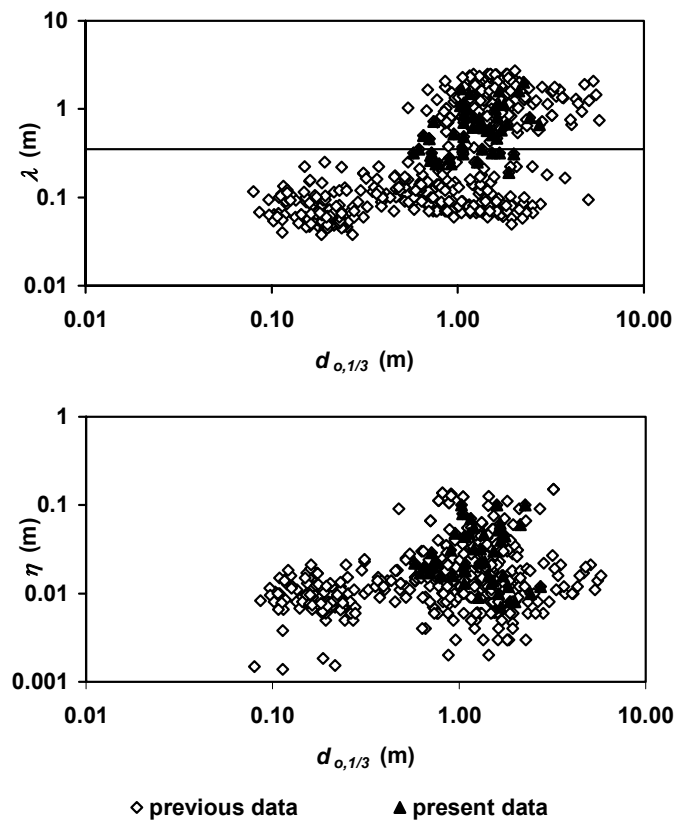


Figure 4.1. Ripple length versus significant near bed orbital diameter $d_{0,1/3}$ (A) and ripple height versus significant orbital diameter $d_{0,1/3}$ (B).

The present field measurements of bed forms are presented and compared to previously published field and laboratory measurements by Inman (1957), Van Rijn et al. (1993), Van Rijn and Havinga (1995), Grasmeyer and Van Rijn (1999) and Hanes et al. (2001) as a function of the significant near-bed fluid orbital diameter (Figure 4.1). There are large variations in the data but the ripple lengths seem to cluster into two different groups with a sparsely populated gap in the ripple lengths around ~ 0.35 m. The ripple

heights seem to cluster into two different groups with a sparsely populated gap in the significant orbital diameters $d_{0,1/3}$ of ~ 0.40 m. Generally, the laboratory data of Van Rijn et al. (1993), Van Rijn and Havinga (1995), Grasmeyer and Van Rijn (1999) occurred at $d_{0,1/3}$ values smaller than 0.40 m and the field data of Inman (1957), Hanes et al. (2001) and the present field data occurred at $d_{0,1/3}$ values larger than 0.40 m, which is naturally related to the difference in scale between laboratory and field measurements.

To distinguish between different types of bed forms measured in the field, the present measurements were subdivided into two groups, i.e. short wave ripples (SWR) with wavelengths of ~ 0.19 - 0.35 m and long wave ripples (LWR) with wavelengths of ~ 0.37 - 2.0 m, see Table 4.1. The identification of two scales of bed form lengths is consistent with the observations of Osborne and Vincent (1993) and Hanes et al. (2001). In this study the same cutoff ($\lambda = 0.35$ m) is used as adopted by Hanes et al. (2001) to discriminate between SWR and LWR. The seabed was regarded plane if the bedform height was less than 0.005 m. Examples of the bed form types measured in the nearshore zone of Egmond aan Zee are shown in Figure 4.2.

Table 4.1. Bed form types and dimensions as measured across a nearshore profile near the coast of Egmond aan Zee, the Netherlands.

Bed form type	Height	Length
Short wave ripples (SWR)	0.007 – 0.047 m	0.19 – 0.35 m
Long wave ripples (LWR)	0.01 – 0.10 m	0.37 – 2.0 m
Plane bed	< 0.005 m	

The present bed forms were measured at different locations across an inner nearshore bar and under various hydrodynamic conditions. LWR were generally found in the trough region between the inner nearshore bar and the beach while SWR and plane bed were found at the seaward flank and on the crest of the bar. The occurrence of the bed forms also clearly shows a relation with the hydrodynamic conditions. The influence of the hydrodynamic conditions upon the occurrence of the bed form types can be examined by plotting them as a function of the significant near-bed mobility number (Figure 4.3). This mobility number reads as

$$\psi = \frac{u_{1/3}^2}{\Delta g D_{50}} \quad (4.42)$$

where Δ is the relative sediment density in water (~ 1.65) [-], g is the acceleration of gravity [m/s^2], $u_{1/3}$ is the mean peak orbital velocity (mean of $u_{1/3,on}$ and $u_{1/3,off}$) [m/s], D_{50} is the median grain diameter [m].

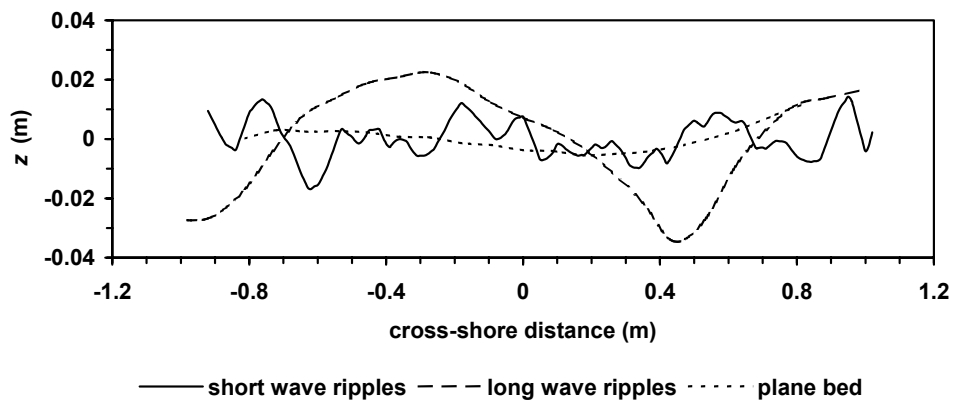


Figure 4.2. Examples of bed forms measured in the nearshore of Egmond aan Zee, the Netherlands.

The percentages in Figure 4.3 refer to the number of measurements relative to the total number of measurements for which bed form data are available for that particular wave condition. For example, '41% SWR' means that a SWR was observed for 41% of the available measurements. The near bed concentrations are plotted also in Figure 4.3. The concentration data points in Figure 4.3 represent the average of ten or more tests. The error bars represent the standard error between the tests. The average value for $\psi = 298$ is based on only two tests.

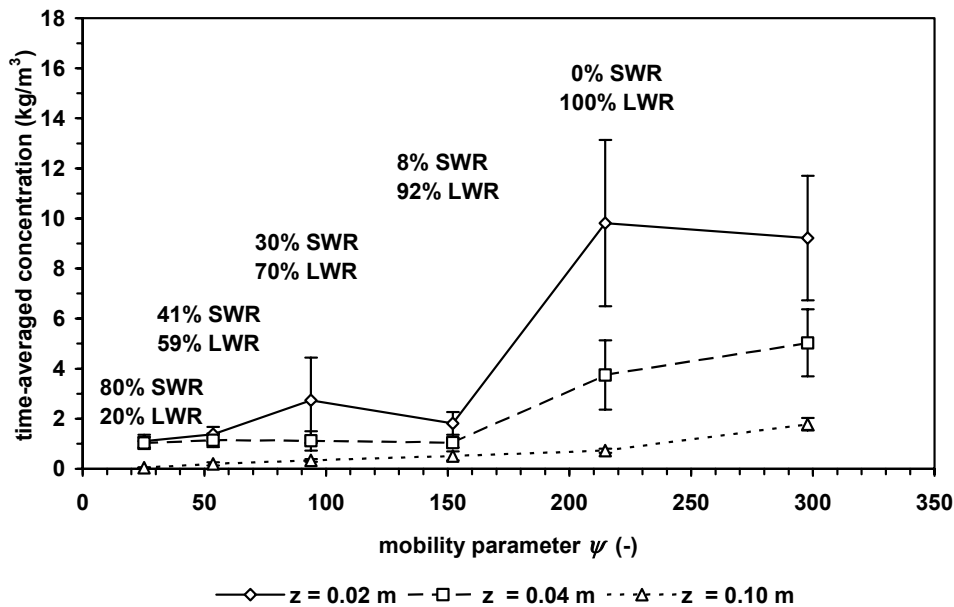


Figure 4.3. Measured bed forms and near bed concentrations as a function of the mobility number. Egmond aan Zee, the Netherlands.

The present bed forms generally change from SWR for small mobility numbers to LWR for larger mobility values. Measured near-bed concentrations are shown in Figure 4.3 also, giving an indication of the effect of the change in bed form type on the magnitude of the near-bed concentrations. Where increasing concentrations are expected with

increasing mobility number, the measured concentrations in Figure 4.3 show more or less constant values between $\psi = 25-94$ and sometimes even decreasing with increasing ψ . This might be attributed to the change in bed form type. Vincent et al. (1991) also observed that concentrations close to the bed (0.02-0.10 m) might decrease as the wave height increases and interpreted this in terms of a decrease in the ripple steepness as the wave height increases. Sand is ejected high above the bed when the bed consists of steep ripples but as the steepness decreases with increasing bed shear stress beyond the break-off point (Grant and Madsen, 1982) the efficiency of vortex ejection, and hence suspended sand concentrations decreases. This stresses the importance of an accurate prediction of the bed form roughness for sand transport computations.

4.3.4. PREDICTING BED ROUGHNESS

Predictive bedform models reveal the factors that determine ripple dimensions. For example, Grant and Madsen (1982) identified two distinct stages ripples go through. The first stage is known as the equilibrium range, in which flow is relatively slow and sediment transport is low. Both ripple height η and ripple length λ tend to increase until ripple steepness and ripple roughness reach their maximum. Within the equilibrium range, the length of the ripples scales with the near bed wave orbital diameter A (orbital ripples). As flow strength is further increased, ripples enter the second stage defined as the break-off range. When this break-off range is reached, ripple height will decrease while ripple length stays roughly constant or decreases slightly. This will lead to the decrease in ripple steepness and ripple roughness, and also the de-correlation between wave orbital diameter and ripple length (anorbital ripples). Finally, the ripples are washed out leaving a plane seabed.

Description of bedform models

Here, three empirical ripple prediction models are tested to calculate the bed form dimensions, i.e. Grant and Madsen (1982) (hereafter referred to as G&M), Van Rijn (1993) and Nielsen (1981). The predicted ripple dimensions are based on measured hydrodynamics and are compared with bed forms measured in the laboratory and the field. Three aspects have to be considered:

- 1) The ripple predictors are valid only for non-breaking wave conditions, while the present data also contain tests with breaking waves. The breaking of waves might lead to a more irregular bed surface.
- 2) The mobility number is based on the significant orbital velocity near the bed defined as $u_{1/3} = (u_{1/3,on} + u_{1/3,off})/2$. If no velocity data were available the significant orbital velocity was computed from linear wave theory using the significant wave height $H_{1/3}$, the water depth h and the wave spectrum peak period T_p . Possible effects of time-averaged currents are not taken into account.
- 3) The ripple height has been made nondimensional with the significant orbital excursion A , which is computed using the significant orbital velocity $u_{1/3}$.

Grant and Madsen (1982) present a set of empirical equations for the prediction of rippled height η and ripple length λ . For conditions below the break-off point where ripple steepness is increasing, the nondimensional ripple height is given by:

$$\frac{\eta}{A} = 0.22 \left(\frac{\theta'}{\theta_c} \right)^{-0.16} \quad (4.43)$$

and the nondimensional ripple length by:

$$\frac{\lambda}{\eta} = 6.25 \left(\frac{\theta'}{\theta_c} \right)^{0.04} \quad (4.44)$$

For condition above the break-off point where ripple steepness begins to decrease, the nondimensional ripple height is given by:

$$\frac{\eta}{A} = 0.48 S_*^{0.8} \left(\frac{\theta'}{\theta_c} \right)^{-0.15} \quad (4.45)$$

and the nondimensional ripple length by:

$$\frac{\lambda}{\eta} = 3.6 S_*^{-0.6} \left(\frac{\theta'}{\theta_c} \right) \quad (4.46)$$

where A is the near-bed orbital excursion, θ' is the maximum nondimensional bed shear stress over a wave cycle, θ_c is the critical Shields parameter and S_* is a nondimensional sediment parameter (Grant and Madsen, 1982).

Li et al. (1996) modified the G&M model to obtain better comparison with the ripple dimensions found near Duck, NC, USA. However, the modified formulations by Li et al. (1996) show a sudden jump around the break-off region, which would lead to numerical instabilities when using these formulations in a morphological model.

Van Rijn (1993) proposes the following expressions to predict ripple dimensions under irregular waves. The nondimensional ripple height is expressed as:

$$\begin{aligned} \frac{\eta}{A} &= 0.22 & \psi &\leq 10 \\ \frac{\eta}{A} &= 2.8 \cdot 10^{-13} (250 - \psi)^5 & 10 &< \psi < 250 \\ \frac{\eta}{A} &= 0 & \psi &\geq 250 \end{aligned} \quad (4.47)$$

and the ripple steepness is expressed as:

$$\begin{aligned}
\frac{\eta}{\lambda} &= 0.18 & \psi &\leq 10 \\
\frac{\eta}{\lambda} &= 2 \cdot 10^{-7} (250 - \psi)^{2.5} & 10 &< \psi < 250 \\
\frac{\eta}{\lambda} &= 0 & \psi &\geq 250
\end{aligned} \tag{4.48}$$

where ψ is the mobility number. Nielsen (1981) proposes the following semi-empirical formulae to predict the height η and length λ of ripples under irregular waves. Nondimensional ripple height is expressed as:

$$\begin{aligned}
\frac{\eta}{A} &= 21\psi^{-1.85} & \psi &> 10 \\
\frac{\eta}{A} &= 0.275 - 0.022\psi^{0.5} & \psi &< 10
\end{aligned} \tag{4.49}$$

and the nondimensional ripple length is expressed as:

$$\frac{\lambda}{A} = \exp\left(\frac{693 - 0.37 \ln^8 \psi}{1000 + 0.75 \ln^7 \psi}\right) \tag{4.50}$$

Nielsen (1981) independently fit curves for ripple steepness, giving:

$$\frac{\eta}{\lambda} = 0.342 - 0.344\sqrt{\theta_{2.5}} \tag{4.51}$$

The nondimensional bed shear stress $\theta_{2.5}$ is defined by $\theta_{2.5} = 1/2 f_{2.5} \psi$, where $f_{2.5}$ is the Swart (1974) friction factor with a roughness of $2.5D_{50}$.

Model data comparison

The G&M model curves for ripple height and steepness are shown in Figure 4.4 along with the measured ripple dimensions. Maximum and minimum predictions of ripple height and steepness are shown, which are mainly determined by a difference in wave period ($T_p = 2$ and 16 s), and to a lesser extent by a difference in grain diameter ($D_{50} = 0.1$ and 1.0 mm). Generally, an increasing wave period and grain diameter both lead to a larger ripple height and ripple steepness in the G&M model. This effect was not observed in the measured data. In contrast, the laboratory data show a larger ripple height and ripple steepness than the field data, though the wave period and grain diameter is generally smaller. The G&M model slightly overestimates the nondimensional ripple height when considering all the data including the LWR field data (Figure 4.4 A). Discrepancies are larger when leaving out the LWR field data (Figure 4.4 B). The G&M model reproduces the previous laboratory data and the LWR field data better than the SWR field data. The G&M model also overestimates the ripple steepness values (Figure 4.4 C), especially the field data in the break-off range. The

comparison between observed and modelled ripple steepness values slightly improves when leaving out the LWR field data.

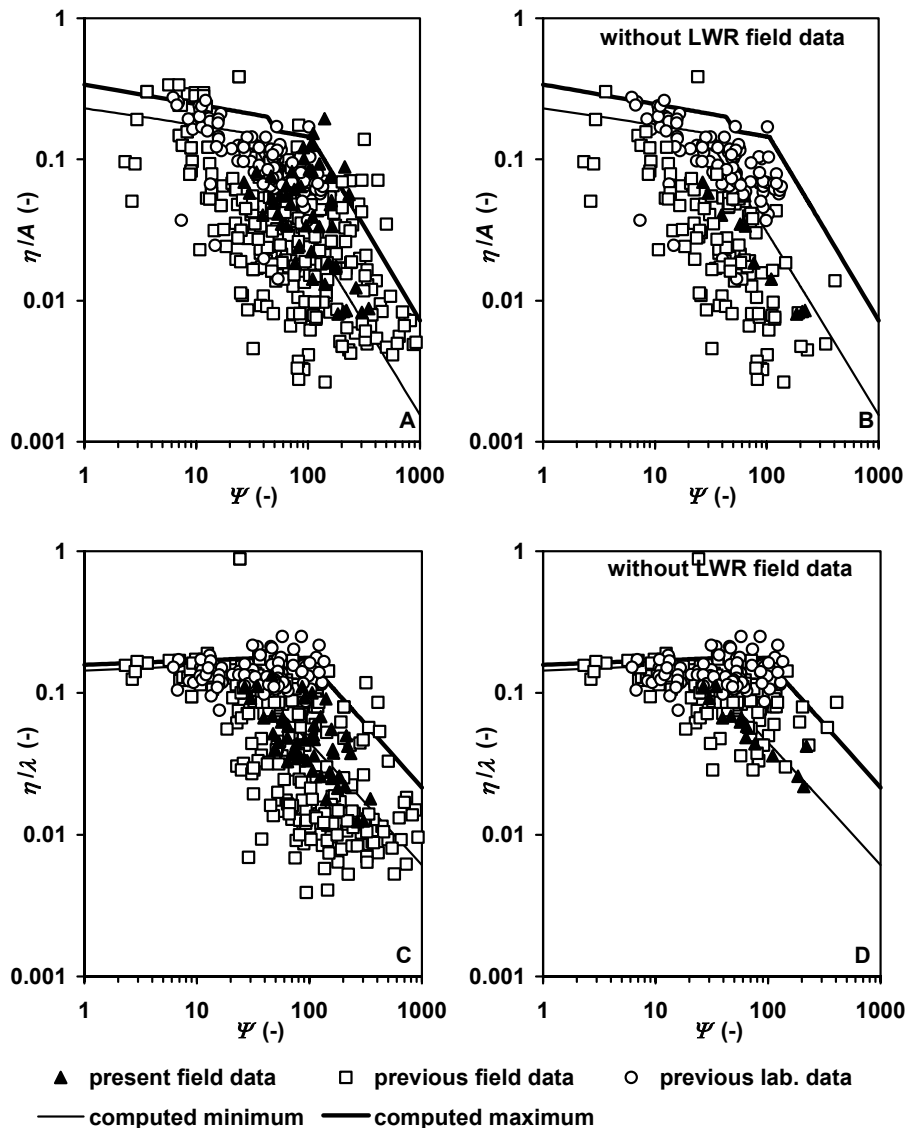


Figure 4.4. Nondimensional ripple height versus mobility number using all data with LWR field data (A) and without LWR field data (B); ripple steepness using all data with LWR field data (C) and without LWR field data (D). Lines denote the Grant and Madsen (1982) model curves.

The Van Rijn ripple model curves are compared with measurements in Figure 4.5. The Van Rijn model shows a steep decrease of nondimensional ripple height with increasing mobility number whereas the measurements including the LWR field data show a more gradual decrease (Figure 4.5A). The Van Rijn model captures the ripple height trend for the previous laboratory data but overestimates the nondimensional ripple heights in the field when leaving out the LWR field data. As for the predicted nondimensional ripple height, the predicted ripple steepness also decreases more rapidly than is observed in the

measurements (Figure 4.5C). Leaving out the LWR field data slightly improves the comparison (Figure 4.5D). The Van Rijn model predicts plane bed conditions for a mobility number of 250 whereas the measurements show a nondimensional ripple height and ripple steepness of about 0.01, though this is mainly caused by the presence of LWR.

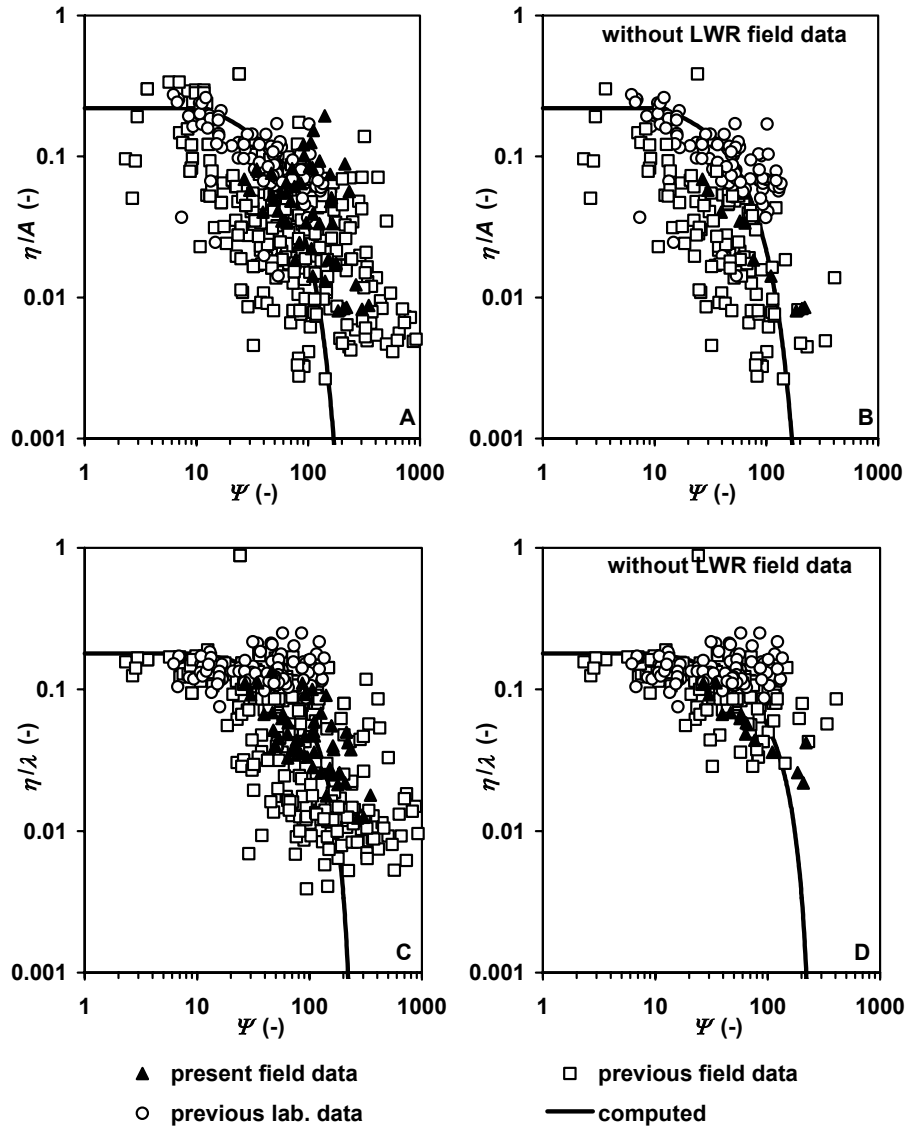


Figure 4.5. Nondimensional ripple height versus mobility number using all data with LWR field data (A) and without LWR field data (B); ripple steepness using all data with LWR field data (C) and without LWR field data (D). Lines denote the Van Rijn (1993) model curves.

The Nielsen model underestimates nondimensional ripple heights when considering the entire data set including the LWR field data (Figure 4.6A). Leaving out the LWR field data, the Nielsen model captures the trends for the field data more correctly but the nondimensional ripple heights from previous laboratory data are still underestimated. Figure 4.6 C and D show the maximum and minimum predictions of ripple steepness

with the Nielsen model. The minimum and maximum curves are mainly determined by a difference in wave period ($T_p = 2$ and 16 s) through increasing ripple steepness with wave period, and to a lesser extent by a difference in grain diameter ($D_{50} = 0.1$ and 1.0 mm) through a decreasing ripple steepness with grain diameter. These effects in the Nielsen model were not observed in the measured data. The Nielsen model reasonably represents the observed trends in ripple steepness using all data including the LWR field data (Figure 4.6C), although the scatter in the data is quite large. Leaving out the LWR field data slightly improves the predictions (Figure 4.6D). As the Van Rijn model, the Nielsen model shows a somewhat steeper decrease of the ripple steepness with increasing mobility number than is observed in the measurements.

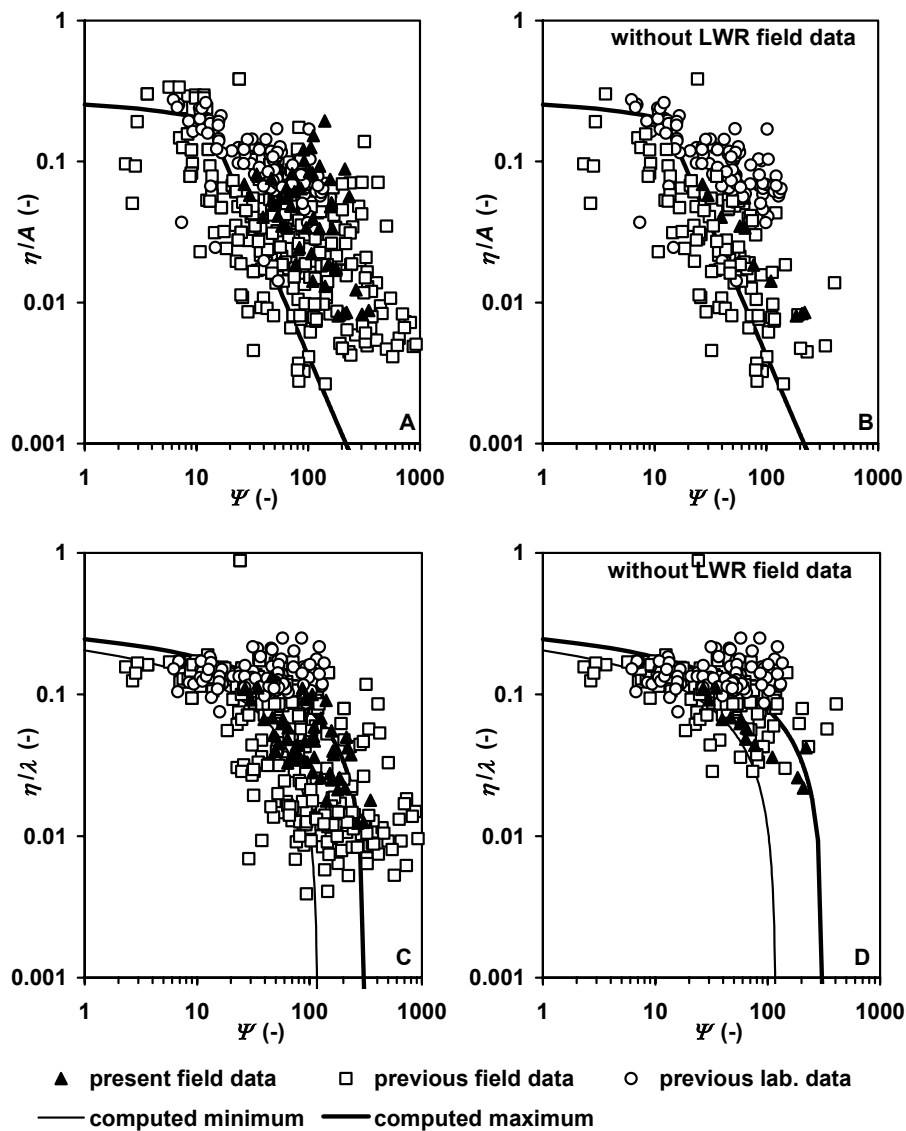


Figure 4.6. Nondimensional ripple height versus mobility number using all data with LWR field data (A) and without LWR field data (B); ripple steepness using all data with LWR field data (C) and without LWR field data (D). Lines denote the Nielsen (1981) model curves.

A measure for the relative error between measured and predicted values can be defined as

$$\varepsilon_{rma} = \frac{\overline{|X_{predicted} - X_{measured}|} - X_{error}}{\overline{|X_{measured}|}} \quad (4.52)$$

where X is the parameter of interest, the overbar represents an average and X_{error} is a constant measurement error, which is assumed to be 0.005 in this case. The ε_{rmae} gives an indication of the variation about the predicted value. For example, if ε_{rmae} equals 0.37, the average error is equal to 37%. The Nielsen (1981) irregular wave ripple model performed best for the prediction of nondimensional ripple height. As shown in Table 4.2, the ε_{rmae} for nondimensional ripple height is 0.89, 0.79 and 0.72 for the G&M, Van Rijn and Nielsen ripple models, respectively. Leaving out the LWR field data hardly affects the model performance. The models were better at predicting ripple steepness than at predicting nondimensional ripple height. The G&M model had a ε_{rmae} of 0.55, whereas the Van Rijn and Nielsen model had ε_{rmae} values of 0.53 and 0.59 in predicting the ripple steepness, respectively. The relative mean absolute errors decreased when leaving out the LWR field data.

Table 4.2. Relative mean absolute error between measured and predicted ripple dimensions

	G&M		Van Rijn		Nielsen	
	With LWR	Without LWR	With LWR	Without LWR	With LWR	Without LWR
Ripple height	0.89	0.94	0.79	0.82	0.72	0.70
Ripple steepness	0.55	0.42	0.53	0.42	0.59	0.43

It is interesting to see that the Nielsen model performs best in predicting the nondimensional ripple height, while from comparing the figures the Nielsen model seems to overestimate the value of η/A more than the other models do. However, the correlation squared r^2 between measured and computed η/A was found to be 0.32, 0.42 and 0.48 for the G&M, the Van Rijn and the Nielsen model, respectively. This means that the Nielsen model captures the trend of the nondimensional ripple heights better than the other two models do, which overall leads to a smaller relative mean absolute error.

The errors in predicting η/λ are smaller than the errors for η/A , which suggests that the models are better at predicting the ripple steepness than at predicting the nondimensional ripple height. However, the value of r^2 between measured and computed η/λ was 0.14, 0.14 and 0.10 for the G&M, the Van Rijn and the Nielsen model, respectively, which is much smaller than the r^2 values between measured and computed η/A . Therefore, the relative mean absolute errors are not smaller because the models are better at predicting the ripple steepness but more because the scatter in the η/λ data is smaller than the scatter in η/A data.

Of the predictive ripple models tested here, the Nielsen model seems to be the most promising to be applied in predicting the bed roughness $k_s = \alpha\eta^2/\lambda$. The errors in predicting η/A were smallest and the correlation squared between measured and computed η/A were largest when using the Nielsen model. The errors in predicting the ripple steepness were in the same range as the other two models. Nonetheless, the Nielsen model still underestimated η/A for large part of the data used here and the decrease of the ripple steepness with mobility number is stronger than observed from the measurements. Therefore, the Nielsen model was modified to improve the predictions. Changes were made to the formulation of nondimensional ripple height in the break-off range and a new formulation for the ripple steepness is suggested.

The following empirical formulae to predict the height η and length λ of ripples under irregular waves are proposed. Nondimensional ripple height is expressed as:

$$\begin{aligned} \frac{\eta}{A} &= 2\psi^{-1} & \psi > 10 \\ \frac{\eta}{A} &= 0.275 - 0.022\psi^{0.5} & \psi < 10 \end{aligned} \quad (4.53)$$

The ripple steepness is expressed as:

$$\begin{aligned} \frac{\eta}{\lambda} &= -0.078 + 0.355 \psi^{-0.221} & \psi > 10 \\ \frac{\eta}{\lambda} &= 0.14 & \psi < 10 \end{aligned} \quad (4.54)$$

The relative mean absolute errors between measured ripple dimensions and the computed values using the modified Nielsen model are given in Table 4.3. As can be seen, the modified Nielsen model generally gives better predictions than the original Nielsen model and the G&M and Van Rijn models (compare Table 4.2 and Table 4.3). The correlations squared r^2 between measured and computed values were also found to be similar or larger than for the other models, namely 0.48 and 0.18 for nondimensional ripple height η/A and ripple steepness η/λ , respectively.

Table 4.3. Relative mean absolute error between measured and predicted ripple dimensions.

	Nielsen modified	
	With LWR	Without LWR
Ripple height	0.59	0.61
Ripple steepness	0.40	0.46

Commonly, the bed roughness k_s is assumed to be directly proportional to the ripple dimensions according to $k_s = \alpha\eta^2/\lambda$. The experimental values for α are 8, 20 and 27.7 according to Nielsen (1992), Van Rijn (1993) and Grant and Madsen (1982), respectively. Models with a similar dependence have been proposed by Lettau (1969) for the aerodynamic roughness ($15\eta^2/\lambda$) and by Swart (1977) for waves ($25\eta^2/\lambda$). Because of the uncertainty in the value of α , this parameter is considered as a

calibration factor and the values of η^2/λ are compared herein. Based on the field and laboratory data used here, it is difficult to discriminate between the effect of SWR and LWR on the bed roughness. Therefore, the entire data set including the LWR field data is used to compare measured and predicted values of η^2/λ . Figure 4.7 shows measured values of η^2/λ and the minimum and maximum predictions from the G&M, Van Rijn, Nielsen and modified Nielsen models. The minimum and maximum curves are mainly determined by a difference in wave period ($T_p = 2$ and 16 s) through an increasing value of η^2/λ with wave period, and to a lesser extent by a difference in grain diameter ($D_{50} = 0.1$ and 1.0 mm) through a decreasing value of η^2/λ with grain diameter.

The G&M method generally overestimates η^2/λ compared to the measured data (Figure 4.7A). For relatively long waves ($T_p = 16$ s) and coarse sand ($D_{50} = 1.0$ mm), the G&M model produces a maximum η^2/λ of almost 0.10 m. Maximum η^2/λ is found for mobility values between 30 and 100. The sudden switch from increasing to decreasing ripple roughness is caused by a rather abrupt transition to the break-off range in the G&M model. It is also clear that the G&M method is rather sensitive to the wave period and to a lesser extent sensitive to the grain diameter. An increase of the wave period from 2 to 16 s leads to an increase of the predicted η^2/λ value of about a factor 10, while an increase of the grain diameter from 0.1 to 1.0 mm leads to an increase of the predicted η^2/λ value with about a factor 5. This wave period and grain diameter sensitivity though is not observed in the measured data. For example, the η^2/λ values from the previous laboratory ($D_{50} \sim 0.1$ to 0.2 mm, $T_p \sim 2$ to 3 s) and the (present and previous) field data are ($D_{50} \sim 0.1$ to 1.6 mm, $T_p \sim 2$ to 16 s) of the same magnitude and show comparable trends, despite the difference in wave period and grain diameter.

The Van Rijn model shows a gentler transition from equilibrium to the break-off range compared to G&M. Maximum η^2/λ value (largest value about 0.04 m) is found for mobility values between 10 and 20 (calm weather). In the break-off range, the Van Rijn model shows a strong decrease with mobility number while the measured data show a more gradual decrease with mobility number. The Van Rijn model is slightly less sensitive to the wave period than the G&M model.

The minimum and maximum η^2/λ values computed with the Nielsen model approximate the range of observed values better than the G&M and Van Rijn models. However, the Nielsen model still tends to underestimate η^2/λ . This is partly due to an underestimation of the nondimensional ripple height (see Figure 4.6A), but also to a stronger decrease of the ripple steepness with increasing mobility number than is observed in the measurements (see Figure 4.6C). Maximum η^2/λ value (largest value about 0.04 m) is found for $\psi = 10$. The Nielsen model is slightly less sensitive to wave period and grain diameter than the G&M model.

The modified Nielsen model, described by Equations (4.53) and (4.54), captures the range of measured η^2/λ values better than the G&M, Van Rijn and original Nielsen model do, which is naturally based on an improved prediction of the nondimensional ripple height and ripple steepness. Main differences with the original Nielsen model are the more gradual decrease of η^2/λ with mobility number and the less pronounced effect of wave period and grain diameter. Maximum η^2/λ value (largest value about 0.025 m) is found for $\psi = 10$.

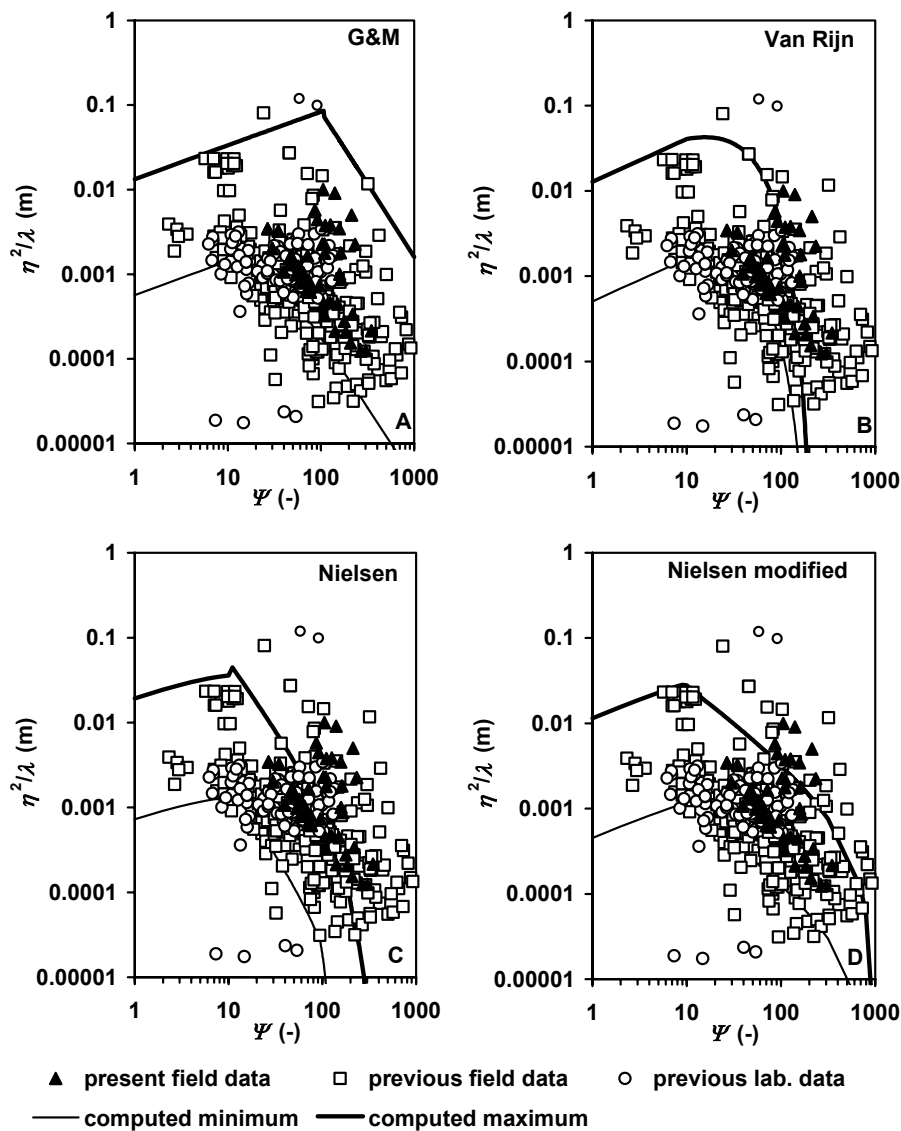


Figure 4.7. Measured and computed values of η^2 / λ using computed ripple dimensions (lines) and measured ripple dimensions (symbols).

There is evidence that the movement of sediment enhances the ripple-related roughness (Grant and Madsen, 1982). A simple way to account for the roughness contribution from the moving sand is to add a term to Equation (4.41). Most investigators propose an expression that depends on some sort of mobility-parameter. Houwman (2000) compared three formulations including this sediment transport effect and found differences of a factor 100 between the methods. The transport roughness is most effective in sheet flow conditions. Under these conditions, the sand transport related roughness can be roughly estimated to be equal to the thickness of the sheet flow layer, which is roughly of the order of 0.01 m or about $30 D_{90}$ for sediment of 0.2 to 0.3 mm (Ribberink and Al-Salem, 1992a). However, because of the large uncertainties the transport effect on the bed roughness is not taken into account here.

4.3.5. DISCUSSION AND CONCLUSIONS

The present field data of nondimensional ripple height and ripple steepness were found to be in the same range and showed the same trends as previous laboratory and field measurements. Although the field data used in the present analysis seemed to cluster into two different groups with a sparsely populated gap in the ripple lengths around ~ 0.35 m, of which the smaller ripple lengths were defined as short wave ripples (SWR) and the longer ripple lengths as long wave ripples (LWR), comparison with laboratory data did not justify such a distinction. Therefore, both SWR and LWR were used in comparing measured ripple dimensions with three predictive models, i.e. Grant and Madsen (1982), Van Rijn (1993) and Nielsen (1981).

The errors in predicting η/A were smallest and the correlations between measured and computed values was best when using the Nielsen model. The errors in predicting the ripple steepness were in the same range as the other two models. Nonetheless, the Nielsen model still underestimated η/A for large part of the data used here and the decrease of the ripple steepness with mobility number was stronger than observed from the measurements. Therefore, the Nielsen model was modified to improve the predictions. Changes were made to the formulation of nondimensional ripple height in the break-off range and a new formulation for the ripple steepness was suggested.

Commonly, the bed roughness k_s is assumed to be directly proportional to the ripple dimensions according to $k_s = \alpha\eta^2/\lambda$, in which α is a calibration factor. Therefore, measured and predicted η^2/λ were compared. The G&M method generally overestimated η^2/λ compared to the measured data and produced a rather sudden switch from increasing to decreasing ripple roughness, caused by a rather abrupt transition to the break-off range. The G&M method was found to be rather sensitive to the wave period and to a lesser extent sensitive to the grain diameter. The Van Rijn model showed a gentler transition from equilibrium to the break-off range compared to G&M. In the break-off range, the Van Rijn model decreased strongly with mobility number while the measured data showed a more gradual decrease. The Van Rijn model was slightly less sensitive to the wave period than the G&M model. The minimum and maximum η^2/λ values computed with the Nielsen model approximated the range of observed values better than the G&M and Van Rijn models. However, the Nielsen model still underestimated η^2/λ . The modified Nielsen model captured the range of measured η^2/λ values better than the G&M, Van Rijn and original Nielsen model did. Main differences with the original Nielsen model are a more gradual decrease of η^2/λ with mobility number and a less pronounced effect of wave period and grain diameter. The general applicability of the modified Nielsen model await more field data for different grain sizes and wave-current flow conditions. The roughness predictors discussed in this section were implemented in the sediment transport model and will be compared in the next sections.

When bedforms have grown large, their reaction to changing conditions becomes tardy because the sediment volume in bedforms reshaping likewise increases. As a result, hysteresis of their dimensions can be observed, which has consequences for the bed roughness height. Hysteresis of bedforms has been observed by Boyd et al. (1988), Li and Amos (1999) and Traykovski et al. (1999). Consequently, bedform types may be out of phase with the concurrent flow conditions, especially in waning storm. Traykovski et al. (1999) observed ripples whose reaction to decreasing orbital diameter seemed to be one day. This hysteresis effect is not taken into account here.

4.4. MODELLING THE CURRENT-RELATED SUSPENDED TRANSPORT RATE

4.4.1. INTRODUCTION

The current-related suspended load transport ($q_{s,c}$) is defined as the transport of sediment particles by the time-averaged current velocities given by:

$$q_{s,c} = \rho_s \int_a^h cu \, dz \quad (4.55)$$

The four roughness models presented in Section 4.3 are used here for the prediction of ripple height, ripple length and roughness values. These predictions are used in the analysis of the time-averaged concentrations and current-related transport rates. The sensitivity of the sediment transport model due to changes in the bed roughness parameters will be illustrated by describing the influence on the time-averaged concentration profile and on the current-related sediment transport rate.

The roughness models have been implemented in the sand transport model in order to verify if an accurate prediction of the concentration distribution and transport rates is possible using a predicted bed roughness height. A comparison between measured and computed concentrations and transport rates provides insight in the usefulness of a particular roughness model in the sand transport model.

First, suspended sediment concentrations measured in the Delta Flume of Delft Hydraulics are compared to model predictions (Section 4.4.2). Then, suspended sediment concentrations and current-related transport rates measured near the coast of Egmond aan Zee in the Netherlands are compared to model predictions (Section 4.4.3).

4.4.2. LARGE-SCALE LABORATORY EXPERIMENTS

The experiments used here were carried out in the Delta Flume of Delft Hydraulics. The experiments are described in detail in Section 2.4 of this thesis. Table 4.4 gives a summary with relevant data for the discussion in this section.

Table 4.4. Basic experimental data of Delta Flume experiments.

	grain size	wave height	wave period	water depth	ripple height	ripple length
	D_{50} (mm)	$H_{1/3}$ (m)	T_p (s)	h (m)	η (m)	λ (m)
A	0.33	1.00	5.0	4.5	0.053	0.38
B	0.33	1.25	5.0	4.5	0.055	0.39
C	0.16	1.00	5.0	4.5	< 0.010	0.94
D	0.16	1.25	5.0	4.5	not measured	not measured
E	0.16	1.50	5.0	4.5	not measured	not measured

Time-averaged concentrations

Computations of time-averaged concentrations were made using measured wave heights and current velocities and fixed bed roughness heights of 0.01, 0.02, 0.03 and 0.04 m. The computed concentrations based on these roughness values are compared with measured concentrations. The suspended sediment grain size was taken to be equal to the grain size of the bed material.

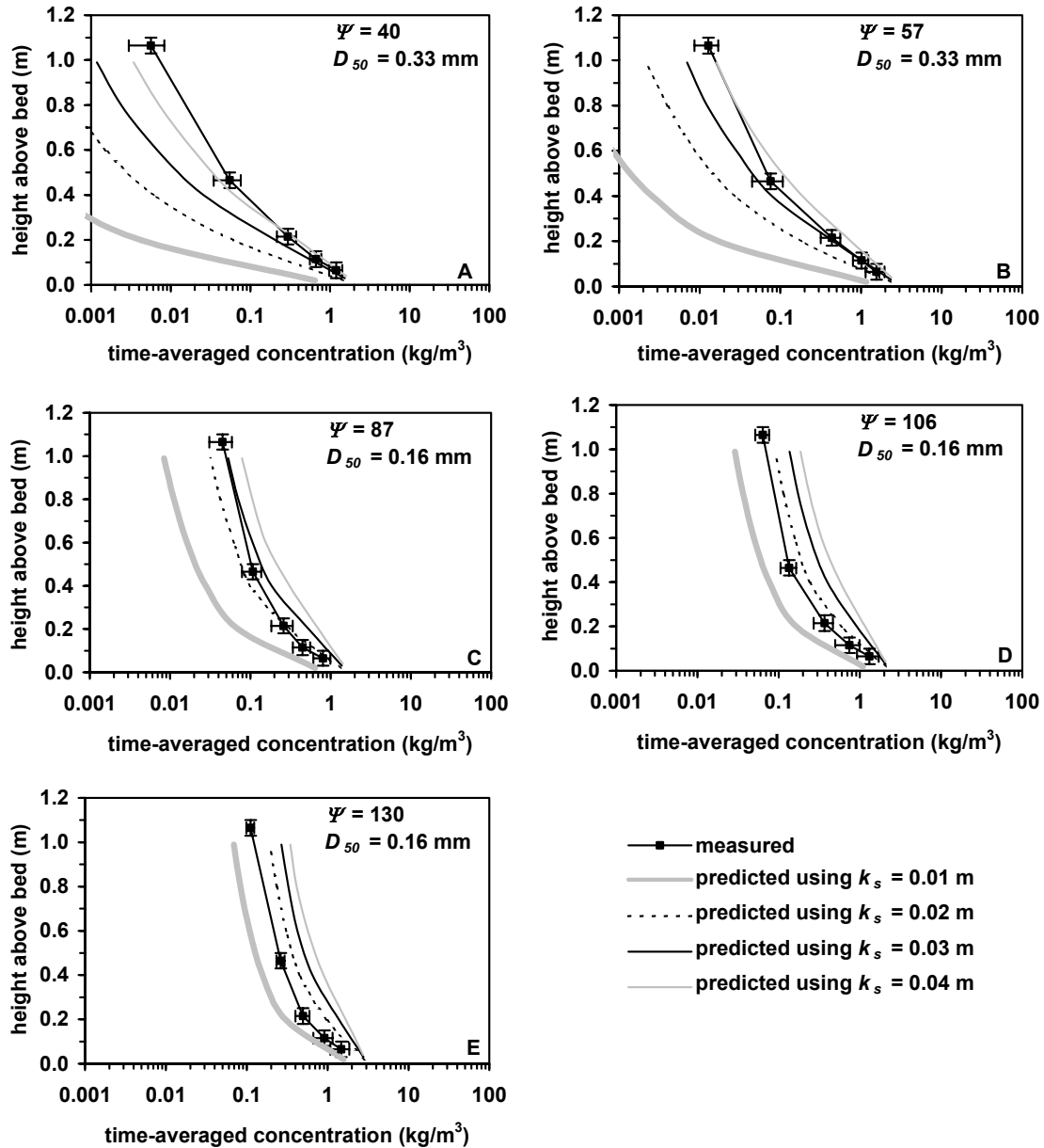


Figure 4.8. Effect of bed roughness on predicted time-averaged concentration distribution. Delta Flume tests: A) $H_{1/3} = 1.0$ m, B) $H_{1/3} = 1.25$ m, C) $H_{1/3} = 1.0$ m, D) $H_{1/3} = 1.25$ m, E) $H_{1/3} = 1.5$ m. For all tests: $T_p = 5.0$, $h = 4.5$ m.

Figure 4.8 shows the predicted and measured time-averaged concentration profiles for the five test series. The data points correspond to the average values of 3 or more tests.

The horizontal error bars indicate the standard error in measured concentrations between the tests. The vertical error bars indicate the uncertainty of the vertical position of the instruments above the bed.

The model shows good agreement with the measured concentrations using $k_s \sim 0.04$ m for the tests with coarse sand (A and B). The near bed concentrations are well reproduced by the model and the vertical distribution shows favorable comparison to the measurements. A smaller roughness height of $k_s \sim 0.02$ m suffices for the tests with fine sand (C, D and E). Relative mean absolute errors between measured and computed concentrations are shown in Figure 4.9.

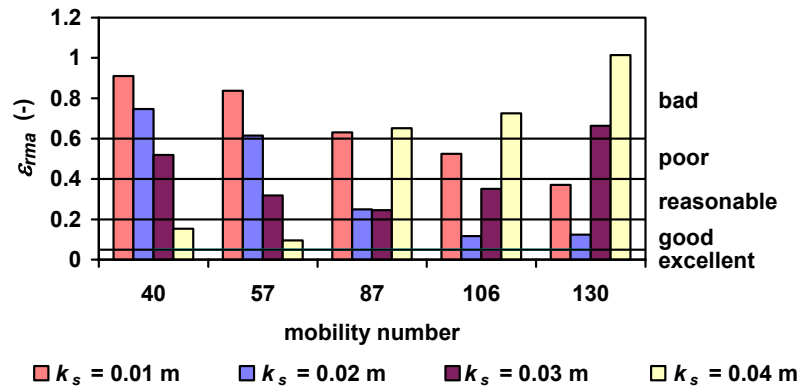


Figure 4.9. Relative mean absolute errors ϵ_{rma} between measured and computed concentrations for Delta Flume experiments using four different k_s values.

Figure 4.8 also shows the effect of the bed roughness on the sediment mixing in the model. An increasing roughness height leads to more sediment mixing and therefore to a more uniform predicted concentration profile. This effect is described by Equations (4.8)-(4.11), in which the sediment mixing depends rather strongly on the wave-related roughness height $k_{s,w}$.

Table 4.5. Predicted ripple roughness heights for Delta flume experiments from G&M, Van Rijn, Nielsen and modified Nielsen bed roughness predictors.

	ψ	D_{50}	k_s			
			G&M	Van Rijn	Nielsen	Nielsen modified
	(-)	(mm)	(m)	(m)	(m)	(m)
A	40	0.33	0.055	0.065	0.010	0.031
B	57	0.33	0.027	0.020	0.010	0.020
C	87	0.16	0.010	0.010	0.010	0.011
D	106	0.16	0.010	0.010	0.010	0.010
E	130	0.16	0.010	0.010	0.010	0.010

The k_s values for the Delta Flume experiments predicted by the different models are presented in Table 4.5. The experimental values for α are taken to be 8, 20 and 27.7 according to Nielsen (1992), Van Rijn (1993) and Grant and Madsen (1982), respectively. An α value of $\alpha = 27.7$ is also used for the modified Nielsen model. The G&M and Van Rijn models predict $k_s = 0.020 - 0.065$ m for the tests with coarse sand (A and B) and 0.010 m for the tests with fine sand (C, D and E). Nielsen predicts a roughness height of 0.010 m for all tests. For all models the minimum roughness height was set to 0.010 m. Compared to the G&M and Van Rijn model, the modified Nielsen model predicts roughness heights that are slightly smaller for the coarse sand (0.020-0.031 m) and slightly larger for the fine sediment (0.010-0.011 m).

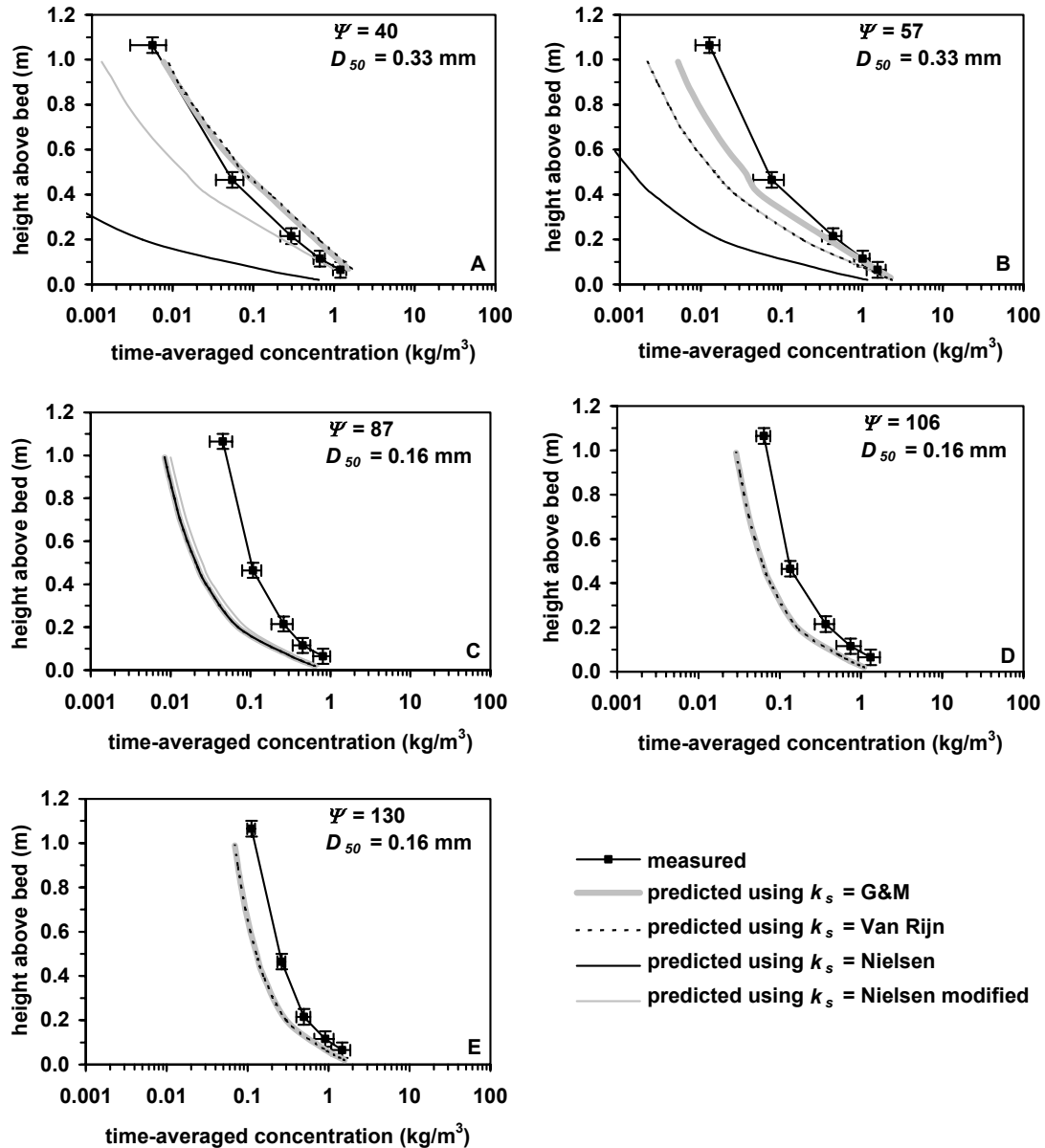


Figure 4.10. Effect of different bed roughness predictors on time-averaged concentration distribution. Delta Flume tests: A) $H_{1/3} = 1.0$ m, B) $H_{1/3} = 1.25$ m, C) $H_{1/3} = 1.0$ m, D) $H_{1/3} = 1.25$ m, E) $H_{1/3} = 1.5$ m. For all tests: $T_p = 5.0$, $h = 4.5$ m.

Figure 4.10 shows a comparison between the computed concentration profiles using the different roughness predictors and the measured concentrations. Relative mean absolute errors are given in Figure 4.11. Generally, best predictions are obtained using the modified Nielsen model, while predictions are worst using the original Nielsen model, which is due to the relatively small value of $\alpha = 8$ in Equation (4.41) proposed by Nielsen. The effect of using different roughness models on the predicted sediment concentration profiles is most pronounced for the tests with coarse sand. Differences are negligible for the tests with fine sand, which is due to the minimum roughness height of 0.010 m in all roughness models.

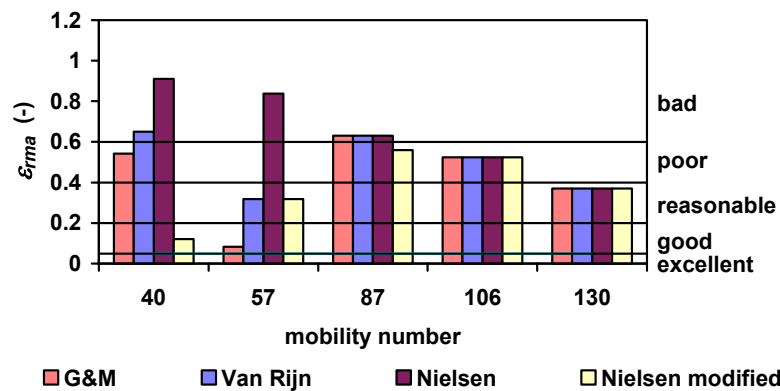


Figure 4.11. Relative mean absolute errors between measured and computed concentrations for Delta Flume experiments using G&M, Van Rijn, Nielsen and modified Nielsen bed roughness predictors.

The present sediment transport model gives a very reasonable estimate of the near bed concentrations for the tests with coarse sand, but underestimates the concentrations higher up in the water column for these tests. This may be caused by an underestimation of the roughness length scale or by vertical sorting of sediment. Pump samples taken near the ASTM sensors revealed that the median grain size of the suspended sediment was 60-80% of the D_{50} of the bed material, consistent with findings by Wolf (1997). The D_{50} of the bed material was used in the model.

Indicative computations using a suspended sand grain size of 80% of the bed material led to an improvement of the concentration predictions for the coarse grained sand (figures not shown). For the fine sands however, the concentrations higher up in the water column were found to be somewhat over-predicted in this case (50-100% for $\psi = 130$). The effect of vertical sorting on sediment transport rates is beyond the scope of this study. Siermans and Van Rijn (2003) studied the vertical sorting of sediment and its effect on suspended sediment transport rates in more detail.

The shape of the predicted concentration profiles for the fine grain tests agrees favourably with the measured shape but the magnitudes are underestimated.

4.4.3. LARGE-SCALE FIELD EXPERIMENTS

Large-scale field experiments were performed at a field site near Egmond aan Zee, the Netherlands. Measurements of wave height, velocity, and sediment concentration at four or five locations in a cross-shore array over the inner nearshore bar were performed using the Coastal Research Instrumented Sledge (CRIS). Sand transport measurements were performed at eight elevations above the bed from 0.02 to 1.0 m. The field measurements are described in more detail in Section 2.6 of this thesis.

Herein, the measured and computed concentrations and transport rates are clustered into classes to show the general trend in the data. The clustering is based on hydrodynamic conditions. Each class contains about 10 tests and is represented by the mobility number ψ , which yields six hydrodynamic classes with mobility numbers $\psi = 25, 54, 94, 152, 215$ and 298 , corresponding to orbital velocities $u_{1/3} = 0.30, 0.44, 0.59, 0.75, 0.89$ and 1.05 m/s.

Time-averaged concentrations

The predicted concentrations based on measured wave heights and current velocities and on bed roughness heights of 0.01, 0.02, 0.03 and 0.04 m are compared with measured concentrations. The suspended sediment grain size is taken to be $D_{50} = 0.24$ mm, based on analysis of bed samples.

The measured concentration profiles in the field show much stronger gradients in the near bed region than the Delta Flume tests. The concentrations near the bed are of the same order of magnitude as in the Delta Flume tests but the decrease of concentrations with height is much stronger (Figure 4.12). This may be related to: 1) advective transport related to the presence of a steady current in the field, 2) a smaller eddy viscosity related to a smaller ripple roughness in the field.

A larger bed roughness height results in an increase of the predicted near-bed concentrations (Figure 4.12). The bed roughness effect on the near bed concentrations is strongest under relatively calm conditions, e.g. an increase of the bed roughness with 1 cm under calm conditions leads to an increase of the predicted near bed concentrations with about 20%. This value is about 10% under storm conditions.

The influence of the bed roughness on the shape of the concentration distribution can also be observed from Figure 4.12. An increasing bed roughness causes more sediment mixing which results in a steeper concentration distribution. The concentration distribution near the bed ($z < 0.2$ m) is reasonably predicted for $\psi = 94$ and 152 . The predicted concentration distribution is too steep (too much mixing) near the bed for relatively calm conditions ($\psi = 25$ and 54) and for relatively energetic conditions ($\psi = 251$ and 298). For calm conditions ($\psi = 25$ and 54) the model underestimates the mixing higher up in the water column, even when using the larger roughness heights (0.04 m). The latter might be related to the vertical sorting of sediment where the finer fractions are stirred up higher into the water column than the coarse sand. This is not taken into account when using the model in single fraction mode. Indicative computations with the model in multi-fraction mode showed better agreement between the measured and computed concentration profiles under calm conditions, which is attributed to this

vertical sorting effect. The multi-fraction mode was not used in the present study. The model reasonably predicts the mixing higher up in the water column for more energetic conditions ($\psi = 215$ and 298). Near bed concentrations are however underestimated under these circumstances.

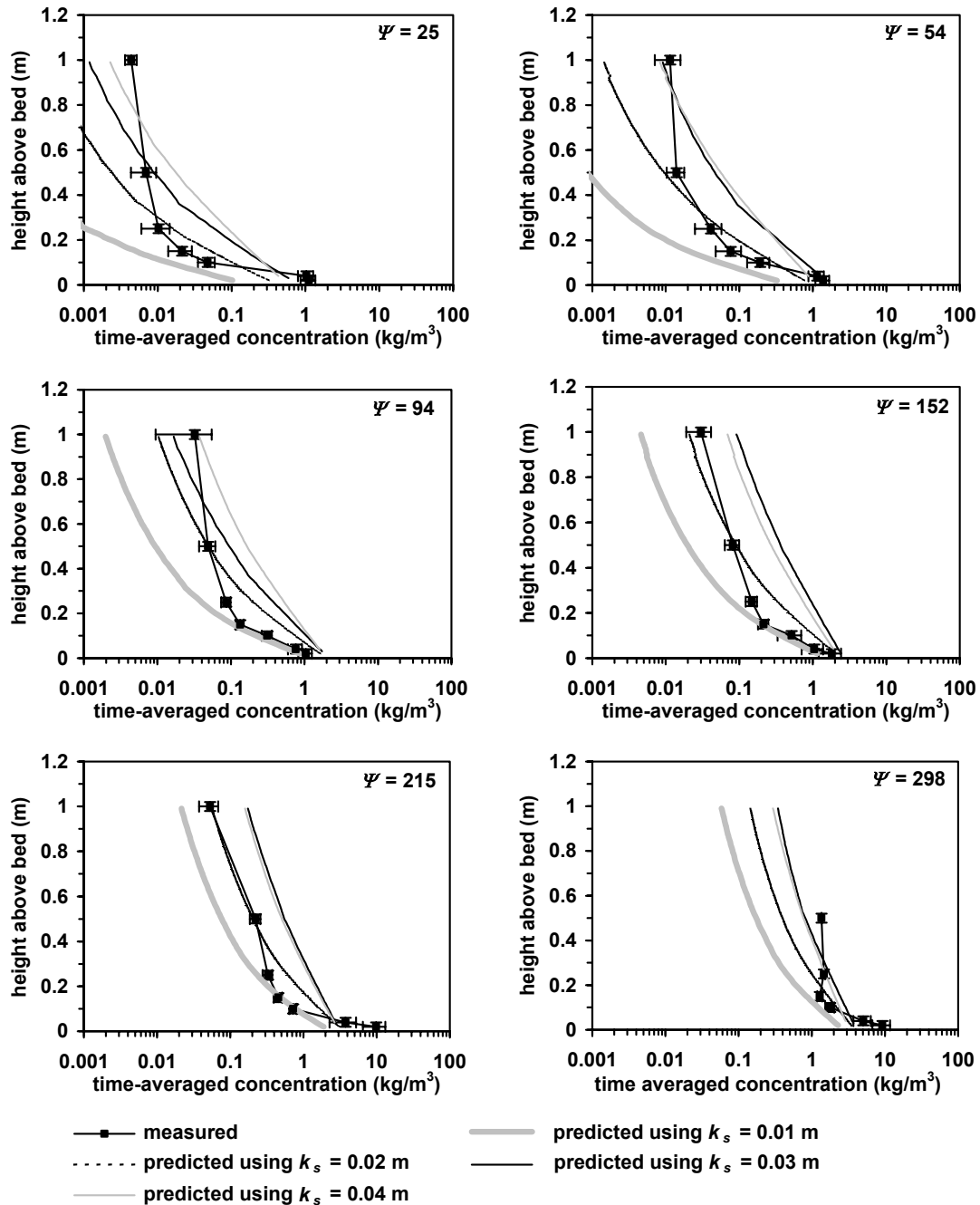


Figure 4.12. Effect of bed roughness on predicted time-averaged concentration distribution for Egmond aan Zee field tests.

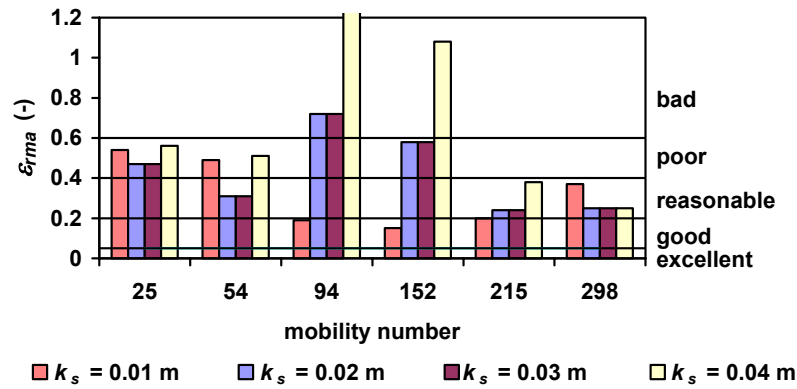


Figure 4.13. Relative mean absolute errors between measured and computed concentrations for Egmond aan Zee field tests using four different bed roughness values.

Figure 4.12 shows that the measured near bed concentrations ($z \leq 0.04$ m) do not increase with mobility number for $\psi < 152$. This was attributed to the change in bed form type with changing conditions (see Figure 4.3). Figure 4.12 indicates that for relatively calm conditions ($\psi = 25-54$) a roughness height of $k_s = 0.02 - 0.03$ m gives the best model results, while for the rougher conditions ($\psi = 94-215$) a bed roughness height of $0.01 - 0.02$ m suffices. Relative mean absolute errors are given in Figure 4.13. The model underestimates the concentrations for the moderate storm conditions ($\psi = 298$). It is noted though that for these conditions the measured class-averaged concentrations are based on only two tests whereas the other profiles are based on ten or more tests.

The roughness models presented in Section 4.3 have been implemented in the sand transport model to see if an accurate prediction of the concentration distribution and transport rates is possible for field conditions using a computed bed roughness height. The class-averaged ripple roughness values for the Egmond field tests predicted by the different models are presented in Table 4.6. The values in parenthesis represent the standard deviations within one class.

Table 4.6. Predicted ripple roughness heights (class-averaged values) for Egmond aan Zee field tests from G&M, Van Rijn, Nielsen and modified Nielsen bed roughness predictors. Standard deviations within one class are given between brackets.

ψ	D_{50}	k_s	k_s			
			G&M	Van Rijn	Nielsen	Nielsen modified
(-)	(mm)	(m)	(m)	(m)	(m)	(m)
1	25 (8)	0.24	0.170 (0.074)	0.145 (0.044)	0.022 (0.022)	0.073 (0.031)
2	54 (12)	0.24	0.073 (0.059)	0.078 (0.046)	0.010 (0.000)	0.038 (0.016)
3	94 (13)	0.24	0.027 (0.016)	0.027 (0.017)	0.010 (0.000)	0.021 (0.007)
4	152 (26)	0.24	0.019 (0.011)	0.014 (0.009)	0.010 (0.000)	0.017 (0.006)
5	215 (25)	0.24	0.011 (0.003)	0.010 (0.000)	0.010 (0.000)	0.012 (0.002)
6	298 (37)	0.24	0.011 (0.002)	0.010 (0.000)	0.010 (0.000)	0.012 (0.003)

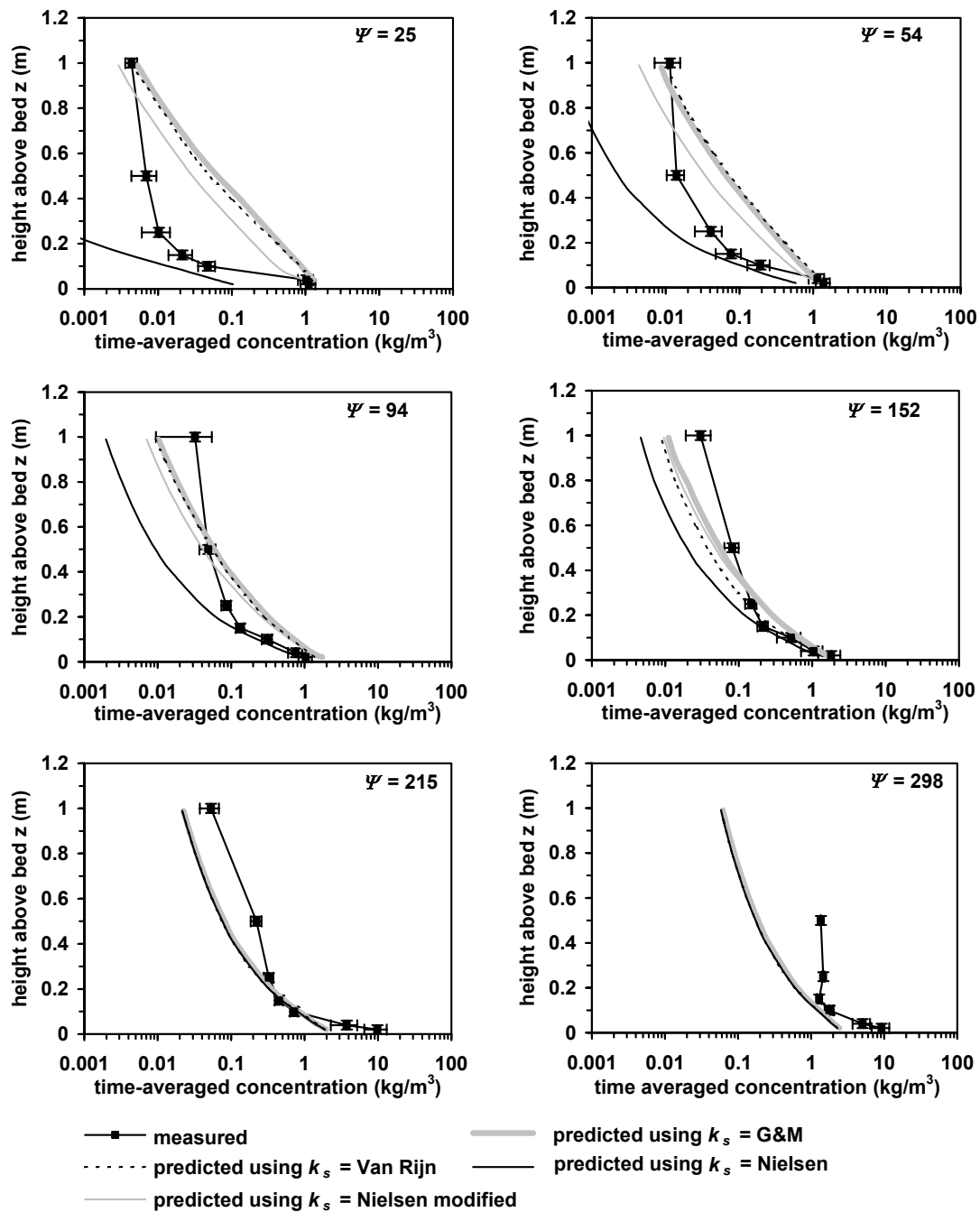


Figure 4.14. Effect of different bed roughness predictors on predicted time-averaged concentration distribution for Egmond aan Zee field tests, clustered for different values of ψ .

The average roughness values predicted by the G&M and the Van Rijn model are in the same range and show a similar trend with increasing mobility number, though the Van Rijn method produces smaller variations within one class. The modified Nielsen model predicts smaller roughness values for calm conditions and larger roughness values for moderate storm conditions than the G&M and Van Rijn models. The Nielsen bed

roughness predictor produces significantly smaller values than the other roughness models.

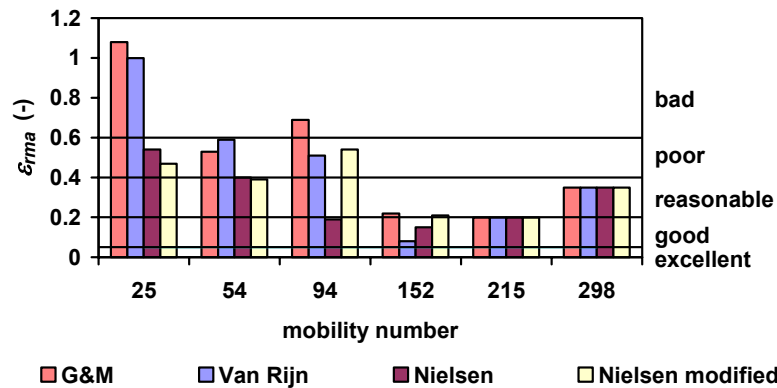


Figure 4.15. Relative mean absolute errors between measured and computed concentrations for Egmond aan Zee field tests using G&M, Van Rijn, Nielsen and modified Nielsen bed roughness predictors.

Figure 4.14 shows a comparison between the computed concentration profiles using the different roughness models and the measured concentrations. For small mobility numbers (calm conditions), the use of the G&M and Van Rijn roughness predictors result in a reasonable estimate of the near bed concentrations but the concentrations higher up in the water column are significantly overestimated, which leads to large ϵ_{rma} values (Figure 4.15). The smaller roughness heights predicted by the Nielsen and the modified Nielsen roughness models results in better agreement with the measured concentrations. For larger mobility numbers (moderate storm conditions), the effect of a different roughness predictor is less critical. Generally, over the range of conditions considered here, best concentration predictions are obtained using the Nielsen or the modified Nielsen roughness predictor.

Current-related transport rates

Figure 4.16 presents a comparison between the measured current-related transport rates (cross-shore) and the computed values using fixed bed roughness heights of $k_s = 0.01, 0.02, 0.03$ and 0.04 m, respectively. For the calm conditions a bed roughness height of 0.02 to 0.03 m gives best agreement between measured and computed transport rates. A smaller roughness height between 0.01 and 0.02 m yields better results for the moderate storm conditions.

Computed current-related transport rates using different ripple roughness predictors are compared to measured transports in Figure 4.17. Use of the G&M, Van Rijn and modified Nielsen roughness predictors leads to an overestimation of the current-related transport rates under calm conditions and an underestimation under moderate storm conditions. Generally, using these roughness predictors in a morphodynamic profile model will lead to smaller transport gradients across a nearshore profile and thus smaller morphological changes compared to using a constant roughness height. Use of the original Nielsen roughness predictor leads to an underestimation of the current-

related transport rates under all conditions, which is due to the relatively small value of $\alpha = 8$ in Equation (4.41) proposed by Nielsen.

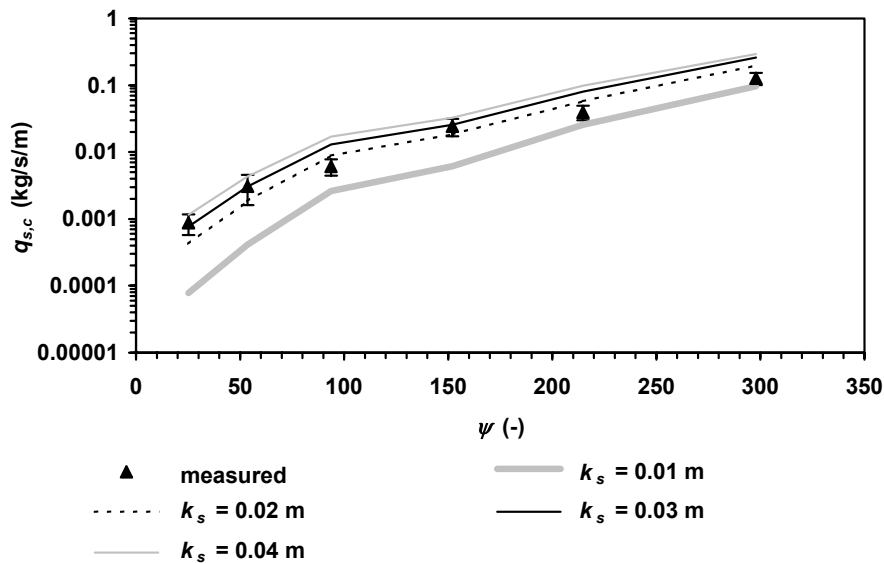


Figure 4.16. Measured and predicted class-averaged current-related transport rates (absolute values) in cross-shore direction; effect of bed roughness; Egmond aan Zee field tests.

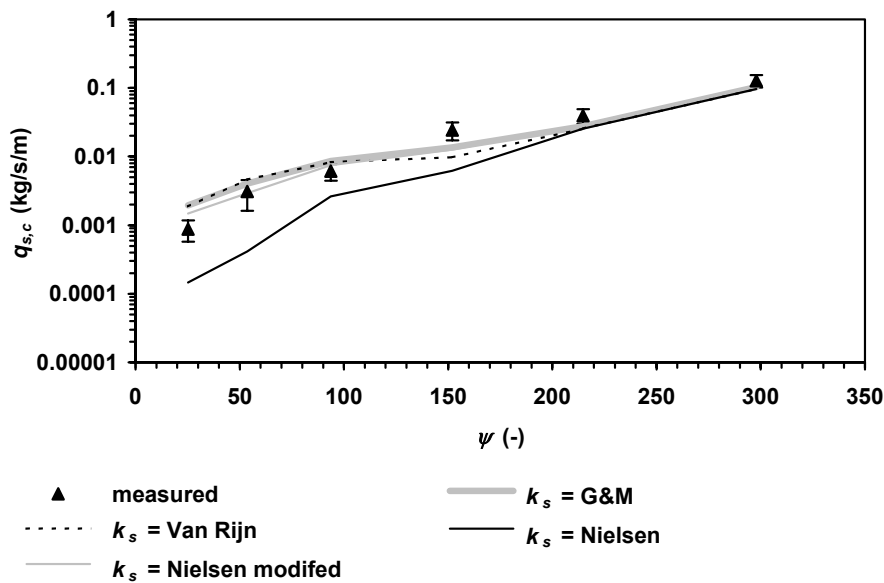


Figure 4.17. Measured and predicted class-averaged current-related transport rates (absolute values) in cross-shore direction; effect of different bed roughness predictors; Egmond aan Zee field tests.

4.4.4. DISCUSSION AND CONCLUSIONS

Sand suspension and concentration variation are controlled by the balance of near-bed skin friction and ripple development. Under low-energy fair weather conditions, ripples

are in equilibrium range and ripple roughness increases with bed shear stress. This increased ripple roughness causes strong vortex activity close to the bed and thus higher concentrations. Under high-energy storm conditions, ripple roughness decreases with bed shear stress. This reduces vortex activity close to the bed. These phenomena have an important effect not only on the magnitude of the suspended sediment concentrations but also on the timing of suspensions relative to the phase in the wave cycle. In case of a plane bed, sand is suspended at the onshore stroke of the wave, whereas in case of a rippled bed sand is ejected at flow reversal from on- to offshore direction, which leads to relatively large concentrations at the offshore stroke of the wave.

Using the sand transport model as described in Section 4.2, the present laboratory and field data of measured suspended sediment concentrations suggest a ripple roughness of about 0.03-0.04 m for low-energy conditions and about 0.015 m for high-energy storm conditions. Although the concentrations were still somewhat overestimated for the very calm conditions, reasonable agreement with the measured concentrations and current-related suspended transport rates was found using the modified Nielsen ripple roughness predictor based on a large set of laboratory and field data as proposed in Section 4.3. The Grant and Madsen (1982) and Van Rijn (1993) ripple roughness predictors overestimated these values for calm conditions and gave too small values for storm conditions. The Nielsen (1981) roughness predictor produced roughness values that were too small in all cases.

4.5. MODELLING THE WAVE-RELATED SUSPENDED TRANSPORT RATE

4.5.1. INTRODUCTION

The wave-related suspended sand transport is defined as the transport of sand particles by the oscillating velocity components (cross-shore orbital motion). Field and laboratory measurements have shown, that this oscillatory (time-dependent or intra-wave) component cannot be neglected and is strongly affected by the bedform dimensions (Vincent and Green, 1990; Osborne and Greenwood, 1992; Ruessink et al., 1998; Grasmeijer and Van Rijn, 1999).

The influence of the bed form dimensions on the wave-related suspended transport rate is best illustrated looking at the suspension pattern for a rippled bed and a plane bed under the same hydrodynamic conditions. The difference in suspension pattern between a plane bed and a rippled bed situation is illustrated here using two time series measured at approximately the same location near the coast of Egmond aan Zee (Section 2.6). The hydrodynamic conditions were comparable with $H_{1/3}/h \sim 0.25$, $\bar{v} \sim 0.05$ m/s, $\bar{u} \sim 0.05$ m/s and $T_p \sim 7$ s. An impression of the suspension mechanism and its relationship to the phase of the wave cycle was obtained by ensemble-averaging the suspension due to the passage of many waves. The ensemble-averaged wave was determined from the surface

elevation time series and the concentration was ensemble-averaged in relation to its phase in the wave cycle.

Two different suspension mechanisms are shown in Figure 4.18. The upper panel shows the normalized ensemble-averaged surface elevation, i.e. the significant wave profile normalized with its positive amplitude, and the concentration at $z = 0.02$ m over a plane bed. Two concentration peaks can be discerned during a single wave cycle. The largest concentration peak of about 0.48 kg/m^3 occurs during the onshore stroke of the wave and a smaller peak of 0.46 kg/m^3 during the offshore stroke. The concentration signal is more or less in phase with the wave cycle.

The patterns of suspension during measurement under rippled bed conditions are very different (lower panel Figure 4.18). The wave conditions are similar, although the waves are somewhat less asymmetric than for the plane bed conditions. The concentrations are an order of magnitude larger than those during the plane bed test. The ensemble-averaged concentrations show a structure of suspension correlation to the timing of flow reversal. A concentration peak of almost 4 kg/m^3 occurs at flow reversal from onshore to offshore direction, which is due to the ejection of sand-laden vortices from close to the bed up into the water column.

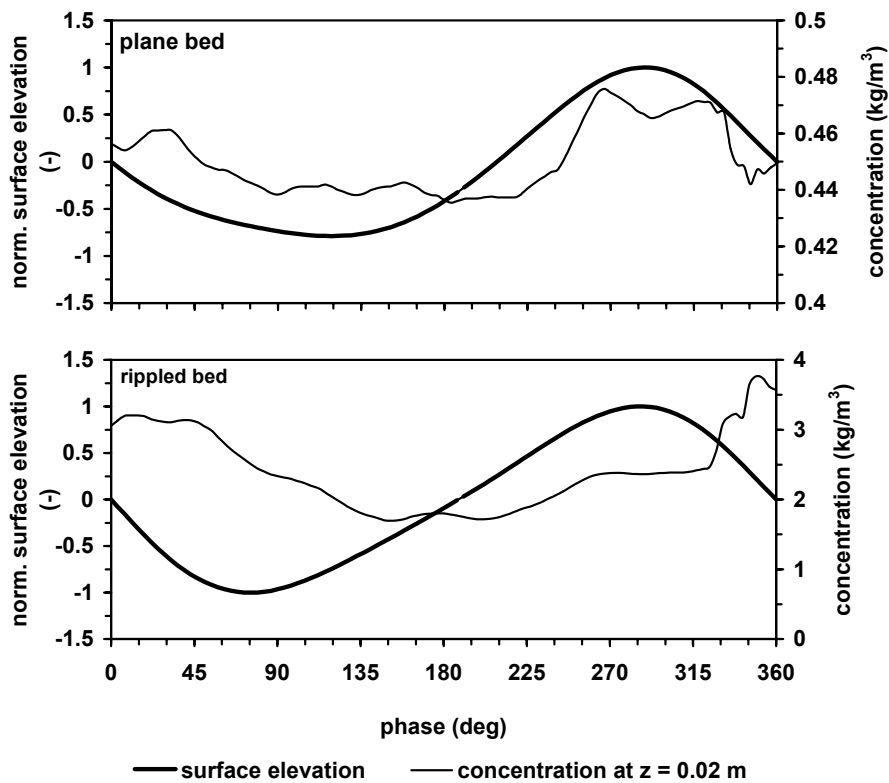


Figure 4.18. Ensemble-averaged surface elevation (normalized) and concentration in relation to the phase of the wave cycle for a test with a plane sand bed (upper panel) and a rippled sand bed (lower panel).

A point that has to be considered when interpreting the analysis results of Figure 4.18 is that the horizontal position of the instruments relative to the ripple crest is not known. The bed forms interacting with the near-bed currents impose distinct constraints on both the timing and magnitude of suspension events relative to the phase of the wave motion. Bosman and Steetzel (1986) and Osborne and Vincent (1996) analyzed sand concentration and velocity data at several positions along a rippled bed in laboratory conditions and found that the phase relationships between velocity and concentration are such that it could give completely opposite phase-relations between the velocity and the concentration values at different positions along the bed form. However, the phenomena shown in Figure 4.18 were observed in nearly all tests under similar conditions but with different bed forms. During the measurement period ripples migrated under the fixed measurement position. In this way the effects of the horizontal position relative to the ripple crest on the measured concentrations is averaged out. In addition, the ensemble-averaging procedure comprehends the averaging of a large number of data points maintaining phase information.

4.5.2. WAVE-RELATED SUSPENDED TRANSPORT FORMULA

In the present model, the oscillatory suspended transport component is accounted for by means of a quasi-steady approach as proposed by Houwman and Ruessink (1996). They considered the mean sediment concentration at a certain height above the bed to be the time-averaged value of two sediment concentration peaks per wave cycle, one during the onshore directed wave motion and the other during the offshore directed wave motion. Based on the velocity moments approach (Bagnold, 1966), the shape of the sediment concentration peaks was assumed to be equal to the shape of $|u|^3$. Houwman and Ruessink (1996) further assumed that each half wave cycle can be described with linear wave theory with different amplitudes but with equal duration, resulting in:

$$\begin{aligned}\bar{c}(z) &= k_p \rho_s \left[\left| \frac{2}{T} \int_0^{T/2} u_{on}^3 \sin^3 \omega t \, dt \right| + \left| \frac{2}{T} \int_{T/2}^T u_{off}^3 \sin^3 \omega t \, dt \right| \right] \\ &= k_p \rho_s \left[u_{on}^3 + u_{off}^3 \right] \left| \frac{2}{T} \int_0^{T/2} \sin^3 \omega t \, dt \right|\end{aligned}\quad (4.56)$$

where the left term is the time-averaged sediment concentration at height z above the bed, u_{on} and u_{off} refer to the onshore and offshore peak orbital velocity, respectively, T and ω are the wave period and angular frequency respectively, and k_p is a proportionality factor.

The oscillatory suspended sediment transport at a certain height z above the bed can be related to the fourth order moment $u|u|^3$. The wave-averaged oscillatory sediment transport rate $q(z)$ through a layer dz is then described by (Houwman and Ruessink, 1996):

$$\begin{aligned}
q_{s,w}(z) &= \frac{1}{T} \rho_s \int_0^T k_p u(t) |u(t)|^3 dt dz \\
&= k_p \rho_s [u_{on}^4 - u_{off}^4] dz * \frac{1}{T} \int_0^{T/2} \sin^4 \omega t dt \\
&= k_{as} \bar{c}(z) * \frac{u_{on}^4 - u_{off}^4}{u_{on}^3 + u_{off}^3} dz
\end{aligned} \tag{4.57}$$

with:

$$k_{as} = \frac{1}{2} \int_0^{T/2} \sin^4 \omega t dt \left(\int_0^{T/2} \sin^3 \omega t dt \right)^{-1} = \frac{9\pi}{64} \approx 0.44 \tag{4.58}$$

After integration over the water depth the oscillatory suspended sediment transport is obtained. This approach gives an upper limit for the suspended oscillatory sediment transport, assuming that there are no phase lags between $u(t)$ and $c(t)$ and that the sediment always responds instantaneously to the third power of the orbital velocity, which always results in an onshore directed oscillatory suspended sediment transport rate. However, both field (Houwman and Ruessink, 1996; Vincent and Green, 1990) and laboratory measurements (Grasmeijer and Van Rijn, 1999) have shown that phase lags are present, sometimes even resulting in an offshore directed oscillatory suspended sediment transport rate. Therefore, Houwman and Ruessink (1996) derived an empirical expression for the efficiency factor k_{as} based on field measurements:

$$\begin{aligned}
k_{as} &= [(2.5z - 0.292)u_{on} - 3z + 0.42] \tanh(6.5(z_{max} - z)) \\
\text{if } k_{as} < 0 \text{ then } k_{as} &= 0
\end{aligned} \tag{4.59}$$

A tanh function was used to force the efficiency coefficient to zero at height $z = z_{max}$ above the bed to prevent large oscillatory fluxes at high elevations above the bed. Houwman and Ruessink (1996) used a constant value of $z_{max} = 0.6$ m. Houwman and Ruessink (1996) determined the k_{as} coefficient based on mean concentrations computed with the Van Rijn (1993) model, and measured significant onshore and offshore orbital velocities. They observed the efficiency coefficient to range between 0 and 0.2 instead of having a fixed value of 0.44. Laboratory measurements by Dang Huu Chung and Grasmeijer (1999) also have indicated a value of about 0.2.

In the present model, a similar approach is used as the one proposed by Houwman and Ruessink (1996). However, instead of a high-frequency transport varying with height above the bed, in the present approach the high-frequency suspended transport rate is computed as a depth-integrated value between the reference height z_a and 0.6 m above the bed. Above 0.6 m the correlations between the velocity and concentration signals are assumed to be small.

$$q_{s,w} = k_{as} \frac{u_{on}^4 - u_{off}^4}{u_{on}^3 + u_{off}^3} \int_{z_a}^{0.6m} c dz \tag{4.60}$$

In Section 4.5.3, the k_{as} value is determined based on measurements of sediment concentration and transport in the Delta Flume of Delft Hydraulics. A comparison is made between measured and predicted wave-related transport rates. The wave-related transport rate under field conditions is discussed in more detail based on measurements near the coast of Egmond aan Zee in the Netherlands. Measured and predicted wave-related transport rates under these conditions are compared in Section 4.5.4.

4.5.3. LARGE-SCALE LABORATORY EXPERIMENTS

Data from the Delta Flume experiments described in Section 2.4 are used here to test the formulation for the wave-related transport rate. Substituting the measured time-averaged concentrations and significant onshore and offshore peak orbital velocities ($u_{1/3,on}$, $u_{1/3,off}$) into Equation (4.60) in combination with the measured wave-related transport rates facilitates the determination of the efficiency factor k_{as} . Using a least-squares-method, $k_{as} = 0.25$ and 0.14 was found for coarse sand ($D_{50} = 0.33$ mm) and fine sand, ($D_{50} = 0.16$ mm), respectively. Figure 4.19 shows the measured and computed high-frequency suspended transport rates as a function of mobility number. The data presented in this figure are depth-integrated between the lowest and the highest measurement points. Average values of three or more tests are presented. The error bars indicate the standard error between the tests.

The measured wave-related transport rates for the coarse sand are relatively large compared to the fine sand (Figure 4.19), owing to the presence of steep ripples during the coarse sand experiment, leading to larger near-bed concentrations. The ripples during the fine sand tests were flatter. The difference in near-bed concentrations between the two test series can be observed from Figure 4.8 in the previous section. Equation (4.60) gives quite reasonable agreement with the measured wave-related transport rates when using an efficiency factor of 0.25 for the coarse sand and 0.14 for the fine sand. The computed transport rates are within 30% of the measured values. Although the present laboratory conditions are limited in range (relatively calm conditions without a current), these k_{as} values give an indication of the magnitude this factor has under comparable field conditions.

The efficiency coefficient k_{as} can be seen as a measure for the coherence between the velocity and the concentration signal, based on cross-spectral analysis. Ruessink et al. (1998) found this coherence to be insignificant at all frequencies for relatively calm conditions ($H_{1/3}/h < 0.29$ and $H_{1/3}/h < 0.35$). Measurements under more energetic conditions showed significant coherences around the wave spectrum peak period. The coherence decreased with height above the bed. This is consistent with the change in bed form dimensions with the conditions. Where ripples exist under relatively calm conditions, the correlation between velocity and concentration is expected to be small because of the complex turbulence related to the flow over these bed forms. This would lead to a small efficiency coefficient. The present data suggest a value of about 0.2 . Under more energetic conditions, the bed becomes plane and the correlation between velocity and concentration increases. Under sheet flow conditions ($\psi > 250$) largest correlations are expected. Assuming no phase lags between the velocity and the concentration, under these conditions the efficiency coefficient might reach the upper limit of 0.44 according to Equation (4.58).

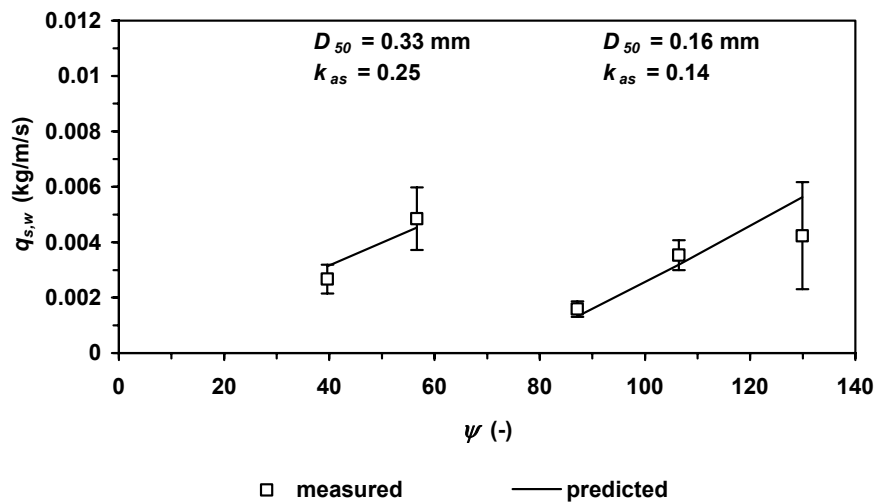


Figure 4.19. Measured and predicted wave-related suspended transport rates as a function of mobility number. The predictions are based on Equation (4.60) using measured velocities and measured concentrations.

Figure 4.20 shows the effect of changing the roughness height on the predicted wave-related suspended sediment transport rate. The predicted transport rates are based on predicted concentrations and using $k_{as} = 0.25$ and 0.14 for the coarse and the fine sand, respectively. The model shows good agreement with the measured wave-related transport rates using a roughness height of about 0.03 m for the tests with coarse sand (tests A and B). A smaller roughness height between 0.01 m and 0.02 m suffices for the tests with fine sand (tests C, D and E). This is consistent with the predictions of the suspended concentration profiles in Section 4.4.2.

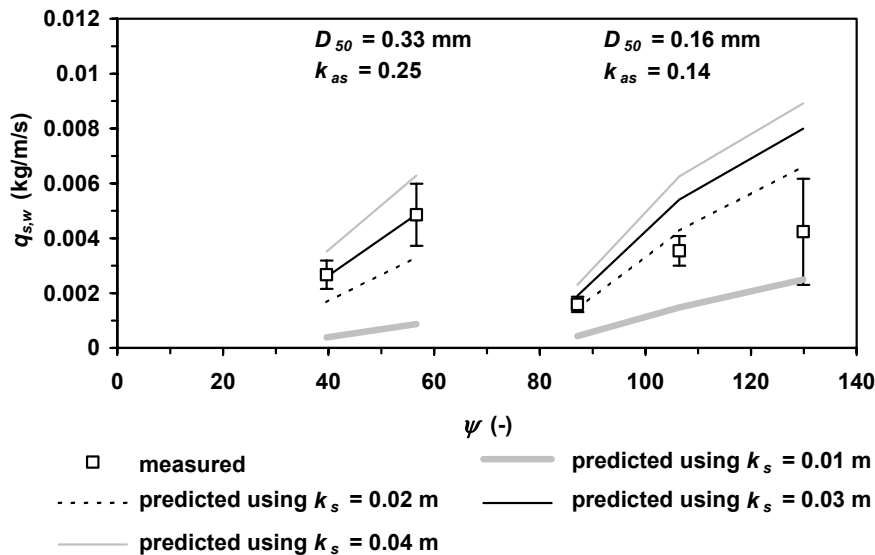


Figure 4.20. Measured and predicted wave-related suspended transport rates as a function of mobility number and for varying roughness heights. The predictions are based on Equation (4.60) using measured velocities and predicted concentrations.

4.5.4. LARGE-SCALE FIELD EXPERIMENTS

The data used here were measured across a nearshore bar near the coast of Egmond aan Zee in the Netherlands (Section 2.6). Sand transport measurements were performed at eight elevations above the bed from 0.02 to 1.0 m. More than 80 tests were done. The tests were class-averaged based on the mobility number. Figure 4.21 shows the measured and computed class-averaged wave-related transport rates as a function of the mobility number. The computed wave-related transport rate increases with the mobility number. In contrast, the measured wave-related transport stays more or less constant or even decreases for mobility values between 25 and 152. Under these conditions, the presence of ripples causes vortex shedding, which results in relatively large phase lags between the velocity and the concentration. The measured wave-related transport increases for larger mobility values, although the scatter in the measurements is quite large in this region.

Increasing the bed roughness in the model results in an increase of the suspended sediment load and hence the transport rate (Figure 4.21). Increasing the roughness with a factor 4 leads to 3-4 times higher wave-related transport rates. The model predicts wave-related transport rates that are much higher than the measured values. Best agreement is obtained using a relatively small roughness height of 0.01 m, although even then the predictions are too large. However, using this roughness height would lead to an underestimation of the suspended sediment concentrations (see Figure 4.12). The overestimation of the wave-related transport rates is therefore not so much a result of a bad prediction of the suspended sediment concentrations but more the effect of the efficiency factor in Equation (4.19) being too large for the Egmond field site. In addition, not only the amount of sediment in suspension in Equation (4.19) depends on the bed roughness, but also the efficiency factor is likely to depend on the bed form dimensions. Roughly, in case of a plane bed, sediment is brought into suspension at the onshore stroke of the wave, whereas in case of a rippled bed the sediment is stirred up around flow reversal or at the offshore stroke of the wave. These two phenomena would lead to a different value of the efficiency factor. In case of the concentrations and velocities being out of phase, the efficiency factor might even be negative.

The computed wave-related transport rates using different bed roughness predictors are presented in Figure 4.22. It can be seen that the G&M, Van Rijn and the modified Nielsen bed roughness predictors yield comparable results (difference less than a factor 2). Use of the Nielsen bed roughness predictor results in smaller wave-related transport rates than when using the other models. An important effect of the use of a bed roughness predictor compared to using a fixed bed roughness of for example 0.02 m in the sediment transport model is the difference in trend with increasing mobility number. The wave-related transport rate becomes more than 300 times larger with increasing mobility number from 25 to 298 when using a fixed bed roughness of 0.02 m (Figure 4.21). In contrast, use of e.g. the G&M bed roughness predictor leads to an increase with a factor 50 in this case. Applying a bed roughness predictor in a cross-shore profile model instead of a fixed roughness therefore leads to more realistic sediment transport results and smaller gradients of the wave-related transport rate.

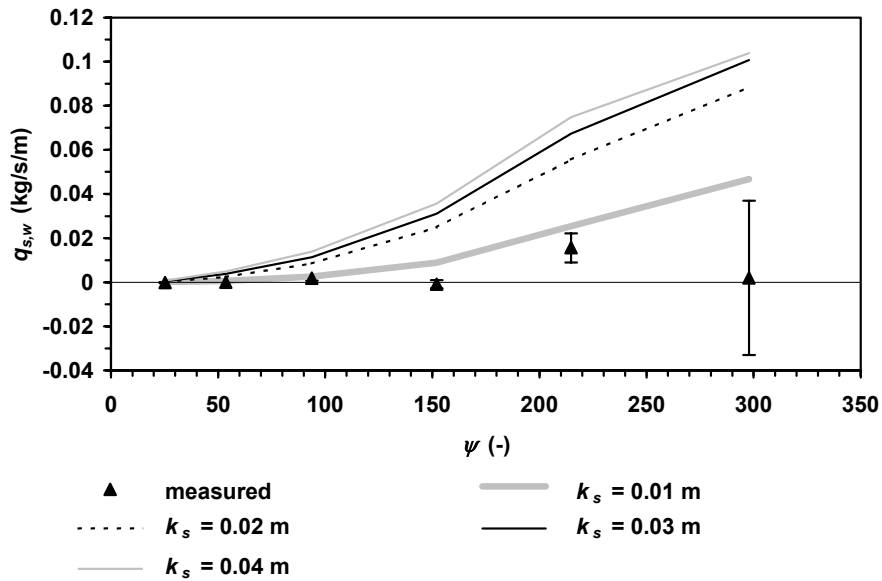


Figure 4.21. Measured and computed class-averaged wave-related transport rates in cross-shore direction ($k_{as} = 0.2$); effect of bed roughness; Egmond aan Zee.

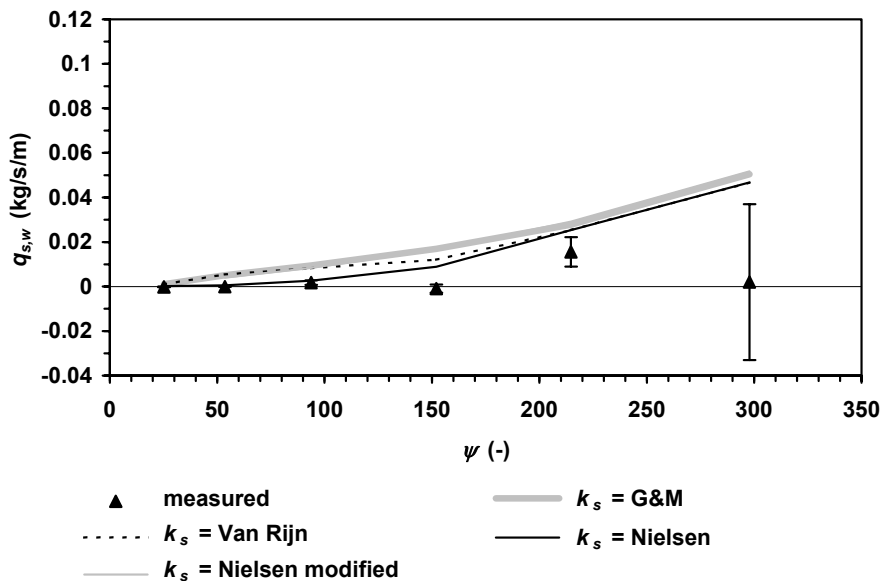


Figure 4.22. Measured and computed class-averaged wave-related transport rates in cross-shore direction ($k_{as} = 0.2$); effect of different bed roughness predictors; Egmond aan Zee.

4.5.5. DISCUSSION AND CONCLUSIONS

The present laboratory data of measured concentrations and velocities suggest that the wave-related suspended transport rate can be modelled with reasonable accuracy using a method proposed by Houwman and Ruessink (1996). The efficiency factor in this method, which can be seen as a measure for the coherence between the velocity and the

sediment concentrations, depends on the hydrodynamics and associated bed form conditions. Where ripples exist under relatively calm conditions, the coherence between velocity and concentration is small because of the complex turbulence related to the flow over these bed forms. This leads to a small efficiency coefficient and the present laboratory data suggest a value between 0.14 and 0.25. However, the concentration and velocity measurements were done at elevations between 0.065 and 1.0 m above the sandbed, while much of the wave-related transport rate takes place nearer to the bed. Therefore, the values for the efficiency coefficient based on the laboratory data are only indicative for the values that might be expected under relatively calm wave conditions in the field. Using an efficiency factor of 0.2 (midrange between values determined from the laboratory experiments) results in wave-related transport rate predictions within a factor 2 of the measured values. Under more energetic conditions, the bed becomes plane and the correlation between velocity and concentration increases. Under sheet flow conditions ($\psi > 250$) larger correlations are expected. Assuming no phase lags between the velocity and the concentration, under these conditions the efficiency coefficient might reach the theoretical upper limit of 0.44.

Using an efficiency factor of 0.2, the Houwman and Ruessink (1996) method overestimates wave-related transport rates measured between 0.02 and 1.0 m above the seabed near the coast of Egmond aan Zee. The predicted values increase too strongly with mobility number when using a fixed bed roughness height. Although better agreement is obtained using a bed-roughness predictor, the field measurements suggest the efficiency coefficient to be smaller than 0.2 under relatively calm wave conditions.

4.6. MODELLING THE BED-LOAD TRANSPORT RATE

4.6.1. INTRODUCTION

The total load of moving sediment is generally considered to be composed of two parts, the suspended load and the bed-load. The bed load has been defined in different ways depending on the context. In relation to measurements it is often defined as that part of the total load, which travels below a certain level (often the lowest measurement point) or the part that gets caught in bed-load traps. For modelling purposes it is more convenient to define the bed-load as the mode of transport that involves rolling, sliding and hopping of grains along the bed, in which the weight of the grains is borne by contact with other grains rather than by the upward fluid motions as is the case for the suspended load transport. However, a given grain may well be supported partly by the forces between grains and partly by fluid drag and hence contribute to both the suspended load and the bed-load. This makes the bed-load hardly measurable in situations where suspended sediment is present as well.

In the present study, the instruments used for measuring the suspended sediment load transport could be adjusted at a minimum elevation of 0.02 m above the bed. This is in the order of the thickness of the wave-boundary layer. Therefore, pragmatically, herein the bed-load is defined as that part of the sediment that travels below 0.02 m above the bed.

4.6.2. COMPARISON OF BED-LOAD TRANSPORT FORMULAE

At present, it is not possible to measure the bed-load transport rate under field conditions. Therefore, the Van Rijn (2000) bed-load transport formulation as used in the present cross-shore profile model (see Section 4.2.3), is compared to two commonly used bed-load transport formulae, i.e. the model by Ribberink (1998) and the model by Bailard (1981).

The formulae of Ribberink (1998) and Bailard (1981) are based on a multi-wave approach, using the complete measured velocity time series as an input, whereas the method of Van Rijn (2000) is based on a single-wave approach. This latter method involves a schematized representative horizontal velocity profile that is reconstructed from the significant on- and offshore peak near bed orbital velocities, which means that the bed-load under the smaller (and less asymmetric) waves is not taken into account. The intra-wave variation of the orbital velocities is represented by a sine function. The formula of Ribberink was slightly modified to simplify the computations.

In Section 4.6.3, the formulations are tested against measurements in the Grosser Wellenkanal of the Universities Hannover/Braunschweig. In Section 4.6.4, the models are compared using the Egmond aan Zee field data.

The bed-load transport rate from the Van Rijn model is based on the significant wave height and significant on- and offshore peak orbital velocities; see Equation (4.20).

Bed-load transport formula by Van Rijn (2000)

The Van Rijn (2000) bed-load transport formula is given by

$$\overline{q_b} = 0.5 \frac{D_{50} \rho_s u_* T}{D_*^{0.3}} \quad (4.61)$$

where D_{50} is the median grain diameter [m], ρ_s is the sediment density [kg/m^3], u_* is the bed shear velocity [m/s], T is the nondimensional bed shear stress [-], D_* is a nondimensional particle parameter [-]. The overbar denotes time-averaging. The instantaneous bed shear velocity and the nondimensional bed shear stress are computed from the significant on- and offshore peak orbital velocities.

Bed-load transport formula by Ribberink (1998)

The near-bed transport rate is expressed as (Ribberink, 1998):

$$\overline{q_b} = m \overline{(|\theta'| - \theta_{cr, shields})^n} \frac{\theta'}{|\theta'|} \rho_s \sqrt{(s-1)gD_{50}^3} \quad (4.62)$$

where s is the relative density of sediment (ρ_s/ρ) [-], g is acceleration of gravity [m/s^2], m and n are coefficients [-], θ' is the instantaneous nondimensional bed shear stress [-], $\theta_{cr, shields}$ is the critical nondimensional bed shear stress [-]. The overbar denotes time-averaging.

The instantaneous nondimensional bed shear stress θ' is calculated from the velocity time series as described by Equation (4.64). The threshold value $\theta_{cr, shields}$ is calculated according to the classical Shields curve. Ribberink (1998) calibrated Equation (4.62)

against a large set of laboratory data (steady flows and oscillatory flows) and found the following coefficients:

$$m = 11$$

$$n = 1.65$$

Based on data from a large oscillating water tunnel, Grasmeyer et al. (1999) found that the Ribberink (1998) and the Bailard (1981) approach (also tested here) gave comparable results. The standard error between the measured and computed transport rates was less than 20%.

Bed-load transport formula by Bailard (1981)

The bed-load transport rate can be estimated with the Bailard (1981) energetics expression as

$$\overline{q_b} = \frac{\rho_s}{(\rho_s - \rho)} \frac{\rho}{g} C_f \frac{\varepsilon_b}{\tan \phi} \overline{|u_t|^2} u \quad (4.63)$$

where ρ is the mass density of water [kg/m³], C_f is the drag coefficient [-], ε_b is an efficiency factor [-] u is the instantaneous cross-shore flow [m/s], u_t is the total instantaneous velocity vector [m/s], $\tan \phi$ is the tangent of angle of repose (≈ 0.63). The overbar denotes time-averaging.

A value has to be specified for the coefficients C_f and ε_b . The reader is referred to Nairn and Southgate (1993) for an extensive overview of the calibration of the efficiency factors. Stive (1986) proposed that the friction coefficient C_f may be estimated by $0.5f_{cw}$. Bailard (1981) proposed the efficiency factor ε_b to be 0.21. These values are used here. The wave-current friction factor f_{cw} was computed as described by Equation (4.66). Measured velocity time series were used in Equation (4.63).

Instantaneous nondimensional bed shear stress

The instantaneous nondimensional bed shear stress is computed as:

$$\theta' = \frac{\tau'}{(\rho_s - \rho)gD_{50}} \quad (4.64)$$

An approach as suggested by Grant and Madsen (1979) is used by assuming that the bed shear stress can be expressed as a quadratic function of the combined wave-current velocity u at some height z above the bed (above the wave boundary layer):

$$\tau' = \frac{1}{2} \rho f_{cw} u |u| \quad (4.65)$$

The quadratic friction law is used together with a weighted friction coefficient for currents and waves. Following van Van Rijn (1993):

$$f_{cw} = \alpha f_c + (1 - \alpha) f_w \quad (4.66)$$

with:

$$\alpha = \frac{v_{r,\delta}}{v_{r,\delta} + u_{w,\delta}} \quad (4.67)$$

$$u_{w,\delta} = \frac{1}{2}(u_{1/3,on} + u_{1/3,off}) \quad (4.68)$$

$$f_c = 0.24 \left(\log \left(\frac{12h}{k_{s,c}} \right) \right)^{-2} \quad (4.69)$$

where $v_{r,\delta}$ is the mean near-bed velocity at the top of the wave boundary layer and $u_{w,\delta}$ is the peak near-bed orbital velocity without mean current.

The wave-related friction factor is calculated according to Swart (1974):

$$f_w = \exp \left(-6 + 5.2 \left(\frac{\hat{A}_\delta}{k_{s,w}} \right)^{-0.19} \right) \quad (4.70)$$

$$f_{w,max} = 0.3 \quad (4.71)$$

with:

$$\hat{A}_\delta = \frac{2\pi}{T_p} \hat{u}_\delta \quad (4.72)$$

The wave-related roughness height $k_{s,w}$ is computed following Ribberink (1998):

$$\begin{aligned} k_{s,w} &= D_{50} & \text{for } |\overline{|\theta|}| < 1 \\ k_{s,w} &= D_{50} \left(1 + 6 \left(|\overline{|\theta|}| - 1 \right) \right) & \text{for } |\overline{|\theta|}| \geq 1 \end{aligned} \quad (4.73)$$

The current-related roughness height $k_{s,c}$ is computed following Ribberink (1998):

$$k_{s,c} = \max \{ 3D_{90}, k_{s,w} \} \quad (4.74)$$

4.6.3. COMPARISON OF BED-LOAD FORMULAE USING LARGE-SCALE FLUME DATA

The data used here were measured during experiments in the Grosser Wellenkanal of the Universities Hannover/Braunschweig (Section 2.5). Sand was used with grain size characteristics: $D_{10} = 0.14$ mm, $D_{50} = 0.23$ mm, $D_{90} = 0.34$ mm. Bed profiles were measured to determine the small-scale morphology and the bed profile changes were determined to get a rough estimate of the total sediment transport rate. The bed profiles were measured along the centerline of the flume using a mobile carriage. Irregular waves were generated with a significant wave height of $H_{m0} = 1.25$ m and a wave spectrum peak period of $T_p = 6.0$ s. The water depth was kept constant at a value of 3.5 m at the test section.

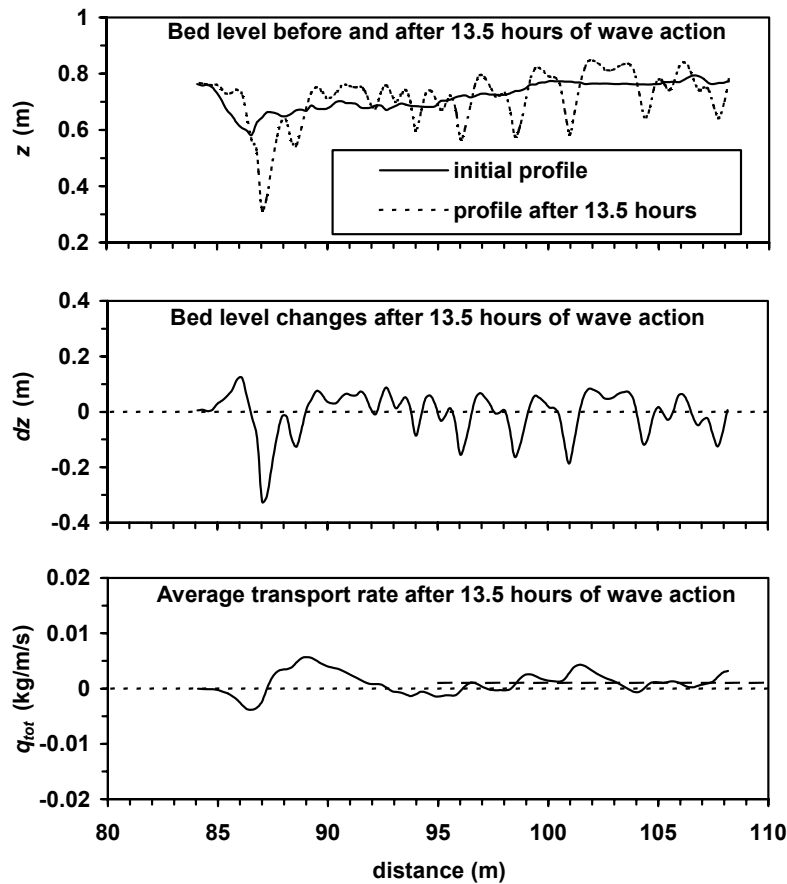


Figure 4.23. Bed level changes and resulting total net transport rates during 13.5 hours of testing with irregular waves, $H_{m0} = 1.25$ m, $h = 3.5$ m, $T_p = 5.9$ s, $D_{50} = 0.23$ mm.

Bed levels before and after 13.5 hours of testing, the resulting bed level changes and the net total transport rates based on these changes are presented in Figure 4.23. This figure clearly shows the generation of bed forms during the tests (height of about 0.2 m; length of about 2 to 3 m). The net total transport rate varies significantly along the measured profile, ranging between -0.004 and 0.006 kg/s/m. The oscillations in the transport patterns between $x = 95$ and 108 m are most likely caused by ripple migration. The bed-averaged net transport rate is about 0.001 ± 0.003 kg/s/m. The instruments were deployed at $x = 113$ m. The profile soundings could only be performed up to $x = 108$ m because of the dimensions of the tripod in which the instruments were mounted. Hence, the effect of the bed profile changes between $x = 108$ and 113 m on the net transport could not be taken into account.

The net transport rate at the position of the tripod ($x = 113$ m) is assumed to be equal to the bed-averaged transport rate between $x = 95$ and 108 m, being 0.001 ± 0.003 kg/s/m. It is noted that the bed level soundings have only been performed in the middle of the flume. Much more longitudinal sounding tracks (at least 5) across the flume width are required for accurate determination of net transport rates.

Table 4.7 presents the measured suspended transport components and the computed bed-load transport rates based on measured instantaneous velocities near the bed

(average over 12 tests). The net suspended transport rate above $z = 0.02$ m is dominated by the onshore-directed high-frequency oscillatory component $q_{s,high}$ and the offshore-directed time-averaged current-related component $q_{s,c}$. The sum of the two results in an onshore directed net suspended transport rate q_s . The bed-load transport rates computed with the different models are all of the same order of magnitude as the suspended load transport rate and offshore directed.

Table 4.7. Measured depth-integrated suspended transport rates and computed bed-load transport rates. The depth-integration is defined between $z = 0.02$ and 1.0 m. Grosser-Wellenkanal experiments. A negative sign denotes an offshore direction; a positive sign denotes an onshore direction.

	q_s	$q_{s,high}$	$q_{s,low}$	$q_{s,c}$	$q_{b, VanRijn}$	$q_{b, Ribberink}$	$q_{b, Bailard}$
	(kg/m/s)	(kg/m/s)	(kg/m/s)	(kg/m/s)	(kg/m/s)	(kg/m/s)	(kg/m/s)
average	0.009	0.019	-0.002	-0.008	-0.009	-0.010	-0.010
st. error	(± 0.002)	(± 0.002)	(± 0.000)	(± 0.000)	(± 0.001)	(± 0.001)	(± 0.001)

In Table 4.8 a comparison is made between transport rates based on concentration and velocity measurements (averaged over 12 tests) and the transport rate based on bed level changes. It is noted that the bed level soundings have only been performed in the middle of the flume. Much more sounding tracks (at least 5) across the flume width are required for accurate determination of net transport rates. Despite this, the comparison shows that both methods result in a total net transport rate that is almost zero.

Table 4.8. Comparison of transport rates measured in the Grosser Wellenkanal.

	$q_{s, measured}$	$q_{b, computed}$	q_{total}
Based on velocities and concentrations	0.009 (± 0.002)	-0.010 (± 0.001)	-0.001 (± 0.003)
Based on bed level changes	-	-	0.001 (± 0.003)

4.6.4. COMPARISON OF BED-LOAD FORMULAE USING FIELD DATA

Herein the bed-load transport rates computed with the Van Rijn (2000) formulation are compared to results from formulae of Ribberink (1998) and Bailard (1981) using the Egmond aan Zee field data (Section 2.6). The transport rates are presented as a function of the mobility number in Figure 4.24. The formulae by Ribberink and Bailard yield comparable results. The bed-load transport computed with these models is onshore directed for relatively calm conditions and changes in direction for mobility values between 50 and 100. Both models compute an offshore-directed bed-load transport for moderate storm conditions.

The Van Rijn (2000) bed-load transport model shows a very different behavior, with onshore-directed transport rates for nearly all conditions, and values that are significantly larger than the values from the other two models. The difference between the Van Rijn (2000) model and the Ribberink (1998) and Bailard (1981) was quantified

using the relative mean absolute error ε_{rma} , which for the Van Rijn (2000) and the Ribberink (1998) model becomes:

$$\varepsilon_{rma} = \frac{\overline{|q_{b, Van Rijn} - q_{b, Ribberink}|} - q_{b, error}}{\overline{|q_{b, Ribberink}|}} \quad (4.75)$$

in which the class-averaged bed-load transport rates were used and $q_{b, error}$ was taken to be the standard error within one class. The overbar denotes averaging over all classes. The ε_{rma} between the Van Rijn (2000) model using $H_{1/3}$ and the Ribberink (1998) and Bailard (1981) models was 1.09 and 2.18, respectively.

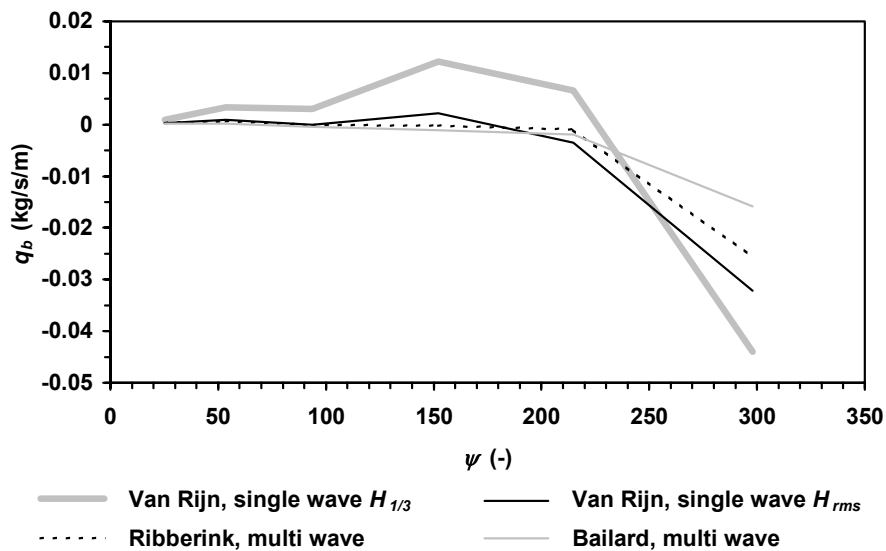


Figure 4.24. Computed class-averaged bed-load transport rates in cross-shore direction; comparison of different bed-load transport models. The computations are based on wave height and velocity measurements near the coast of Egmond aan Zee, The Netherlands.

The discrepancy between Van Rijn (2000) model using $H_{1/3}$ and the Ribberink (1998) and Bailard (1981) is likely due to the fact that the Van Rijn (2000) model is based on a single wave in which the intra-wave velocity variation is reconstructed from the on- and offshore peak near bed orbital velocities as computed from $H_{1/3}$. This results in a relatively strong effect of the higher waves. In contrast, the Ribberink (1998) and Bailard (1981) models use the complete velocity time series as an input, in this way taking into account the contribution of the smaller waves, which after time-averaging leads to a smaller bed-load transport rate and under calm conditions to a stronger effect of the mean current. This idea was tested by computing the bed-load transport rates with the Van Rijn (2000) model using the measured velocity time series instead of using the reconstructed velocity profile. The model gave results (not presented here) comparable to the Ribberink (1998) and Bailard (1981) model in this case. Better comparison with the Ribberink (1998) and Bailard (1981) models was obtained also by using the H_{rms} instead of the $H_{1/3}$ to computed the on- and offshore near-bed orbital velocities in the Van Rijn (2000) model. The relative mean absolute error ε_{rma} between the Van Rijn (2000) model using H_{rms} and the Ribberink (1998) and Bailard (1981) models was 0.20

and 0.81, respectively. Computed class-averaged bed-load transport rates and standard errors within one class are given in Table 4.9.

Table 4.9. Class-averaged bed-load transport rates computed with 1) Van Rijn model using $H_{1/3}$, 2) Van Rijn model using H_{rms} , 3) Ribberink model, 4) Bailard model. Standard errors \mathcal{E}_{std} within one class are given also.

ψ	$q_{b, Van Rijn}$ with $H_{1/3}$		$q_{b, Van Rijn}$ with H_{rms}		$q_{b, Ribberink}$		$q_{b, Bailard}$	
	average	\mathcal{E}_{std}	average	\mathcal{E}_{std}	average	\mathcal{E}_{std}	average	\mathcal{E}_{std}
25	0.0009	0.0003	0.0003	0.0001	0.0002	0.0001	0.0002	0.0001
54	0.0034	0.0008	0.0010	0.0003	0.0006	0.0004	0.0002	0.0002
94	0.0030	0.0019	0.0000	0.0008	-0.0001	0.0008	-0.0005	0.0005
152	0.0122	0.0028	0.0022	0.0014	-0.0003	0.0023	-0.0011	0.0013
215	0.0066	0.0039	-0.0035	0.0018	-0.0010	0.0019	-0.0019	0.0011
298	-0.0440	0.0048	-0.0321	0.0028	-0.0257	0.0171	-0.0158	0.0090

4.6.5. DISCUSSION AND CONCLUSIONS

Results from the bed-load transport formulation by Van Rijn (2000), as used in the present cross-shore profile model, were compared to results from the Ribberink (1998) and Bailard (1981) bed-load transport formulae based on large-scale wave flume data and Egmond aan Zee field data. Comparison with irregular wave tests in a large scale wave flume showed that the Ribberink (1998), the Bailard (1981) and the Van Rijn (2000) model predict bed-load transports of the same order of magnitude as values determined from bed level changes and velocity and concentration measurements. The comparison was made for one test condition with a wave height of $H_{1/3} = 1.25$ m, a wave spectrum peak period of $T_p = 6$ s and a water depth of $h = 3.5$ m, no current was present. Comparing the three models for a wider range of field conditions however revealed that the Van Rijn (2000) model predicts bed-load transport rates that are of a different order of magnitude and show a different direction than the bed-load transport rates predicted by the other two models. This is likely due to the fact that in the Van Rijn (2000) model the instantaneous bed shear stress is based on a single wave in which the intra-wave velocity variation is reconstructed from the significant on- and offshore peak near bed orbital velocities. This results in a relatively strong effect of the higher waves. In contrast, the Ribberink (1998) and Bailard (1981) models use the complete velocity time series as an input, in this way taking into account also the contribution of the smaller waves, which after time-averaging leads to a smaller bed-load transport rate and under calm conditions to a stronger effect of the mean current. Use of the complete velocity time series in the Van Rijn model yielded results similar to the other two bed-load transport models. This suggests that the use of one single representative wave is not enough for an accurate prediction of the near bed transport rates. For an accurate prediction of the bed-load transport rates it appears to be necessary to use a multi-wave approach. Another option is to modify the parameterization for the bed-load transport rate when using a single-wave approach. Using the root-mean-square on- and offshore

peak orbital velocities instead of the significant values gave more realistic bed-load transport rates in the present single-wave model, though further study is necessary to accurately parameterize the bed-load transport rate based on a single wave approach. However, the importance of an accurate prediction of the bed-load transport rate also depends on the relative importance of this component compared to the suspended load component. This will be discussed in the next section.

Another important aspect that has to be considered here is the use of bed-load transport formulae in the ripple regime where they were actually derived for sheet flow conditions only. Although the experiments in the Grosser Wellenkanal have shown that the models predict bed-load transports of the same order of magnitude as the measured values, the uncertainties are large (estimated to be about a factor 2-3). Moreover, the measurements in the Grosser Wellenkanal were done for only one test condition. Whether the bed-load models used here are valid under field conditions with combined wave and currents remains to be seen, and should still be investigated. At present, the bed-load transport rates under conditions in the ripple regime are not well understood because neither the velocity distribution nor the concentrations through the bed-load layer are well known. In addition, the calibration of the bed-load transport formulae is based mainly on data from oscillating water tunnels. It is still uncertain whether these bed-load transport rates measured in a water tunnel are comparable to those present under field conditions.

4.7. RELATIVE CONTRIBUTION OF TRANSPORT COMPONENTS

4.7.1. INTRODUCTION

The net suspended cross-shore transport rate depends upon the contributions from: 1) short waves, 2) long waves, and 3) mean currents. The short wave component is often directed onshore under skewed shoaling waves. However, the opposite can occur in response to bed-form changes and the presence or absence of separation vortices. The long wave component is generally directed offshore in the presence of group-forced bound long waves (Ruessink, 1998a). Mean currents are directed offshore above the wave boundary layer and increase in magnitude as waves break. Together with an increasing time-averaged sediment concentration this can result in an offshore-directed sediment flux dominated by the mean transport component.

The overall net transport rate depends on the relative contribution of each of these transport components. The present field experiments near the coast of Egmond aan Zee (Section 2.6) provide field data on the local time-varying suspended sediment flux at 7 elevations above the seabed under shoaling and breaking waves in a barred nearshore environment. These measurements are used to evaluate the roles of the different transport components in the cross-shore transport of suspended sediment. These transport rates are then compared with results from the model as described in Section 4.2 and the relatively simple sediment transport model of Bailard (1981).

4.7.2. MEASURED TRANSPORT RATES

Figure 4.25 illustrates the vertical variations in the current- and wave-related transport components, the sum of which equals the net suspended sediment transport rate. The data shown in this figure represent class-averaged values of the Egmond aan Zee field data. Error bars are not shown for reasons of legibility. The class-averaged value for $\psi = 298$ are based on only 2 tests and should therefore be treated with caution.

The current-related transport rate is offshore directed and increases with mobility number, except for the very calm conditions. It is interesting to see that for mobility numbers larger than about 50, the high-frequency wave-related transport near the bed is of the same order of magnitude as the current-related component. However, in the vertical the high-frequency contribution decreases much more rapidly to zero than the current-related component.

The high-freq. wave-related transport component is offshore directed for calm conditions (small mobility numbers). In general, this is related to the presence of ripples causing vortex shedding resulting in relatively large phase lags between the velocity and the concentration. The high-freq. wave-related transport near the bed ($z = 0.02$ m) changes to an onshore direction with increasing mobility number. As long as short wave ripples (SWR) are present however (see also Figure 4.3), the high-freq. wave-related transport remains offshore directed at 0.04 and 0.10 m above the bed.

The low-frequency transport component is relatively small compared to the other two components and is offshore directed in most cases, likely related to the presence of group-bound forced long waves (Osborne and Greenwood, 1992; Ruessink et al., 1998). Cross-correlations between the short-wave envelope and the long wave oscillatory motion revealed the presence of bound long waves. However, the cross-correlation were relatively small (about 0.4), explaining only 16% of the low-frequency oscillatory motion. This means that 84% of the long wave motion has a different origin. This 84% is likely not to contribute to the low-frequency transport rates because of the lack of correlation between the short and long wave motion. The small bound long wave correlations are consistent with the relatively small low-frequency transport rates.

The total net suspended transport rate under field conditions near Egmond aan Zee is dominated by two components, viz. the mean current-related component and the high-frequency oscillatory component. Another picture of the relative contribution of the different components is obtained after integrating the suspended transport rates between the lowest and highest measurement point. The importance of a transport component can then be expressed as its relative contribution to the total suspended sediment transport rate (sum of absolute values).

Figure 4.26 shows the relative contribution of the wave and current-related transport components to the total suspended transport rate as a function of the mobility number. The data points in this figure denote the average of 10 or more tests (except for $\psi = 298$, which is based on 2 tests) while the error bars indicate the standard error between the tests. The current-related component dominates the total transport rate for all conditions. This component accounts for about 70% of the total transport rate. The contribution of the high-frequency wave-related component is smaller (about 25%) and tends to

decrease with increasing mobility number, although this trend is not very clear. The low-frequency component is smallest and accounts on average for about 5% to the total transport rate. The contribution of this component increases with mobility number, which is consistent with observations under breaking wave conditions in shallower water depths (e.g. Aagaard and Greenwood, 1994; Beach and Sternberg, 1991), where the net flux is dominated by low-frequency waves, especially under dissipative conditions.

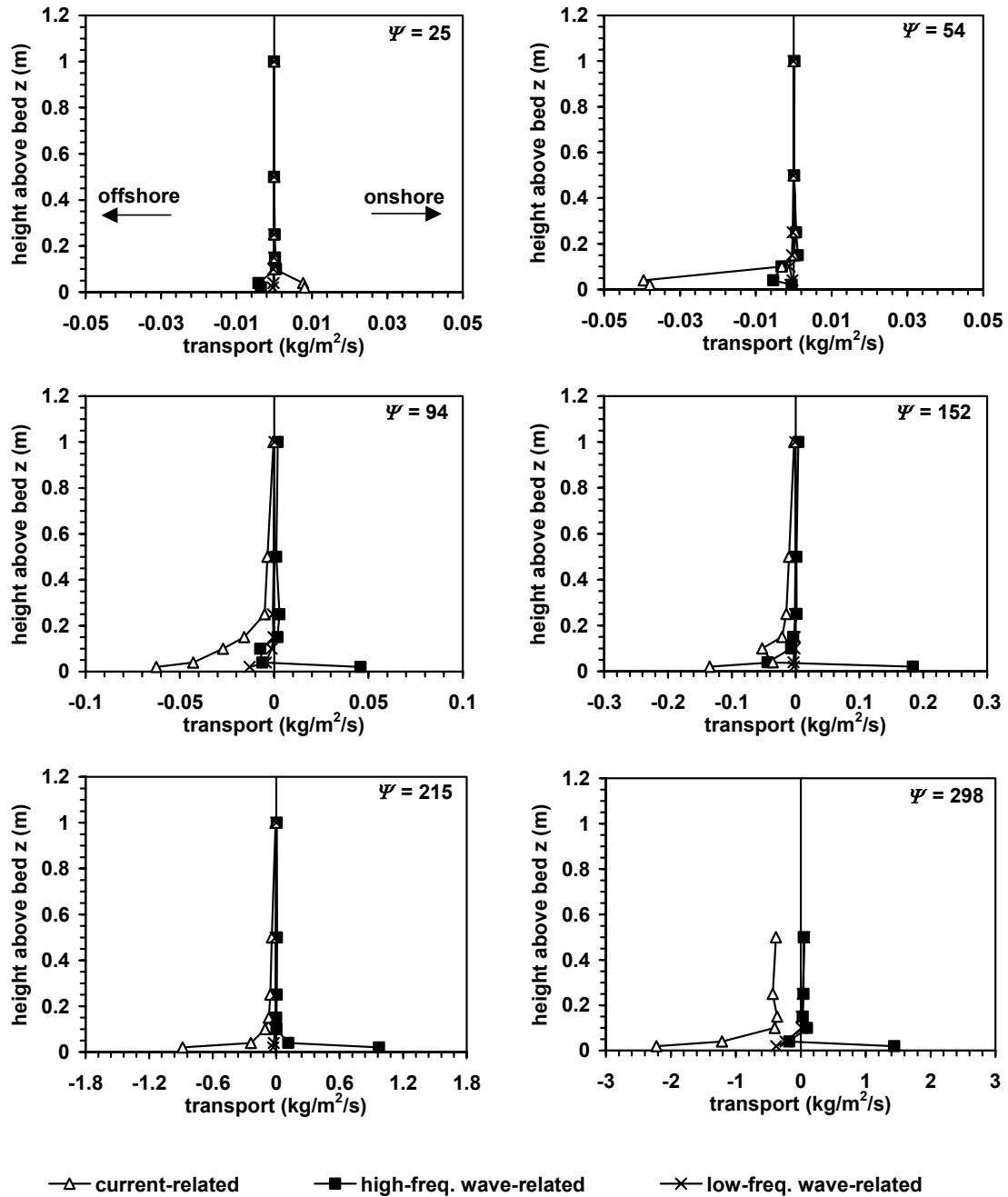


Figure 4.25. Vertical distribution of transport components; Egmond aan Zee field tests.

The results indicate that, at least in water depths between 1 and 4 m, the low-frequency transport is negligible, which is an assumption often made in process-based sediment transport models. Ruessink et al. (1998) have shown that in larger water depths (3 to 9 m) the largest contributions to the total transport are made also by the short waves and the undertow, but that under these conditions the high-frequency oscillatory component and the current-related component are equal in magnitude but with an opposite sign, leading to the low-frequency transports, although small in magnitude, to have a relatively large influence on the net sediment transport rate.

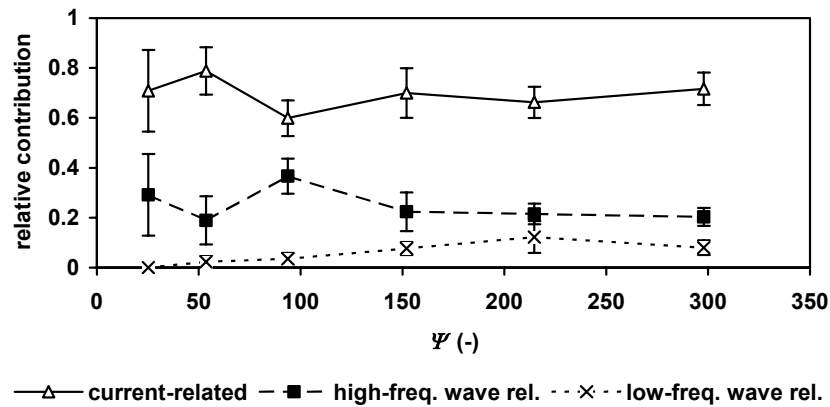


Figure 4.26. Relative contribution of measured current-related, high-frequency wave-related and low-frequency wave-related transport rates as a function of the mobility number. The error bars around each class-averaged value equal the standard error

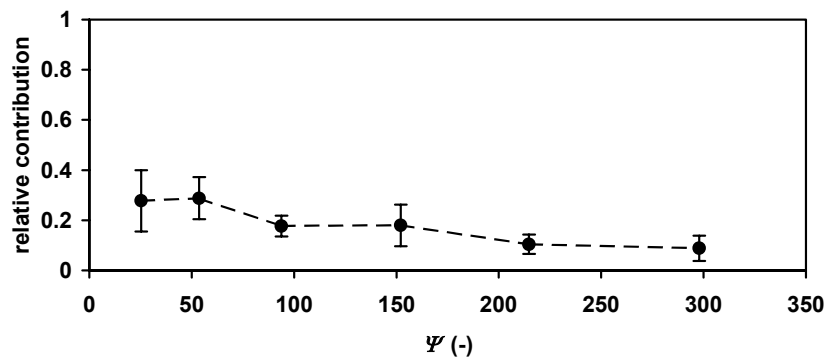


Figure 4.27. Relative contribution of bed-load to the total-load transport rate. A relative contribution of 0.5 would indicate equal bed-load and suspended load contributions

Second important question is whether the suspended load or the bed-load dominates the total load transport rate. The bed-load transport rates could not be measured under the present field conditions. Therefore, the formula of Van Rijn (2000) (using H_{rms} instead of $H_{1/3}$) was used to get an estimate of the bed-load transport rates. This is the same bed-load transport formula as applied in the cross-shore profile model discussed in this thesis. The importance of the bed-load is expressed as the ratio of this transport to the total load transport rate (= computed bed-load + measured suspended load transport). The relative contribution of the bed-load transport rate is shown in Figure 4.27. It can be seen that the bed-load transport accounts for about 30% of the total load transport rate

under relatively calm conditions. This decreases to about 10% under moderate storm conditions. Based on the Bailard (1981) model, Ruessink et al. (1998) found that the suspended load dominated progressively with increasing relative wave height. They found that under breaking wave conditions, the suspended load transport was about 10 times as large as the bed-load. This is consistent with the present findings.

4.7.3. PREDICTED TRANSPORT RATES

The sand transport model (consisting of various sub-models) presented in Section 4.2 has been used to compute the transport rates based on the measured hydrodynamics in the field near Egmond aan Zee in order to verify if an accurate prediction of the various transport components is possible using a process-based sand transport model. A comparison between measured and predicted transport rates provides insight in the applicability and accuracy of this model for this field site. The net transport rates are compared also with the relatively simple approach of Bailard (1981).

Figure 4.28 shows the relative contributions of the wave and current-related transport components to the total suspended transport rate according to the model as a function of the mobility number. The model behaves very differently from the measurements. The model demonstrates a comparatively strong contribution of the high-frequency wave-related transport rate for the calm conditions whereas the measurements show a much smaller contribution of this component (see Figure 4.26). The modelled high-frequency wave related transport rates account for more than 60% of the total transport rate where the measurements showed a contribution of only 30% in case of low-energy conditions. For moderate storm conditions the contribution of the modelled high-frequency transport component decreases to values that are more in line with the measurements.

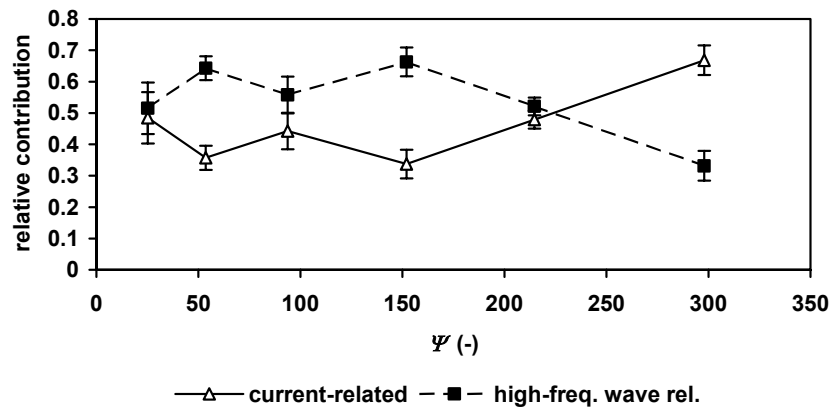


Figure 4.28. Relative contribution of computed current-related and high-frequency wave-related transport rates as a function of the mobility number. The error bars around each class-averaged value equal the standard error.

As mentioned before (see Section 4.5), the high-frequency transport rates are overestimated by the model when using a fixed efficiency coefficient of $k_{as} = 0.2$ in the wave-related transport formula (4.60). The present field data suggest a smaller efficiency factor for the calm conditions. The following relationship is proposed:

$$k_{as} = 0.09 + 0.05 \tanh(0.01\psi - 3) \quad (4.76)$$

Using Equation (4.76) the efficiency factor increases from about 0.04 for calm conditions to 0.13 for high-energy storm conditions, reflecting the increasing coherence between velocity and concentration with more energetic conditions (Ruessink et al., 1998). The behavior of Equation (4.76) is shown in Figure 4.29. Although for the present field data Equation (4.76) gives good results, the general applicability of the proposed relationship awaits more field data for different grain sizes and wave-current flow conditions.

The relative contributions of the wave-related and current-related suspended load transport rate to the total suspended load transport using the proposed relationship for k_{as} is shown in Figure 4.30. Especially during calm conditions the contribution of the high-frequency wave-related part is drastically reduced and more in line with measurements.

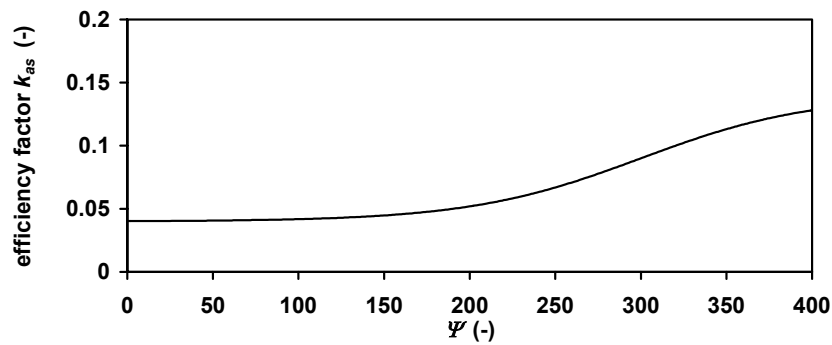


Figure 4.29. Wave-related transport efficiency coefficient k_{as} as a function of mobility number, see Equation (4.76).

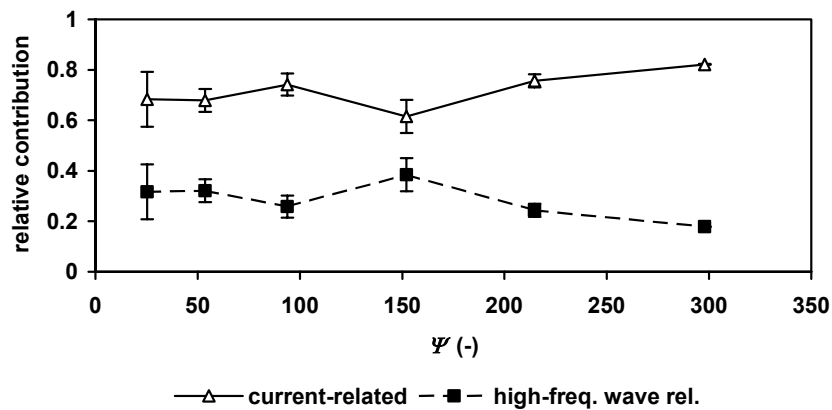


Figure 4.30. Relative contribution of computed current-related and high-frequency wave-related transport rates as a function of the mobility number, using the efficiency factor as described by Equation (4.76) The error bars around each class-averaged value equal the standard error

Computations were made also with a model based on the energetics approach of Bailard (1981). Nairn and Southgate (1993) provide an extensive overview of the development

of the energetics expressions. The energetics approach has often been applied in laboratory and field experiments (e.g. Roelvink and Stive, 1989; Thornton et al., 1996; Thornton et al., 1996). The adjustable variables in the method include two efficiency factors for the bed-load and suspended load, ε_b and ε_s , respectively, and a friction coefficient C_f . Here, ε_b and ε_s were set to 0.21 and 0.025, respectively. These values are the same as those determined by Bailard (1981) based on two sets of laboratory data and one field data set. The friction coefficient C_f was estimated by $0.5f_w$ (Stive, 1986), where the wave friction factor f_w is defined by Equation (4.24).

In the present model, the grain size of the suspended sediment was taken to be equal to the grain size of the bed material. The bed roughness k_s was predicted using the modified Nielsen model (see Section 4.3). As a first approximation the efficiency coefficient for the wave-related transport rate was taken to be $k_{as} = 0.2$.

The measured hydrodynamics and grain sizes of $D_{50} = 0.24$ mm and $D_{90} = 0.30$ mm were used in both models. The sediment fall velocity was computed using the method of Van Rijn (1993).

Figure 4.31 shows a comparison between measured and computed net suspended transport rates ($= q_{s,c} + q_{s,w}$). As can be seen, both the Van Rijn and the Bailard (1981) sand transport model significantly under-predict the net suspended transport rates. This is likely due to the relatively strong contribution of the high-frequency wave-related transport component in both models. In the present model this can easily be verified by applying the efficiency factor k_{as} according to Equation (4.76), in this way significantly reducing this component for the calm conditions. The resulting transport rates are compared with the measured values in Figure 4.32.

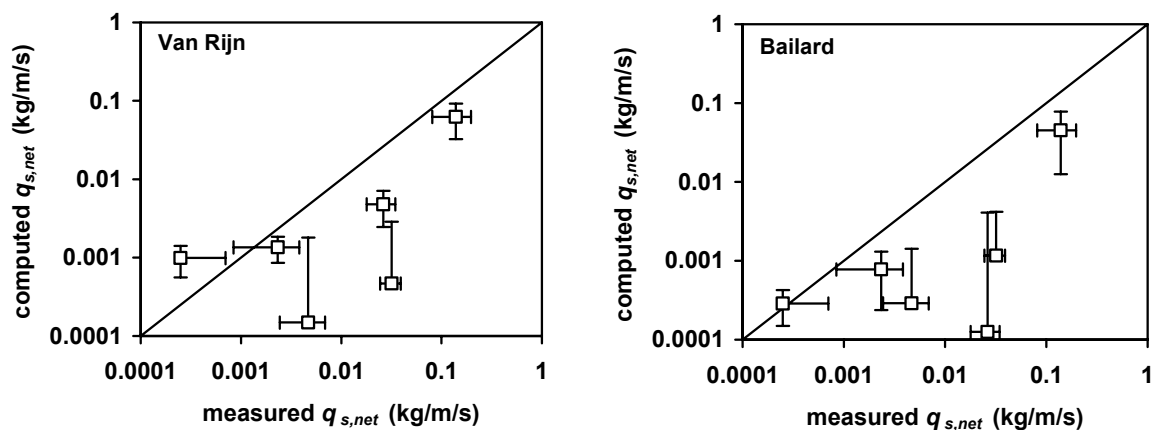


Figure 4.31. Comparison of measured and computed transport rates

The predictions improve significantly when applying a wave-related transport efficiency factor depending on the wave conditions. It has been shown before that the model when using a fixed efficiency factor of 0.2 significantly overestimates the wave-related transport rates under calm conditions in the field. Consequently, adding the offshore directed current-related component and the onshore-directed wave-related component leads to a significant underestimation of the net suspended transport rates, in this case.

This effect is even stronger in the Bailard (1981) model because of the assumption that the instantaneous sediment transport rate responds immediately to changes in the velocity field, which would come down to an efficiency factor of 0.44 (see Section 4.5). Bowen (1980) also suggests that this assumption is probably the most serious limitation of the Bailard (1981) model. Bowen (1980), Bailard (1981) and Stive (1986) agree that this limitation restricts the application of the model to situations where the seabed is plane.

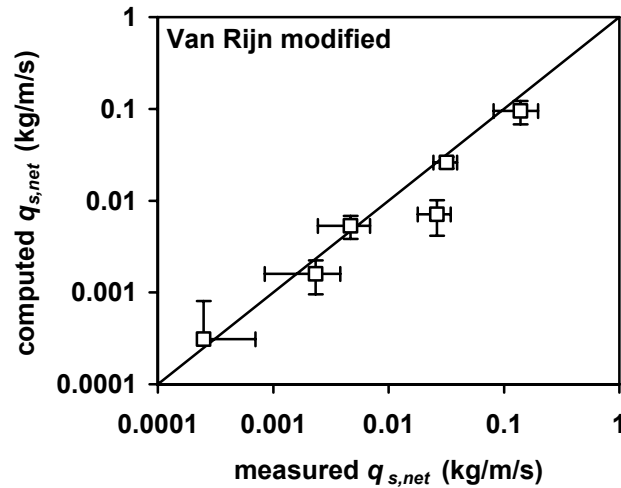


Figure 4.32. Comparison of measured and computed transport rates.

4.8. DISCUSSION AND CONCLUSIONS

The above analysis has shown that in principle the modelling of the measured suspended transport rates in the field is possible using a single-wave process-based model as described in Section 4.2. The bed form roughness appears to be a key parameter in the prediction of the suspended sediment concentrations and current- and wave-related suspended transport rates. An accurate prediction of the ripple roughness is therefore essential.

The present field data of nondimensional ripple height and ripple steepness were found to be in the same range and showed the same trends as previous laboratory and field measurements. Measurements of ripple dimensions under field and laboratory conditions were compared with three predictive models, i.e. Grant and Madsen (1982), Van Rijn (1993) and Nielsen (1981).

The errors in predicting η/A were smallest and the correlation squared between measured and computed η/A were largest when using the Nielsen model. The errors in predicting the ripple steepness were in the same range as the other two models. Nonetheless, the Nielsen model still underestimated η/A for large part of the data used here and the decrease of the ripple steepness with mobility number was stronger than observed from the measurements. Therefore, the Nielsen model was modified to improve the predictions. Changes were made to the formulation of nondimensional

ripple height in the break-off range and a new formulation for the ripple steepness was suggested.

The modified Nielsen model captured the range of measured η^2/λ values better than the G&M, Van Rijn and original Nielsen model did. Main differences with the original Nielsen model are a more gradual decrease of η^2/λ with mobility number and a less pronounced effect of wave period and grain diameter. The general applicability of the modified Nielsen model await more field data for different grain sizes and wave-current flow conditions.

The Houwman and Ruessink (1996) wave-related suspended transport model based on the energetics approach of Bailard (1981) was tested. Assuming that the instantaneous sediment transport rate responds immediately to changes in the near bed velocity, this approach led to wave-related suspended transport rates that were much larger than measured values. An empirically derived efficiency coefficient is proposed that takes into account the effect of a phase lag and smaller coherence between velocity and concentration under calm conditions with ripples.

In the present study, the bed-load is defined as that part of the sediment that travels below 0.02 m above the bed. These transport rates were computed using the bed-load transport formula of Van Rijn (2000) as applied in the present cross-shore profile model. The Van Rijn (2000) bed-load transport formulation was compared to two commonly used bed-load transport formulae, i.e. the model by Ribberink (1998) and the model by Bailard (1981). Comparison of the results of the three bed-load transport models with large-scale wave flume data revealed the predicted bed-load transport rates to be of the same order of magnitude as the measured values. Comparing the three models for a wider range of field conditions however revealed that the Van Rijn (2000) model predicts bed-load transport rates that are of a different order of magnitude and show a different direction than the bed-load transport rates predicted by the other two models. This is likely due to the fact that in the Van Rijn (2000) model the instantaneous bed shear stress is based on a single wave in which the intra-wave velocity variation is reconstructed from the significant on- and offshore peak near bed orbital velocities. This results in a relatively strong effect of the higher waves. In contrast, the Ribberink (1998) and Bailard (1981) models use the complete velocity time series as an input, in this way taking into account also the contribution of the smaller waves, which after time-averaging leads to a smaller bed-load transport rate and under calm conditions to a stronger effect of the mean current. Use of the complete velocity time series in the Van Rijn model yielded results similar to the other two bed-load transport models. This suggests that the use of one single representative wave is not enough for an accurate prediction of the near bed transport rates. For an accurate prediction of the bed-load transport rates it appears to be necessary to use a multi-wave approach. Another option is to modify the parameterization for the bed-load transport rate when using a single-wave approach. Using the root-mean-square on- and offshore peak orbital velocities instead of the significant values gave more realistic bed-load transport rates in the present single-wave model. However, the relative importance of an accurate prediction of the bed-load transport rate also depends on the relative importance of this component compared to the suspended load component.

The relative contribution of the various transport components was studied using Egmond aan Zee field measurements. Based on measured suspended transport rates and computed bed-load transport it is observed that the bed-load accounts for 30% of the total load under calm conditions and 10% under moderate storm conditions. This relatively small contribution of the bed-load transport rate does not make it necessary to use a multi-wave approach for a more accurate description of this component. The use of the root-mean-square wave height as a representative wave suffices to get an estimate of the bed-load transport rate under calm conditions. As regards the suspended transport rate, the current-related component accounts for about 70% of the total suspended transport rate. The contribution of the high-frequency wave-related component is smaller (about 25%) and tends to decrease with increasing mobility number. The low-frequency component is smallest and accounts for about 5% to the total transport rate. The contribution of this component increases with mobility number, which is consistent with observations under breaking wave conditions in shallower water depths.

5. MODELLING OF NEARSHORE PROFILE DEVELOPMENT

5.1. INTRODUCTION

Morphodynamic coastal profile models are commonly used for hind- and forecasting studies of nearshore bathymetry, often in response to human interference in the nearshore, for instance related to implementation of shoreface nourishments. They are developed to predict the short-term hydrodynamic and sediment transport processes and associated morphological change. Process-based profile models are frequently used on storm scale with time spans of days to weeks. On seasonal scale with time spans of months, process-based models are not expected to produce realistic results because of the propagation and accumulation of errors (De Vriend, 1997). However, to what extent and on which time scales process-based models can be used is not yet clear.

Coastal morphological changes take place at a variety of temporal and spatial scales. On storm scale, high-energy wave conditions cause erosion of the dune and beach and offshore migration of nearshore bars due to the strong undertows induced by the wave breaking (Lee et al., 1998). Beach recovery takes place during fair weather wave conditions with onshore bar migration. On seasonal scale, the typical beach-bar behavior is the offshore-onshore migration cycle with offshore migration of the bar system during the storm season and onshore migration and beach recovery during the relatively calm periods. Seasonal variation is a general characteristic of nearshore morphological behavior, but the character of morphological change varies widely. Along Pacific coasts for example, the nearshore bars often disappear during the summer period (bar welding to beach); along many other coasts, the nearshore bars are permanent features. The knowledge of the seasonal variability of nearshore bars has increased considerably during recent years due to the use of video remote sensing techniques (Lippmann et al., 1993; Van Enckevort, 2001). Depending on the season, the outer nearshore bar near Duck, NC, USA has been observed to migrate offshore over about 100 m and onshore over about 50 m on a time span of 4 to 5 months (Lippmann et al., 1993). The outer bar near Noordwijk, Netherlands, has been observed to migrate on- and offshore over about 20 m over 4 to 5 months, while the inner bar migration was about 10 m on this time span. At both sites, offshore migration dominated. On decadal scale, nearshore bars often show an offshore migration cycle with decay of the outer bar at the edge of the surf zone and generation of a new bar in front of the beach face (Wijnberg, 1995). This phenomenon has been observed near Duck and along the Dutch coast (Ruessink and Kroon, 1994; Hoekstra et al., 1996; Shand et al., 1999). This migration cycle has a period of 5 to 15 years depending on the size of the bars and the width of the surf zone. The different time scales are closely related to spatial scales. For small time spans (days to weeks), net bar crest changes are mainly longshore non-uniform with local disturbances such as rip channels, and crescentic and meandering bar patterns. Longshore length scales of these disturbances are 100 to 1000 m (Lippmann and Holman, 1990; Ruessink et al., 2000; Van Enckevort, 2001). For larger time spans (months to years) longshore uniform changes dominate (Van Enckevort, 2001).

These observations lead to a paradox in the application of process-based cross-shore profile models. Because of the assumption of longshore uniformity, use of a process-based cross-shore profile model would be most suitable for predicting morphological changes on time scales of months to years. On the other hand, because of the propagation and accumulation of errors, using a process-based profile model on these long time scales may lead to unrealistic results. A possible resolution of this paradox may lie in the application of longshore-averaged profiles, in this way reducing longshore non-uniformities. This approach is used by Van Rijn et al. (2002b). Another approach would be to predict the morphological changes for individual profiles. This approach is used herein.

In chapter 3 of this thesis it has been shown that a multi-wave approach is not superior over a single-wave approach with respect to the prediction of hydrodynamics in the nearshore. Chapter 4 concluded that the nearshore sediment transport rates can be predicted with reasonable accuracy (within a factor 2) using a relatively simple single-wave engineering approach.

The specific question that will be addressed in this chapter is whether and to what extent a single-wave cross-shore profile model is capable of predicting nearshore morphological changes on the time scale of storms and seasons, simplifying the coastal system to an longshore-averaged 2-D system. Cross-shore profile changes predicted by the model are compared to observed profile changes on storm and seasonal scale. Part of the work presented in this chapter is published in Grasmeijer et al. (2000) and Van Rijn et al. (2002b). The latter is the final overview publication on profile modelling of the EU-COAST3D Egmond aan Zee project.

The present cross-shore profile model is described in Section 5.2. Section 5.3 explains the Brier Skill Score that is used to quantify the model performance. The effect of varying the free model parameters on the model results is discussed in Section 5.4. In Section 5.5, a comparison is made between measured and predicted morphological changes for large-scale laboratory tests and two contrasting field sites near Egmond aan Zee in the Netherlands and Duck, NC, USA. In addition, the model is applied for a shoreface nourishment. Finally, the main findings are discussed and summarized in Section 5.7.

5.2. MODEL DESCRIPTION

The morphological model used in this study includes the interaction between hydrodynamic conditions and bed profile evolution. This means that the hydrodynamic conditions adjust themselves to the actual bed topography, which in turn is developing as a function of the hydrodynamics and the sediment transport. The model procedure is sketched in Figure 5.1. First, the hydrodynamic conditions across the profile are computed using the hydrodynamic module as described in Chapter 3, using the initial bathymetry. Then, the cross-shore sediment transport rates are computed using the transport module as described in Chapter 4. Following that, the bed levels are updated according to the continuity Equation (5.1). To solve this equation a modified Lax-Wendroff scheme is used. The scheme is implicit and ensures conservation of the total

amount of sediment. The on- and offshore boundaries are assumed open allowing for a net gain or loss of sediment from the profile. The computation is repeated using the new bathymetry. A definitions sketch of the model is shown in Figure 5.2.

$$\frac{dz}{dt} = \frac{dq}{dx} \quad (5.1)$$

The cross-shore and longshore sediment transport calculations are made using the transport module as described in the previous chapter. The longshore transport calculations are made for descriptive purposes, they do not affect the profile change.

There are two input files, one relating to the profile, tidal conditions and general data such as the time step and bed roughness heights, and a second describing the variable wave conditions. The initial sand bed profile must always be specified as input; a profile can generally be described by 30 to 40 coordinates. With the designation of a variable grid width pattern in the input file, a subroutine further divides the profile into approximately 300-400 computational grid sections. Although the model can be used in the multi-fractions mode, in which the grain diameter may vary across the profile, the present computations are based on a single representative grain size for the entire profile. The sediment fall velocity is calculated internally. The bed roughness heights are given as an input in the model and can be varied across the profile.

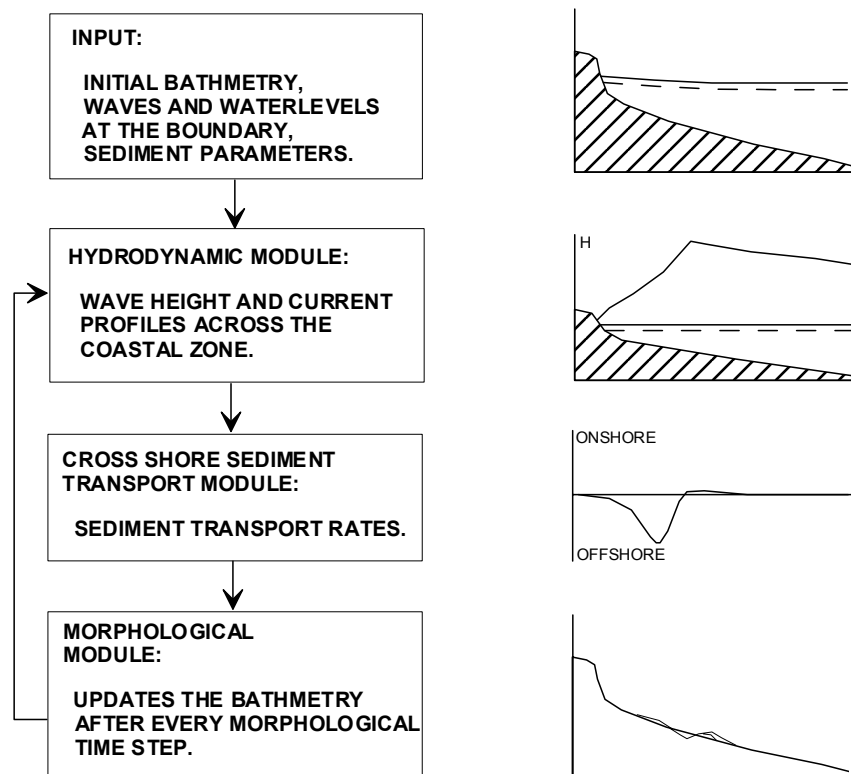


Figure 5.1 Diagram of modules in morphological model

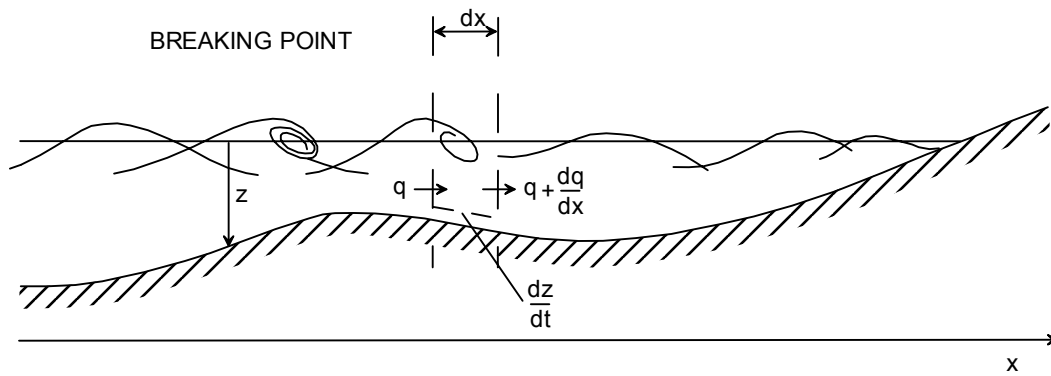


Figure 5.2 Definition sketch of profile model

5.3. MODEL PERFORMANCE

The model performance is evaluated on the basis of the Brier Skill Score s_{bs} (Murphy and Epstein, 1989; Van Rijn et al, 2002b):

$$s_{bs} = 1 - \frac{\overline{(|z_{c,i} - z_{m,i}| - \Delta z_m)^2}}{\overline{(z_{b,i} - z_{m,i})^2}} \quad (5.2)$$

where z_m is a set of N measurements with $z_{m,i}$ the i -th value in space of the set ($i = 1 \dots N$). z_c is a set of N model predictions (the forecast) with $z_{c,i}$ the i -th value of the set ($i = 1 \dots N$) being at the same position in space and/or time as $z_{m,i}$. z_b is a set of N baseline predictions with $z_{b,i}$ the i -th prediction at the same position in space/time as $z_{m,i}$. Δz_m is the error of the measured bed level. The overbar denotes averaging in space. The numerator in Equation (5.2) should be set to zero when $|z_{c,i} - z_{m,i}| - \Delta z_m < 0$.

Table 5.1 Qualification of error ranges

Qualification	Brier skill score
	s_{bs}
Excellent	1.0-0.8
Good	0.8-0.6
Reasonable/fair	0.6-0.3
Poor	0.3-0.0
Bad	<0

This skill score compares the mean square difference between the prediction and observation with the mean square difference between baseline prediction and observation. Perfect agreement gives a Brier skill score of 1 whereas modelling the baseline condition gives a score of 0. If the model prediction is further away from the final measured condition than the baseline prediction, the skill score is negative. In

applying the Brier skill score to morphological models it may be important to judge the accuracy on a small group of points or a single point if such quantities are the critical ones for a design job or management decision, e.g. in case of a shoreface nourishment.

The s_{bs} is very suitable for the prediction of bed evolution. The baseline prediction for morphodynamic modelling will usually be that the initial bed remains unaltered. In other words, the initial bathymetry is used as the baseline prediction for the final bathymetry. This means that the s_{bs} is not altered by the inclusion of an inactive (usually offshore) region in the model. If such a region is included in a model (as here) neither the measured or model results change in this region so the sum of the square of the differences do not increase. The mean square error reduces, however, as the average is calculated over a larger number of points. However, the ratio of the mean square differences on the right hand side of the s_{bs} -expression remains the same as both terms reduce by the same proportion with the inclusion of an inactive area. Therefore, the s_{bs} remains unaltered. The baseline prediction can also be taken as the long-term average at each point. The qualifications of the error ranges are given in Table 5.1.

5.4. SENSITIVITY FOR FREE MODEL PARAMETERS

5.4.1. INTRODUCTION

The most common fit parameters or free model parameters in process-based models include the current and wave-related bed roughness $k_{s,c}$ and $k_{s,w}$, the wave front slope β , and sediment characteristics (Walstra et al., 1998; Walstra, 2000). Besides these, the present model includes the wave-related transport (or efficiency) factor k_{as} as a free model parameter.

Table 5.2. Applied range of model- and process parameters and default settings for sensitivity analysis based on LIPID model runs

Parameter	range of values	default value
current-related roughness, $k_{s,c}$ [m]	0.01-0.04	0.03
wave-related roughness, $k_{s,w}$ [m]	0.01-0.04	0.02
wave front slope, β [-]	0.04-0.1	0.05
wave-related transport factor, k_{as} [-]	0.0-0.2	0.05
median sediment grain size, D_{50} [mm]	0.18-0.26	0.22
90% sediment grain size, D_{90} [mm]	$2*D_{50}$	$2*D_{50}$
median suspended sediment grain size, D_{ss} [mm]	D_{50}	D_{50}

The sensitivity of the model for the free model parameters was examined using data from LIPID tests done in the Delta Flume of Delft Hydraulics. The details of the tests can be found in Arcilla et al. (1994) and Roelvink and Reniers (1995). The test selected

here (1B) represents erosive short-period storm waves with an offshore wave height of about $H_{rms} = 1.0$ m and a wave spectrum peak period of $T_p = 5$ s. A small bar was present at the start of the experiment. The median sediment grain size was 0.22 mm. Since the initial bed profile was not in equilibrium with the imposed waves, wave action redistributed the sand to approach a stable profile of the course of the run. The test used here exhibits offshore sand bar movement and corresponding bar formation with the waves breaking on the bar. In this section, the effect of varying the free model parameters on the model results will be shown. The applied range of model- and process parameters and default settings are given in Table 5.2. A comparison between measured and predicted morphological changes will be made in Section 5.5.

5.4.2. BED ROUGHNESS

Since there will almost always be uncertainty about the exact dimensions of the bed forms and thus the bed roughness during a specific event, it is very useful to assess the effect of variations in the bed roughness. The bed roughness is an important consideration because of its direct effect not only on the hydrodynamics but also on the sediment transport computations, which is discussed in detail in Chapter 3 and 4, respectively. Herein, the effect on the morphodynamic computations is analyzed. Distinction is made between a current-related roughness height $k_{s,c}$ and a wave-related roughness height $k_{s,w}$. Understandably, the first characterizes the flow resistance between the time-averaged current and the seabed, while the second represents the resistance between the oscillatory wave motion and the seabed. The influence of these two roughness parameters is discussed here separately.

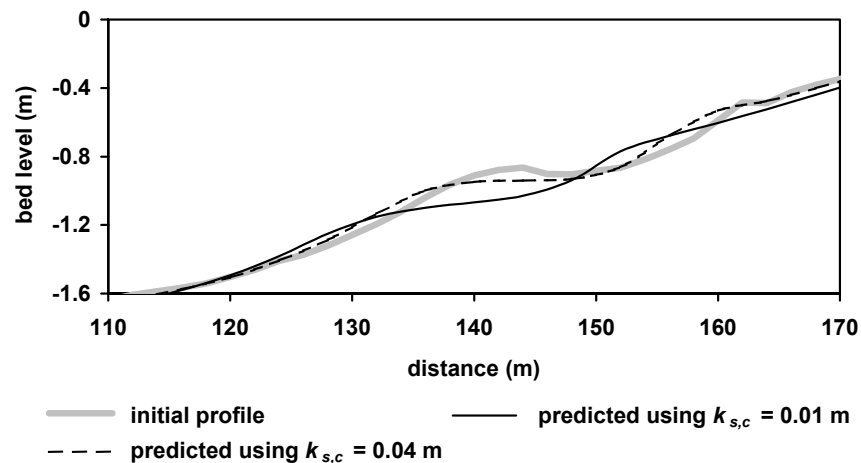


Figure 5.3. Predicted bed profile development after 18 hours showing the effect of changing the current-related roughness $k_{s,c}$. LIPIID Delta Flume experiments, test 1B.

To verify the effect of changing the current-related roughness height, $k_{s,c}$ was varied between 0.01 and 0.04 m, which are realistic values in the nearshore zone of a sandy coast (see Chapter 4). Other parameters were kept constant ($k_{s,w} = 0.02$ m, $k_{as} = 0.05$). Increasing $k_{s,c}$ increases the current boundary layer thickness. This increases the

concentration reference height above the bed z_a and decreases the reference concentration c_a according to Equation (4.15). In case of relatively small time-averaged current-velocities, and thus small current-related bed shear stresses, this leads to decreasing suspended sediment concentrations and suspended sand transport rates, and thus smaller morphological changes (Figure 5.3). Increasing $k_{s,c}$ from 0.01 to 0.04 m results in less flattening of the sand bar. This effect becomes smaller when relatively large time-averaged currents are present.

Changing the wave-related roughness $k_{s,w}$ from 0.01 to 0.04 m has more or less the opposite effect. Increasing the $k_{s,w}$ increases the wave boundary layer thickness and consequently the concentration reference height above the bed z_a . This would reduce the suspended sediment concentrations according to Equation (4.15). However, increasing $k_{s,w}$ also increases the wave-related bed shear stress τ_w which, in case of relatively large orbital velocities, results in an increase of the suspended sand transport rates and thus larger morphological changes. Figure 5.4 shows relatively small morphological changes when using $k_{s,w} = 0.01$ m and large changes (flattening of the profile) when using $k_{s,w} = 0.04$ m.

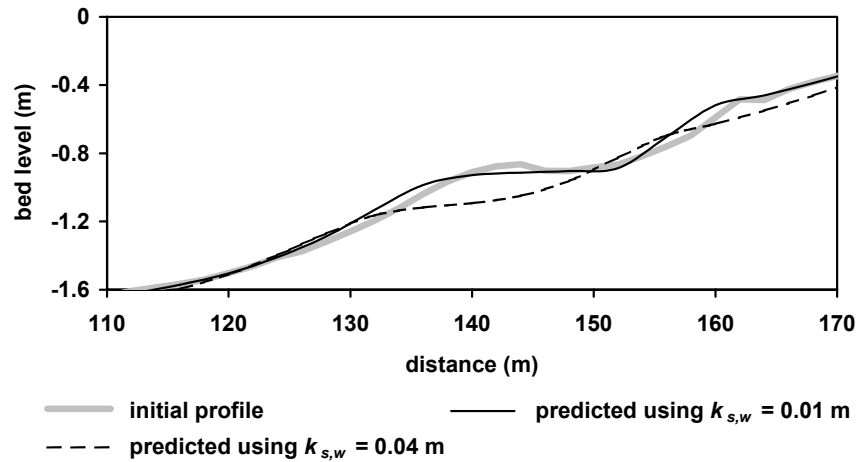


Figure 5.4. Predicted bed profile development after 18 hours showing the effect of changing the wave-related roughness $k_{s,w}$. LIPIID Delta Flume experiments, test 1B.

5.4.3. WAVE FRONT SLOPE

The wave front slope β controls the advection length of the roller in the model. A decreasing β increases the advection length, which increases the cross-shore currents and shifts the maximum cross- and longshore currents shoreward. Strictly speaking, the wave front slope, which is assumed constant across the profile, is not a free model parameter because its value was determined by calibration. However, Walstra et al. (1996) have shown that β is not a constant. Therefore, it is useful to assess the sensitivity of the model for different β values.

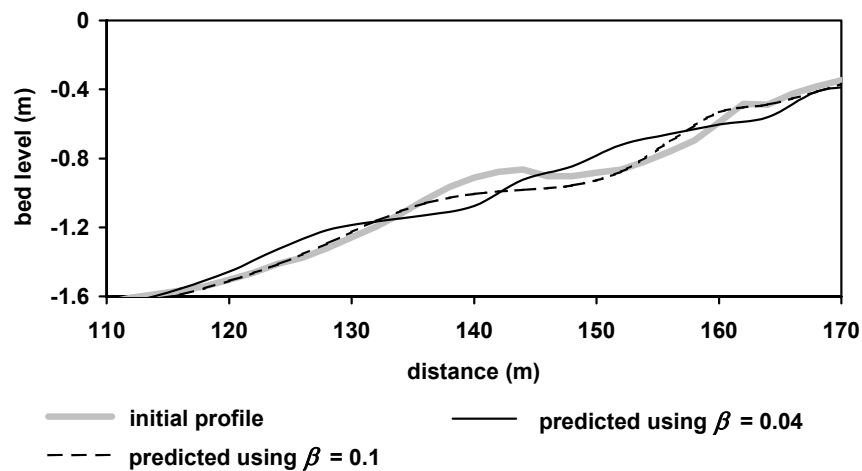


Figure 5.5. Predicted bed profile development after 18 hours showing the effect of changing the wave front slope β . LIPIID Delta Flume experiments, test 1B.

The effect of changing the wave front slope β is shown in Figure 5.5. Other parameters were kept constant with default settings (Table 5.2). A decreasing wave front slope results in increasing morphological changes. The model runs with a β smaller than 0.04 became unstable.

5.4.4. WAVE-RELATED TRANSPORT FACTOR

The magnitude of wave-related suspended sand transport component depends on the degree of wave skewness and an efficiency factor k_{as} . (Section 4.5) Comparison with field and laboratory data revealed this factor to range between about 0.0 (no wave-related suspended transport) and 0.2. Figure 5.6 demonstrates the effect of changing k_{as} on the model predictions. The model tends to flatten the profile when using $k_{as} = 0$ (no wave-related suspended transport) and maintains a more pronounced bar feature when using $k_{as} = 0.2$.

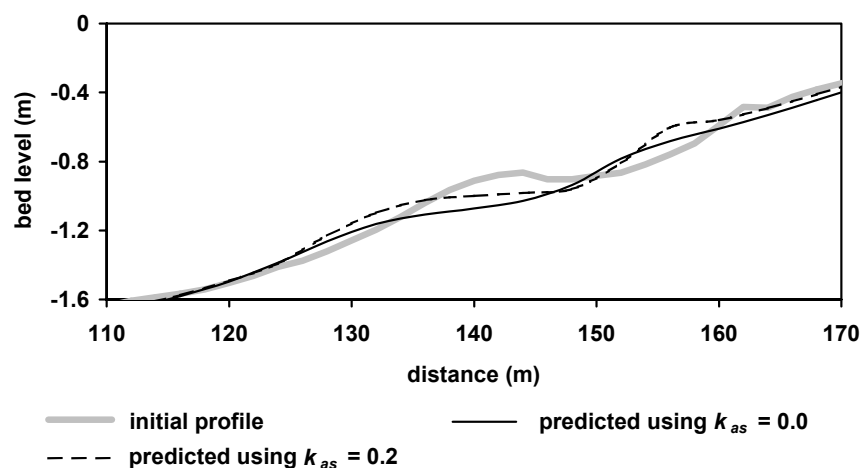


Figure 5.6. Predicted bed profile development after 18 hours showing the effect of changing the wave-related transport factor k_{as} . LIPIID Delta Flume experiments, test 1B.

5.4.5. CONCLUSIONS

Varying the wave-related transport factor k_{as} has a substantial effect on the model predictions. Increasing k_{as} also has a stabilizing effect. A decreasing wave front slope β leads to larger morphological changes, smoothing the profile. Most pronounced changes occur when varying the wave-related bed roughness $k_{s,w}$ and, to a lesser extent the current-related bed roughness $k_{s,c}$. These appear to be the most effective parameters in tuning the model. Decreasing $k_{s,w}$ or increasing $k_{s,c}$ has a stabilizing effect on the predictions. Predicted morphological changes become larger with increasing $k_{s,w}$ or decreasing $k_{s,c}$. Hence, the wave- and current-related bed roughness heights will be the most important parameters to focus on when comparing and tuning the model to measured morphological changes.

5.5. MODEL-DATA COMPARISON

5.5.1. INTRODUCTION

The cross-shore profile model assumes nearshore morphological changes to be brought about only by cross-shore processes. Strictly speaking, this is solely the case under laboratory conditions in a wave flume. In the field, the assumption of longshore uniformity is often violated because of the presence of e.g. rip channels or crescentic bars. The cross-shore profile model can be applied to individual transects. However, the longshore variability may be so large that bed level changes of individual transects over short periods are not significantly different in a statistical sense. Therefore, another approach is to average the available cross-shore profiles longshore. The longshore variability can be represented by the standard error between the different cross-shore profiles. Bed level changes in time are then for example only regarded as significant when there is no overlap of the standard error bands. The longshore-averaging distance should be chosen such that longshore non-uniformities are averaged out. This latter approach has been followed in this section for two field cases.

To verify the model for a strict cross-shore situation, a comparison is made with data from large-scale flume experiments in the Delta Flume of Delft Hydraulics. For the field situation, model predictions are compared to data from two large field experiments, the first near Egmond aan Zee in the Netherlands, and the second near Duck, NC, in the USA.

5.5.2. STORM SCALE: LABORATORY EXPERIMENTS

The model predictions are compared to measurements during the LIPIID experiments in the Delta Flume of Delft Hydraulics. The details of the tests can be found in Arcilla et al. (1994) and Roelvink and Reniers (1995). As reported earlier, the test selected here (1B) represents erosive short-period storm waves with an offshore wave height of about $H_{rms} = 1.0$ m and a wave spectrum peak period of $T_p = 5$ s. A small bar was present at the start of the experiment. The median sediment grain size was 0.22 mm. The test used

here exhibits offshore sand bar movement and corresponding bar formation with the waves breaking on the bar.

The initial profile, shown in Figure 5.7, contains a single bar located at $x \sim 145$ m. The bar migrated about 10 m offshore during 18 hours of wave action, with erosion of the trough and growth of the bar. In total 11 model runs were performed, which are summarized in Table 5.3. The first run is the base run, i.e. the default or optimum run for all parameters based on calibration in the previous chapters. In the base run, $k_{s,w}$ is 0.02 m based on comparison with measured concentration profiles, and $k_{s,c} = 0.03$ m, based on comparison with measured longshore currents (but not relevant here). The default D_{50} was set to 0.22 mm. In the subsequent runs, one of the free parameters is varied; the other parameters are kept constant.

Table 5.3. Model runs, free model parameters, and Brier Skill Scores for LIPIID, Test 1B, Delta Flume. Bed level error $\Delta z_m = 0.05$ m.

run	$k_{s,c}$ (m)	$k_{s,w}$ (m)	k_{as}	s_{bs} (-)
1	0.03	0.02	0.05	0.6
2	0.02	0.02	0.05	0.4
3	0.04	0.02	0.05	0.7
4	0.03	0.03	0.05	0.4
5	0.03	0.02	0.1	0.6
6	0.03	0.02	0.2	0.7
7	0.03	0.02	0.05	0.6
8	0.03	0.02	0.05	0.6
9	0.03	0.02	function	0.6
10	function	function	0.05	0.6
11	function	function	function	0.6

Brier Skill Scores s_{bs} for each model run are given in Table 5.3. The base run shows reasonable to good agreement with the measured bed level changes ($s_{bs} = 0.6$). Good agreement ($s_{bs} = 0.7$) between measurements and predictions is found using a relatively large $k_{s,c}$ of 0.04 m with a smaller $k_{s,w}$ of 0.02 m. Disparities between the measured profile and the predictions are largest using equal values for $k_{s,w}$ and $k_{s,c}$ ($s_{bs} = 0.4$). Varying the horizontal mixing coefficients ε_0 (run 7 and 8) has no effect on the results in the present 2D case.

The envelope of model predictions (maximum and minimum predicted bed levels), based on 11 model runs, are shown in Figure 5.7 as well. Generally, the predicted profile evolution shows offshore movement of sediment, erosion of the bar crest and flattening of the profile. The measured erosion in the trough is not predicted by the model, neither is the measured bar growth.

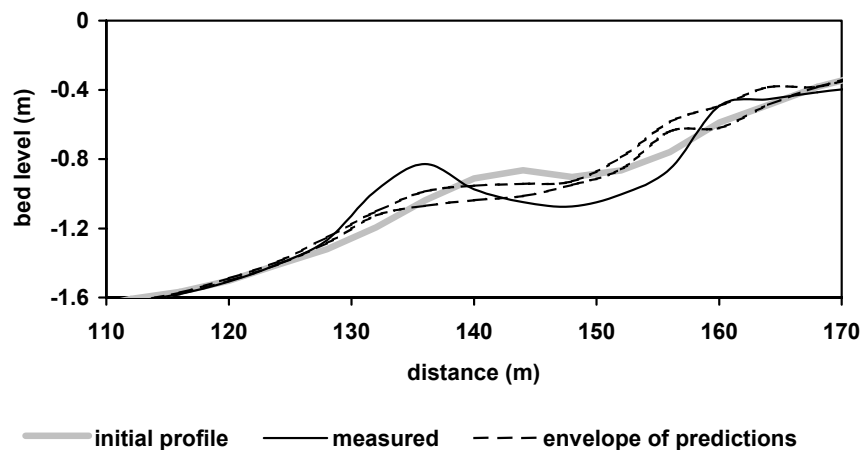


Figure 5.7. Measured and predicted morphological changes after 18 hours for Test 1 B of the LIPIID experiments in the Delta Flume of Delft Hydraulics.

It was noted in Section 5.4 that, compared to the other free model parameters, the roughness heights are the most effective in tuning the model. The roughness heights were however taken constant over the entire profile. In contrast, the laboratory data used here clearly showed a bed form pattern with ripple heights and lengths varying along the bed profile. No ripples or relatively small and flat ripples were found near the bar crest and further seaward. Relatively large ripples were found in the trough shoreward of the bar crest. This argues for a roughness height varying across the profile. To test this effect on the model output, the wave-related roughness height $k_{s,w}$ was varied between 0.01 m on the bar crest and 0.03 m in the trough region. The current-related roughness $k_{s,c}$ was kept constant at 0.03 m. Figure 5.8 shows the computed profile based on these settings. As can be seen, the effect of using a varying wave-related roughness height is significant. Agreement between the measured and predicted profile is excellent with $s_{bs} = 0.8$.

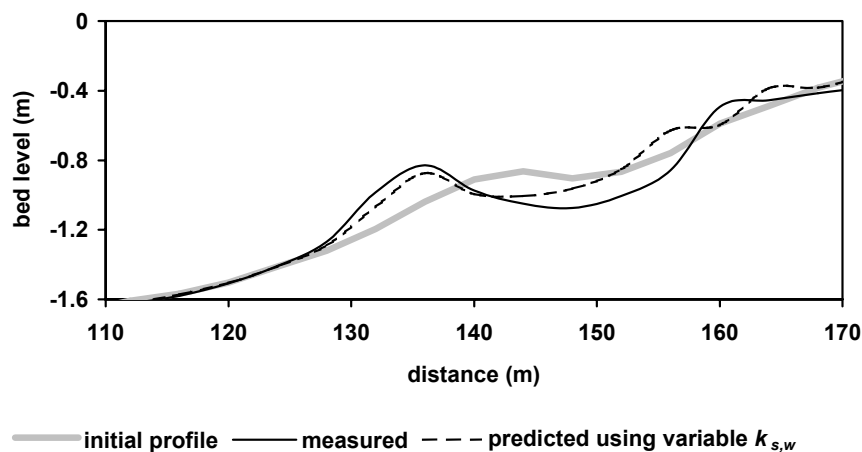


Figure 5.8. Measured and predicted morphological changes after 18 hours for Test 1 B of the LIPIID experiments in the Delta Flume of Delft Hydraulics.

5.5.3. STORM SCALE (DAYS-WEEKS): EGMOND AAN ZEE

The model is compared to measured morphological changes near the coast of Egmond aan Zee during three selected periods of 6, 7 and 12 days, respectively. The initial and boundary conditions are described first. After that, the measured morphological changes during the three individual periods are described. Finally, model predictions are compared to measured morphological changes.

Initial and boundary conditions

The coastline near Egmond aan Zee is part of the central Netherlands coast (Short, 1992; Wijnberg, 1995). The nearshore zone of Egmond aan Zee is generally characterized by two subtidal nearshore bars (Figure 5.9). The outer nearshore bar is located at about 550m and the inner nearshore bar at 200 m from the shore. The field site is described in more detail in Section 2.6 of this thesis.

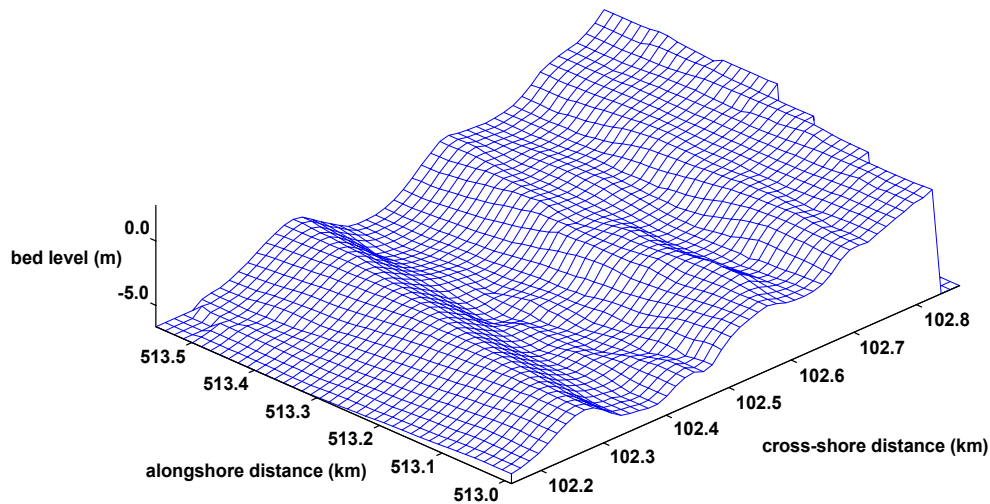


Figure 5.9. Three-dimensional plot of the nearshore bathymetry near the coast of Egmond aan Zee, The Netherlands, 23 March 1998.

Herein the measured and computed morphological changes are compared for three periods:

- period 1: from 18 to 24 October 1998 (bursts 9168-9312)
offshore wave conditions: $H_{rms} = 0.6 - 2$ m, $T_p = 4-11$ s, $\theta = -49$ to 52° .
- period 2 from 24 to 31 October 1998 (bursts 9312-9480)
offshore wave conditions: $H_{rms} = 0.6 - 3.5$ m, $T_p = 4-11$ s, $\theta = -33$ to 61° .
- period 3 from 31 October to 12 November 1998 (bursts 9480-9768)
offshore wave conditions: $H_{rms} = 0.5 - 2.8$ m, $T_p = 3-9$ s, $\theta = -74$ to 61° .

The incident wave conditions are taken to be those measured by a directional Waverider at about 5 km from the shore (Figure 5.10). The averaged tidal gauge data from IJmuiden and Petten-Zuid are used as an input for the tidal water level variations. The wind input consists of wind data obtained from a meteo pole at about 500 m offshore. Tide driven longshore velocities are taken to be the low-pass filtered longshore velocities from station E1 at about 550 m offshore (Section 2.6). The filtering was done

to eliminate wave driven longshore currents from the measured signal. The model is initiated with the bed level measured by an amphibious vehicle on the first day of the selected period. A median grain diameter of $D_{50} = 0.24$ mm is used.

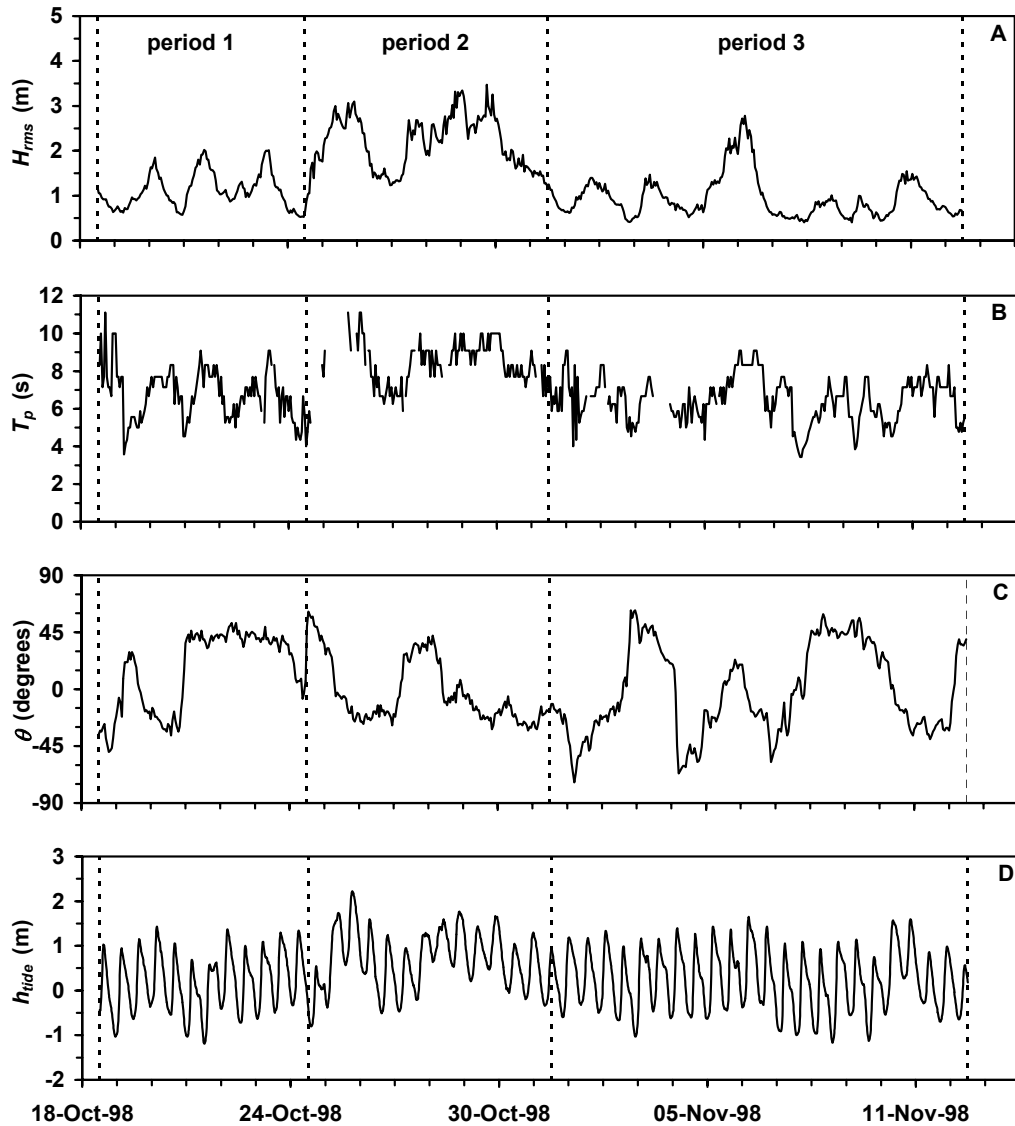


Figure 5.10. Wave height (A), wave period (B), wave direction (C) and tide level (D) versus time measured at 5 km from the shore at Egmond. Vertical dashed lines separate the selected periods.

Measured cross-shore changes

The principal requirement for use of the model is longshore uniformity in bathymetry and waves. A non-uniform bathymetry results in a longshore-varying wave field. In such a case, the longshore current may reverse or weaken at points and the nearshore flow pattern may tend to form rip currents with longshore currents serving as feeder currents between the rips. On large longshore scale (10 km) and on long term (years) the

bars near Egmond are 2-dimensional in the sense that they are continuous and of the same form in longshore direction and show the same overall migration pattern (Van Enckevort, 2001). On smaller spatial scale (1 km), and shorter time spans (weeks to months), longshore non-uniformities may develop as local disturbances, which are superimposed on the overall straight bar pattern yielding a 3-dimensional morphological system. This spatial variability was reduced by longshore averaging of the available cross-shore profiles. These longshore-averaged profiles were used for the model simulations. Caljouw and Kleinhout (2000) studied the longshore averaging in detail for the Egmond aan Zee field site. They averaged six transects with a spacing of 100 m for the three periods. The longshore variability is expressed as a standard error band around the mean profile. The longshore-averaged profiles and the error bands around the mean profiles are presented in Figure 5.11.

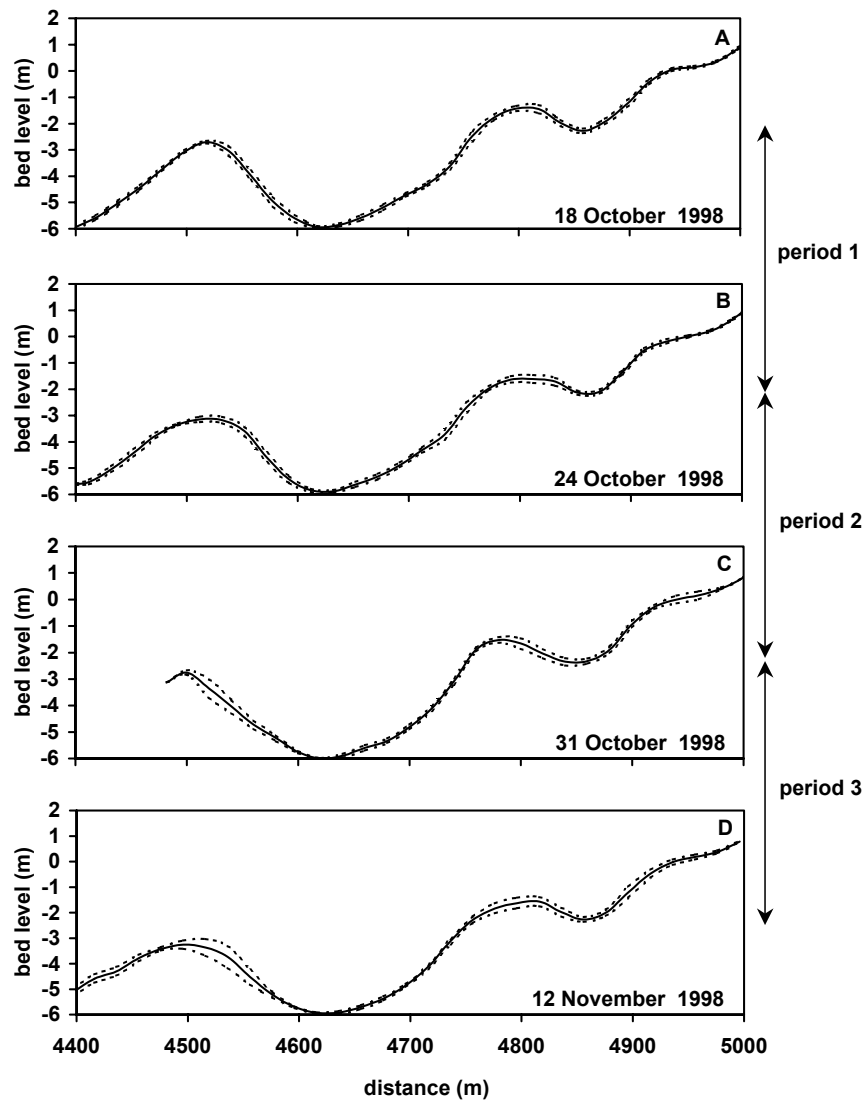


Figure 5.11. Measured longshore-averaged profiles (solid lines) and standard error band (dashed lines) near Egmond.

Morphological changes between October 18 and October 24 (period 1) are relatively small (Figure 5.11A and B). There is some erosion (~ 0.5 m) of the outer bar crest and the slope of the seaward flank of the outer bar becomes flatter. The trough between the inner and outer bar and the inner bar remain stable. Large morphological changes take place during period 2 between October 24 and October 31 (Figure 5.11B and C). The outer bar migrates about 50 m offshore and the inner bar migrates about 10 m offshore. The troughs remain stable and the changes near the beach are small. Measured morphological changes during period 3, between October 31 and November 12, are again small (Figure 5.11C and D). Slight erosion occurs on the outer bar crest while the inner bar migrates about 30 m onshore.

The difference in profile behavior between period 1 and 3 is interesting. Although wave conditions are relatively calm during both periods, the onshore bar migration during period 3 does not occur during period 1. This might be related to: 1) the long period of calm weather during period 3 with onshore transport dominating the storm event on 6 November, 2) the change of bed forms to flat bed by the high-energetic conditions during the period 2 leading to a dominance of onshore transport near the bed in period 3.

In general, the inner and outer nearshore bars show a rather two-dimensional behavior during the three selected periods. The standard error between the profiles used in the longshore-averaging procedure is largest ($\sim 10\%$) at the shoreward slope of the outer bar and near the crest of the inner bar. As regards the outer bar, this is partly caused by a change in orientation to a more oblique one. The bar troughs of the inner and outer bar are very stable.

Predicted cross-shore changes

For each period, 11 model runs were performed, which are summarized in Table 5.4. The first run is the base run, i.e. the default or optimum run for all parameters based on calibration in the previous chapters. In the base run, $k_{s,w}$ is 0.02 m based on comparison with measured concentration profiles (see Chapter 4), and $k_{s,c} = 0.03$ m, based on comparison with measured longshore currents (see Chapter 3). The default D_{50} was set to 0.24 mm. In the subsequent runs, one of the free parameters is varied; the other parameters are kept constant.

Brier skill scores s_{bs} for each model run are given in Table 5.4. Two s_{bs} values are given for each run. The first is based on the entire profile ($4200 < x < 5000$ m). The second is based on the outer nearshore bar ($4200 < x < 4660$ m). Generally, model skills for the outer bar are better than when considering the entire profile, which is logical because processes occurring in the upper nearshore and beach regions are not incorporated in the model. It is therefore more appropriate to leave out these zones in the computation of s_{bs} .

Table 5.4. Model runs and Brier skill scores on storm scale at Egmond. Bed level measurement error $\Delta z_m = 0.10$ m.

run	$k_{s,c}$ (m)	$k_{s,w}$ (m)	k_{as}	ϵ_0 (m ² /s)	period1		period 2		period 3	
					S_{bs} (-)		S_{bs} (-)		S_{bs} (-)	
					total	outer	total	outer	total	outer
1	0.03	0.02	0.05	2.0	0.3	0.7	<0	<0	0.0	<0
2	0.02	0.02	0.05	2.0	<0	0.2	<0	<0	<0	<0
3	0.04	0.02	0.05	2.0	0.6	0.9	<0	<0	0.3	<0
4	0.03	0.03	0.05	2.0	<0	0.6	<0	<0	<0	<0
5	0.03	0.02	0.1	2.0	0.3	0.8	<0	<0	0.2	<0
6	0.03	0.02	0.2	2.0	0.1	0.9	<0	<0	0.3	0.6
7	0.03	0.02	0.05	0.5	<0	0.2	<0	<0	<0	<0
8	0.03	0.02	0.05	1.0	<0	0.5	<0	<0	<0	<0
9	0.03	0.02	function	2.0	0.3	0.8	<0	<0	0.0	<0
10	function	function	0.05	2.0	0.3	0.7	<0	<0	0.0	<0
11	function	function	function	2.0	0.3	0.8	<0	<0	0.1	<0

Changing the input parameters leads to markedly different skill scores. The morphological changes during period 1 and 3 are predicted with reasonable to good accuracy using a somewhat larger current-related roughness height ($k_{s,c} = 0.04$ m) or a relatively large wave-related transport factor ($k_{as} = 0.2$) than the base run. Both effectuate a larger onshore-directed (or smaller offshore-directed) transport rate keeping more sediment in the profile. Prediction of the morphological changes during the storm period is bad for all input settings.

The envelopes of the model predictions (maximum and minimum predicted bed levels), based on 11 model runs, are shown in Figure 5.12. Despite the different skill scores, all model runs for a given period show a similar behavior. This is most clearly observed for the period 2 model predictions (Figure 5.12B) for which the entire range of model predictions shows too much flattening of the inner and outer nearshore bar. Changing the input parameters does not change the general behaviour of the model. This suggests that the overall discrepancies between the model predictions and the measurements are not so much related to uncertainties in the input parameters but more to processes not included in the present model or imperfect representation of the incorporated processes.

The measured cross-shore profile changes during the three selected periods are relatively small. Even for a longer time span of about a month, with five major storms attacking the beach in November 1998 (not shown here), the beach and inner bar were found to be quite stable. The longshore changes were often much larger than the cross-shore changes (compare Figure 5.11 and Figure 5.12). At some transects the overall

beach face level was about 0.3 m lower or higher. Furthermore, the inner bar was dissected by a rip channel (local depression of about 0.5 to 1 m), which moved longshore over about 100 m during the storm period. The prediction of these small natural changes might be possible in the future by applying an appropriate coastal area model.

It is encouraging to see that the model represents the measured small morphological changes during the relatively calm periods 1 and 3 rather well. However, predicted morphological changes during the more energetic conditions of period 2 are too large.

The model behaves similarly for the three periods when changing the input parameters. Generally, best predictions are obtained using a relatively large $k_{s,c}$ value of 0.04 m (run 3) or a relatively large k_{as} value of 0.2 (run 6). Predictions are worst using similar $k_{s,c}$ and $k_{s,w}$ (run 2 and 4).

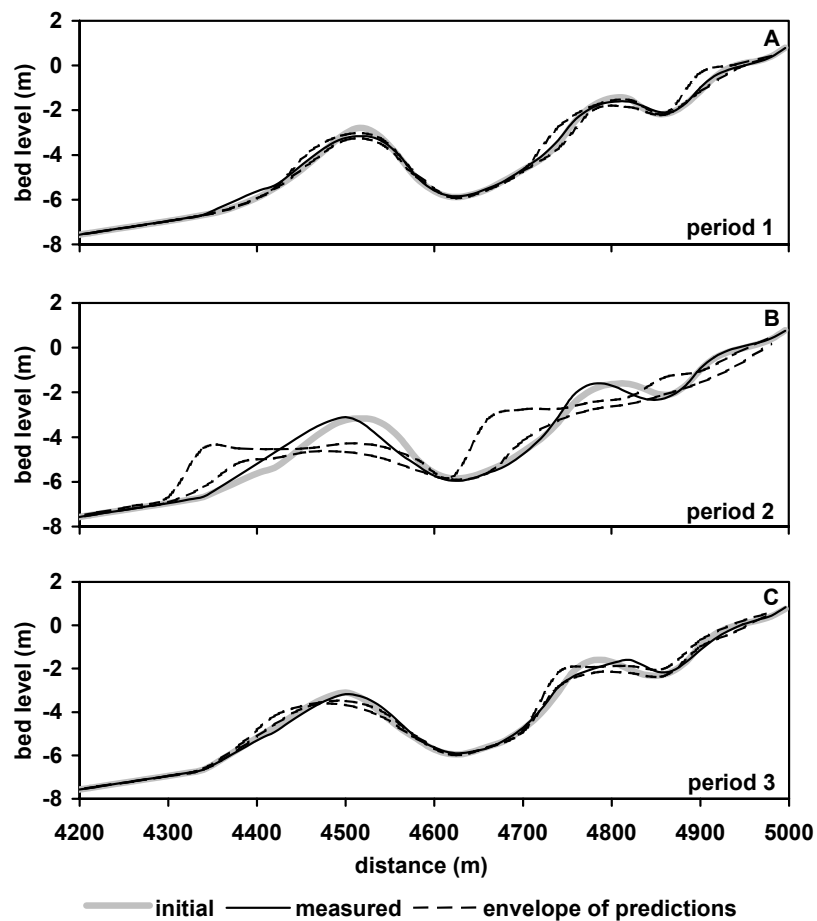


Figure 5.12. Measured and predicted morphological changes near Egmond for period 1 between October 18 and October 24 (A), period 2 between October 24 and October 31 (B), and period 3 between October 31 and November 12 (C).

5.5.4. STORM SCALE (MONTHS): DUCK, NC, USA

The data from the field site near Duck, NC, USA (Figure 5.13), were obtained during the Duck94 field experiment in September and October 1994. The Duck field site is situated on the east (Atlantic) coast of the USA. The tidal range is about 1 m and the tidal currents are weak (0.1 to 0.3 m/s). The winter period is dominated by storm waves and the summer period is dominated by long-period swell. The bed profile generally shows a single bar in the surf zone and sometimes a low outer bar is present. A description of the experimental set-up and of the nearshore bar behavior during the Duck94 measurement campaign is given by Gallagher et al. (1998). The model was used to simulate different morphological events between September 21 and October 20, 1994. Wave conditions are shown in Figure 5.14.

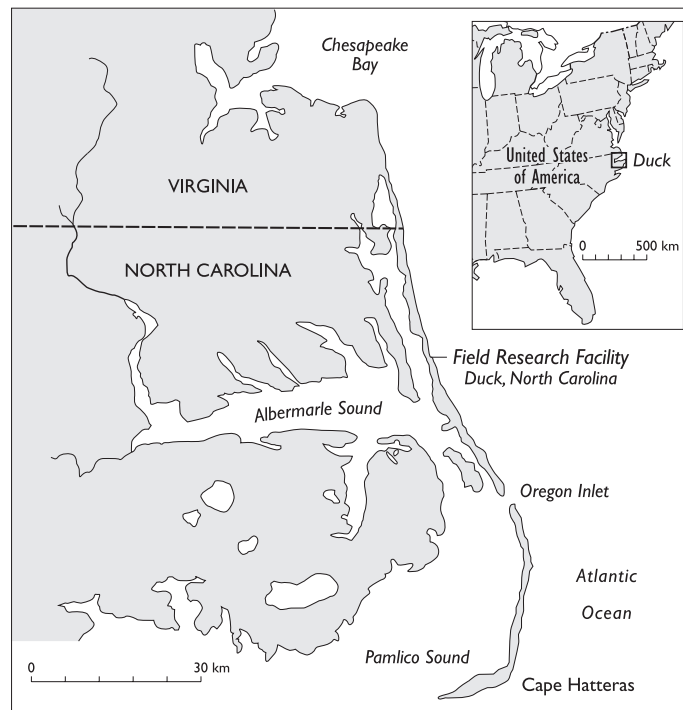


Figure 5.13. Map of the Atlantic East coast of the USA showing the Duck field site.

Initial and boundary conditions

The first selected period is a relatively calm one between 21 September and 4 October 1994. Although two minor storms occurred on September 22 and October 3 with an offshore H_{rms} of about 1.8 m (Figure 5.14), most of the time wave heights were small (< 1.0 m). Wave periods T_p ranged between 4 and 15 s. Wave directions varied between -50° (south) and $+50^\circ$ (north) relative to shore normal. The period between October 4 and October 10 was not selected because conditions differed not much from those in period 1. The second selected period is a more energetic one from October 10 to October 14 with offshore H_{rms} between 1.0 and 1.6 m and T_p between 6 and 8 s. Waves turned from north ($+50^\circ$) to south (-15°). The third selected period includes a severe storm between October 14 and October 20 with almost perpendicularly incoming waves with H_{rms} between 1.0 and 2.8 m and T_p between 8 and 15 s.

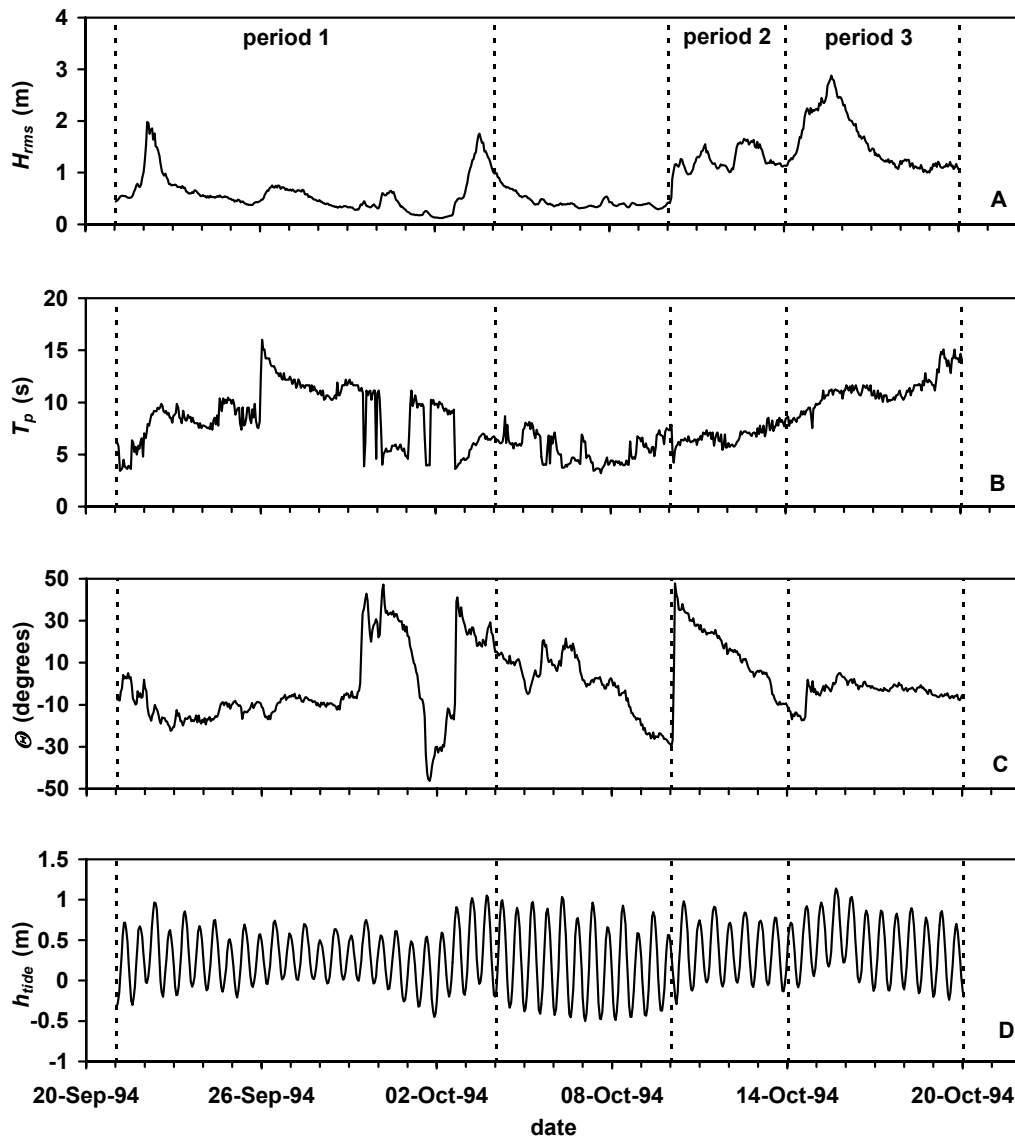


Figure 5.14. Wave height (A), wave period (B), wave direction (C) and tide level (D) versus time measured at 800 m from the shore at Duck, NC. Vertical dashed lines separate the selected periods.

Measured cross-shore changes

The longshore variability of the bathymetry was reduced by averaging 8 cross-shore profiles over a longshore distance of 500 m. Figure 5.15 shows the resulting profiles and their standard error bands. As illustrated by Figure 5.15E, the error bands for the profile on October 20 are relatively large, indicating that longshore non-uniformities in the bathymetry were relatively large. Between September 21 and October 4 erosion took place near the bar trough and sedimentation near the crest, which resulted in a more pronounced bar feature but not in migration of the bar. During this period, a minor storm occurred on September 22 with an H_{rms} wave height of about 1.8 m at a position

800 m offshore. For the rest of time the conditions were relatively calm with offshore H_{rms} wave heights between 0.3 and 0.7 m. Morphological changes were small during the calm weather period between October 4 and October 10. Offshore migration over about 25 m occurred during the high-energy wave conditions between October 10 and October 14. The bar migrated further offshore between October 14 and October 20. This period also shows an overall flattening of the profile.

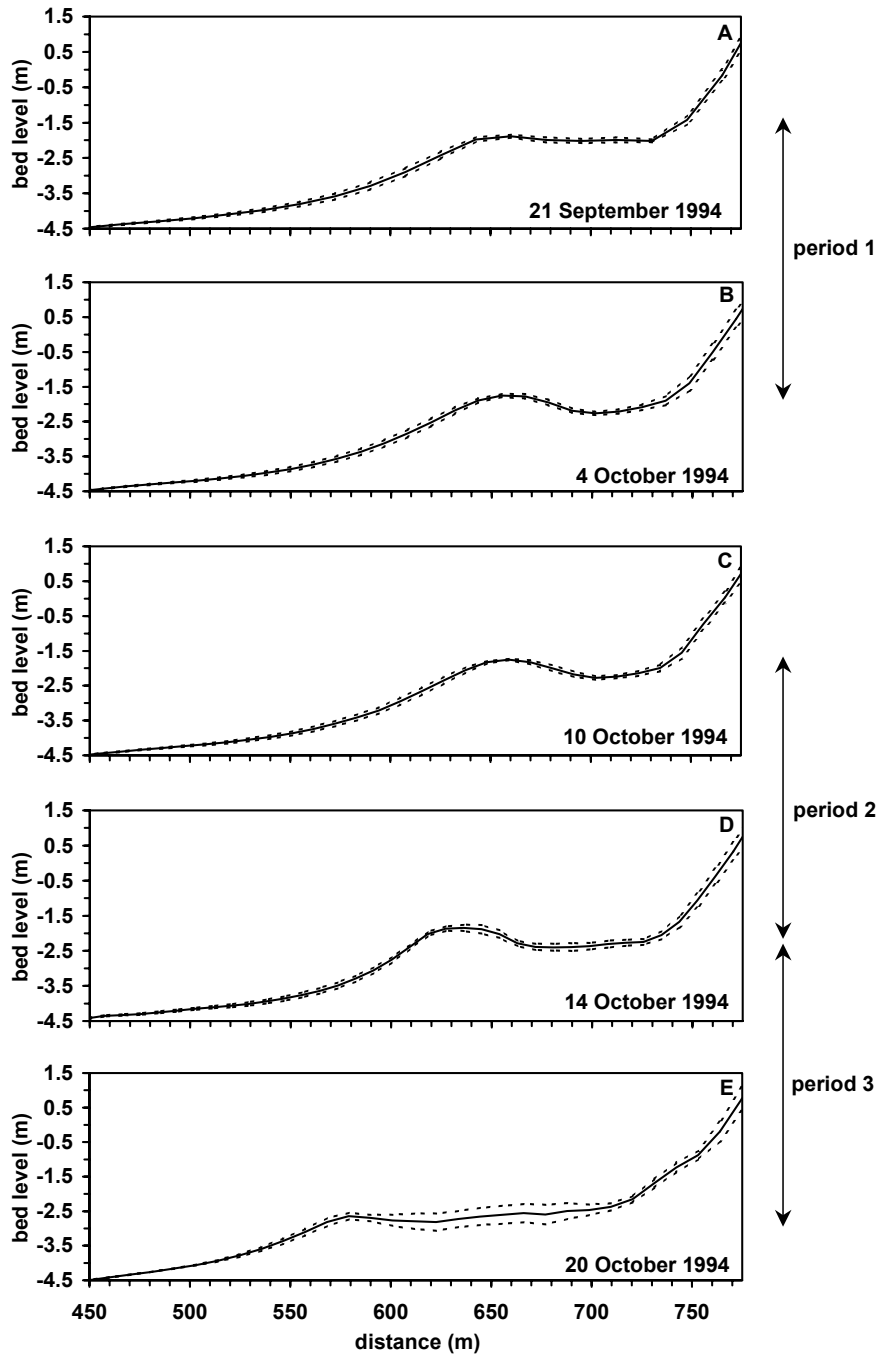


Figure 5.15. Measured longshore averaged profiles (solid lines) and standard error band (dashed lines) near Duck, NC, USA.

Predicted cross-shore changes

The longshore-averaged profiles as shown in Figure 5.15 A, C and D were used as input in the profile model for the three selected periods, respectively. For each period, 11 model runs were performed, which are summarized in Table 5.5. The first run is the base run, i.e. the default or optimum run for all parameters based on calibration in the previous chapters. In the base run, $k_{s,w}$ is 0.02 m based on comparison with measured concentration profiles, and $k_{s,c} = 0.03$ m, based on comparison with measured longshore currents. The default D_{50} was set to 0.20 mm (Gallagher et al., 1998). In the subsequent runs, one of the free parameters is varied; the other parameters are kept constant. Brier skill scores for each model run are also given in Table 5.5. As for the Egmond case, two s_{bs} values are given. The first is based on the entire profile. The second is based on the outer nearshore bar ($400 < x < 700$ m).

Table 5.5. Model runs and Brier skill scores for Duck.

run	$k_{s,c}$ (m)	$k_{s,w}$ (m)	k_{as}	ε_0 (m ² /s)	period 1		period 2		period 3	
					s_{bs} (-)		s_{bs} (-)		s_{bs} (-)	
					total	outer	total	outer	total	outer
1	0.03	0.02	0.05	2.0	<0	<0	<0	0.7	<0	<0
2	0.02	0.02	0.05	2.0	<0	<0	<0	0.2	<0	<0
3	0.04	0.02	0.05	2.0	<0	<0	<0	0.8	<0	<0
4	0.03	0.03	0.05	2.0	<0	<0	<0	0.4	<0	<0
5	0.03	0.02	0.1	2.0	<0	<0	<0	0.8	<0	<0
6	0.03	0.02	0.2	2.0	<0	<0	0.0	0.8	<0	<0
7	0.03	0.02	0.05	0.5	<0	<0	<0	0.7	<0	<0
8	0.03	0.02	0.05	1.0	<0	<0	<0	0.7	<0	<0
9	0.03	0.02	function	2.0	<0	<0	<0	0.7	<0	<0
10	function	function	0.05	2.0	<0	<0	<0	0.3	<0	<0
11	function	function	function	2.0	<0	<0	<0	0.3	<0	<0

As for the Egmond case, model predictions are bad to poor when considering the entire profile in the computation of the s_{bs} , which is caused by a bad prediction of the inner nearshore and the beach. Processes occurring in these regions are not incorporated in the model. The envelopes of model predictions (maximum and minimum predicted bed levels), based on 11 model runs, are shown in Figure 5.16. Despite the different skill scores, it can be seen that all model runs for a given period show a similar behavior. Predictions are bad for period 1 (Figure 5.16A). The model tends to flatten the profile instead of generating a more pronounced bar feature as measured. The model transports too much sediment onshore from the bar to the lower beach and from the upper to the lower beach, leading to accretion in the trough, where the measured changes are negligible. Agreement between measurements and predictions for the outer bar is reasonable to good for period 2 although the model tends to flatten the profile. Best

predictions are obtained using a relatively large current-related roughness height $k_{s,c}$ (0.03-0.04 m) in combination with a smaller wave-related roughness height $k_{s,w}$ (0.02 m) or using a relatively large wave-related transport factor k_{as} of 0.1 or 0.2. Predictions for period 3 are again bad. The model flattens the profile too much. Although varying the input parameters has a substantial effect on the model predictions, the general trend remains the same. This suggests that the overall discrepancies between the model predictions and the measurements is not so much related to uncertainties in the input parameters but more to factors not included in the present model.

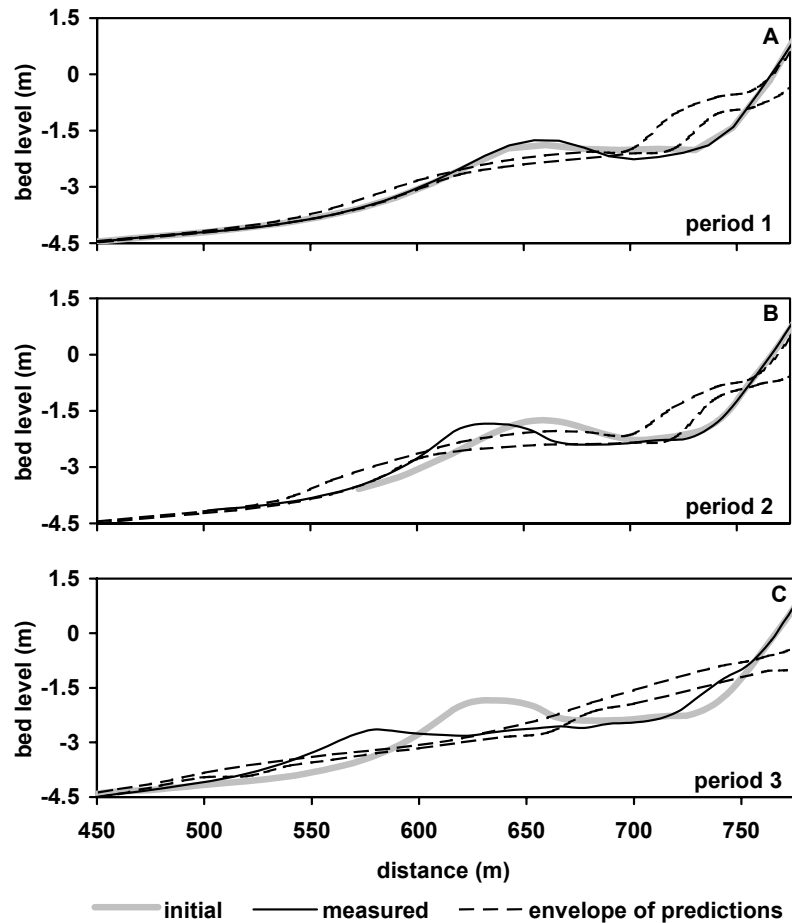


Figure 5.16. Measured and predicted morphological changes near Duck for period 1 between September 21 and October 4 (A), period 2 between October 10 and October 14 (B), and period 3 between October 12 and October 20 (C).

5.5.5. SEASONAL SCALE (MONTHS): EGMOND AAN ZEE

Introduction

Process-based cross-shore profile models are generally applied on time scales not longer than days or weeks. Reasons for this are the expected erroneous developments due to the build up of errors with increasing number of time steps and uncertainties in the input

parameters. On the other hand and as noted previously, on longer time scales the nearshore bathymetry behaves more 2-dimensional in the sense that the migration of nearshore bars is more longshore uniform, which would favor the use of a 2D cross-shore profile model. Van Enkevort (2001) has shown that the relative importance of longshore uniform bar crest behavior increases with time span. For small time spans (days to weeks, storms), net bar crest changes are mainly longshore non-uniform, whereas for larger time spans (months, seasons) longshore uniform changes dominate. Considering this, use of a cross-shore profile model would be most suitable for predicting morphological changes on a seasonal time scale. This leads to the paradox that the application of a cross-shore profile model seems to be more appropriate on longer time scales, while the question is whether the processes incorporated in the present cross-shore profile model are adequate to describe the profile behavior on these long time scales with sufficient accuracy.

In this section, measured longshore-averaged profile changes over a period of several months are compared to model predictions. As for the short term comparisons, input parameters are varied between physically realistic values to reflect uncertainties in the model and to provide insight in the inaccuracies of the model predictions. The question is addressed to what extent a 2D cross-shore process-based profile model is applicable for morphodynamic predictions on the time scale of months.

Initial and boundary conditions

The cross-shore profile changes predicted by the model are compared to observed profile changes for two morphodynamic periods of a few months, i.e.

- period 1 between 11 May 1998 to 24 October 1998 (summer period),
- period 2 between 24 October 1998 to 25 February 1999 (winter period).

The start and end date of the periods were selected based on availability of bathymetric data. The summer period (period 1) is characterized by relatively calm conditions with a maximum offshore H_{rms} of about 3 m (see Figure 5.17). Two moderate storms occur with $2 < H_{rms} < 3$ m while $H_{rms} < 1.0$ m for about 60% of the time. The wave period T_p ranges between 4 and 8 seconds with an average of 6 s. There is no dominant wave direction and wind-driven water level setup is always smaller than 0.80 m.

The winter period (period 2) is characterized by high-energy wave conditions with maximum H_{rms} of about 4.5 m. Two severe storms occur with $H_{rms} > 3$ m and three moderate storms with $2 < H_{rms} < 3$ m while $H_{rms} < 1.0$ m during about 45% of the time. Wave period T_p ranges between 4 and 11 s with an average of 6.0 s. The incident wave direction is predominantly southwest and storm setup often exceeds 0.80 m. Besides the wind-driven water level set-up shown in Figure 5.17, the water level has been varied through the tide (not shown). Wave conditions during summer and winter are compared in Figure 5.18. Clearly, relatively small waves occur more frequently in summer than in winter.

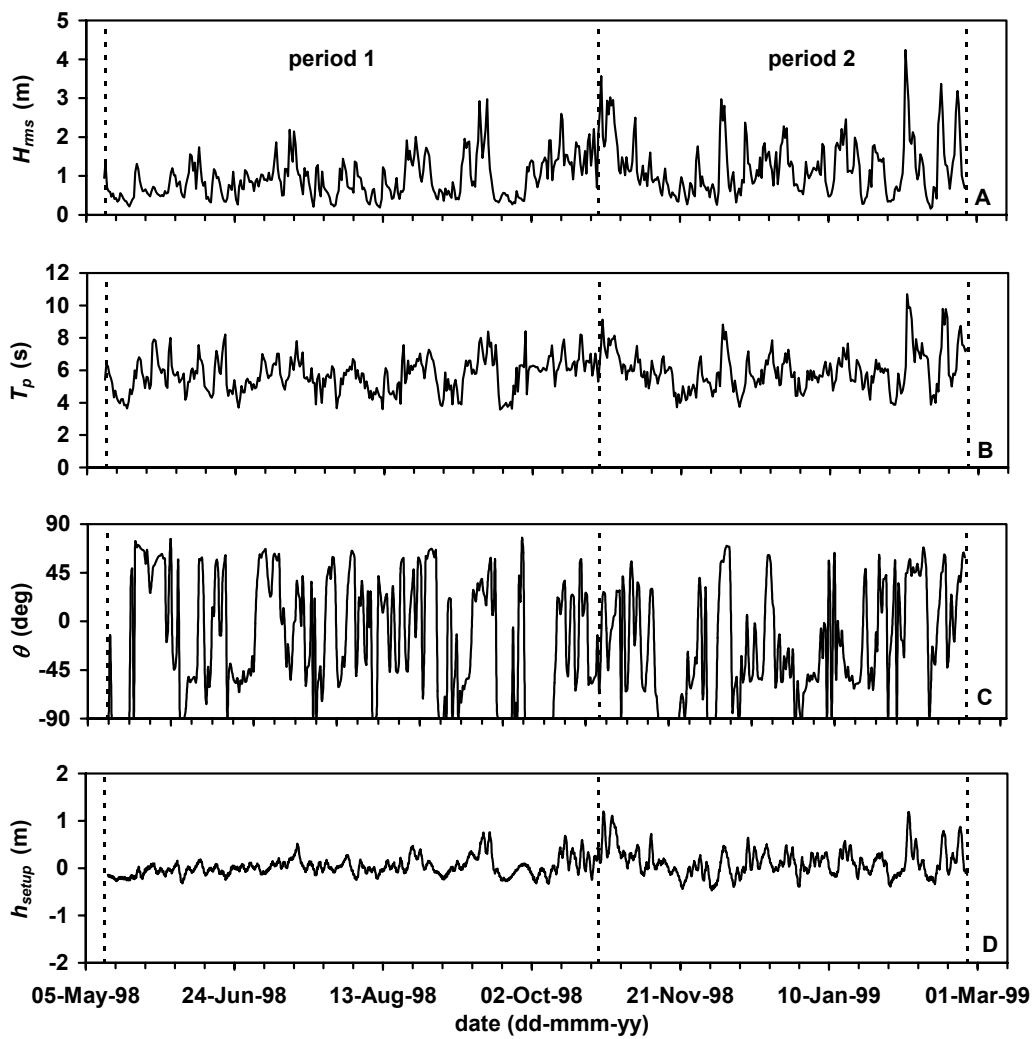


Figure 5.17. Wave height (A), wave period (B), wave direction (C) and wind-driven water level setup (D) versus time measured during a 10 month period in 1998 at Egmond aan Zee.

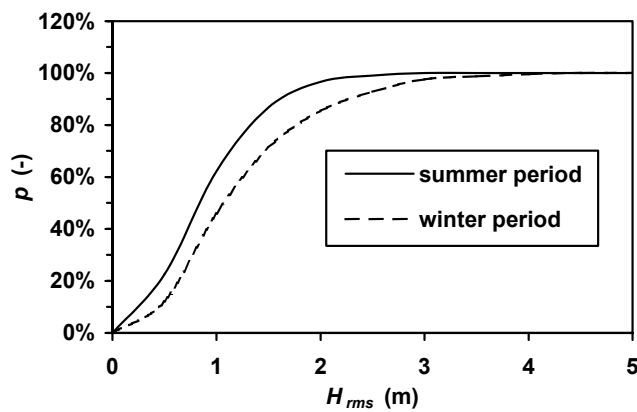


Figure 5.18. Probability of exceedance of H_{rms} during winter and summer period at Egmond.

Measured cross-shore changes

The longshore-averaged bed profiles are shown in Figure 5.19. The averaging was done using 9 profiles over a longshore distance of 800 m. The summer period (Figure 5.19 A and B) is characterized by growth of the outer (~0.4 m) and inner (~0.5 m) nearshore bar and erosion of the trough between the two bars. The winter period (Figure 5.19 B and C) is characterized by erosion and significant offshore migration of both outer (~100 m) and inner (~50 m) nearshore bar. The error bands for 11 May and 24 October 1998 are relatively small which means that, longshore non-uniformities are small although the shoreward slope of the outer bar shows some longshore variability. This is also the case for the inner nearshore bar and the beach on 25 February 1999. Longshore variability of the outer nearshore bar is somewhat larger on this date. For both periods though, cross-shore changes are most pronounced and larger than the longshore variability.

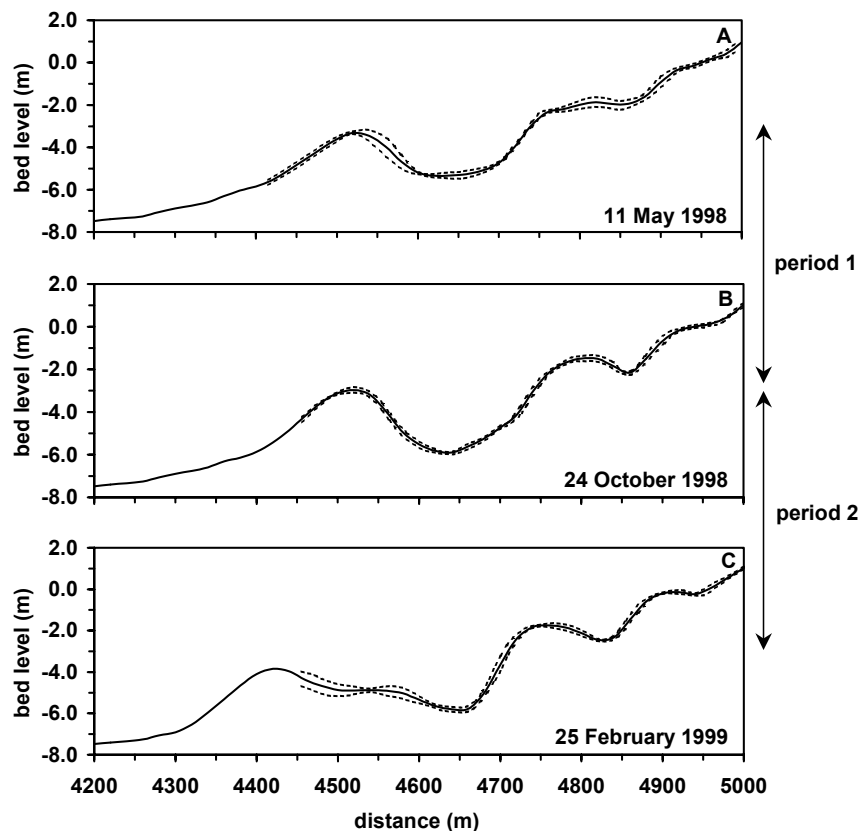


Figure 5.19. Measured longshore-averaged profiles (solid lines) and standard error band (dotted lines) versus cross-shore distance near Egmond.

Predicted cross-shore profile changes

Agreement between measured and predicted morphological changes was found to be bad, irrespective of the chosen combination of input parameters. All runs showed negative s_{bs} values for both periods (table not shown), which means that model predictions are worse than the baseline-scenario (= no change). A clear picture of the

medium-term model behavior can be observed from Figure 5.20, in which the envelope of model predictions are shown, based on 11 model runs. Generally the model runs show a similar behaviour with flattening of the profile and the formation of a step in the profile in the inner nearshore zone at a water depth of about 4 m. The most important parameter affecting the medium-term predictions was found to be the wave-related transport factor k_{as} .

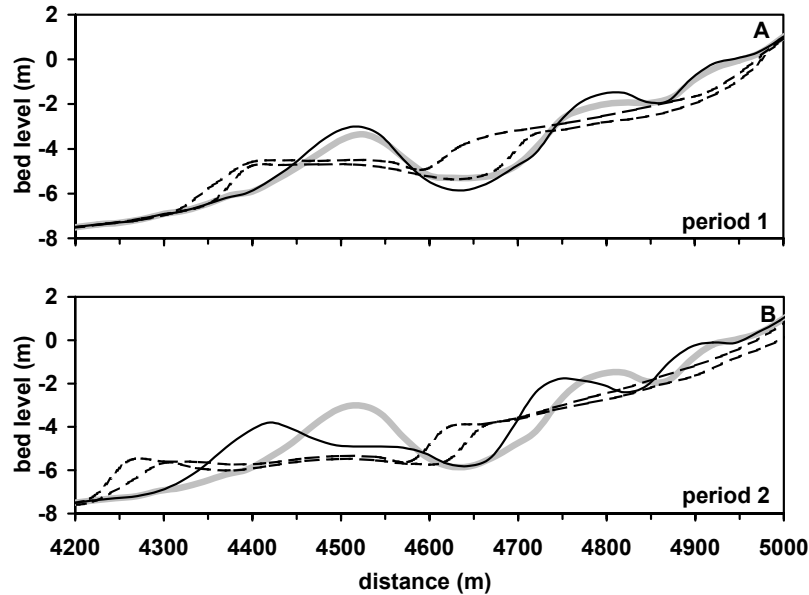


Figure 5.20. Measured and predicted medium-term morphological changes near Egmond for period 1 between 11 May 1998 and 24 October 1998 (A), and period 2 between 24 October 1998 and 25 February 1999 (B). See Figure 5.17 for wave conditions.

5.5.6. SEASONAL SCALE: A SHOREFACE NOURISHMENT

In August 1999 a shoreface nourishment was implemented along the Egmond aan Zee coast to stabilize the existing coastline. In terms of design dimensions in total 900.000 m³ of sediment was involved and this sediment was supplied on the seaward flank of the outer nearshore bar at about 700 m offshore (Figure 5.21).

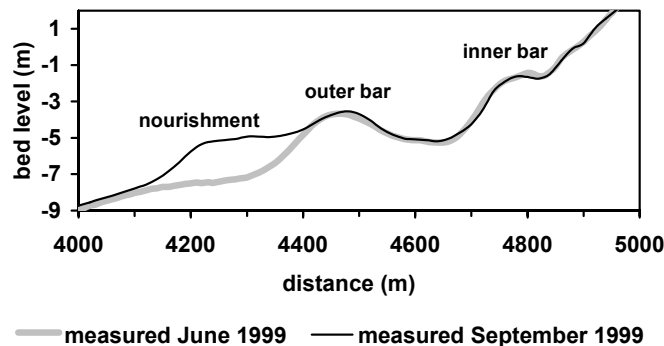


Figure 5.21. Longshore-averaged cross-shore profiles before and after implementation of a shoreface nourishment in 1999 near the coast of Egmond aan Zee.

For the nourished zone, the amount of sediment supplied was equivalent to an average vertical change in seabed elevation of about 2 m and, in a longshore direction the amount of nourished sediment per cross-section was in the order of 400 m³/m. The nourishment with a total length of about 2.2 km is located in the depth interval between -5 and -7 m below NAP. Figure 5.21 shows the cross-shore profile just before and after the implementation of the nourishment, respectively.

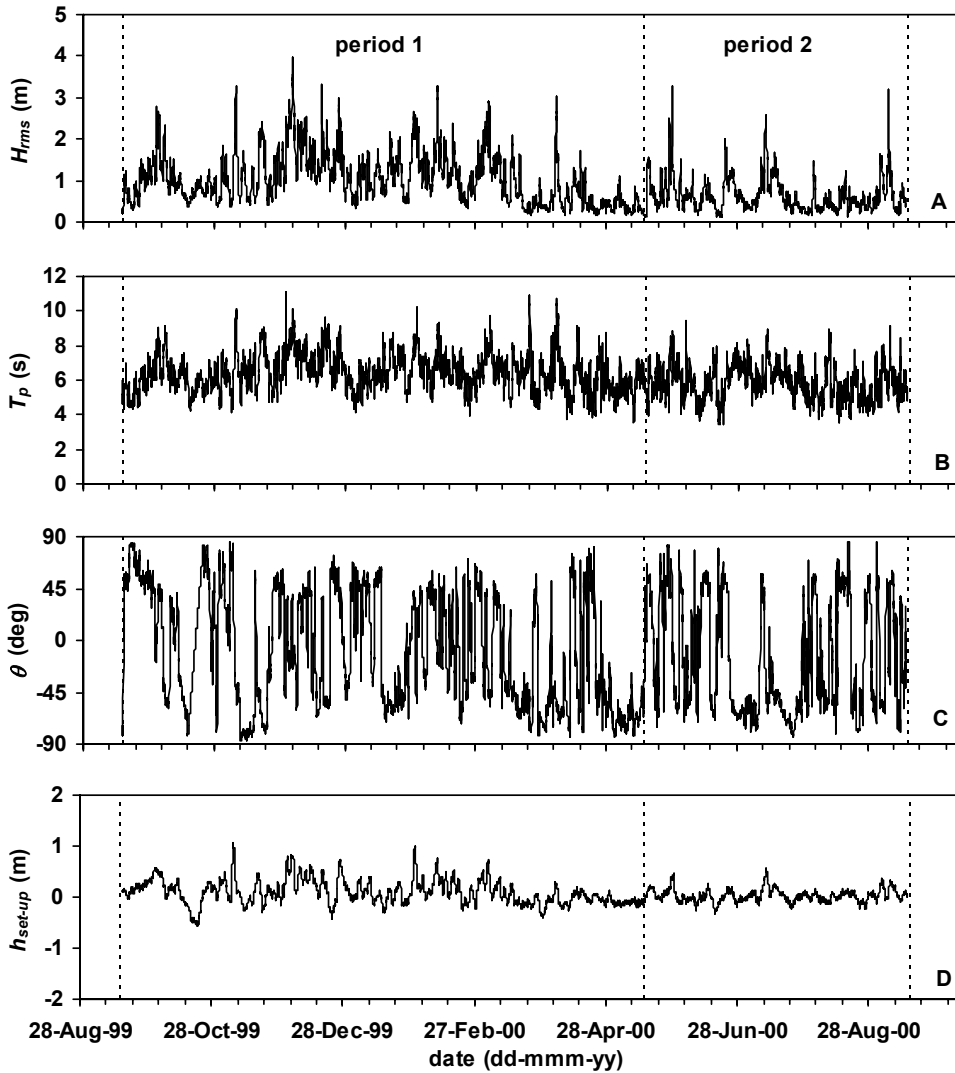


Figure 5.22. Wave height (A), wave period (B), wave direction (C) and wind-driven water level setup (D) versus time measured between September 1999 and September 2000 at Egmond. Vertical dashed lines separate the selected periods.

The basic assumption underlying the design and implementation of the shoreface nourishment is that eventually sand will be carried to the shore. This section will focus on the medium-term developments of the shoreface nourishment near the coast of Egmond aan Zee in nearly two years after the implementation. The cross-shore profile

changes predicted by the model are compared to observed profile changes for two morphodynamic periods of a few months, i.e.

- period 1: from September 1999 to May 2000 (winter period),
- period 2: from May 2000 to September 2000 (summer period).

The 8-month winter period immediately after implementation of the nourishment (period 1) is characterized by high-energy wave conditions with maximum H_{rms} of about 3.8 m (see Figure 5.22). Three severe storms occur with $H_{rms} > 3$ m and about eight moderate storms with $2 < H_{rms} < 3$ m while $H_{rms} < 1.0$ m during about 45% of the time. Wave period T_p ranges between 4 and 11 s with an average of 6.4 s.

The incident wave direction is predominantly southwest and storm setup often exceeds 0.80 m. The 4-month summer period (period 2) is characterized by relatively calm conditions with a maximum offshore H_{rms} of about 3 m. Three moderate storms occur with $2 < H_{rms} < 3$ m while $H_{rms} < 1.0$ m for about 60% of the time. The wave period T_p ranges between 4 and 9 seconds with an average of 5.8 s. There is no dominant wave direction and wind-driven water level setup is always smaller than 0.80 m.

Figure 5.23 shows the longshore-averaged cross-shore profiles of the nourished area between June 1999 and June 2001. The nourishment was carried out in August 1999. Some of the nourished sand has moved onshore but overall the nourished area remains rather stable during 8 months after the implementation (Figure 5.23 B-C). The development of the nourishment and outer bar area shows the formation of a trough between the nourishment and the outer bar. The nourishment starts to behave like an outer bar and the original outer bar is forced to migrate onshore. During this migration, the original inner bar reduces or disappears. In other words, the implementation of the shoreface nourishment sets the bar system back in time in the overall offshore bar migration cycle (Wijnberg, 1995; Van Enckevort, 2001).

The morphological changes are small in the summer period between May and September 2000 (Figure 5.23 C-D). The nourished area and the outer bar remain at their position and the inner bar migrates about 30 m onshore. The nourished area remains stable between September 2000 and April 2001 (Figure 5.23 D-E). Erosion on the seaward flank of the outer bar takes place and the trough between the inner and outer bar is filled up. The inner bar feature disappears. Morphological changes are again small for the summer period between April 2001 and June 2001.

After two years of monitoring, it appears that much of the nourished sand is still present in the nearshore profile. The nourishment has remained at its cross-shore position and the outer nearshore bar has migrated about 150 m onshore, which has resulted in the formation of a three bar system.

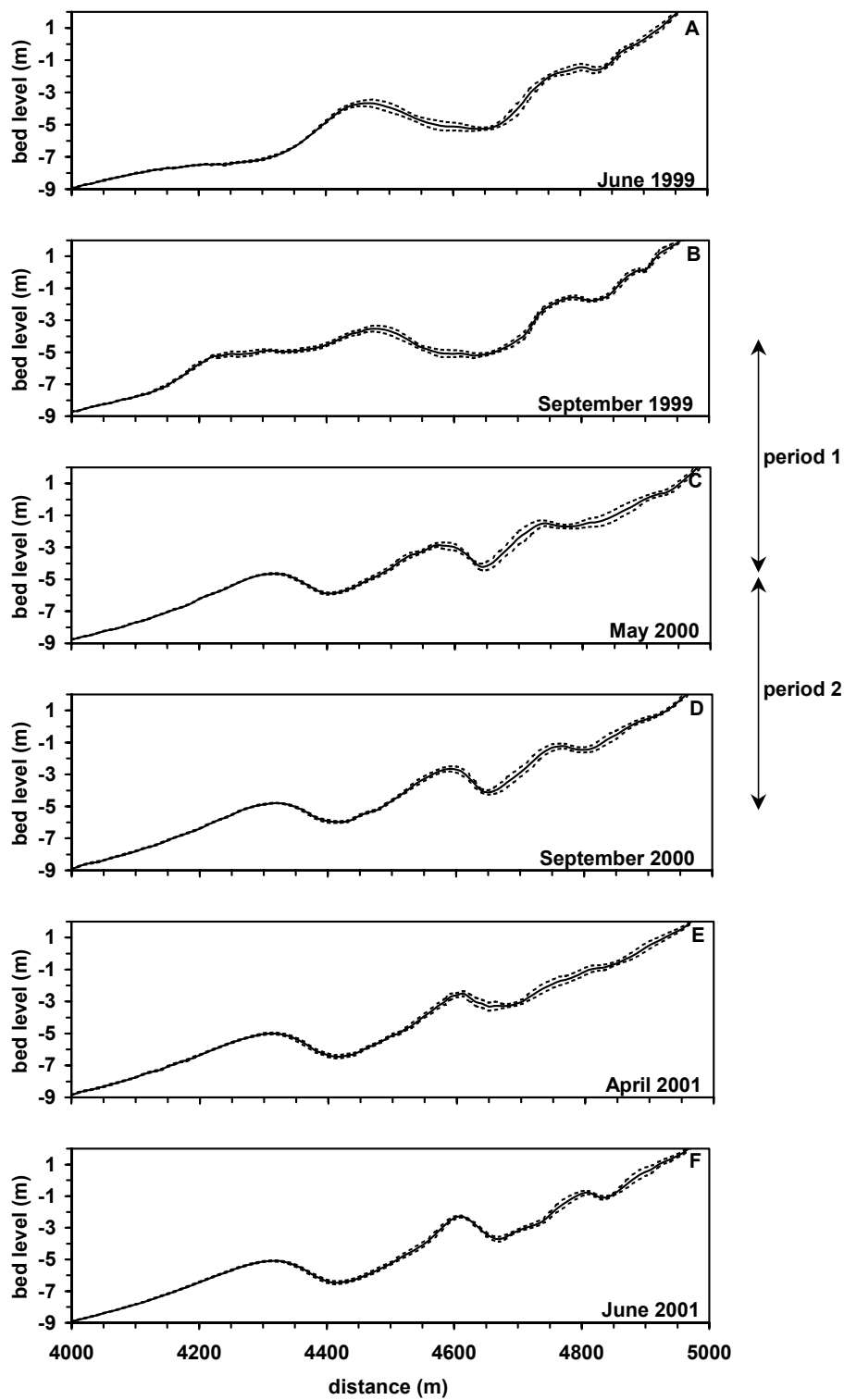


Figure 5.23. Longshore-averaged cross-shore profiles of the nearshore zone of Egmond aan Zee before (A) and after (B-F) the implementation of a shoreface nourishment on the seaward flank of the outer nearshore bar.

Figure 5.24A shows the measured and predicted morphological changes of the nourished profile during period 1 (winter). The measurements show the nourished area to be rather stable. The outer bar migrates about 100 m onshore filling up the trough between the outer and inner nearshore bar. The model predictions also show a filling of the trough between the outer and inner nearshore bar but this is a result from offshore transport of sand from the beach. The model flattens the entire profile for all period 1 runs.

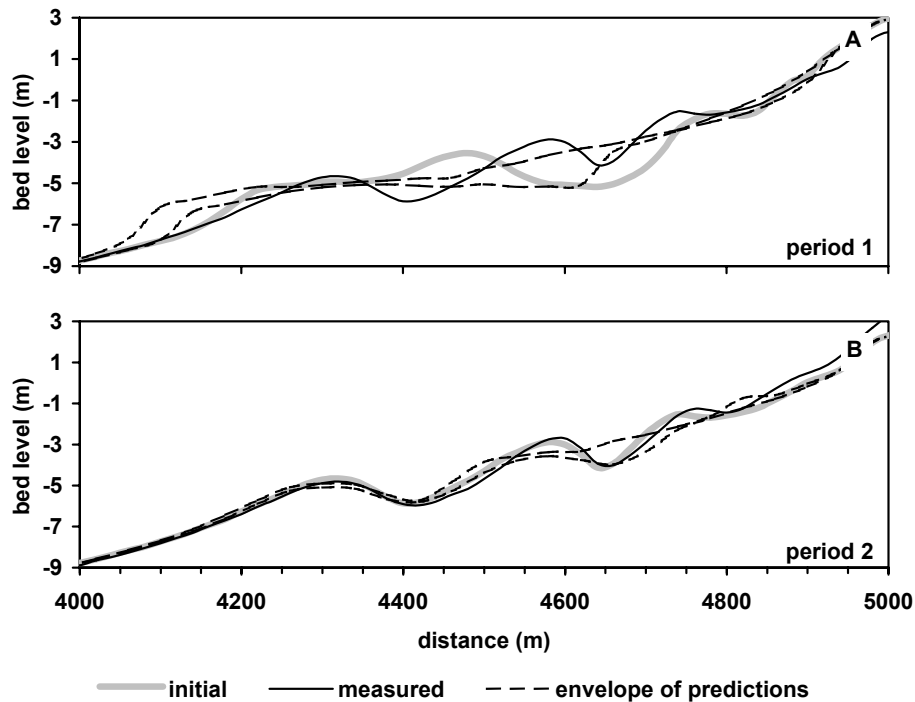


Figure 5.24. Measured and predicted medium-term morphological changes after the implementation of a shoreface nourishment near Egmond aan Zee for period 1 between September 1999 and May 2000 (A) and period 2 between May 2000 and September 2000 (B).

The measured morphological changes during period 2 (summer) are small (Figure 5.24B). The nourishment is stable during this period and the outer and inner nearshore bars migrate about 10 m onshore. The model also predicts relatively small morphological changes but the predicted changes are larger than the measurements.

Brier skill scores for the total profile ($4100 < x < 5000$ m), the nourishment ($4100 < x < 4400$ m) and the outer bar ($4400 < x < 4640$ m) are given in Table 5.6. The behaviour of the nourished area is reasonably (period 1) to excellently (period 2) predicted using a relatively large wave-related efficiency factor k_{as} of 0.2.

Table 5.6. Model settings and Brier skill scores for nourishment model runs Egmond aan Zee.

run	$k_{s,c}$ (m)	$k_{s,w}$ (m)	k_{as} (-)	ε_0 (m ² /s)	period 1			period 2		
					s_{bs} (-)			s_{bs} (-)		
					total	nourish ment	outer	total	nourish ment	outer
1	0.03	0.02	0.05	2.0	0.4	<0	0.4	<0	<0	<0
2	0.02	0.02	0.05	2.0	<0	<0	<0	<0	<0	<0
3	0.04	0.02	0.05	2.0	0.4	<0	0.4	0.0	0.3	<0
4	0.03	0.03	0.05	2.0	<0	<0	0.9	<0	<0	<0
5	0.03	0.02	0.1	2.0	0.5	0.3	0.4	0.0	0.5	<0
6	0.03	0.02	0.2	2.0	<0	0.4	<0	0.3	0.9	0.1
7	0.03	0.02	0.05	0.5	<0	<0	<0	<0	0.0	<0
8	0.03	0.02	0.05	1.0	0.4	<0	0.4	<0	<0	<0
9	0.03	0.02	function	2.0	0.4	0.1	0.3	<0	0.2	<0
10	function	function	0.05	2.0	<0	<0	0.4	<0	<0	<0
11	function	function	function	2.0	<0	<0	0.6	<0	0.2	<0

5.6. EFFECT OF WAVE CHRONOLOGY

The wave chronology may play an important role in determining how nearshore profiles evolve (Southgate, 1995; Aarninkhof et al., 1998). The measured sequence of wave events was used as an input for the model runs in the previous sections. This section demonstrates the effect of changing the sequence of wave events (wave chronology) on the morphological predictions. Consideration of this wave chronology is important because future sequencing of wave conditions are predictable for a limited time (typically several days), which corresponds to the predictability of future meteorological conditions or the time of travel of distantly generated waves. A further issue is that of the cyclic variation in wave conditions. There is, for example, a positive correlation between wave conditions during one storm season and during the next. This could mean that, if wave chronology effects were small on a short time span (days to weeks) and there would be a positive correlation between the short-term events, predictions on a longer time span (months to years) would simply come down to computing morphological changes using the same short-term wave conditions cyclically. The methodology adopted here starts with the measured time series of wave and tide data near the coast of Egmond aan Zee. New series are generated by sorting the time series in ascending and descending wave heights. The only modification is a re-ordering of the time series. The wave-tide combinations are preserved. Two wave sequences are used, the first is based on a short-term term (7 days) storm period from 24 to 31 October 1998 (see Section 5.5.3), the second is based on a medium term (5 months) calm period from 11 May 1998 to 24 October 1998 (see Section 5.5.5). The wave sequences used here are of durations shorter than the seasonal variations, thus no account has been taken of seasonal (or other cyclic) variations in wave conditions.

Figure 5.25 shows the effect of changing the wave chronology on the predicted morphological changes. Using an ascending wave height leads to slightly less offshore migration of the inner nearshore bar than when using a descending wave height for the short-term runs, but the differences are small (Figure 5.25A). The effect of changing the wave chronology is also small for the medium-term runs (Figure 5.25B). Generally, the effect of changing the wave chronology on the model predictions is negligible compared to the effect of changing free model parameters such as the bed roughness (see Section 5.4.2). This is consistent with findings by Southgate (1995) who studied the effect of changing the wave chronology on predicted morphological changes using a process-based profile model. He found that wave sequences with strong waves at the start did not have a markedly different effect on the predicted morphological changes than those with strong waves at the end. Aarninkhof et al. (1998) also found close correspondence between the position of nearshore bars from model runs with ascending and descending waves, though the height of the bars was affected by wave chronology.

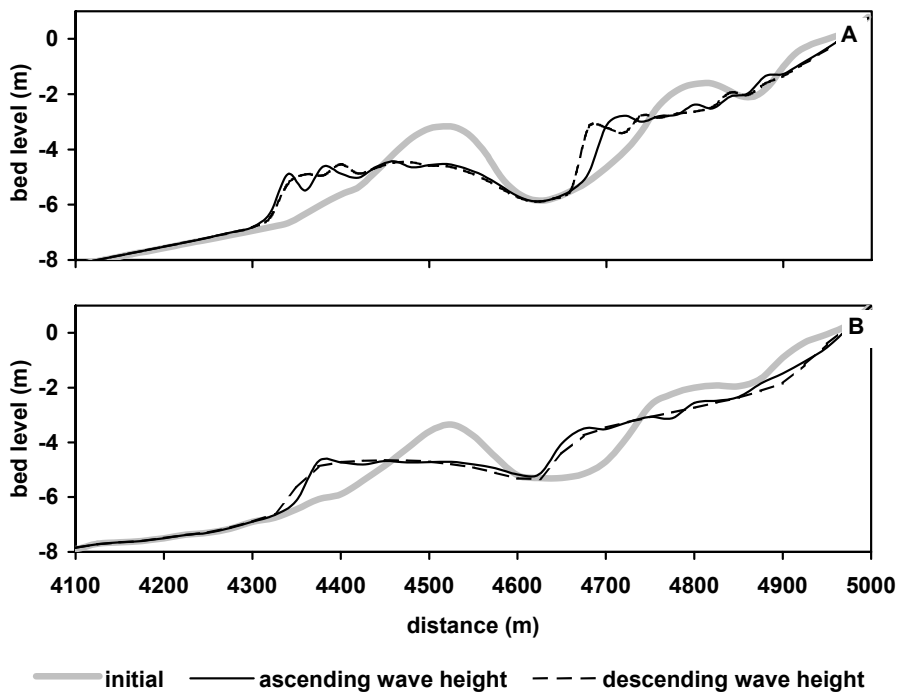


Figure 5.25. Effect of changing the wave chronology on the predicted short-term (A) and medium-term (B) morphological changes.

These findings suggest that nearshore profile behavior depends on the cumulative amount of energy input rather than the sequence of events. This would mean that the limited horizon of predictability of weather conditions (characteristically 5 days) does not form a limitation for the prediction of nearshore profile behavior. Long-term predictions could be done using randomly generated realistic time series of wave events based on the statistics of the wave-climate from long-term field measurements. Although the question may be raised to what extent the predicted nearshore profile behaviour is controlled by model characteristics and to what extent system and forcing

characteristics play a role, the consistency between the results from three different models (Southgate (1995), Aarninkhof et al. (1998), and present) suggests that the small effect of wave chronology on the predicted profile behaviour is not a result from model characteristics but a result from process characteristics.

5.7. DISCUSSION AND CONCLUSIONS

In this chapter, the morphological module of a process-based cross-shore profile model was presented. The model was compared to measured data considering two different time scales, i.e. storm (days to weeks) and seasonal scale (months). Data was used from laboratory experiments in the Delta Flume of Delft Hydraulics and from field experiments near Egmond aan Zee, in the Netherlands, and near Duck, NC, in the USA.

For the laboratory case, on a storm time scale, agreement between measured and predicted profile changes was reasonable to good, based on a tuned model. Excellent agreement was obtained by varying the wave-related roughness $k_{s,w}$ across the profile, with $k_{s,w}$ in the trough larger than on the bar crest.

For the field cases, on a storm time scale, the comparison between measurements and predictions were based on longshore-averaged profiles. Model predictions for the Egmond aan Zee site showed good to excellent agreement with measured profile changes under calm conditions. In contrast, the model had no skill in predicting the profile changes near Egmond aan Zee under storm conditions. The comparison with field data measured near Duck showed a similar tendency. Generally, predicted cross-shore profiles were too flat. Best predictions on storm time scale were obtained using a relatively large current-related roughness height $k_{s,c}$ in combination with a somewhat smaller wave-related roughness height $k_{s,w}$, or using a relatively large wave-related transport factor k_{as} . These settings were found necessary to keep the profile stable with a limited amount of sediment transported offshore.

On seasonal scale, agreement between measured and predicted profiles, based on longshore-averaged profiles, was bad. Skill scores were found to be negative for all model settings. The model flattens the entire profile.

Apparently, the model lacks basic bar generation and migration mechanisms, especially in the inner nearshore zone. This might be due to a bad prediction of the undertow. The model overestimates undertow velocities just seaward of a bar and underestimates the undertow velocities just shoreward of a bar. In other words, the measurements show a shoreward shift of the maximum undertow velocities that is not predicted by the model. Second cause for the discrepancies between observed and predicted morphological changes is the effect of the surface roller on the vertical structure of the undertow velocities. In the present model, no effect of the surface roller on the vertical structure of the undertow is taken into account, whereas in nature the presence of a surface roller influences the undertow profile significantly. No roller is present at the onset of breaking (seaward of a bar), which results in a rather uniform velocity profile. A fully developed surface roller (just shoreward of a bar crest) causes an onshore-directed shear stress on the water column at the wave trough level. This leads to a decrease of the offshore-directed velocities in the upper part of the velocity profile and mass balance

results in an increase of the velocities in the lower part of the profile under these conditions. Based on the same concentration profile and the same depth-averaged undertow velocity, the presence of a fully developed roller causes a larger offshore-directed transport rate than when no roller is present. Besides the shoreward shift of the maximum cross-shore current velocities, this roller effect on the vertical distribution of the cross-shore velocity is believed to be an important bar generation and migration mechanism.

Mechanisms such as phase lags of suspended transport, as included in advection-diffusion models (e.g. Katapodi et al., 1992), might also be required for modelling bar migration in the nearshore region. This type of models adjusts the time-averaged concentration to the equilibrium value during an adaptation time that depends on the water depth and the fall velocity of the suspended sediment.

Both on storm and seasonal scale, predictions of the morphological changes of the outer nearshore zone were better than that of the inner nearshore zone and the beach. This may not only be related to an inaccurate prediction of the undertow velocities but also to an insufficient description of the physical processes in the inner nearshore region. In the complex zone near the beach, processes are dominated by the tide and storm surge levels, long wave effects, wave runup phenomena (e.g. swash-backwash processes) and 3D morphology. Variability is relatively large and hence morphodynamic predictability is relatively low, because accurate predictions of the small residual transport rates are difficult and long wave phenomena are neglected.

At the present stage of research the accurate prediction of the precise profile development to derive beach levels and widths does not seem possible. A 3D modelling approach seems to be required to deal with the complicated phenomena in the inner bar and beach zones. However, the modelling of small residual transport processes, as present in natural situations close to equilibrium, is inherently difficult and perhaps impossible. Errors will accumulate leading to large deviations increasing with time and ultimately to model failure. Therefore, the prediction of the precise bed evolution in the inner surf and beach zone does not seem feasible, no matter what type of model is used. The only solution here would be to focus on the prediction of bulk volume integrated over larger space and time scales rather than on the prediction of precise bed levels. Hindcast studies of dune erosion assuming the storm surge level to be known, have shown that dune erosion expressed as bulk volumes can be simulated quite well on the storm time scale (Steetzel, 1993). From a predictive point of view, Steetzel (1993) suggests that his model may be used to evaluate worst-case scenarios for assumed storm surge levels. A similar approach could be feasible for the present model with respect to shoreface nourishments, focusing on the behavior of bulk volumes (longshore-averaged over 1-2 km) rather than on precise nearshore profile development. Studies on shoreface nourishments using process-based profile models have not been performed in detail. However, use of these models would reduce the empiricism of present nourishment design.

Modelling of the bar system on the decadal time scale has hardly been performed. Roelvink et al. (1995) made a first attempt by simulating the cyclic bar behavior (excluding the beach zone) at the barrier island coast of Terschelling (The Netherlands).

Morphodynamic calibration focusing on the breaker delay effects and the bar slope terms of the sand transport model appeared to be of vital importance. More research is required to improve on this, including the chronology of wave events, which might be more important on decadal scale (years) than on seasonal scale (months). The timescale of predictability of the bar system is also strongly related to the effect of forcing chronology on profile evolution. Generally, the larger the effect of forcing chronology on morphological response (bar behavior, shoreline change), the smaller is the timescale of predictability. For example, if re-ordering of wave events within a wave record of one year has a relatively large effect on predicted bar behavior over one year, then the timescale of predictability will be considerably shorter. Forcing chronology effects on predicted cross-shore bed profiles over a period of a few months have been studied by Southgate (1995) using a process-based profile model. Wave chronology effects were found to give minimum and maximum bed levels differing by a factor 2 from the mean value. The sequence of high wave events (at the start or at the end) did not have a significant effect on the mean bed level, but there was more variability in the case where the high wave conditions were at the start of the sequence. This indicates that chronology effects of a period of high waves within a period of low waves are more important when they precede a period of low waves than when they follow it, or in other words: the final profile resulting from high waves is relatively insensitive to the immediately preceding profile. High waves will create large breaker bars at or close to the breaker line anyhow, whatever profile may have been formed by the preceding low wave sequence. Similar results have been obtained by Aarninkhof et al. (1998) for a barred profile over a period of 6 months. They also made long-term computations (10 years) varying wave chronology. The results show that the height of the bars is dominated by wave chronology but that the bar location was not much influenced by wave chronology.

The following aspects should receive further attention in the development and improvement of process-based cross-shore profile models: 1) effect of spatially-varying bed roughness (bed-roughness predictor, see Chapter 4), 2) the undertow in storm conditions (vertical structure, roller contribution, see Chapter 3), 3) inclusion of overall rip current effect on profile evolution, 4) inclusion of beach, swash processes and cliff-type erosion processes to better model beach and dune erosion 5) inclusion of non-local suspended sand transport processes (lag effects) by solving the 2DV mass balance equation for the suspended sediments. Field measurements in the surf zone under storm conditions are essential for a better understanding of the processes involved and further development of process-based cross-shore profile models.

6. SYNTHESIS

The central aim of this thesis is to improve the understanding of the short (storms) to medium-term (seasonal) behavior of barred profiles. The central hypothesis is that nearshore bar behavior can be represented by the break-point concept and that a single-wave process-based cross-shore profile model can accurately describe the mechanisms involved. Based on this hypothesis, the following research questions are addressed.

6.1. HYDRODYNAMICS

- Can the nearshore hydrodynamic processes be represented sufficiently accurate by a parametric model or is a probabilistic approach considering the full wave spectrum required to accurately predict nearshore wave and current conditions?

The parametric mode can predict the cross-shore variation of H_{rms} with a high level of accuracy (within 10%). The probabilistic mode accurately predicts the $H_{1/3}$ variation across a nearshore profile (within 10%). However, wave height distributions (probability of occurrence of wave height classes) inside the surf zone are not predicted well by the probabilistic mode. The model consistently over-predicts the probabilities in the upper tail of the wave height distribution. Use of a probabilistic breaker criterion improves the shape of the distribution as compared to measured data. However, both under laboratory and field conditions, the measured wave height distributions do not differ much from a Rayleigh distribution. The results show that the Rayleigh distribution slightly under-predicts the probability density at the mean value in the surf zone, but is nevertheless able to give a better estimate of the distribution than a wave-by-wave approach based on a deterministic breaker criterion. At present, the lack of knowledge on the breaking process of individual waves makes it difficult to provide an accurate description of the wave height distribution in the nearshore. Moreover, as regards the other hydrodynamic parameters, there is no advantage of a multi-wave approach above a single-wave approach. Waves and currents in the nearshore are predicted with at least the same accuracy. Differences between a single-wave and a multi-wave approach are generally less than 10%. A major advantage of the single-wave approach is the relatively small computation time, which is an advantage for morphological modelling.

As regards the mean currents, the comparison between both approaches and measurements is poor, especially in the cross-shore case. The model overestimates cross-shore velocities just seaward of a nearshore bar and underestimates velocities just shoreward of a nearshore bar. Most important reason for the overestimation of the undertow velocities on the seaward flank and near the crest of a nearshore bar is likely to be the use of linear wave theory to compute the mean mass transport associated with the organized wave motion. Dally and Brown (1995) have shown that the use of stream function wave theory leads to more accurate predictions of the undertow velocities compared to linear wave theory. As regards the underestimation of the undertow velocities just shoreward of a nearshore bar, the present results suggest that the roller delays the maximum undertow velocity insufficiently, even with a rather small wave

front slope. The measured maximum undertow velocities are located more shoreward than those computed with the model.

The rather poor model performance with respect to the prediction of the cross-shore mean currents is not a specific feature of the present model. Within the EU-COAST3D project, five process-based cross-shore models, including the present, have been tested against the Egmond aan Zee field data set. All models can predict the wave height variation in the nearshore zone (errors less than 10%), but none of the models can represent the cross-shore currents with sufficient accuracy (see Van Rijn et al., 2002b). All models underestimate the relatively large undertow velocities measured during major storm events near the coast of Egmond aan Zee. These large offshore-directed current velocities of up to -0.6 m/s suggest the presence of rip currents, but it is very unlikely that rip currents can still exist in the presence of relatively large longshore currents up to 1.3 m/s during storm events. Results of area models suggest that 3D circulations are absent during storm events (Van Rijn et al., 2002a). These circulations are more pronounced at depressions in the inner bar during low tide in combination with relatively calm wave conditions. The profile models that include cross-shore mixing and breaker delay effects do not produce better predictions of the longshore and cross-shore current velocities. Most models produce reasonable results for the longshore current distribution in the nearshore.

- Is it acceptable to ignore long-wave oscillations in predicting the wave and flow field in the nearshore zone?

Based on analysis of small-scale laboratory data it appears that relatively large low-frequency velocity oscillations may be present at locations just shoreward of a nearshore bar crest. These long wave phenomena cannot be entirely attributed to the presence of bound long waves, break point related long waves or free long waves. Just shoreward of a nearshore bar crest, where the fraction of breaking waves is relatively large, low-frequency velocity oscillations are likely induced by long period fluctuations of the undertow (pulsating return flow), in addition to the bound long wave effect. The pulsating undertow is likely to be driven by measured set-down fluctuations across the bar profile (low-frequency variation in water level gradient). Relatively large low-frequency oscillations are also manifest in the field (Van Rijn et al., 2002a), especially during low tide. Significant long-wave heights between 10% and 35% of the water depth have been observed. These long wave oscillations are considerably smaller during high tide. Therefore, from a hydrodynamic point of view, long wave oscillation cannot be ignored in predicting the flow field in the nearshore zone.

- What are the most important parameters determining model performance?

The most pronounced effect on the model results is the breaker criterion γ . This parameter not only influences the wave energy dissipation in the nearshore and thus the wave height variation across the nearshore profile but also significantly affects the magnitude and distribution of the cross-shore and longshore currents. Good to excellent wave height predictions are obtained using a locally varying breaker criterion dependent on local wave steepness and local bottom slope (standard wave breaking function in the present model).

Of second importance is the wave-related roughness height $k_{s,w}$ that influences the wave energy dissipation further offshore and thus the amount of wave energy that reaches the shore. This also significantly affects the cross- and longshore currents in the nearshore. The current-related roughness height $k_{s,c}$ only affects the longshore current. The wave front slope β affects the cross-shore and longshore current model predictions. Increasing β from 0.03 to 0.1 generally improved both the cross-shore and longshore current predictions for locations on the seaward slope of a nearshore bar but made results worse for locations on the landward slope. Best overall agreement was obtained using $\beta = 0.06$, although cross-shore current predictions remained rather poor. The horizontal mixing coefficient ε only affects the longshore current distribution across a nearshore profile. Compared to the other free model parameters, ε has a minor effect on the model results. Model predictions slightly improved when increasing ε from 0.5 to 2.0 m^2/s .

The schematization of the longshore current also is an important parameter at the offshore boundary as it affects the predicted longshore currents at the seaward flank of the outer nearshore bars. However, it hardly affects the predicted velocities in the inner nearshore region. Although the effect of changing the longshore current at the offshore boundary on the morphological runs is negligible, it has to be considered that longshore current model performance is influenced by uncertainties of the longshore current boundary condition for locations in the outer nearshore region. If an accurate description of the longshore transports is required this tidal schematization is important. On the other hand, there is no need for a detailed description of the longshore tidal currents if the cross-shore profile development is the main interest.

6.2. SEDIMENT TRANSPORT

- Can the nearshore sediment transport rate be predicted with a relatively simple engineering model based on a single-wave approach or is a multi-wave approach required?

In principle the nearshore suspended sediment transport rates can be predicted with reasonable accuracy (within a factor 2) using a relatively simple single-wave engineering approach. The bed form roughness is the key parameter in the prediction of the suspended sediment concentrations and current- and wave-related suspended transport rates. An accurate prediction of the ripple roughness is therefore essential. The use of one single representative wave is not sufficient for an accurate prediction of the bed-load transport rates. For this component it is necessary to use a multi-wave approach, in this way also taking into account the contribution of the smaller waves, which after time-averaging leads to a smaller bed-load transport rate and under calm conditions to a stronger effect of the mean current. Another option is to modify the parameterization for the bed-load transport rate when using a single-wave approach. A first suggestion is to use the root-mean-square on- and offshore peak orbital velocities instead of the significant values. This gives more realistic bed-load transport rates in a single-wave model. Further study is necessary to accurately parameterize the bed-load transport rate based on a single wave approach. However, the importance of an accurate

prediction of the bed-load transport rate also depends on the relative importance of this component compared to the suspended load component.

- What is the relative contribution of the wave-related (high- and low-frequency) and current-related suspended transport component to the net suspended transport rate?

The current-related component accounts for about 70% of the total suspended transport rate. The contribution of the high-frequency wave-related component is smaller (about 25%) and tends to decrease with increasing mobility number. The low-frequency component is smallest and accounts for about 5% to the total transport rate. The contribution of this component increases with mobility number, which is consistent with observations under breaking wave conditions in shallower water depths.

- What is the relative contribution of the bed-load and suspended load component to the total depth-integrated transport rate?

The bed-load accounts for 30% of the total load under calm conditions and 10% under moderate storm conditions. This relatively small contribution of the bed-load transport rate does not make it necessary to use a multi-wave approach for a more accurate description of this component. The use of the root-mean-square wave height as a representative wave suffices to get an estimate of the bed-load transport rate under calm conditions.

- What are the key parameters in the prediction of suspended sediment concentrations and current- and wave-related suspended sediment transport rates?

The bed form roughness is the key parameter in the prediction of the suspended sediment concentrations and current- and wave-related suspended transport rates. Ripple roughness predictors by Grant and Madsen (1982) and Van Rijn (1993) overestimate ripple roughness in field conditions while the Nielsen (1992) method tends to under-predict ripple roughness. The Nielsen roughness predictor was modified based on a wide range of laboratory and field data. The modified Nielsen roughness predictor captured the range of measured η^2/λ values better than the Grant and Madsen (1982), Van Rijn and original Nielsen predictors did. Main differences with the original Nielsen model are a more gradual decrease of η^2/λ with mobility number and a less pronounced effect of wave period and grain diameter. The general applicability of the modified Nielsen roughness predictor awaits more field data for different grain sizes and wave-current flow conditions.

- Is it for morphodynamic purposes acceptable to ignore the long wave component of the sediment fluxes?

The low-frequency component accounts on average for about 5% to the total suspended transport rate, which suggests that in the nearshore zone, the low-frequency transport is negligible. This is confirmed by the relatively low cross-correlations between short wave energy and long wave orbital velocities (see Figure 2.20 in Section 2.6.4). The cross-correlations indicate that less than 16% of the long wave velocity variance is explained by short wave energy and more than 84% of the long wave velocity is not. This means that for 84% of the long wave velocity does not contribute to the low-frequency transport rate, as there is no correlation with the stirring of sediment by the

short waves. The 16% explained variance is relatively small and not likely to significantly contribute to the total suspended transport rate. Therefore, for morphodynamic predictions in the nearshore zone it is acceptable to ignore the long wave component of the sediment fluxes. This is not the case for morphodynamic predictions of the beach zone. Observations under breaking wave conditions in the shallow water depths near the beach (e.g. Beach and Sternberg, 1991; Aagaard and Greenwood, 1994) have shown that the net flux is dominated by low-frequency waves, especially under dissipative conditions. Swash zone hydrodynamics and low-frequency effects should be included to deal with the processes in this beach zone.

6.3. MORPHODYNAMICS

- Is a cross-shore profile model capable of predicting nearshore morphological changes on the time scale of storms and seasons (weeks to years), simplifying the coastal system to a longshore-averaged 2-D system.

The model is capable of accurately predicting morphological changes in a pure 2D case in a wave flume on a storm scale, provided that the undertow velocities are accurately predicted and the wave-related bed roughness is varied across the profile according to observed bed form dimensions. The morphodynamic behavior of the outer bar on the storm time scale (a few days) in field conditions can be simulated with reasonable accuracy provided that the proper settings are used. The model is also capable of predicting the relatively small morphological changes under relatively calm condition on a short time scale. The model clearly has no skill in predicting the nearshore profile behavior under storm conditions in the field on the time-scale of several months. Model predictions show a tendency for flattening of the inner and outer bars.

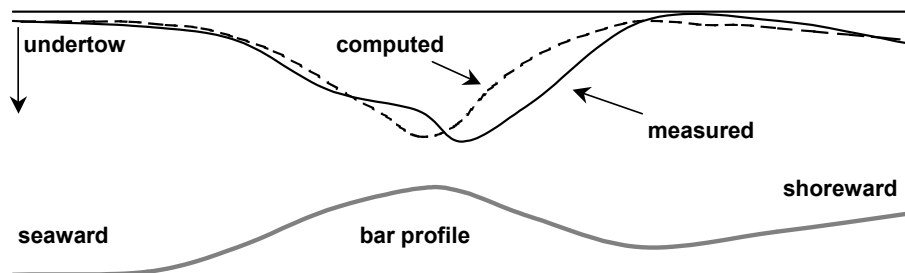


Figure 6.1. Principle sketch of measured and computed undertow velocities. The measurements generally reveal a shoreward shift of the body of the current profile that is not modelled.

The most important cause for the poor morphological predictions is a bad prediction of the undertow velocities (Figure 6.1). Observed maximum undertow velocities are located further shoreward than predicted. Most important way of improving the predictive capability of the current model is: 1) to use stream function wave theory instead of linear wave theory to compute the mean mass transport associated with the organized wave motion (Dally and Brown, 1995), and 2) to delay the surface roller more than is predicted by the commonly used roller model.

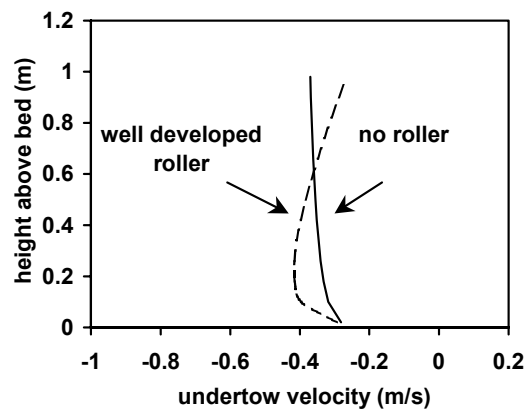


Figure 6.2. Roller effect on vertical structure of undertow velocities

Second cause for the discrepancies between observed and predicted morphological changes is the vertical structure of the undertow velocities. The presence of a surface roller influences the undertow profile significantly. No roller is present at the onset of breaking (seaward of a bar), which results in a rather uniform velocity profile (Figure 6.2). A fully developed surface roller (just shoreward of a bar crest) causes an onshore-directed shear stress on the water column at the wave trough level. This leads to a decrease of the offshore-directed velocities in the upper part of the velocity profile and mass balance results in an increase of the velocities in the lower part of the profile under these conditions. Based on the same concentration profile and the same depth-averaged undertow velocity, the presence of a fully developed roller causes a larger offshore-directed transport rate than when no roller is present. Besides the shoreward shift of the maximum cross-shore current velocities, this roller effect on the vertical distribution of the cross-shore velocity is believed to be an important bar generation and migration mechanism.

Thirdly, the discrepancy between measured and predicted morphological changes in the field might be related to the direct response of the suspended sediment concentrations to the changing hydrodynamics in the present model. In nature, it not only takes some time for the concentration profile to reach equilibrium, but it also takes time for the sediment to settle after wave and current action has diminished. This effect becomes more important with increasing water depth. These phenomena are included in advection-diffusion models (see e.g. Katapodi et al., 1992).

The relatively poor performance of the present model with respect to the morphology is not a specific feature of the present model. Within the EU-COAST3D project five process-based cross-shore profile models including the present model have been compared (Van Rijn et al., 2002b). All profile models could reasonably simulate the behavior of the outer bar on the storm scale after sufficient tuning; the behavior of the inner bar and beach could not be modelled with sufficient accuracy on the storm time scale. None of the models could predict the behavior of the outer and inner bars and the beach on the seasonal time scale. The behavior of the outer bar on the seasonal time scale could only be represented properly after tuning using measured bed profiles. The

simulation of the inner bar and the beach morphology on the seasonal time scale could not be improved by tuning.

The natural behaviour of an outer bar in a multiple bar system may be less difficult to predict than the natural behaviour of an inner bar, which is more problematic due to the presence of 3-dimensional circulations. At the present stage of research the behaviour of the inner bar system cannot be simulated with sufficient accuracy. The predictability of the inner bar may however increase for increasing time scales (5 to 10 years), because the net bar migration will increase and the 2-dimensional behavior dominate. Modelling of the bar system on the decadal time scale has hardly been performed. Roelvink et al. (1995) made a first attempt by simulating the cyclic bar behaviour (excluding the beach zone) at the barrier island coast of Terschelling, the Netherlands. Morphodynamic calibration focussing on the breaker delay effects and the bar slope terms of the sand transport model appeared to be of vital importance. Much more research is required to improve on this.

- Can the nearshore morphological changes be predicted using a single-wave approach or is a multi-wave approach required?

As regards the hydrodynamics, there is no advantage of a multi-wave approach above a single-wave approach. Waves and currents in the nearshore are predicted with at least the same accuracy. Sediment transport rates can be predicted with reasonable accuracy using a single-wave approach. Therefore, the present analysis does not argue for the use of a multi-wave approach. A major advantage of the single-wave approach is the relatively small computation time.

- What are the most influential parameters for nearshore bar behaviour?

An accurate prediction of the undertow is of vital importance. Besides this, most important parameters for nearshore bar behavior are the bed roughness height, and the wave-related suspended transport.

- Can a cross-shore profile model be used for simulation of a shoreface nourishment?

A process-based cross-shore profile model is potentially suitable for the simulation of a shoreface nourishment. At the present stage of research the prediction of the precise bed evolution in the inner nearshore and beach zone is not feasible, no matter what type of model is used (see Van Rijn et al., 2002b). The only solution here is to focus on the prediction of bulk volume integrated over larger space and time scales rather than on the prediction of precise bed levels. Hindcast studies of dune erosion assuming the storm surge level to be known, have shown that dune erosion as a bulk volumes can be simulated quite well on the storm time scale (Steetzel, 1993). From a predictive point of view the models may then be used to evaluate worst-case scenarios for assumed storm surge levels. A similar approach should be feasible for beach nourishment, focussing on the behaviour of bulk volumes (averaged over sufficient alongshore distance of about 1 to 2 km) rather than on precise beach profile development. Studies on beach nourishment using process-based models have not been performed in great detail and are highly recommended to reduce the empiricism of beach nourishment design.

SAMENVATTING

Kustdwarse profielmodellen worden veel gebruikt in het kustbeheer. Bijvoorbeeld bij het voorspellen van het gedrag van zandsuppleties waarbij extra zand vlak voor de kust wordt aangebracht ter bescherming van het strand. Een kustprofielmodel beschrijft de waterbeweging (golven, stroming) in een lijn loodrecht op de kust. Op basis van golfhoogtes en stromingen wordt het zandtransport berekend en daaruit worden de bodemveranderingen bepaald. De ontwikkeling van deze kustmodellen staat nog in haar kinderschoenen. Veel is nog onbekend van het gedrag van golven, stroming en zandtransport dichtbij de kust.

In dit proefschrift wordt een 'state-of-the-art' kustdwars profielmodel beschreven. Berekeningen met het model zijn vergeleken met metingen onder laboratorium condities maar ook met metingen in de natuur. Uit deze vergelijking blijkt het voor een voldoende nauwkeurige beschrijving van de golven en stroming niet nodig te zijn alle golven afzonderlijk te berekenen. Het gaat ook al goed op grond van één representatieve golf. Het is echter erg lastig om in modellen de onderstroom onder brekende golven te berekenen. Vooral vanwege het gebruik van de relatief eenvoudige lineaire golftheorie (sinusvormige golven) voor het berekenen van een deel van die onderstroom. Een meer geavanceerde golftheorie zoals de 'stream-function' golftheorie zal een duidelijke verbetering geven. Een ander probleem is de onvoldoende landwaartse verschuiving van de maximale onderstroom. Volgens het model ligt de maximale waarde van de onderstroom dichtbij de top van een zandbank, maar uit metingen blijkt de maximale onderstroom verder landwaarts hiervan te liggen. Een betere voorspelling van de onderstroom zou mogelijk zijn door de hoeveelheid water die door een brekende golf landwaarts wordt getransporteerd wat langer met de golf mee te laten lopen.

Het model voorspelt het zandtransport dichtbij de kust redelijk goed. De invloed van op de zeebodem aanwezige ribbels is echter van doorslaggevend belang. In dit proefschrift worden de geschatte ribbelafmetingen volgens drie ribbelvoorspellende formules vergeleken met gemeten ribbelafmetingen in laboratorium en natuurlijke situaties. De beste voorspeller is in dit proefschrift verbeterd maar desondanks blijken de onzekerheden nog erg groot. Er is nog veel onbekend over het ontstaan van ribbels onder golven en stroming.

Het modelleren van de verplaatsing van zandbanken dwars op de kust blijft nog een uitdaging. De verplaatsing van een zandbank in het laboratorium kan goed worden voorspeld, mits de onderstroom onder brekende golven nauwkeurig wordt berekend en de invloed van ribbels op de zandbodem wordt meegenomen. De verplaatsing van zandbanken in de natuur is moeilijk te voorspellen omdat de onderstroom onder brekende golven nog niet goed kan worden berekend en het nog onbekend is wat de afmetingen van de zandribbels zijn.

SUMMARY

Coastal profile models are commonly used for hind- and forecasting studies of nearshore bathymetry, often in response to human interference in the nearshore, for instance related to implementation of shoreface nourishments. They are developed to predict wave heights and currents in a line perpendicular to the coast. Based on these wave heights and currents, sediment transport rates are computed and from these the bed level changes are determined. At the present stage of research, the predictive capability of these models generally is rather low in quantitative sense. Actually, these models are still in their infancy. Much of the behaviour of waves, currents and sediment transport near the shore is still unknown.

This thesis describes a 'state-of-the-art' cross-shore profile model. The model computations are compared with measurements in a laboratory and in nature. From this comparison it appears that waves and currents in the nearshore can be described at least with the same accuracy using a single representative wave as when computing all waves independently. Modelling the undertow velocity under breaking waves remains difficult however. In particular because of the use of the relatively simple linear wave theory to compute part of the undertow. Dally and Brown (1995) have shown that the use of stream function wave theory leads to more accurate predictions of the undertow velocities. Another aspect is the insufficient landward shift of the maximum undertow velocity. The measured maximum undertow velocities are located more shoreward than those computed with the model. Model predictions might improve by making the amount of water that is transported shoreward in a breaking wave travel with the wave somewhat longer than is predicted in the present models.

The model reasonably predicts sediment transport rates near the shore. However, the presence of ripples is of crucial importance. In this thesis, computed ripple dimensions from three ripple formulae are compared with the dimensions measured in the laboratory and in nature. The best predictor is adapted to improve agreement with the measurements. Nevertheless, uncertainties remain large. Much is still unknown on the generation of ripples under waves and currents.

Predicting nearshore sandbar migration by a coastal profile model remains a challenge. The migration of a sandbar in the laboratory could rather well be predicted, provided that the undertow under breaking waves is accurately predicted and the effect of ripples on the sandbed is taken into account. Predicting nearshore sandbar migration in nature is difficult because of inaccurate predictions of the undertow under breaking waves and uncertainties on the dimensions of sand ripples.

CURRICULUM VITAE

Bart Grasmeijer werd geboren op 20 augustus 1969 in Delfzijl. In 1985 behaalde hij het Mavo, in 1987 het Havo en in 1989 het VWO diploma. Aansluitend ging hij Civiele Techniek studeren aan de Technische Universiteit Delft. Deze studie sloot hij in oktober 1995 af met als specialisatie kustwaterbouwkunde. Binnen zijn afstudeeronderzoek richtte hij zijn aandacht vooral op zandtransportprocessen onder brekende golven in de brandingszone. Van oktober 1995 tot mei 1996 voerde hij een verkennende studie uit naar het relatieve belang van de verschillende zandtransportcomponenten en lange golf effecten over een kustnabije bank, op grond van metingen verricht in een kleine laboratoriumgoot. Dit onderzoek werd uitgevoerd in opdracht van het Waterloopkundig Laboratorium. In mei 1996 werd hij aangesteld als Assistent in Opleiding aan de Universiteit van Utrecht. Het tijdens deze aanstelling uitgevoerde onderzoek heeft geleid tot dit proefschrift. In mei 2000 werd hij aangesteld als junior docent onderzoeker aan de Universiteit Utrecht. Vanaf april 2002 zal hij deelnemen aan onderzoek in het kader van het Sandpit project van de Europese Gemeenschap. Doel van dit onderzoek is het ontwikkelen van betrouwbare voorspellingstechnieken en richtlijnen voor een beter inzicht, simulatie en voorspelling van het gedrag van grootschalige zandwinputten op waterdieptes van 10-20 m.

REFERENCES

- Aagaard, T. (1990), Infragravity waves and nearshore bars in protected storm-dominated coastal environments. *Marine Geology*, 94, pp. 181-203.
- Aagaard, T. and Greenwood, B. (1994), Suspended sediment transport and the role of infragravity waves in a barred surf zone. *Marine Geology*, 118, pp. 23-48.
- Aagaard, T. and Greenwood, B. (1995), Longshore and cross-shore suspended sediment transport at far infragravity frequencies in a barred environment. *Continental Shelf Research*, 15(10), pp. 1235-1249.
- Aagaard, T., Nielsen, J., and Greenwood, B. (1998), Suspended sediment transport and nearshore bar formation on a shallow intermediate state beach. *Marine Geology*, 148, pp. 203-225.
- Aarninkhof, S. G. J., Hinton, C., and Wijnberg, K. M. (1998), On the predictability of nearshore bar behaviour. *Proceedings Coastal Engineering*, pp. 2409-2422, ASCE, New York.
- Arcilla, A. S., Roelvink, J. A., O'Connor, B. A., Reniers, A. J. H. M., and Jiménez, J. A. (1994), The Delta Flume '93 experiment. *Coastal Dynamics*, pp. 489-502, ASCE, New York.
- Bagnold, R.A. (1940), Beach formation by waves. *Journal of the Institute of Civil Engineers*, 15, pp. 27-52.
- Bagnold, R.A. (1966), An approach to the sediment transport problem from general physics. *Physiographic and hydraulic studies of rivers*, pp. 1-37.
- Bailard, J.A. (1981), An energetics total load sediment transport model for a plane sloping beach. *Journal of Geophysical Research*, 86(C11), pp. 10,938-10,954.
- Baldock, T.E., Holmes, P., Bunker, S., and Van Weert, P. (1998), Cross-shore hydrodynamics within an unsaturated surf zone. *Coastal Engineering*, 34, pp. 173-196.
- Battjes, J. A. (1975), Modelling of turbulence in the surfzone. *Proceedings Symposium Modeling Techniques*, pp. 1050-1061, ASCE, New York, USA.
- Battjes, J.A. (1988), Surf zone dynamics. *Annual Review of Fluid Mechanics*, 20, pp. 257-293.
- Battjes, J.A. and Janssen, J. P. F. M. (1978), Energy loss and set-up due to breaking of random waves. *Proceedings Coastal Engineering*, pp. 569-587.
- Battjes, J.A. and Stive, M. J. F. (1985), Calibration and Verification of a Dissipation Model for Random Breaking Waves. *Journal of Geophysical Research*, 90(C5), pp. 9159-9167.
- Beach, R. A. and Sternberg, R. W. (1991), Infragravity driven suspended sediment transport in the swash, inner and outer surf zone. *Proceedings Coastal Sediments*, pp. 114-128, ASCE, New York.
- Bell, P. S., Thorne, P. D., and Williams, J. J. (1998), Acoustic measurements of sand ripple profile evolution under controlled wave conditions. *Proceedings European Conference on Underwater Acoustics*, pp. 353-358, Istituto di Acustico "O.M. Corbino", Rome, Italy.
- Berend, O., Schmidt-Koppenhagen, R., and Durstthof, W. (1997), Measurement of sand beach profiles in the large wave flume. *Proceedings of the Offshore and Polar Engineering Conference*, Honolulu.
- Boczkar-Karakiewicz, B., Bona, J. L., Naguszewski, A., and Romanczyk, W. (1995), Dynamics of sand bars in coastal zones. *Proceedings Coastal Dynamics*, pp. 862-867, ASCE, New York.
- Boczkar-Karakiewicz, B. and Davidson-Arnott, R. G. D. (1987), Nearshore bar formation by non-linear wave processes - a comparison of model results and field data. *Marine Geology*, 77, pp. 287-304.
- Bosman, J. J. and Steetzel, H. J. (1986), Time- and bed-averaged concentrations under waves. *Proceedings Coastal Engineering*, ASCE, New York.
- Bowen, A.J. (1980), Simple models of nearshore sedimentation; beach profiles and longshore bars. *The coastline of Canada*, (80-10), pp. 1-11.
- Bowen, A.J. and Holman, R. A. (1989), Shear Instabilities of the mean longshore current. 1. Theory. *Journal of Geophysical Research*, 94(c12), pp. 18023-18030.
- Boyd, R., Forbes, D.L., and Heffler, D.E. (1988). Time-sequence observations of wave-formed sand ripples on an ocean shoreface. *Sedimentology* 35, pp. 449-464.
- Brander, R. W. (2000), Measurements of flow velocity and sediment transport in a ripp current. *Proceedings Coastal Engineering*, pp. 3395-3408, ASCE, Reston, Virginia, USA.
- Bryan, K.R. and Bowen, A. J. (1998), Bar-trapped edge waves and longshore currents. *Journal of Geophysical Research*, 103(C12), pp. 27867-27884.
- Bryan, K.R., Howd, P. A., and Bowen, A. J. (1998), Field observations of bar-trapped edge waves. *Journal of Geophysical Research*, 103(C1), pp. 1285-1305.

- Caljouw, M. and Kleinhout, K. (2000), Morphodynamics of the Egmond field site, May 1998 to September 1999. Report Z2822.25, WL|Delft Hydraulics, Delft, The Netherlands.
- Carter, R.W.G. and Balsillie, J. H. (1983), A note on the amount of wave energy transmitted over nearshore sandbars. *Earth Surface Processes and Landforms*, 8, pp. 213-222.
- Carter, T.G., Liu, P. F. L., and Mei, C. C. (1973), Mass transport by waves and offshore sand bedforms. *Journal of Waterways, Harbors and Coastal Engineering Division*, 99(WW2), pp. 165-185.
- Dally, W. R. and Dean, R. G. (1986), Transformation of random breaking waves on surf beat. *Proceedings Coastal Engineering*, pp. 109-123, ASCE, New York, USA.
- Dally, W. R. (1987), Longshore bar formation - surf beat or undertow? *Proceedings Coastal Sediments*, pp. 71-86, ASCE, New York.
- Dally, W.R. (1992), Random breaking waves: field verification of a wave-by-wave algorithm for engineering application. *Coastal Engineering*, 16, pp. 369-397.
- Dally, W.R. and Brown, C. A. (1995), A modeling investigation of the breaking wave roller with application to cross-shore currents. *Journal of Geophysical Research*, 100(C12), pp. 24873-24883.
- Dally, W.R. and Dean, R. G. (1984), Suspended sediment transport and beach profile evolution. *Journal of Waterway, Port, Coastal and Ocean Engineering*, 110(1), pp. 15-33.
- Dang Huu, C. and Grasmeyer, B. T. (1999), Analysis of sand transport under regular and irregular waves in large-scale wave flume. Report R 99-05, University of Utrecht, Utrecht, The Netherlands.
- Davidson-Arnott, R.G.D. and McDonald, R. A. (1989), Nearshore water motion and mean flows in a multiple parallel bar system. *Marine Geology*, 86, pp. 321-338.
- De Vriend, H. J. (1997), Prediction of aggregated-scale coastal evolution. *Proceedings Coastal Dynamics*, pp. 644-653, ASCE, New York.
- De Vriend, H.J. and Stive, M. J. F. (1987), Quasi-3D modelling of nearshore currents. *Coastal Engineering*, 11, pp. 565-601.
- De Vriend, H.J., Zyserman, J., Roelvink, J. A., Pèchon, P., and Southgate, H. N. (1993), Medium-term 2DH coastal area modelling. *Coastal Engineering*, 21, pp. 193-225.
- Dean, R.G. (1991), Equilibrium beach profiles: characteristics and applications. *Journal of Coastal Research*, 7(1), pp. 53-84.
- Deigaard, R. (1993), A note on the three-dimensional shear stress distribution in a surf zone. *Coastal Engineering*, 20, pp. 157-171.
- Deigaard, R., Jakobsen, J. B., and Fredsøe, J. (1999), Net transport under wave groups and bound long waves. *Journal of Geophysical Research*, 104(C6), pp. 13559-13575.
- Doering, J. C. and Bowen, A. J. (1987), Fundamental interactions in the nearshore? *Proceedings Coastal Sediments*, pp. 710-722, ASCE, New York.
- Doering, J. C. and Bowen, A. J. (1988), Wave-induced flow and nearshore suspended sediment. *Proceedings Coastal Engineering*, pp. 1452-1463, ASCE, New York.
- Dohmen-Janssen, C. M., 1999. Grain size influence on sediment transport in oscillatory sheet flow., Delft University of Technology, Delft
- Douglas, S.L. (1995), Estimating landward migration of nearshore constructed sand mounds. *Journal of Waterway, Port, Coastal and Ocean Engineering*, 121(5), pp. 247-250.
- Dulou, C., Belzons, M., and Rey, V. (2000), Laboratory study of wave bottom interaction in the bar formation on an erodible sloping bed. *Journal of Geophysical Research*, 105(C8), pp. 19745-19762.
- Duncan, J. H. (1981), An empirical investigation of breaking waves produced by a towed hydrofoil. *Proc. Roy. Soc. Lond.*, pp. 331-348,
- Dyhr-Nielsen, M. and Sørensen, T. (1970), Some sand transport phenomena on coasts with bars. *Coastal Engineering*, pp. 855-865, ASCE, New York.
- Eldeberky, Y. and Battjes, J. A. (1996), Spectral modeling of wave breaking: application to Boussinesq equations. *Journal of Geophysical Research*, 101(C1), pp. 1253-1264.
- Elfrink, B., Rakha, K. A., Deigaard, R., and Brøker, I. (1999), Effect of near-bed velocity skewness on cross-shore sediment transport. *Proceedings Coastal Sediments*, pp. 33-47, ASCE, Reston, Virginia, USA.
- Elgar, S., Gallagher, E. L., and Guza, R. T. (2001), Nearshore sandbar migration. *Journal of Geophysical Research*, 106(C6), pp. 11623-11627.
- Elgar, S. and Guza, R. T. (1985), Observations of bispectra of shoaling surface gravity waves. *Journal of Fluid Mechanics*, 161, pp. 425-448.

- Elgar, S., Guza, R. T., Raubenheimer, B., Herbers, T. H. C., and Gallagher, E. L. (1997), Spectral evolution of shoaling and breaking waves on a barred beach. *Journal of Geophysical Research*, 102(C7), pp. 15797-15805.
- Feddersen, F., Guza, R. T., Elgar, S., and Herbers, T. H. C. (1998), Alongshore momentum balance in the nearshore. *Journal of Geophysical Research*, 103(C8), pp. 15667-15676.
- Feddersen, F., Guza, R. T., Elgar, S., and Herbers, T. H. C. (2000), Velocity moments in alongshore bottom stress parameterizations. *Journal of Geophysical Research*, 105(C4), pp. 8673-8686.
- Gallagher, E.L., Elgar, S., and Guza, R. T. (1998), Observations of sand bar evolution on a natural beach. *Journal of Geophysical Research*, 103(C2), pp. 3203-3215.
- Galvin, C.J. (1968), Breaker type classification on three laboratory beaches. *Journal of Geophysical Research*, 73(12), pp. 3651-3659.
- Garcez Faria, A.F., Thornton, E. B., and Stanton, T. P. (2000), Undertow over a barred beach. *Journal of Geophysical Research*, 105(C7), pp. 16999-17010.
- Goda, Y. (1975), Irregular wave deformation in the surf zone. *Coastal Engineering in Japan*, 18, pp. 13-26.
- Grant, W.D. and Madsen, O. S. (1979), Combined wave and current interaction with a rough bottom. *Journal of Geophysical Research*, 84(C4), pp. 1797-1808.
- Grant, W.D. and Madsen, O. S. (1982), Movable bed roughness in unsteady oscillatory flow. *Journal of Geophysical Research*, 87(C1), pp. 469-481.
- Grasmeijer, B. T., Dang Huu, C. and Van Rijn, L. C. (1999), Depth-integrated sand transport in the surf zone. *Proceedings Coastal Sediments*, pp. 325-340, ASCE, Virginia, USA.
- Grasmeijer, B. T. and Van Rijn, L. C. (1998), Breaker bar formation and migration. *Proceedings Coastal Engineering*, pp. 2750-2758, ASCE, Virginia, USA.
- Grasmeijer, B.T. and Van Rijn, L. C. (1999), Transport of fine sands by currents and waves III: breaking waves over barred profile with ripples. *Journal of Waterway, Port, Coastal and Ocean Engineering*, 125(2), pp. 71-79.
- Grasmeijer, B. T. and Van Rijn, L. C. (2001), Sand transport in the surf zone of a dissipative beach. *Proceedings Coastal Dynamics*, pp. 102-111, ASCE, Reston, Virginia, USA.
- Grasmeijer, B. T., Van Rijn, L. C., Elgar, S., and Gallagher, E. L. (2000), Verification of a cross-shore profile model using field data. *Proceedings Coastal Engineering*, pp. 2522-2535, ASCE, Reston, Virginia, USA.
- Greenwood, B. and Davidson-Arnott, R. G. D. (1979), Sedimentation and equilibrium in wave-formed bars: a review and case study. *Canadian Journal of Earth Science*, 16, pp. 312-332.
- Greenwood, B. and Osborne, P. D. (1990), Vertical and horizontal structure in cross-shore flows: an example of undertow and wave set-up on a barred beach. *Coastal Engineering*, 14, pp. 543-580.
- Greenwood, B. and Sherman, D. J. (1982), Shore parallel flows in a barred nearshore. *Proceedings Coastal Engineering*, pp. 1677-1696, ASCE, New York.
- Greenwood, B. and Sherman, D. J. (1986), Longshore current profiles and lateral mixing across the surf zone of a barred nearshore. *Coastal Engineering*, 10, pp. 149-167.
- Guza, R. T., Thornton, E. B., and Holman, R. A. (1984), Swash on steep shallow beaches. *Coastal Engineering*, pp. 708-723, ASCE, New York.
- Haines, J.W. and Sallenger, A. H. Jr. (1994), Vertical structure of mean cross-shore currents across a barred surf zone. *Journal of Geophysical Research*, 99(C7), pp. 14223-14242.
- Hanes, D.M., Alymov, V., and Chang, Y. S. (2001), Wave-formed ripples at Duck, North Carolina. *Journal of Geophysical Research*, 106(C10), pp. 22575-22592.
- Hoekstra, P., Houwman, K. T., Kroon, A., Ruessink, B. G., Roelvink, J. A., and Spanhoff, R. (1996), Morphological development of the Terschelling shoreface nourishment in response to hydrodynamic and sediment transport processes. *Proceedings Coastal Engineering*, pp. 2897-2910, ASCE, New York, USA.
- Holman, R.A. and Sallenger, A. H. Jr. (1993), Sand bar generation: a discussion of the Duck experiment series. *Journal of Coastal Research*, (Special Issue No. 15), pp. 76-92.
- Houwman, K. T., 2000. Tide, wind- and wave-driven flow processes in the nearshore zone. Ph.D. Thesis, University of Utrecht, Utrecht

- Houwman, K. T. and Ruessink, B. G. (1996), Cross-shore sediment transport mechanisms in the surf zone on a timescale of months to years. *Proceedings Coastal Engineering*, pp. 4793-4806, ASCE, New York.
- Hulsbergen, C. H. (1974), Origin, effect and suppression of secondary waves. *Proceedings Coastal Engineering*, pp. 392-411, ASCE, New York.
- Hulscher, S. J. M. H., 1996. Formation and migration of large-scale rhythmic sea-bed pattern. Ph.D. Thesis, University of Utrecht, Utrecht, ISBN: 90-393-1447-0
- Huntley, D. A. and Hanes, D. M. (1987), Direct measurement of suspended sediment transport. *Proceedings Coastal Sediments*, pp. 723-735, ASCE, New York.
- Inman, D. L. (1957), Wave generated ripples in near-shore sands. Report Tech. Memo. 100, U.S. Army Corps of Engineers, Beach Erosion Board, Washington, D.C., USA.
- Isobe, M. and Horikawa, K. (1982), Study on water particle velocities of shoaling and breaking waves. *Coastal Engineering in Japan*, 25, pp. 109-123.
- Jaffe, B. E., Sternberg, R. W., and Sallenger, A. H. Jr. (1984), The role of suspended sediment in shore-normal beach profile changes. *Proceedings Coastal Engineering*, pp. 1983-1996, ASCE, New York.
- Kamphuis, J.W. (1995), Comparison of two-dimensional and three-dimensional beach profiles. *Journal of Waterway, Port, Coastal and Ocean Engineering*, 121(3), pp. 155-161.
- Katapodi, I., Kitou, N., and De Vriend, H. J. (1992), Coupling of a quasi-3D model for the transport with a quasi-3D model for the wave induced flow. *Proceedings Coastal Engineering*, pp. 2150-2163, ASCE, New York.
- King, C.A.M. and Williams, W. W. (1949), The formation and movement of sand bars by wave action. *Geographical Journal*, 113, pp. 70-85.
- Komar, P. D. (1998), *Beach processes and sedimentation*. Prentice-Hall, Inc., New Jersey, ISBN 0-13-754938-5.
- Kroon, A., 1994. Sediment transport and morphodynamics of the beach and nearshore near Egmond, The Netherlands. Ph.D., University of Utrecht, Utrecht, ISBN: 90-6809-192-1
- Kuriyama, Y and Nakatsukasa, T. (1999), Undertow and longshore current on a bar-trough beach. Report 38, Port and Harbour Research Institute, Hazaki.
- Lanckneus, J., Van Lancker, V., Martens, C., and Moerkerke, G. (1999), Small-scale morphology and sedimentological response of the nearshore area of Egmond aan Zee (NL). Report, Magelas BVBA-University of Gent, Gent, Belgium.
- Larson, M., Kraus, N. C., and Wise, R. A. (1999), Equilibrium beach profiles under breaking and non-breaking waves. *Coastal Engineering*, 36, pp. 59-85.
- Lettau, H.H. (1969). Note on aerodynamic roughness-parameter estimation on the basis of roughness element description, *Journal of Applied Meteorology*, 8, pp. 828-832.
- Lee, G., Nicholls, R. J., and Birkemeier, W. A. (1998), Storm driven variability of the beach nearshore profile at Duck, North Carolina, USA, 1981-1991. *Marine Geology*, 148, pp. 163-177.
- Li, M.Z., and Amos, C.L. (1999). Sheet flow and large wave ripples under combined waves and currents: field observations, model predictions and effects on boundary layer dynamics. *Continental Shelf Research* 19, pp. 637-663.
- Li, M.Z., Wright, L. D., and Amos, C. L. (1996), Predicting ripple roughness and sand suspension under combined flows in a shoreface environment. *Marine Geology*, 130, pp. 139-161.
- Lippmann, T.C. and Holman, R. A. (1990), The spatial and temporal variability of sand bar morphology. *Journal of Geophysical Research*, 95(C7), pp. 11575-11590.
- Lippmann, T.C., Holman, R. A., and Hathaway, K. K. (1993), Episodic, nonstationary behavior of a double bar system at Duck, North Carolina, U.S.A., 1986-1991. *Journal of Coastal Research*, Special Issue No. 15, pp. 49-75.
- List, J. H. (1987), Wave groupiness as a source of nearshore long waves. *Coastal Engineering*, pp. 497-511, ASCE, New York.
- List, J.H. (1992), A model for the generation of two-dimensional surf beat. *Journal of Geophysical Research*, 97(C4), pp. 5623-5635.
- Longuet-Higgins, M.S. (1953), Mass transport in water waves. *Philos. Trans. R. Soc.*, 345, pp. 535-581.
- Longuet-Higgins, M.S. (1970), Longshore currents generated by obliquely incident sea waves. *Journal of Geophysical Research*, 75(33), pp. 1-35.

- Longuet-Higgins, M.S. and Stewart, R. W. (1964), Radiation stresses in water waves; a physical discussion, with applications. *Deep Sea Research*, 11, pp. 529-562.
- Madsen, P.A., Sørensen, O. R., and Schäffer, H. A. (1997), Surf zone dynamics simulated by a Boussinesq type model. Part I. Model description and cross-shore motion of regular waves. *Coastal Engineering*, 32(4), pp. 255-287.
- Mase, H. and Iwagaki, Y. (1982), Wave height distributions and wave grouping in surf zone. *Proceedings Coastal Engineering*, pp. 58-76, ASCE, New York.
- Miles, J.R., Russel, P., Ruessink, B. G., and Huntley, D. A. (2002), Field observations of the effect of shear waves on sediment suspension and transport. *Continental Shelf Research*, 22(4), pp. 657-681.
- Mizuguchi, M. (1982), Individual wave analysis of irregular wave deformation in the nearshore zone. *Coastal Engineering*, pp. 485-504, ASCE, New York.
- Murphy, A.H. and Epstein, E. S. (1989), Skill scores and correlation coefficients in model verification. *Monthly Weather Review*, 117, pp. 572-581.
- Nairn, R. B., Roelvink, J. A., and Southgate, H. N. (1990), Transition zone width and implications for modelling surf zone hydrodynamics. *Proceedings Coastal Engineering*, pp. 68-81, ASCE
- Nairn, R.B. and Southgate, H. N. (1993), Deterministic profile modelling of nearshore processes. Part 2. Sediment transport and beach profile development. *Coastal Engineering*, 19, pp. 57-96.
- Nielsen, P. (1981), Dynamics and geometry of wave-generated ripples. *Journal of Geophysical Research*, 86(C7), pp. 6467-6472.
- Nielsen, P. (1992), *Coastal bottom boundary layers and sediment transport*. World Scientific, Singapore, ISBN 9810204726.
- Nikuradse, J. (1933), *Strömungsgesetze in rauhen Rohren*. Report Forschungsheft 361, VDI
- O'Connor, B. A. and Nicholson, J. (1999), Modelling short-term beach profile changes. *Proceedings Conference on Coastal and Port Engineering in Developing Countries*, pp. 277-287, Cape Town.
- O'Connor, B. A., Pan, S., Nicholson, J., MacDonald, N., and Huntley, D. A. (1998), A 2D model of waves and undertow in the surf zone. *Proceedings Coastal Engineering*, pp. 286-296, ASCE, New York.
- O'Hare, T. J. (1994), The role of long waves in sand bar formation - a model exploration. *Proceedings Coastal Dynamics*, pp. 74-88, ASCE, New York.
- O'Hare, T.J. and Davies, A. G. (1993), Sand bar evolution beneath partially-standing waves: laboratory experiments and model simulations. *Continental Shelf Research*, 13(11), pp. 1149-1181.
- O'Hare, T.J. and Huntley, D. A. (1994), Bar formation due to wave groups and associated long waves. *Marine Geology*, 116, pp. 313-325.
- Oltman-Shay, J., Howd, P. A., and Birkemeier, W. A. (1989), Shear instabilities of the mean longshore current 2. Field observations. *Journal of Geophysical Research*, 94(C12), pp. 18031-18042.
- Osborne, P.D. and Greenwood, B. (1992), Frequency dependent cross-shore suspended sediment transport. 1. A non-barred shoreface. *Marine Geology*, 106, pp. 1-24.
- Osborne, P.D. and Vincent, C. E. (1993), Dynamics of large and small scale bedforms on a macrotidal shoreface under shoaling and breaking waves. *Marine Geology*, 115, pp. 207-226.
- Osborne, P.D. and Vincent, C. E. (1996), Vertical and horizontal structure in suspended sand concentrations and wave-induced fluxes over bedforms. *Marine Geology*, 131, pp. 195-208.
- Özkan-Haller, H.T. and Kirby, J. T. (1999), Nonlinear evolution of shear instabilities of the longshore current. *Journal of Geophysical Research*, 104, pp. 25953-25984.
- Putrevu, U. and Svendsen, I. A. (1992), A mixing mechanism in the nearshore region. *Proceedings Coastal Engineering*, pp. 2758-2771, ASCE, New York, USA.
- Rakha, K.A. (1998), A Quasi-3D phase-resolving hydrodynamic and sediment transport model. *Coastal Engineering*, 34(3-4), pp. 277-311.
- Rakha, K.A., Deigaard, R., and Brøker, I. (1997), A phase-resolving cross shore sediment transport model for beach evolution. *Coastal Engineering*, 31, pp. 231-261.
- Ranasinghe, R., Symonds, G., Black, K. P., and Holman, R. A. (2000), Processes governing rip spacing, persistence, and strength in a swell dominated, microtidal environment. *Proceedings Coastal Engineering*, pp. 454-467, ASCE, Reston, Virginia, USA.
- Rattanapitikon, W. and Shibayama, T. (2000), Simple model for undertow profile. *Coastal Engineering Journal*, 42(1), pp. 1-30.

- Raubenheimer, B., Guza, R. T., and Elgar, S. (1996), Wave transformation across the inner surf zone. *Journal of Geophysical Research*, 101(C11), pp. 25589-25597.
- Reniers, A.J.H.M. and Battjes, J. A. (1997), A laboratory study of longshore currents over barred and non-barred beaches. *Coastal Engineering*, 30, pp. 1-22.
- Reniers, A.J.H.M., Battjes, J. A., Falques, A., and Huntley, D. A. (1997), A laboratory study on the shear instability of longshore currents. *Journal of Geophysical Research*, 102(C4), pp. 8597-8609.
- Ribberink, J.S. (1998), Bed-load transport for steady flows and unsteady oscillatory flows. *Coastal Engineering*, 34, pp. 59-82.
- Ribberink, J. S. and Al-Salem, A. A. (1992a), Near bed sediment transport phenomena under asymmetric waves (sheet flow). *Proceedings Coastal Engineering*,
- Ribberink, J. S. and Al-Salem, A. A. (1992b), Sediment transport, sediment concentrations and bedforms in simulated asymmetric wave conditions. Report H840.20, Part V, Delft Hydraulics, Delft, The Netherlands.
- Ribberink, J.S. and Al-Salem, A. A. (1994), Sediment transport in oscillatory boundary layers in cases of rippled beds and sheet flow. *Journal of Geophysical Research*, 99(C6), pp. 12707-12727.
- Rienecker, M.M. and Fenton, J. D. (1981), A Fourier approximation method for steady water waves. *Journal of Fluid Mechanics*, 104, pp. 119-137.
- Roelvink, J. A., 1993. Surf beat and its effect on cross-shore profile. Ph.D., Delft University of Technology, Delft, The Netherlands
- Roelvink, J.A. and Brøker, I. (1993), Cross-shore profile models. *Coastal Engineering*, 21, pp. 163-191.
- Roelvink, J. A., Meijer, Th. J. G. P., Houwman, K. T., Bakker, R., and Spanhoff, R. (1995), Field validation and application of a coastal profile model. *Coastal Dynamics*, pp. 818-828, ASCE, New York.
- Roelvink, J. A. and Reniers, A. J. H. M. (1995), LipIID Delta Flume Experiments. Report H2130, Delft Hydraulics, Delft, The Netherlands.
- Roelvink, J.A. and Stive, M. J. F. (1989), Bar-generating cross-shore flow mechanisms on a beach. *Journal of Geophysical Research*, 94(C4), pp. 4785-4800.
- Ruessink, B. G. (1995), On the origin of infragravity waves in the surf zone of a dissipative multiple bar system. *Coastal Dynamics*, pp. 93-104, ASCE, New York.
- Ruessink, B. G., 1998a. Infragravity waves in a dissipative multiple bar system. Ph.D. Thesis, University of Utrecht, Utrecht, ISBN: 90-6909-256-1
- Ruessink, B.G. (1998b), The temporal and spatial variability of infragravity energy in a barred nearshore zone. *Continental Shelf Research*, 18(6), pp. 585-605.
- Ruessink, B.G., Houwman, K. T., and Hoekstra, P. (1998), The systematic contribution of transporting mechanisms to the cross-shore sediment transport in water depth of 3 to 9 m. *Marine Geology*, 152, pp. 295-324.
- Ruessink, B.G., Houwman, K. T., and Hoekstra, P. (1999a), Medium-term frequency distributions of cross-shore suspended sediment transport rates in water depths of 3 to 9 m. *Coastal Engineering*, 38, pp. 25-46.
- Ruessink, B.G. and Kroon, A. (1994), The behaviour of a multiple bar system in the nearshore zone of Terschelling, the Netherlands: 1965-1993. *Marine Geology*, 121, pp. 187-197.
- Ruessink, B.G., Miles, J. R., Feddersen, F., Guza, R. T., and Elgar, S. (2001), Modeling the alongshore current on barred beaches. *Journal of Geophysical Research*, 106(C10), pp. 22451-22464.
- Ruessink, B. G., Miles, J. R., and Russell, P. E. (1999b), Infragravity velocity variance partitioning across a subtidal bar. Report Coast3D; Volume of abstracts, Overall workshop, Utrecht, University of Utrecht, Utrecht.
- Ruessink, B.G., Van Enckevort, I. M. J., Kingston, K. S., and Davidson, M. A. (2000), Analysis of observed two- and three dimensional nearshore bar behaviour. *Marine Geology*, 169(1-2), pp. 161-183.
- Russell, P.E. (1993), Mechanisms for beach erosion during storms. *Continental Shelf Research*, 13(11), pp. 1243-1265.
- Sallenger, A.H.Jr. and Howd, P. A. (1989), Nearshore bars and the breakpoint hypothesis. *Coastal Engineering*, 12, pp. 301-313.
- Sallenger, A.H.Jr., Holman, R. A., and Birkemeier, W. A. (1985), Storm induced response of a nearshore-bar system. *Marine Geology*, 64, pp. 237-257.

- Sallenger, A.H. and Holman, R.A. (1987), Infragravity waves over a natural barred profile. *Journal of Geophysical Research*, 92, pp. 9531-9540.
- Schmidt-Koppenhagen, R., Gerdes, M., Tautenheim, E., and Grüne, J. (1997), Online Absorption Control System for Wave Generation. *Proceedings Waves*, pp. 1295-1305, ASCE, New York.
- Schönfeldt, H.J. (1995), On the modification of edge waves by longshore currents. *Continental Shelf Research*, 15(10), pp. 1213-1220.
- Shand, R.D., Bailey, D. G., and Shepherd, M. J. (1999), An inter-site comparison of net offshore bar migration characteristics and environmental conditions. *Journal of Coastal Research*, 15(3), pp. 750-765.
- Shelden, J. G., Rahoy, D. S., Chase, S. A., and Headland, J. R. (1999), Project performance analysis and monitoring for the Coney Island, NY Storm Damage Reduction Project. *Proceedings Coastal Sediments*, pp. 1946-1961, ASCE, Reston, Virginia, USA.
- Shin-ichi Aoki and Yasumi Yamamura (2000), A practical method for estimating bound long waves and its application to the analysis for free long waves. *Proceedings Coastal Engineering*, pp. 3941-3953, ASCE, Reston, Virginia, USA.
- Short, A.D. (1975), Multiple offshore bars and standing waves. *Journal of Geophysical Research*, 80, pp. 3838-3840.
- Short, A.D. (1992), Beach systems of the central Netherlands coast: processes, morphology and structural impacts in a storm driven multi-bar system. *Marine Geology*, 107, pp. 103-137.
- Sistemans, P.G.J. and Van Rijn, L. C. (2003), Transport of graded sediment by irregular waves and a current over a rippled bed. in prep.,
- Smith, J. K., Svendsen, I. A., and Putrevu, U. (1992), Vertical structure of the nearshore current at DELILAH: measured and modeled. *Proceedings Coastal Engineering*, pp. 2825-2838, ASCE, New York, USA.
- Soulsby, R. L. (1998), Coastal sediment transport: the COAST3D project. *Proceedings Coastal Engineering*, pp. 2548-2558, ASCE, Virginia, USA.
- Soulsby, R. L. (2000), Coastal study of three-dimensional sand transport processes and morphodynamics (Project COAST-3D). EU EUROCEAN Conference, Hamburg, Germany.
- Southgate, H.N. (1995), The effects of wave chronology on medium and long term coastal morphology. *Coastal Engineering*, 26, pp. 251-270.
- Southgate, H.N. and Nairn, R. B. (1993), Deterministic profile modelling of nearshore processes. Part 1. Waves and currents. *Coastal Engineering*, 19, pp. 27-56.
- Southgate, H. N. and Wallace, H. M. (1994), Breaking wave persistence in parametric surf zone model. *Proceedings Coastal Dynamics*, pp. 543-555, ASCE, New York, USA.
- Steezel, H. J., 1993. Cross-shore transport during storm surges. Ph.D., Delft Hydraulics, Delft, Netherlands, ISBN: 90-9006345-5
- Stive, M. J. F. (1986), A model for cross-shore sediment transport. *Proceedings Coastal Engineering*, pp. 1550-1564, ASCE, New York, USA.
- Stive, M.J.F. and Battjes, J. A. (1984), A model for offshore sediment transport. *Proceedings Coastal Engineering*, pp. 1-17.
- Stive, M. J. F. and De Vriend, H. J. (1994), Shear stresses and mean flow in shoaling and breaking waves. *Proceedings Coastal Engineering*, pp. 594-608, ASCE, New York.
- Stive, M.J.F. and De Vriend, H. J. (1995), Modelling shoreface profile evolution. *Marine Geology*, 126(1-4), pp. 235-248.
- Stokes, G.G. (1847), On the theory of oscillatory waves. *Transactions of the Cambridge Philosophical Society*, 8, pp. 441-455.
- Stolk, A. (1989), Zandsysteem kust, een morfologische karakterisering (Sandsystem coast, a morphological characterisation). Report Geopro 1989.02, University of Utrecht, Utrecht.
- Stripling, S. and Damgaard, J. S. (1997), Improvement of morphodynamic predictions in Cosmos-2D. Report IT443, HR Wallingford, Wallingford, England.
- Sunamura, T. and Maruyama, K. (1987), Wave-induced geomorphic response of eroding beaches with special reference to seaward migrating bars. *Proceedings Coastal Sediments*, pp. 788-801, ASCE, New York.
- Svendsen, I.A. (1984a), Mass flux and undertow in a surf zone. *Coastal Engineering*, 8, pp. 347-365.
- Svendsen, I.A. (1984b), Wave heights and set-up in a surf zone. *Coastal Engineering*, 8, pp. 303-329.

- Svendsen, I.A. and Lorenz, R. S. (1989), Velocities in combined undertow and longshore currents. *Coastal Engineering*, 13, pp. 55-79.
- Svendsen, I.A., Schäffer, H. A., and Hansen, J. B. (1987), The interaction between the undertow and the boundary layer flow on a beach. *Journal of Geophysical Research*, 92(C11), pp. 11845-11856.
- Swart, D. H. (1974), Offshore sediment transport and equilibrium beach profiles. Report 131, Delft Hydraulics, Delft, The Netherlands.
- Swart, D. H. (1978), Vocooidal water wave theory, Volume 1: Derivation. Report CSIR Report 357, National Research Institute for Oceanology, Stellenbosch.
- Swart, D.W. (1977). Predictive equations regarding coastal transports, *Proceedings Coastal Engineering*, ASCE, New York, USA, pp. 1113-1132.
- Thornton, E.B. and Guza, R. T. (1983), Transformation of wave height distribution. *Journal of Geophysical Research*, 88(C10), pp. 5925-5938.
- Thornton, E.B. and Guza, R. T. (1986), Surf zone longshore currents and random waves: field data and models. *Journal of Physical Oceanography*, 16(7), pp. 1165-1178.
- Thornton, E.B., Humiston, R. T., and Birkemeier, W. A. (1996), Bar/trough generation on a natural beach. *Journal of Geophysical Research*, 101(C5), pp. 12097-12110.
- Traykovski, P., Hay, A.E. Irish, J.D. and Lynch, J.F. (1999). Geometry, migration, and evolution of wave orbital ripples at LEO-15. *Journal of Geophysical Research* 104 (C1), pp. 1505-1524.
- Van Enckevort, I. M. J., 2001. Daily to yearly nearshore bar behaviour. Ph.D. Thesis, University of Utrecht, Utrecht, The Netherlands, ISBN: 90-6809-322-3
- Van Rijn, L. C. (1993), Principles of sediment transport in rivers, estuaries and coastal seas. Aqua Publications, Amsterdam, ISBN 90-800356-2-9.
- Van Rijn, L. C. (1994), Principles of fluid flow and surface waves in rivers, estuaries, seas and oceans. Aqua Publications, Amsterdam, ISBN 90-800356-1-0.
- Van Rijn, L. C. (1998), Principles of coastal morphology. Aqua Publications, Amsterdam, ISBN 90-800356-3-7.
- Van Rijn, L. C. (2000), General view on sand transport by currents and waves: data analysis and engineering modelling for uniform and graded sand (TRANSPOR 2000 and CROSMOR 2000 models). Report Z2899.20 Z2099.30 Z 2824.30, WL | Delft Hydraulics, Delft, The Netherlands.
- Van Rijn, L. C., Grasmeyer, B. T., and Ruessink, B. G. (2000), Measurement errors of instruments for velocity, wave height, sand concentration and bed levels in field conditions. Report, University of Utrecht/Delft Hydraulics, Utrecht.
- Van Rijn, L.C. and Havinga, F. J. (1995), Transport of fine sands by currents and waves. *Journal of Waterway, Port, Coastal and Ocean Engineering*, 121(2), pp. 123-133.
- Van Rijn, L.C., Nieuwjaar, M. W. C., Van der Kaay, T., Nap, E., and Van Kampen, A. (1993), Transport of fine sands by currents and waves. *Journal of Waterway, Port, Coastal and Ocean Engineering*, 119(2), pp. 123-143.
- Van Rijn, L. C., Ruessink, B. G., and Mulder, J. P. M. (2002a), Coast3D-Egmond. The behaviour of a straight sandy coast on the time scale storms and seasons. Aqua Publications, Amsterdam, ISBN 90-800356-5-3.
- Van Rijn, L.C. and Walstra, D.J.R., 2002. Basic features of hydrodynamics in the surf zone of Egmond.: in prep.
- Van Rijn, L. C., Walstra, D. J. R., Grasmeyer, B. T., and Kleinhout, K. (2001), Hydrodynamics and morphodynamics in the surf zone of a dissipative beach. *Proceedings Coastal Dynamics*, pp. 373-382, ASCE, Reston, Virginia, USA.
- Van Rijn, L.C., Walstra, D. J. R., Grasmeyer, B. T., Sutherland, J., Pan, S., and Sierra, J. P. (2002b), The predictability of cross-shore bed evolution of sandy beaches at the time scale of storms and seasons using process-based profile models. *Coastal Engineering*, in press.
- Van Rijn, L.C. and Wijnberg, K. M. (1996), One-dimensional modelling of individual waves and wave-induced longshore currents in the surf zone. *Coastal Engineering*, 28, pp. 121-145.
- Vincent, C.E. and Green, M. O. (1990), Field measurements of the suspended sand concentration profiles and fluxes and the resuspension coefficient γ_0 over a rippled bed. *Journal of Geophysical Research*, 95(C7), pp. 11591-11601.
- Vincent, C.E., Hanes, D. M., and Bowen, A. J. (1991), Acoustic measurements of suspended sand on the shoreface and the control of concentration by bed roughness. *Marine Geology*, 96, pp. 1-17.

- Walstra, D. J. R., Mocke, G. P., and Smit, F. (1994), Roller contributions as inferred from inverse modelling techniques. *Coastal Engineering*, pp. 1205-1218, ASCE, New York.
- Walstra, D. J. R., Mocke, G. P., and Smit, F. (1996), Roller contributions as inferred from inverse modelling techniques. *Proceedings Coastal Engineering*, pp. 1205-1218, ASCE, New York.
- Walstra, D. J. R., Weerakoon, W. M. S., and Van Rijn, L. C. (1998), Validation of Unibest-TC on Egmond data. Report Z2394.20, WL|Delft Hydraulics, Delft, The Netherlands.
- Walstra, D. J. R. (2000), Userguide for Unibest-TC. Report Z2897, WL|Delft Hydraulics, Delft, The Netherlands.
- Weggel, J.R. (1972), Maximum breaker height. *Journal of Waterway, Port, Coastal and Ocean Engineering*, 98(WW4), pp. 529-549.
- Wijnberg, K. M., 1995. Morphologic behaviour of a barred coast over a period of decades. Ph.D. Thesis, University of Utrecht, Utrecht, The Netherlands, ISBN: 90-6266-125-4
- Wolf, F. C. J., 1997. Hydrodynamics, sediment transport and daily morphological development of a bar-beach system. Ph.D. Thesis, University of Utrecht, Utrecht, The Netherlands.
- Wright, L.D. and Short, A. D. (1984), Morphodynamic variability of surf zones and beaches: a synthesis. *Marine Geology*, 56, pp. 93-118.
- Wright, L.D., Nielsen, P., Shi, N.C. and List, J.H. (1986), Morphodynamics of a bar-trough surf zone. *Marine Geology*, 70, pp. 251-285.
- Zhang, D. P. and Sunamura, T. (1994), Laboratory experiment of longshore bars produced by breaker-induced vortex action. *Proceedings Coastal Dynamics*, pp. 29-43, ASCE, New York.